Enzyme inspired proton reduction catalysts

This thesis is submitted in partial fulfilment of the requirements for the degree of Doctor of Philosophy

Shishir Ghosh

2014

I, Shishir Ghosh, confirm that the work presented in this thesis is my own. Where information has been derived from other sources, I confirm that this has been indicated in the thesis.

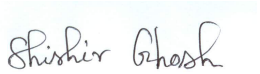

Shishir Ghosh, London, October 2014

Abstract

This thesis demonstrates electrocatalytic proton reduction by a variety of molecular catalysts including biomimetic models of [FeFe]-hydrogenase enzyme. Hydrogenases are group of metalloenzymes capable of reversible reduction of protons into dihydrogen and are divided into three groups according to the metal content in their active sites namely [FeFe]-hydrogenase, [NiFe]-hydrogenase and [Fe]-hydrogenase. The principle objective of this work has been the development of efficient iron-based electrocatalysts that can catalyse the reduction of protons at reasonably mild potentials.

Chapter 1 provides an overview of electrocatalytic proton reduction by earth-abundant metal complexes together with a brief discussion of hydrogenase enzymes and model complexes developed to mimic the function of the [FeFe]-hydrogenase.

The synthesis, characterisation and catalytic properties of diiron biomimetics containing various diamines and diphosphines are detailed in Chapters 2-5. Most of these ligands are electrochemically non-innocent and were used in order to mimic the function of the [FeFe]-hydrogenase active site as the later also bonded to an additional redox co-factor which relays electron to-from the diiron centre during catalysis.

Chapters 6-7 detail the synthesis, structure and electrocatalytic proton reduction ability of octahedral and square-pyramidal mononuclear iron complexes. These complexes have certain features of the active site of [FeFe]-hydrogenase and are shown to be efficient catalysts for the reduction of protons.

Chapters 8-10 detail electrocatalytic proton reduction by low-valent iron carbonyl clusters. All have an electronegative main group element directly bonded to the cluster core which provides a site for acidic hydrogen to interact with metal-bound basic hydride during catalysis. Electrocatalytic proton reduction by related triruthenium 2-aminopyridinate clusters has also been described in Chapter 10.

Acknowledgements

Firstly, I would like to thank my supervisor Dr. Graeme Hogarth for all his help throughout my PhD and his patience with my speculative ideas and interpretations. I would also like to thank my secondary supervisor Professor Gopinathan Sankar for his help during my PhD.

Then, I would like to thank Dr. Katherine B. Holt for helping me with electrochemistry and Professor Michael G. Richmond for carrying out theoretical calculations required for my work. Thanks also to Professors Shariff E. Kabir and Ebbe Nordlander for their excellent collaborations.

I extend special thanks to Dr. Nathan Hollingsworth, a man who never says no to anyone, for his help throughout my PhD. Lastly, I would like to thank all the friends I have made during my PhD. There are too many people to mention but you know who you are, you've made my PhD very enjoyable.

Contents

Index of Figures

Index of Tables

Chapter 1

An overview of electrocatalytic proton reduction by earth-abundant metal complexes

1.1. Introduction

Two of the greatest challenges facing mankind are rapidly dwindling stocks of fossil fuels and the effects of global warming caused by increasing emissions of greenhouse gases. Both issues stem from our over-reliance on fossil fuels as energy sources since one of the products formed during their combustion, carbon dioxide, is the main culprit behind global warming. Hence if we can replace fossil fuels with other eco-compatible energy sources both problems can be alleviated. In addition to fossil fuels, many countries have been using nuclear energy to produce electricity and although less significant we have started harnessing solar and wind energy, but their diffusive and periodic nature require concentration and storage in other useful forms of energy.

At present solar energy is stored in the form of electricity using photovoltaic (PV) cells and related devices whose efficiency is far less from the level required to meet demand. Further, converting solar energy into electricity and storing it in batteries is not sustainable since highly efficient batteries utilise rare metals whose stocks are limited. Thus we have to find different ways for the storage of solar energy other than batteries in order to harness it in a sustainable fashion.

Due to its potential as a clean, high density and transportable energy carrier, a great deal of effort is being devoted to the production of hydrogen *via* economically sustainable methods. Currently, steam reforming is the cheapest way for the large-scale production of hydrogen but uses hydrocarbon fuels as feedstock, so is unsustainable. Hydrogen can also be produced from water *via* electrolysis which is a pragmatic approach to address this problem as electrons required for the reduction of protons can be derived from renewable sources such as solar and wind. The current electrolytic cells used to split water operate at very high over-potentials and thus a large excess of electricity has to be provided to drive the process forward. The over-potential can be lowered by using platinum but the high cost and scarcity of this metal limits its widespread use. Hence the search for efficient electrocatalysts which utilise earth-abundant metals (e.g. Fe, Ni, Co) and are able to

catalyse the reduction of protons at low over-potentials is of great importance. The low cost, high natural abundance and importantly biocompatibility of iron make it most attractive and consequently large numbers iron-complexes are now coming under scrutiny as a potential electrocatalysts for the clean formation of hydrogen.

The vast majority of this effort focuses on biomimetics of the active site(s) of some ancient enzymes, termed hydrogenases [1], especially the [FeFe]-hydrogenases, the structure of which has been established by X-ray crystallography [2,3]. [FeFe]-hydrogenases are highly efficient proton-reduction catalysts and contain a rare example of a bio-organometallic active site (see later). Herein we will briefly discuss the structure and function of the hydrogenase enzymes together with molecular electrocatalysts, based on earth-abundant metals, developed for electrocatalytic proton reduction.

1.2. Electrocatalytic proton reduction by iron complexes

1.2.1. Hydrogenase enzymes and biomimetic models

Hydrogenases are a diverse group of metalloenzymes that catalyze the deceptively simple molecular reaction, the conversion of dihydrogen into protons and electrons and the reverse reaction, the formation of dihydrogen (Eq. 1.1) [6-12]. The active site of these enzymes contain specialized metal centres that dramatically increases the acidity of H_2 and leads to heterolytic cleavage of H–H bond, aided by the presence of a nearby base. The reverse reaction, the generation of hydrogen, involves coupling of H^+ and H^-.

$$2H^+ + 2e^- \rightleftharpoons H_2 \qquad \text{(Eq. 1.1)}$$

Hydrogenases occur in many microorganisms especially in archaea, bacteria, and some eukaryotes. Since they are found only in primitive microorganisms and play a crucial role in the anaerobic microbial metabolism, it is believed that nature developed these enzymes at the early stage of life on Earth when it had an oxygen-deficient atmosphere. Hydrogenases are divided into three groups according to the metal content in their active sites namely; (i) the [FeFe]-hydrogenase whose active site contains two iron atoms [2,3], (ii) the [NiFe]-hydrogenase whose active site contains a nickel and an iron atom [13],

and (iii) the [Fe]-hydrogenase containing a single iron atom in its active site [14,15]. All three classes of hydrogenases are phylogenetically unrelated to each other [16,17].

Both [FeFe]- and [NiFe]-hydrogenases contain iron-sulphur clusters (ferrodoxin clusters) within their protein scaffold (Figures 1.1 and 1.2), while the [Fe]-hydrogenase possesses a special organic cofactor next to iron. The active site of both [FeFe]- and [NiFe]-hydrogenases is buried deep within the protein structure and contain a series of iron-sulphur clusters from the active site to the surface of the enzyme. In [FeFe]-hydrogenase, eighteen iron atoms arranged in a chain of five iron-sulphur clusters: four of the cubane type and one a [2Fe-2S] cluster (Figure 1.1) [17], whereas two cubane type and a [3Fe-4S] cluster consists of eleven iron atoms make this chain in [NiFe]-hydrogenase (Figure 1.2) [17]. These iron-sulphur clusters relay electrons during catalysis i.e. they provide electrons during proton reduction, while removing electrons from the active site during dihydrogen oxidation. Both enzymes also have proton transfer pathway and gas channel from the active site to the enzyme surface through which H^+ and H_2 can reach the deeply buried active site [6,17].

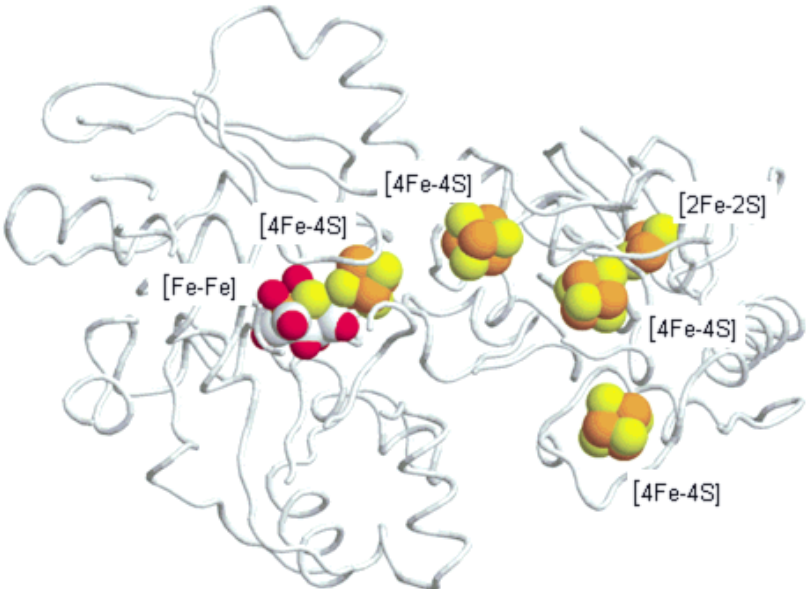

Figure 1.1. Crystal structure of *C. pasteurianum* [FeFe]-hydrogenase [17]. Coordinates are from the Protein Databank file 1FEH. The colour scheme is as follows: iron, orange; nitrogen, blue; oxygen, red; sulphur, yellow.

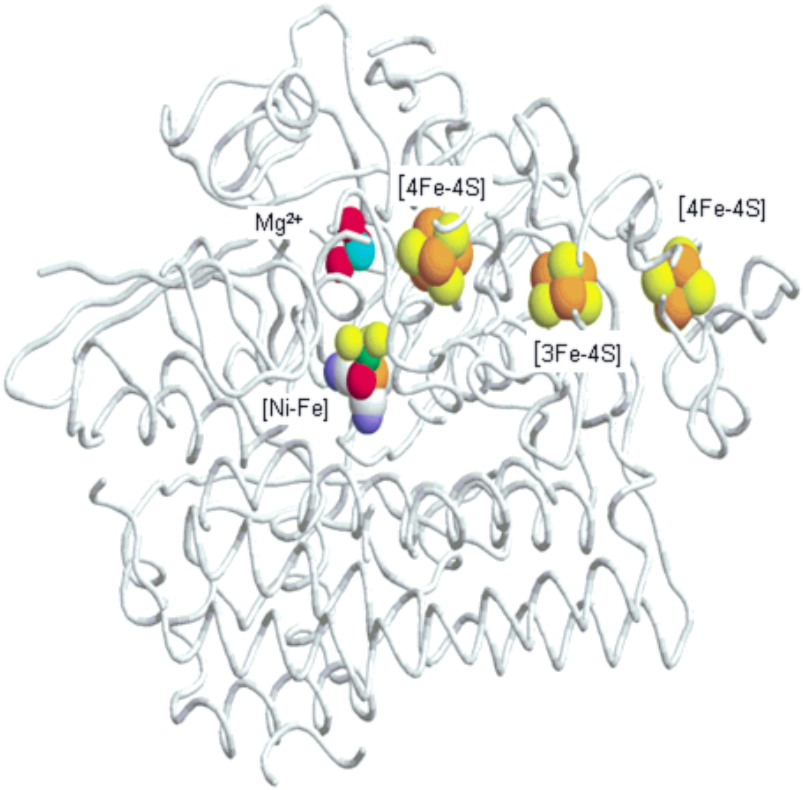

Figure 1.2. Crystal structure of [NiFe]-hydrogenase from *D. gigas* [17]. The Ni-Fe centre is in the centre, with the nickel to the front and iron with CN and CO ligands to the back; the peroxo ligand is in red. Coordinates are from the Protein Databank file 1YQ9. Part of the protein has been sliced away to show the metal centres. The colour scheme is as follows: iron, orange; magnesium, cyan; nickel, green; nitrogen, blue; oxygen, red; sulphur, yellow.

Figure 1.3 shows a schematic representation of the active site of the three hydrogenases. The iron atoms are joined together by an azadithiolato bridge in the active site of [FeFe]-hydrogenase, and are also ligated by biologically unusual CO and CN^- ligands with one CO occupying a semi-bridging position. This diiron unit is also linked to a tetrairon cubane cluster [4Fe4S] *via* a cysteinyl sulphur bridge while the later is anchored to the protein by making bond with three more cysteines located at the backbone of the protein. The iron atom distal to the cubane cluster has a vacant coordination site or a coordinated water molecule in the resting state which is occupied by a carbon monoxide in the CO-inhibited state of the enzyme. The [FeFe]-hydrogenase is more efficient in proton reduction than dihydrogen splitting, although its location dictates its function within a cell. The periplasmic [FeFe]-hydrogenase reduces protons, while it oxidizes dihydrogen when located in cytoplasm.

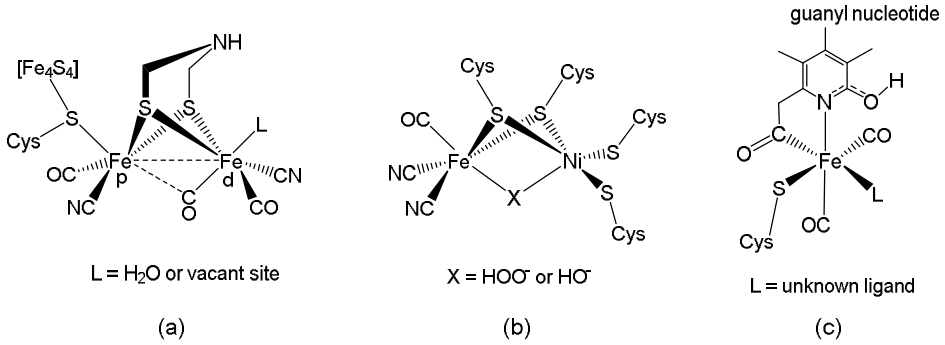

Figure 1.3. Schemetic representation of the active site of (a) [FeFe]-hydrogenase, (b) [NiFe]-hydrogenase, and (c) [Fe]-hydrogenase.

In contrast the [NiFe]-hydrogenase shows similar catalytic efficiency for both proton reduction and dihydrogen oxidation. The nickel and iron in the active site of [NiFe]-hydrogenase are joined by two cysteinyl sulphurs and an oxo- or peroxo-bridge. The nickel atom is further bonded to two cysteine residues of the protein, while two CN^- and a CO complete the coordination sphere of the iron atom. The lone iron atom in the active site of [Fe]-hydrogenase is also ligated by CO and cysteinyl sulphur, the sixth coordination site probably containing a water molecule.

The observation that the [FeFe]-hydrogenase is a superior proton reduction catalyst over the other two enzymes, and the relatively simple preparative method involved in the synthesis of the diiron core of its active site, has meant that much research has been aimed at mimicking the structure and functionality of this enzyme. Several hundred compounds [6,7,9-11] have been studied as structural and functional model of this enzyme since the structure of the enzyme was elucidated crystallographically some fifteen years ago [2,3]. Although considerable success at building the structural model of its active site has resulted, it will take much more effort to mimic the functionality of the enzyme. Hydrogenases catalyse hydrogen evolution from water at potentials close to the thermodynamic potential (–0.41 V *vs.* normal hydrogen electrode, NHE, at pH 7), whereas the most efficient models operate at quite negative potentials [11,12]. The number of models of the active site of [NiFe]-hydrogenase are dramatically fewer [1,18] than those of the [FeFe]-hydrogenase, while model studies of the [Fe]-hydrogenase system have commenced only recently [1].

The catalytic mechanisms involved in dihydrogen production or oxidation by hydrogenases are not yet fully understood. The same catalytic pathway is involved in

both events i.e. the mechanism for proton reduction is just the reverse of that for dihydrogen oxidation and a recent catalytic cycle proposed for [FeFe]-hydrogenase is shown in Scheme 1.1 [8]. As noted earlier, in the resting state the distal iron atom is loosely bonded to an aqua or hydroxo ligand which is lost during enzyme activation *via* reduction. In the active state, the enzyme possesses a vacant coordination site on the distal iron centre and has an oxidation state [Fe(II)Fe(I)].

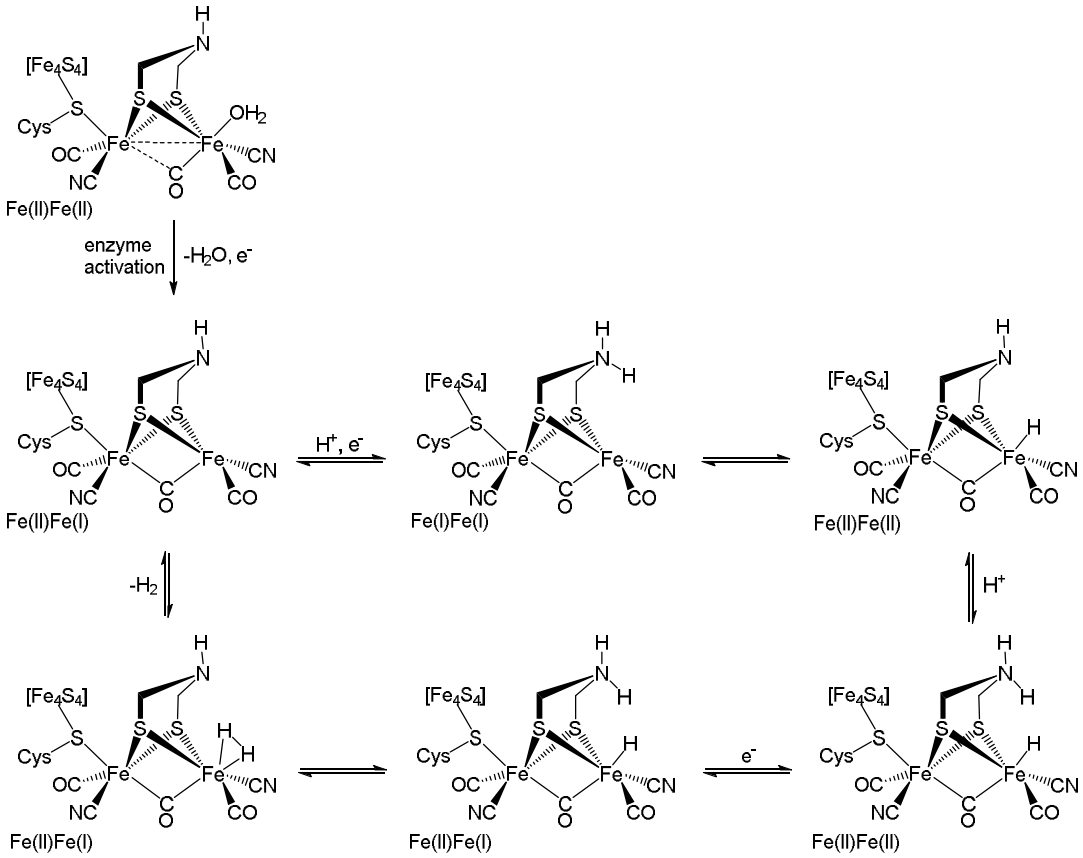

Scheme 1.1. Proposed mechanism for the electrocatalytic hydrogen evolution by [FeFe]-hydrogenase [8].

The next step is concomitant reduction of metal core and protonation at the bridgehead nitrogen. This proton is transferred to the vacant coordination site on the distal iron where it is reduced to a hydride and during this both iron centres are oxidized to the [Fe(II)Fe(II)] state. A second protonation at bridgehead nitrogen followed by reduction regenerates the [Fe(II)Fe(I)] state. At this point, combination of the basic iron-bound hydride and acidic amino proton can produce dihydrogen, which leaves the active site to reform the active [Fe(II)Fe(I)] state with a vacant site on the distal iron, thereby completing the catalytic cycle. Recently, several key intermediates involved in this

mechanism have been isolated and structurally characterized for various biomimetic models [19-21], which strengthens the validity of the proposed mechanism. The presence of a basic metal site for proton reduction and a pendant amino functionality for proton relay in close proximity within the enzyme's active site is the key factor behind its high efficiency. As we will see in the following sections, electrocatalysts that are developed retaining these delicate features are highly efficient in proton reduction although they operate at higher overpotentials than the enzyme.

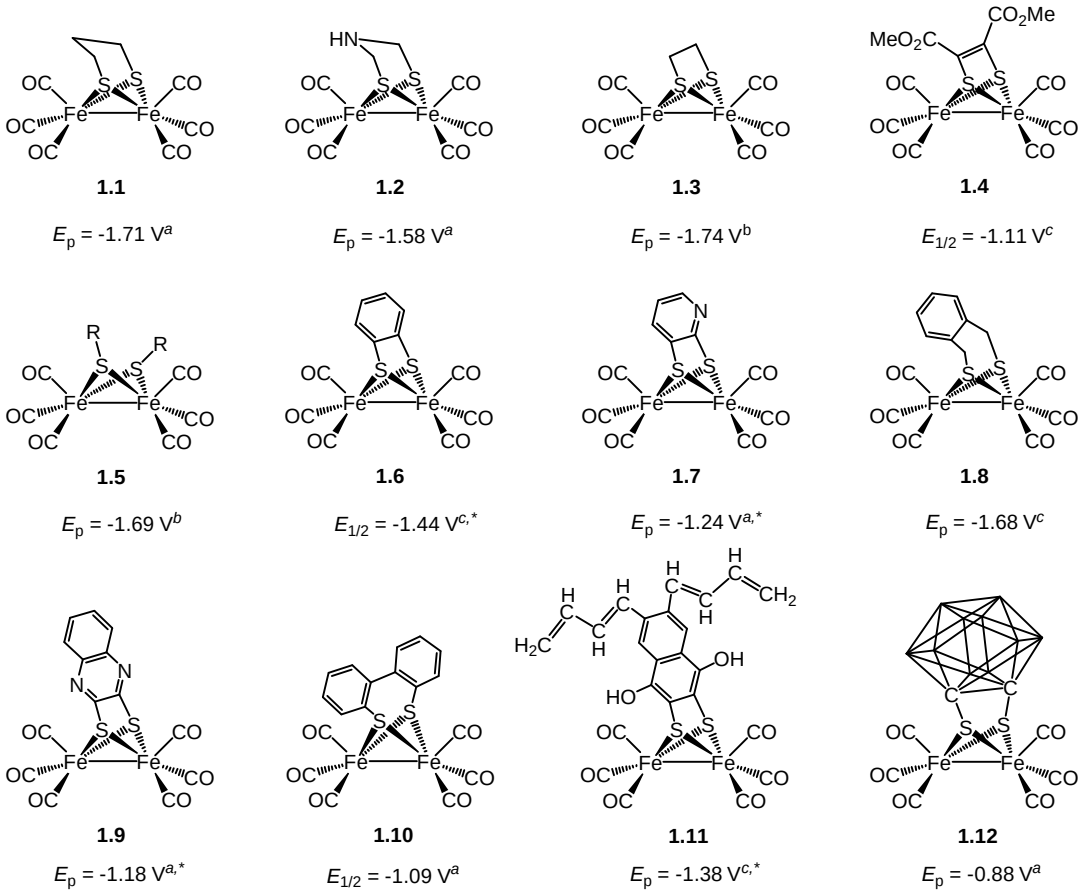

Figure 1.4. Reduction potentials (*vs* $Fc^{+/0}$) of various dithiolate-bridged diiron complexes as model of the active site of [FeFe]-hydrogenase [11, 24-31] ([a]in MeCN, [b]in THF, [c]in CH_2Cl_2, [*]2-electron process).

The active site of [FeFe]-hydrogenase is very similar to the dithiolato-bridged diiron complexes $Fe_2(CO)_6$(μ-pdt) (**1.1**) (pdt = $SCH_2CH_2CH_2S$) [22] and $Fe_2(CO)_6$(μ-adt) (**1.2**) (adt = SCH_2NHCH_2S) [23] and are viewed by inorganic chemists as derivative of them. Hence the research on the development of biomimetic models of the enzyme began with these diiron complexes, and later several other analogous diiron dithiolates have also

been studied (Figure 1.4) [11,24-31]. Although all these complexes have been found to catalyse proton reduction, their efficiency is far less than that of the enzyme, and a large over-potential is also required by most of them. Akin to the enzyme active site, a sufficiently basic diiron core is required for high catalytic efficiency, but none of these hexacarbonyls is basic enough to undergo protonation at diiron centre that will also reduce the catalytic over-potential. In order to circumvent this problem, carbonyl ligands were initially replaced by cyanides to increase the basicity of the diiron core, in accord with the active site. Treatment of these hexacarbonyls with cyanide salts mainly affords the dicyanides, $[Fe_2(CO)_4(CN)_2(\mu\text{-dithiolate})]^{2-}$, under normal conditions with trace amounts of monocyanides [32,33]. However, cyanide can not substitute more than two carbonyls despite its modest steric demands, which indicates that both ligand size and basicity affect the degree of substitution within these diiron dithiolate complexes [32,33]. Cyanide also has a propensity of forming linear M–CN–M′ ensembles [34] and metal cyanides are susceptible to N-protonation by acid which limits their use as a ligand in the biomimetic models. On the other hand, phosphines provide greater flexibility in both electronic and steric properties and their complexes display more versatile solubility without the complicating tendencies of cyanide [35]. Hence, phosphines have been widely used to replace carbonyls to increase the basicity of the diiron centres, and many hundreds of diiron biomimic have been reported in which one or more carbonyl(s) are substituted by phosphine(s) (Figure 1.5) [6,7,11,36]. In addition to these phosphine-substituted biomimetic models, diiron complexes containing amines, carbenes, nitrosyl etc. as ligands have also been tested for the electrocatalytic proton reduction (Figure 1.6) [11,37-41].

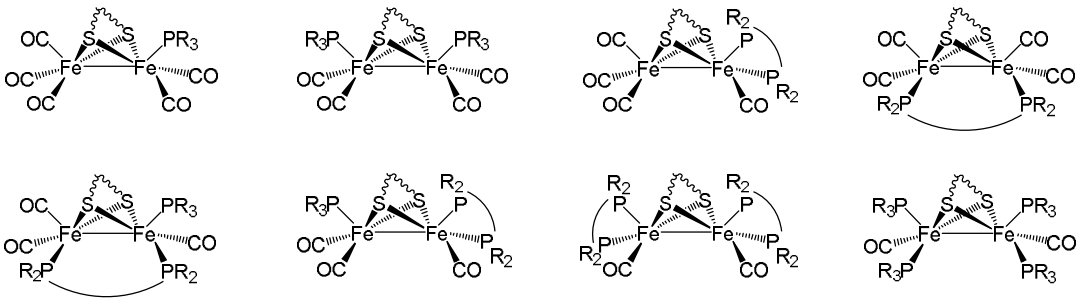

Figure 1.5. Various structural motifs of phosphine containing diiron biomimetics [6,7,11,36].

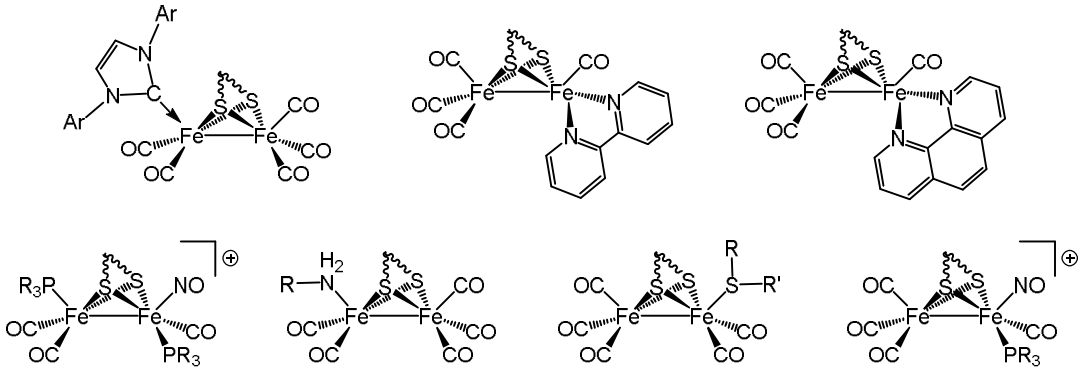

Figure 1.6. Biomimetics of [FeFe]-hydrogenase containing various non-phosphine ligands [11,37-41].

A great deal of information about the structure-activity relationship of the enzyme has also been obtained over the past decade leading to further improvement of biomimetic models. However, despite significant improvement of both catalytic efficiency and potential of the biomimetic models, the development of diiron model catalysts that can closely match the efficiency and catalytic potential of enzyme remains elusive. As noted earlier, the active site is buried deep within the protein structure, hence there are a number of small outer coordination sphere interaction between the active site and protein backbone leading to structural distortion (modification) that is not possible in simple synthetic models. For example, the diiron centre of the active site exists in so-called *rotated* form i.e. the carbonyls and cyanide ligands on one iron are oriented in staggered conformation with respect to those on the other iron, whereas those ligands are oriented in eclipsed conformation in almost all diiron biomimics. Recently, the biomimetic models have been incorporated into supramolecular structures including polymers, gels, micelles and peptide scaffolds in order to mimic the influence of the protein environment [36], which significantly improve both the activity and stability of models. However, this leads to additional complexity in the system, which is unwarranted for practical purposes.

1.2.2. Non-biomimetic iron catalysts

Although hundreds of biomimetic model of the active site of [FeFe]-hydrogenase enzyme have been synthesized and tested for electrocatalytic hydrogen evolution, only a few other iron systems have been electrochemically studied to date as proton reduction catalysts. The first report appeared in 1996, Savéant and co-workers demonstrating the proton reduction ability of the iron porphyrin complex, [(TPP)Fe(Cl)] (**1.13**). This

complex shows catalytic waves in presence of $[HNEt_3]^+$ and is robust under the experimental conditions (Figure 1.7) [42]. A mechanism was put forward involving two-one electron reduction events to afford catalytically active $[Fe^0]^{2-}$, which then protonates to afford $[Fe^{II}H]^-$ and liberates dihydrogen via a heterolytic pathway (Scheme 1.2). More recently, Ott and co-workers have reported electrocatalytic proton reduction by a mononuclear Fe(II) complex, **1.14** (Figure 1.7), containing phosphine, carbonyl and chelating dithiolate ligands [43]. This complex undergoes reversible protonation at sulphur as confirmed by IR and NMR spectroscopic data. Theoretical studies support a mechanism according to which protonation at sulphur followed by a one-electron reduction lead to an iron-sulphur bond scission to form a penta-coordinate Fe(II) intermediate which evolves hydrogen following two different pathways. Recently, several coordinatively and electronically unsaturated mononuclear Fe(II) complexes have been examined by several groups which can catalyze proton reduction at relatively mild potentials (Figure 1.8) [44-46].

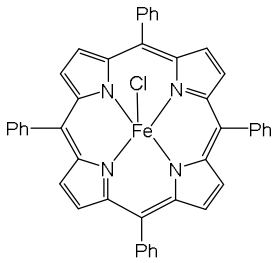

1.13

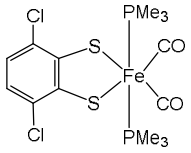

1.14

Figure 1.7. Example of a tetraaza macrocyclic iron complex and a dithiolene iron complex capable of proton reduction [42,43].

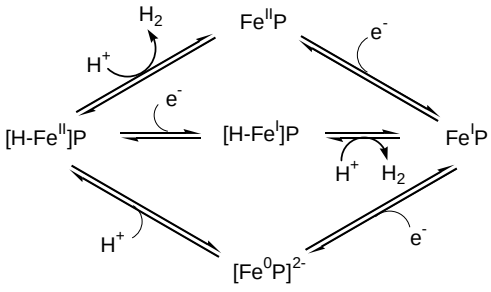

Scheme 1.2. Proposed mechanism for electrocatalytic hydrogen evolution by [(TPP)Fe(Cl)] (**1.13**) [42].

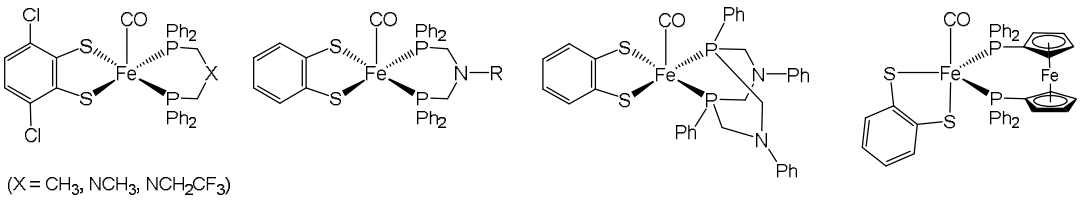

Figure 1.8. Examples of coordinatively and electronically unsaturated mononuclear Fe^{II} complexes capable of proton reduction [44-46].

Rose et al. studied the applicability of the fluorinated diglyoxime-iron complexes **1.15** and **1.16** (Figure 1.9) as electrocatalysts for hydrogen production and showed that more positive catalytic potentials, as compared to the biomimetics of [FeFe]-hydrogenase, can be achieved by tuning the ligand [47]. Turnover frequencies are estimated as 20 s^{-1} (**1.16**) and 200 s^{-1} (**1.15**) with 60-90% Faradic yields. Very recently, McNamara and co-workers reported that the iron polypyridyl complex **1.17** is highly active for the reduction of protons to hydrogen (Figure 1.9) [48], turnover frequencies of up to 1000 s^{-1} being achieved in MeCN, which increases to 3000 s^{-1} in the presence of water.

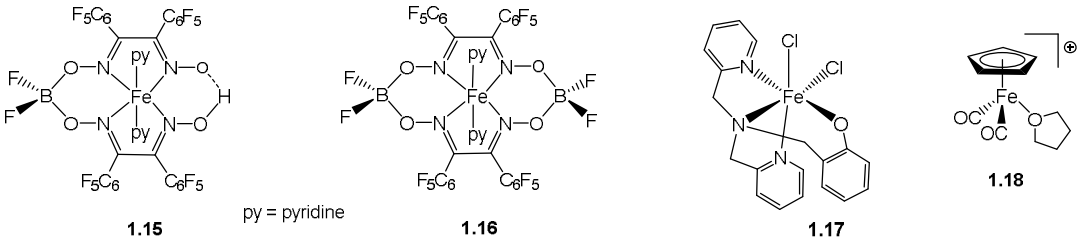

Figure 1.9. Examples of mononuclear iron complexes capable of proton reduction [47,48,50].

Cyclopentadienyl iron carbonyl complexes have also drawn considerable attention as proton reduction electrocatalysts since the electronic properties of the cyclopentadienyl ligand is found similar to that of the $\{Ni(SCys)_2(X)\}$ moiety of the bimetallic active site of the [NiFe]-hydrogenase [49]. For example, the cation **1.18** (Figure 1.9) generates hydrogen from Cl_3CCO_2H in DMF at –0.98 V *vs.* Fc/Fc^+ which is comparable with the catalytic potential of the most efficient diiron biomimics of [FeFe]-hydrogenase reported to date [50]. The proposed mechanism suggests that the actual catalytic species is the radical, $[CpFe(CO)_2]^{\cdot}$, which undergoes a further one-electron reduction to form the anion, $[CpFe(CO)_2]^-$. The latter is able to protonate to form a hydride, which liberates hydrogen upon reaction with acid. However, a major drawback of this system is the

dimerization of intermediate species involved in the catalytic cycle which deactivates the catalyst.

Electrochemical proton reduction using mixed-valence iron-thiolate clusters was shown by both Pickett and our group (Figure 1.10) [51-53]. In the doubly reduced state, the linear 66-electron tetrairon cluster $Fe_4(CO)_8\{\mu\text{-}(SCH_2)_3CMe\}_2$ has been found to reduce protons 500 times more efficiently than the diiron-dithiolate biomimics [51], whereas we have shown the triiron clusters exhibit principal catalytic waves in the one-electron reduced state [52,53]. Substitution of CO by PPh_3 results in a negative shift of catalytic potential as a result of greater electron-density on the triiron centre. Recently, a few iron carbonyl clusters, containing capping main group element, have also been tested for electrocatalytic proton reduction (Figure 1.10) [54-58].

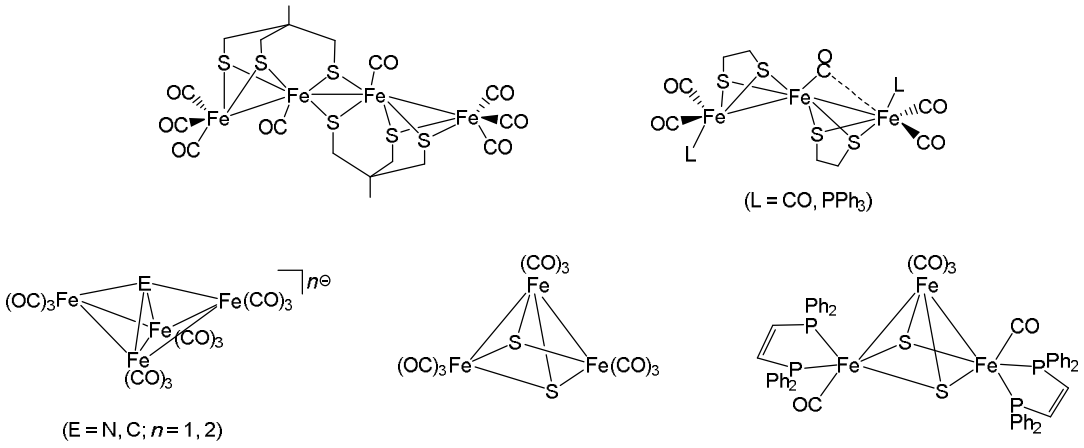

Figure 1.10. Examples of iron-carbonyl clusters capable of proton reduction [51-58].

As we can see, only a handful of non-biomimetic iron complexes were tested for electrocatalytic proton reduction as compared to the large number of biomimetic models. The current surge in the study of non-biomimetic iron catalysts can be attributed to the development of efficient mononuclear cobalt- and nickel-catalysts that can operate in relatively mild potentials compared to the most diiron biomimetics. Investigation on these non-biomimetic models also reveal that such iron complexes show promising catalytic features and deserve more attention.

1.3. Electrocatalytic proton reduction by cobalt complexes

Apart from biomimetics of the active sites of hydrogenases, cobalt complexes are one of the most widely investigated class of metal complexes studied as proton reduction catalysts [59-90]. As early as 1980, while studying the electrochemical reduction of CO_2 using tetraazamacrocyclic cobalt and nickel complexes as catalysts, Eisenberg et al. found that the macrocyclic **1.19** (Figure 1.11) evolves hydrogen from a $MeCN/H_2O$ mixture under nitrogen, which they proposed to occur *via* a cobalt-hydride intermediate [62]. Several polyamino Co^{III}, cobaltocene and cyclopentadienyl cobalt complexes had also been found to catalyse the reduction of protons at that time [63-65].

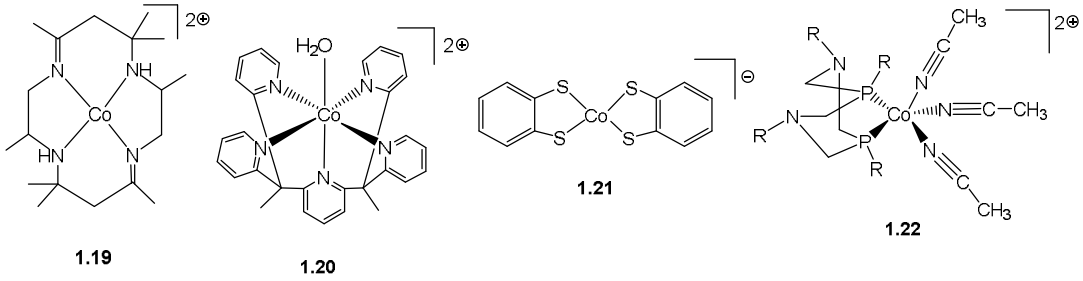

Figure 1.11. Examples of various cobalt complexes tested for the electrocatalytic reduction of protons [62,72,89,90].

Spiro and Kellett showed that water-soluble Co^{II} porphyrin and phthalocyanine complexes (Figure 1.12) are good electrocatalysts for the production of hydrogen from water [67-69]. These complexes reduce water to hydrogen at a mercury pool electrode in presence of CF_3CO_2H with almost 100% current efficiency and are robust under operating conditions but show a propensity to adsorb at the electrode [67,68]. Several polypyridine, iminopyridine and aminopyridine cobalt complexes have also been found to catalyse electrochemical reduction of proton in aqueous medium [71,72-75,87]. For example, **1.20** (Figure 1.11) generates hydrogen from neutral water with a turnover number of 5.5×10^4 and 100% Faradic efficiency. It also shows high stability in water with no loss in activity over 60 h. The catalytic potential of this complex can be tuned by peripheral substitutions on the penta-pyridine ligand [72]. Electrocatalytic proton reduction by a cobalt-dithiolene complex (**1.21**) [89] and a cyclic diphosphino-cobalt(II) complex (**1.22**) [90] with amine functionality on the phosphine backbone has also been reported recently (Figure 1.11).

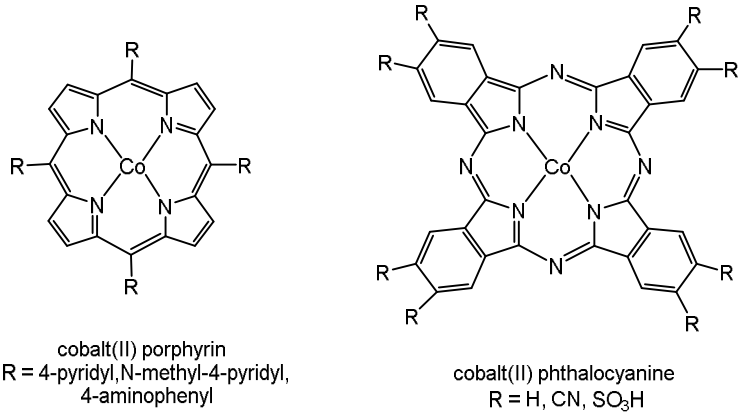

cobalt(II) porphyrin
R = 4-pyridyl,N-methyl-4-pyridyl, 4-aminophenyl

cobalt(II) phthalocyanine
R = H, CN, SO_3H

Figure 1.12. Examples of tetraaza-macrocyclic cobalt complexes capable of proton reduction [67-69].

The good lability of the axial ligands and relatively simple preparative methods keeps the cobalt glyoxime or cobaloxime complexes under continuous investigation. These pseudo-macrocyclic cobalt complexes were first developed as a functional model of vitamin B_{12} and related compounds and have a reputation for being very powerful nucleophiles in the reduced Co^{I} state - a property prerequisite for any proton reduction electrocatalyst [76]. Artero et al. investigated a series of cobaloximes as proton reduction catalysts (Figure 1.13) and found that these complexes are robust at higher pH but degrade quickly in presence of acid (pH ‹ 5) [77]. To overcome this problem a BF_2-linker is introduced in place of the H-bridge and this modification not only makes the BF_2-bridged cobaloximes more acid-resistant but also enables them to catalyze proton reduction at more positive potentials [78-81].

The cobaloxime system has been further studied by using N-propyl linker at one side together with H- or BF_2- linker on the other as well as using N-propyl linker at both ends (Figure 1.13) [74,79,83]. Recently N-aryl substituted cobaloximes were also studied by Peters and co-workers (Figure 1.13) [84]. Mechanistic investigations suggested a heterolytic pathway for hydrogen production with these cobaloximes but a homolytic pathway cannot be ruled out [77,79,80]. Another finding comes of this study is that species with more positive reduction potentials requires stronger acids to show significant catalytic activity than those with less positive reduction potentials. This can be correlated with the nucleophilicity of the complexes since the former species are less nucleophilic than the later. Much better catalytic efficiency has also been found for more nucleophilic cobaloximes i.e. those with more negative reduction potential.

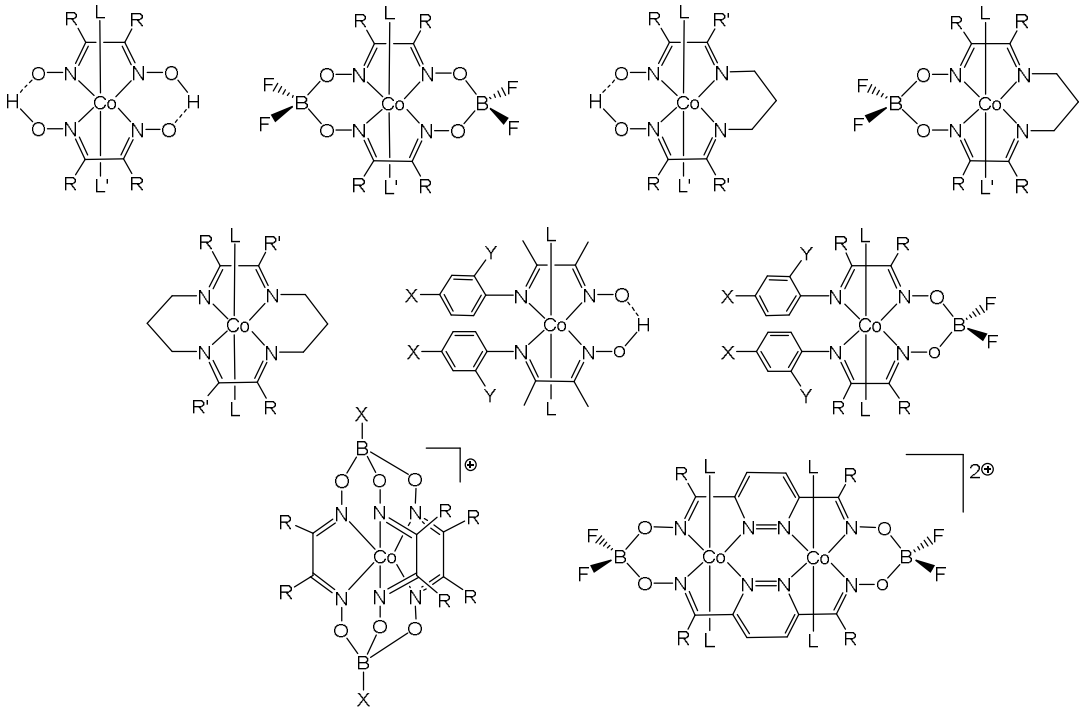

Figure 1.13. Examples of cobaloxime complexes capable of proton reduction [74-82,83-85,88].

Boron-capped tris(glyoximato) cobalt complexes have also been investigated for electrocatalytic proton reduction. These clathrochelate complexes (Figure 1.13) show remarkable catalytic activity for hydrogen evolution at potentials as positive as –0.55 V *vs.* SCE. All of these complexes trigger catalytic waves near the Co^{II}/Co^{I} couple at low acid concentration which exhibit a weak shift to more negative potentitals and an enhancement of intensity upon increasing acid concentration [85]. Recently, a dicobalt macrocyclic system has been shown to catalyze proton reduction by Peters et al. (Figure 1.13) [88].

As we can see a variety of cobalt complexes have been tested as electrocatalyst for proton reduction, and it has been found that these complexes often show better catalytic efficiency as well as relatively small over-potentials compared to the biomimetic models hydrogenases. The active site mimics of hydrogenases reported to date show their catalytic activity only in organic solvents in the presence of a proton source. In contrast, many of the abovementioned cobalt catalysts can operate in purely aqueous media which is essential for future technological applications. As a result, cobalt complexes are now considered as one of the most promising electrocatalysts for proton reduction and this area is rapidly expanding.

1.3. Electrocatalytic proton reduction by nickel complexes

Although Fisher and Eisenberg noted that the tetraazamacrocyclic nickel complex **1.23** (Figure 1.14) can catalyze the electrochemical reduction of proton from a $MeCN/H_2O$ mixture under N_2 almost thirty years ago [62], nickel complexes have not been considered as electrocatalyst for proton reduction until recently. A few more polyazamacrocyclic nickel complexes had also been shown to catalyze electrochemical proton reduction at that time [91,92].

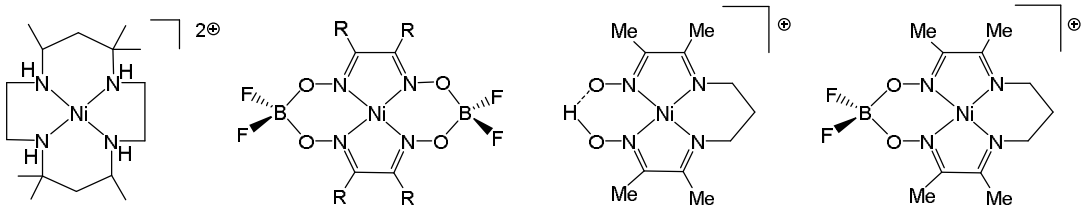

Figure 1.14. Examples of various nickel complexes tested for the electrocatalytic reduction of protons [62,81,83].

A number of glyoxime nickel and diimine-dioxime nickel complexes have also been studied as electrocatalysts for proton reduction (Figure 1.14) [81,83]. Pantani et al. studied the electrocatalytic properties of difluoroboryl annulated bis(glyoximato) nickel derivatives both in solution and on an electrode surface. In DMF, **1.24** which contains peripheral electron-donating methyl substituents triggers a catalytic wave at Ni^{II}/Ni^{I} couple whereas significant catalysis is only observed at Ni^{I}/Ni^{0} couple in case of **1.25** which contains peripheral electron-withdrawing phenyl groups. Since electrocatalytic proton reduction proceeds *via* a metal hydride intermediate, this observation suggests that the nucleophilicity of the metal within these complexes (i.e. the catalytic potential) can be tuned by varying the peripheral substituents. However, they show poor electrocatalytic activity when embedded on an electrode surface [81]. Recently, the proton reduction ability of a series of nickel dithiolene and nickel pyridinethiolate complexes have also been investigated (Figure 1.15) [93,94].

DuBois and his group have developed highly efficient proton reduction electrocatalysts using bis(diphosphine) nickel complexes (Figure 1.16) [95,96]. These $[(phosphine)_4Ni]^{2+}$

complexes have been developed as functional models of the [FeFe]-hydrogenase enzyme and contain pendant amine groups on the phosphine backbone. These model complexes possess two key structural features of the enzyme's active site that are responsible for it's excellent ability to catalyze reversible proton reduction – (i) vacant (or presence of a very labile ligand) coordination site for proton binding, and (ii) pendant amine group for proton relay.

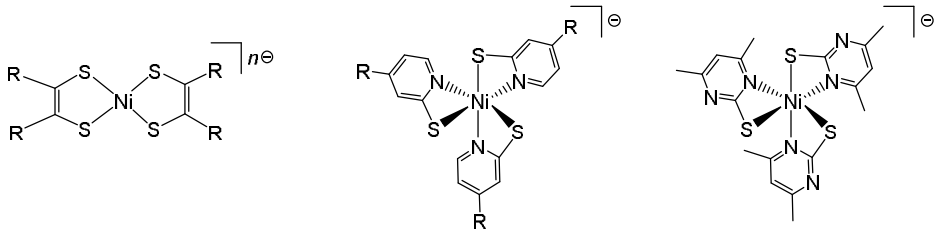

Figure 1.15. Examples of nickel dithiolene and nickel pyridinethiolate complexes capable of proton reduction [93,94].

Complex **1.28**, the first reported electrocatalyst of this kind, shows catalytic wave for proton reduction at –0.86 V *vs.* Fc/Fc^+ in MeCN in the presence of triflic acid with almost 100% current efficiency and a turnover frequency of 130 s^{-1} which is slightly less than that of [NiFe]-hydrogenase (700 s^{-1}) [95]. A recent report showed that covalent attachment of this complex onto multiwalled carbon nanotube results in a highly active catalytic material with exceptional stability (turnover number >100,000) which can operate under strongly acidic conditions with very low over-potential [96]. Further, it has been found that **1.29** can catalyze the electrochemical proton reduction at –1.13 V *vs.* Fc/Fc^+ with turnover frequencies of 33000 s^{-1} in dry MeCN and 106000 s^{-1} in the presence of 1.2 M of water (Figure 1.16) [103].

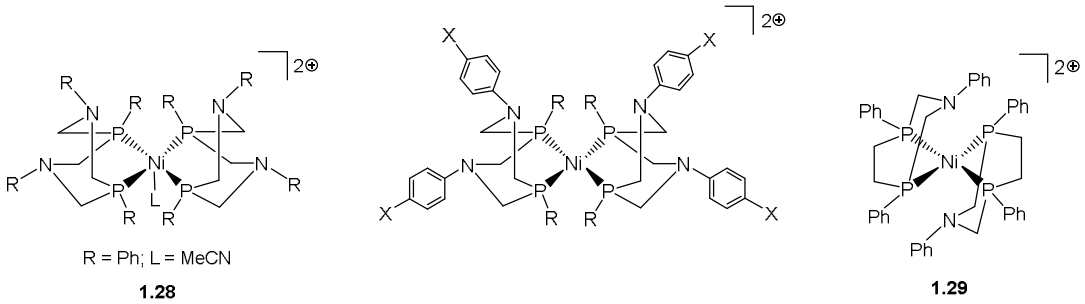

Figure 1.16. Examples of bis(diphosphine) nickel complexes capable of proton reduction [95-98,103].

The catalytic potential can be tuned by substituting the *para*-hydrogen of the phenyl rings bonded to nitrogen of the pendant amine groups even though the substituent is eight bonds away from the nickel, due to the highly effective electronic communication

between the metal and the pendant amines. It has been observed that introduction of an electron-donating substituent at this position shifts the catalytic potential to more negative values while the reverse shift is occurred in case of electron-withdrawing substituent [99]. The turnover frequency has also been found to increase by the presence of electron withdrawing *p*-substituents, a very favourable but unusual phenomenon because generally the turnover frequency decreases with positive shift of the catalytic potential for mononuclear system. Thus the delicate design of this catalyst system, containing both hydride and proton donors within the same molecule, makes them act like bifunctional catalysts for H_2 evolution [99].

Although the bis(diphosphine) nickel catalysts catalyze proton reduction at comparatively more negative potentials than the most cobalt catalysts, they exhibit high turnover numbers and turnover frequencies. The design of complex **1.29** that can catalyze proton reduction far more efficiently than the [FeFe]-hydrogenase is certainly a great achievement towards the development of electrocatalyst capable of serving as a functional model of hydrogenases.

1.4. Electrocatalytic proton reduction by the second and third row transition metal complexes

In addition to the abovementioned iron-, cobalt- and nickel-based electrocatalysts, few second and third row transition metal (especially molybdenum) complexes have been found to catalyze the reduction of protons under electrochemical conditions. For example, a sulphur rich dimolybdenum complex (**1.30**) has been found to electrocatalyze proton reduction with high current efficiency at low over-potentials (Figure 1.17) [104]. It generates hydrogen at –0.70 V *vs.* Fc/Fc^+ from an acetonitrile solution of *p*-cyanoanilinium tetrafluroborate on a glassy carbon electrode. Examination of the effect of substituent on the catalytic activity reveals that its catalytic activity is highly sensitive to the extent of substitution at sulphur as well as to the electronic influence of the cyclopentadienyl ring. The experimental observations and the theoretical calculations carried out to shed light on mechanism, both indicate that hydrogen elimination occurs from a neutral dihydrido intermediate **1.31** (Figure 1.17). Recently, Karunadasa et al. reported a molybdenum-oxo complex (**1.32**) (Figure 1.17) that can produce hydrogen from water at neutral pH or from sea water [105]. This complex electrocatalyzes

hydrogen production from water buffered at pH 7 at a potential of –0.93 V *vs.* SHE whilst it exhibits catalytic waves at –0.81 V *vs.* SHE when sea water (California) is employed as the proton source without any supporting electrolyte.

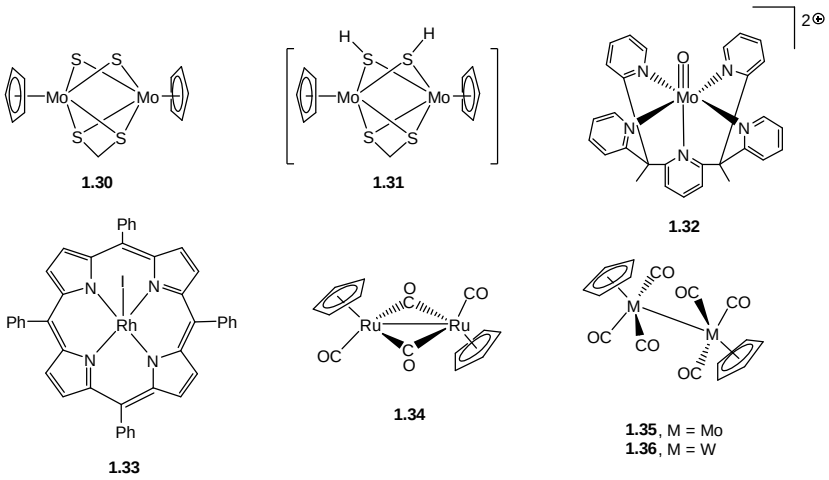

Figure 1.17. Examples of second and third row transition metal based complexes capable of proton reduction [104-107].

The tetraphenylporphyrin-rhodium complex **1.33** can also catalyze electrochemical proton reduction as shown by Savéant and co-workers (Figure 1.17) [106]. During catalysis the initial Rh^{III} complex is directly reduced to Rh^{I} which reacts with proton to give a Rh^{III} hydride. This hydride species undergoes further reduction to form a Rh^{II} hydride which is the key intermediate of the catalytic cycle although in presence of a strong electron-donating ligand (e.g. PEt_3) both Rh^{II} and Rh^{III} hydrides trigger hydrogen evolution. The electrocatalytic proton reduction ability of a series of cyclopentadienyl dimers **1.34-1.36** (Figure 1.17) has been shown by Felton et al. recently [107]. All of these dimers can generate hydrogen from weak acid although a large over-potential is required in every case [107].

1.5. Conclusions and aims

In summary, a great deal of research efforts has been currently ongoing to develop cheap electrocatalysts that can catalyze the reduction of protons at reasonably mild over-potentials with the efficiency of enzymes. Although the vast majority of this effort is mainly focused on the modelling of the active site of [FeFe]-hydrogenase, non-biomimetic models based on iron, cobalt and nickel have attracted considerable attention

in recent years. Some highly efficient nickel catalysts have been developed which can surpass enzymes efficiency with respect to certain parameters. We have been working on both diiron biomimics and non-biomimetic models for quite sometime and will describe some of our findings in the following chapters.

In this thesis, we will report a number of diiron models of the active site of [FeFe]-hydrogenase that are prepared using a range of diamines and diphosphines with particular emphasis on the redox active ligands, since the active site of the enzyme is linked to a redox co-factor (Fe4S4/cubane cluster) which plays key role in catalysis by acting as an electron reservoir. Our aim was to imitate this cooperative interaction between the diiron and tetrairon sites of the enzyme. Non-innocent diamines and bisphosphines such as 2,2'-bipyridine, 1,10-phenanthroline, 4,5-bis(diphenylphosphino)-4-cyclopenten-1,3-dione (bpcd) and bis(diphenylphosphino)ferrocene (dppf) have been introduced to the diiron models either as chelating or bridging ligands for this purpose. Diiron models containing 2,2'-bis(diphenylphosphino)propane have also been prepared to study the chelate-bridge isomerisation within these complexes.

We have also studied iron-based non-biomimetic model catalysts. A number of mono- and poly-nuclear low-valent iron complexes have been prepared and tested for electrocatalytic proton reduction. Most of these model catalysts contain certain structural features of the enzyme's active site and can be prepared following relatively simple synthetic procedures. The mono-nuclear iron complexes have been developed to model of the distal iron atom (distal to the Fe4S4 cluster, Fe_d in Figure 1.3) of the [FeFe]-hydrogenase active site, whilst an electronegative main group element has been incorporated into the cluster core of poly-nuclear low-valent iron complexes in order to facilitate proton-hydride reaction, a key step in electrocatalytic proton reduction.

The electrochemical properties of all these model catalysts has been probed by cyclic voltammetry (sometimes in different solvents) and their reactions with acids have been studied by IR and/or NMR spectroscopy. All these model catalysts have been found to catalyse proton reduction under electrochemical conditions in presence of a suitable acid(s) as the proton source.

1.6. References

(1) C. Tard and C. J. Pickett, *Chem. Rev.*, 2009, **109**, 2245-2274.

(2) J. W. Peters, W. N. Lanzilotta, B. J. Lemon and L. C. Seefeldt, *Science*, 1998, **282**, 1853-1858.

(3) Y. Nicolet, C. Piras, P. Legrand, C. E. Hatchikian and J. C. Fontecillacamps, *Structure*, 1999, **7**, 13-23.

(6) C. Tard and C. J. Pickett, *Chem. Rev.*, 2009, **109**, 2245-2274.

(7) F. Gloaguen and T. B. Rauchfuss, *Chem. Soc. Rev.*, 2009, **38**, 100-108.

(8) C. Greco, M. Bruschi, L. D. Gioia and U. Ryde, *Inorg. Chem.*, 2007, **46**, 5911-5921.

(9) V. Artero and M. Fontecave, *Coord. Chem. Rev.*, 2005, **249**, 1518-1535.

(10) K. A. Vincent, A. Parkin and F. A. Armstrong, *Chem. Rev.*, 2007, **107**, 4366-4413.

(11) G. A. N. Felton, C. A. Mebi, B. J. Petro, A. K. Vannucci, D. H. Evans, R. S. Glass and D. L. Lichtenberger, *J. Organomet. Chem.*, 2009, **694**, 2681-2699.

(12) M. W. W. Adams, *Biochim. Biophys. Acta*, 1990, **1020**, 115-145.

(13) A. Volbeda, M. H. Charon, C. Piras, C. E. Hatchikian, M. Frey and J. C. Fontecillacamps, *Nature*, 1995, **373**, 580-587.

(14) S. Shima, O. Pilak, S. Vogt, M. Schick, M. S. Stagni, W. Meyer-Klaucke, E. Warkentin, R. K. Thauer and U. Ermler, *Science*, 2008, **321**, 572-575.

(15) S. Shima, E. J. Lyon, R. K. Thauer, B. Mienert and E. Bill, *J. Am. Chem. Soc.*, 2005, **127**, 10430-435.

(16) R. Cammack, M. Frey and R. Robson, *Hydrogen as a Fuel: Learning from Nature*, Taylor & Francis: London and New York, 2001.

(17) A. L. De Lacey, V. M. Fernández, M. Rousset and R. Cammack, *Chem. Rev.*, 2007, **107**, 4304-4330.

(18) H. Ogata, W. Lubitz and Y. Higuchi, *Dalton Trans.*, 2009, **37**, 7577-7587.

(19) M. E. Carroll, B. E. Barton, T. B. Rauchfuss and P. J. Carroll, *J. Am. Chem. Soc.*, 2012, **134**, 18843-18852.

(20) J. M. Camara and T. B. Rauchfuss, *Nat. Chem.*, 2012, **4**, 26-30.

(21) A. Jablonskytė, J. A. Wright, S. A. Fairhurst, J. N. T. Peck, S. K. Ibrahim, V. S. Oganesyan and C. J. Pickett, *J. Am. Chem. Soc.*, 2011, **133**, 18606-18609.

(22) A. Winter, L. Zsolnai and G. Huttner, *Z. Naturforsch.*, 1982, **37b**, 1430-1436.

(23) H. Li and T. B. Rauchfuss, *J. Am. Chem. Soc.*, 2002, **124**, 726-727.

(24) S. J. Borg, T. Behrsing, S. P. Best, M. Razavet, X. Liu and C. J. Pickett, *J. Am. Chem. Soc.*, 2004, **126**, 16988-16999.

(25) D. Chong, I. P. Georgakaki, R. Mejia-Rodriguez, J. Sanabria-Chinchilla, M. P. Soriaga and M. Y. Darensbourg, *Dalton Trans.*, 2003,4158-4163.

(26) L.-C. Song, J.-H. Ge, X.-F. Liu, L.-Q. Zhao and Q.-M. Hu, *J. Organomet. Chem.*, 2006, **691**, 5701-5709.

(27) F. Ridley, S. Ghosh, G. Hogarth, N. Hollingsworth, K. B. Holt and D. G. Unwin, *J. Electroanal. Chem.*, 2013, **703**, 14-22.

(28) L. Schwartz, L. Eriksson, R. Lomoth, F. Teixidor, C. Viñas and S. Ott, *Dalton Trans.*, 2008, 2379-2381.

(29) K. Charreteur, M. Kdider, J.-F. Capon, F. Gloaguen, F. Y. Pétillon, P. Schollhammer and J. Talarmin, *Inorg. Chem.*, 2010, **49**, 2496-2501.

(30) P. S. Singh, H. C. Rudbeck, P. Huang, S. Ezzaher, L. Eriksson, M. Stein, S. Ott and R. Lomoth, *Inorg. Chem.*, 2009, **48**, 10883-10885.

(31) L. Schwartz, P. S. Singh, L. Eriksson, R. Lomoth and S. Ott, *C. R. Chimie*, 2008, **11**, 875-889.

(32) M. Schmidt, S. M. Contakes and T. B. Rauchfuss, *J. Am. Chem. Soc.*, 1999, **121**, 9736-9737.

(33) E. J. Lyon, I. P. Georgakaki, J. H. Reibenspies and M. Y. Darensbourg, *Angew. Chem. Int. Ed.*, 1999, **38**, 3178-3180.

(34) H. Vahrenkamp, A. Gei*β* and G. N. Richardson, J. Chem. Soc., *Dalton Trans.*, 1997, 3643-3651.

(35) J. I. van der Vlugt, T. B. Rauchfuss and S. R. Wilson, *Chem.-Eur. J.*, 2005, **12**, 90-98.

(36) T. R. Simmons, G. Berggren, M. Bacchi, M. Fontecave and V. Artero, *Coord. Chem. Rev.*, 2014, **270-271**, 127-150.

(37) J. W. Tye, J. Lee, H.-W. Wang, R. Mejia-Rodriguez, J. H. Reibenspies, M. B. Hall and M. Y. Darensbourg, *Inorg. Chem.*, 2005, **44**, 5550-5552.

(38) M. T. Olsen, M. Bruschi, L. De Gioia, T. B. Rauchfuss and S. R. Wilson, *J. Am. Chem. Soc.*, 2008, **130**, 12021-12030.

(39) M.-Q. Hu, C.-B. Ma, Y.-T. Si, C.-N. Chen and Q.-T. Liu, *J. Inorg. Biochem.*, 2007, **101**, 1370-1375.

(40) L. Schwartz, J. Ekström, R. Lomoth and S. Ott, *Chem. Commun.*, 2006, 4206-4208.

(41) C. M. Thomas, T. Liu, M. B. Hall and M. Y. Darensbourg, *Inorg. Chem.*, 2008, **47**, 7009-7024.

(42) I. Bhugun, D. Lexa and J.-M. Saveánt, *J. Am. Chem. Soc.*, 1996, **118**, 3982-3983.

(43) S. Kaur-Ghumaan, L. Schwartz, R. Lomoth, M. Stein and S. Ott, *Angew. Chem. Int. Ed.*, 2010, **49**, 8033-8036.

(44) M. Beyler, S. Ezzaher, M. Karnahl, M.-P. Santoni, R. Lomoth and S. Ott, *Chem. Commun.*, 2011, **47**, 11662-11664.

(45) A. Orthaber, M. Karnahl, S. Tschierlei, D. Streich, M. Stein and S. Ott, *Dalton Trans.*, 2014, **43**, 4537-4549.

(46) S. Roy, S. K. S. Mazinani, T. L. Groy, L. Gan, P. Tarakeshwar, V. Mujica and A. K. Jones, *Inorg. Chem.*, 2014, **53**, 8919-8929.

(47) M. J. Rose, H. B. Gray and J. R. Winkler, *J. Am. Chem. Soc.*, 2012, **134**, 8310-8313.

(48) G. P. Connor, K. J. Mayer, C. S. Tribble and W. R. McNamara, *Inorg. Chem.*, 2014, **53**, 5408-5410.

(49) D. J. Darensbourg, J. H. Reibenspies, C. H. Lai, W. Z. Lee and M. Y. Darensbourg, *J. Am. Chem. Soc.*, 1997, **119**, 7903-7904.

(50) V. Artero and M. Fontecave, *C. R. Chimie*, 2008, **11**, 926-931.

(51) C. Tard, X. Liu, D. L. Hughes and C. J. pickett, *Chem. Commun.*, 2005, 133-135.

(52) S. Ghosh, G. Hogarth, K. B. Holt, S. E. Kabir, A. Rahaman and D. G. Unwin, *Chem. Commun.*, 2011, **47**, 11222-11225.

(53) A. Rahaman, S. Ghosh, G. Hogarth, D. G. Unwin, S. Basak-Modi, K. B. Holt, S. E. Kabir, E. Nordlander, M. G. Richmond and D. G. Unwin, *Organometallics*, 2014, **33**, 1356-1366.

(54) M. D. Rail and L. A. Berben, *J. Am. Chem. Soc.*, 2011, **133**, 18577-18579.

(55) A. D. Nguyen, M. D. Rail, M. Shanmugam, J. C. Fettinger and L. A. Berben, *Inorg. Chem.*, 2013, **52**, 12847-12854.

(56) A. D. Nguyen, M. D. Rail, M. Shanmugam, J. C. Fettinger and L. A. Berben, *Inorg. Chem.*, 2013, **52**, 12847-12854.

(57) Z. Li, X. Zeng, Z. Niu and X. Liu, *Electrochimica Acta*, 2009, **54**, 3638-3644.

(58) C. A. Mebi, K. E. Brigance and R. B. Bowman, *J. Braz. Chem. Soc.*, 2012, **23**, 186-189.

(59) V. Artero, M. Chavarot-Kerlidou and M. Fontecave, *Angew. Chem. Int. Ed.*, 2011, **50**, 7238-7266.

(60) S. Losse, J. G. Vos and S. Rau, *Coord. Chem. Rev.*, 2010, **254**, 2492-2504.

(61) J. L. Dempsey, B. S. Brunschwig, J. R. Winkler and H. B. Gary, *Acc. Chem. Res.*, 2009, **42**, 1995-2004.

(62) B. J. Fisher and R. Eisenberg, *J. Am. Chem. Soc.*, 1980, **102**, 7361-7363.

(63) V. Houlding, T. Geiger, U. Kölle and M. Grätzel, *J. Chem. Soc., Chem. Commun.*, 1982, 681-683.

(64) P. V. Bernhardt and L. A. Jones, *Inorg. Chem.*, 1999, **38**, 5086-5090.

(65) U. Koelle and S. Ohst, *Inorg. Chem.*, 1986, **25**, 2689-2694.

(66) U. Kölle, E. Raabe, C. Krüger and F. P. Rotzinger, *Chem. Ber.*, 1987, **120**, 979-985.

(67) R. M. Kellett and T. G. Spiro, *Inorg. Chem.*, 1985, **24**, 2373-2377.

(68) R. M. Kellett and T. G. Spiro, *Inorg. Chem.*, 1985, **24**, 2378-2382.

(69) F. Zhao, J. Zhang, T. Abe, D. Wöhrle and M. Kaneko, *J. Mol. Catal. A: Chem.*, 1999, **145**, 245-256.

(70) A. Koca, M. K. Şener, M. B. Koçak and A. Gül, *Int. J. Hydrogen Energy*, 2006, **31**, 2211-2216.

(71) J. P. Bigi, T. E. Hanna, W. H. Harman, A. Chang and C. J. Chang, *Chem. Commun.*, 2010, **46**, 958-960.

(72) Y. Sun, J. P. Bigi, N. A. Piro, M. L. Tang, J. R. Long and C. J. Chang, *J. Am. Chem. Soc.*, 2011, **133**, 9212-9215.

(73) B. D. Stubbert, J. C. Peters and H. B. Gray, *J. Am. Chem. Soc.*, 2011, **133**, 18070-18073.

(74) C. C. L. McCrory, C. Uyeda and J. C. Peters, *J. Am. Chem. Soc.*, 2012, **134**, 3164-3170.

(75) C.-F. Leung, Y.-Z. Chen, H.-Q. Yu, S.-M. Yiu, C.-C. Ko and T.-C. Lau, *Int. J. Hydrogen Energy*, 2011, **36**, 11640-11645.

(76) G. N. Schrauzer, *Acc. Chem. Res.*, 1968, **1**, 97-103.

(77) M. Razavet, V. Artero and M. Fontecave, *Inorg. Chem.*, 2005, **44**, 4786-4795.

(78) X. Hu, B. M. Cossairt, B. S. Brunschwig, N. S. Lewis and J. C. Peters, *Chem. Commun.*, 2005, 4723-4725.

(79) X. Hu, B. S. Brunschwig and J. C. Peters, *J. Am. Chem. Soc.*, 2007, **129**, 8988-8998.

(80) C. Baffert, V. Artero and M. Fontecave, *Inorg. Chem.*, 2007, **46**, 1817-1824.

(81) O. Pantani, E. Anxolabéhère-Mallart, A. Aukauloo and P. Millet, *Electrochem. Commun.*, 2007, **9**, 54-58.

(82) P. Connolly and J. H. Espenson, *Inorg. Chem.*, 1986, **25**, 2684-2688.

(83) P.-A. Jacques, V. Artero, J. Pécaut and M. Fontecave, *Proc. Natl. Acad. Sci.*, 2009, **106**, 20627-20632.

(84) L. A. Berben and J. C. Peters, *Chem. Commun.*, 2010, **46**, 398-400.

(85) O. Pantani, S. Naskar, R. Guillot, P. Millet, E. Anxolabéhère-Mallart and A. Aukauloo, *Angew. Chem. Int. Ed.*, 2008, **47**, 9948-9950.

(86) R. Abdel-Hamid, H. M. El-Sagher, A. M. Abdel-Mawgoud and A. Nafady, *Polyhedron*, 1998, **17**, 4535-4541.

(87) T. Abe and M. Kaneko, *J. Mol. Catal. A: Chem.*, 2001, **169**, 177-183.

(88) N. K. Szymczak, L. A. Berben and J. C. Peters, *Chem. Commun.*, 2009, 6729-6731.

(89) W. R. McNamara, Z. Han, P. J. Alperin, W. W. Brennessel, P. L. Holland and R. Eisenberg, *J. Am. Chem. Soc.*, 2011, **133**, 15368-15371.

(90) G. M. Jacobsen, J. Y. Yang, B. Twamley, A. D. Wilson, R. M. Bullock, M. R. DuBois and D. L. DuBois, *Energy Environ. Sci.*, 2008, **1**, 167-174.

(91) J.-P. Collin, A. Jouaiti and J.-P. Sauvage, *Inorg. Chem.*, 1988, **27**, 1986-1990.

(92) L. L. Efros, H. H. Thorp, G. W. Brudvig and R. H. Crabtree, *Inorg. Chem.*, 1992, **31**, 1722-1724.

(93) A. Begum, G. Moula and S. Sarkar, *Chem.-Eur. J.*, 2010, **16**, 12324-12327.

(94) Z. Han, L. Shen, W. W. Brennessel, P. L. Holland and R. Eisenberg, *J. Am. Chem. Soc.*, 2013, **135**, 14659-14669.

(95) M. R. DuBois and D. L. DuBois, *Acc. Chem. Res.*, 2009, **42**, 1974-1982.

(96) D. L. DuBois and R. M. Bullock, *Eur. J. Inorg. Chem.*, 2011, 1017-1027.

(97) A. D. Wilson, R. H. Newell, M. J. McNevin, J. T. Muckerman, M. R. DuBois and D. L. DuBois, *J. Am. Chem. Soc.*, 2006, **128**, 358-366.

(98) A. L. Goff, V. Artero, B. Jousselme, P. D. Tran, N. Guillet, R. Métayé, A. Fihri, S. Palacin and M. Fontecave, *Science*, 2009, **326**, 1384-1387.

(99) U. J. Kilgore, J. A. S. Roberts, D. H. Pool, A. M. Appel, M. P. Stewart, M. R. DuBois, W. G. Dougherty, W. S. Kassel, R. M. Bullock and D. L. DuBois, *J. Am. Chem. Soc.*, 2011, **133**, 5861-5872.

(100) A. D. Wilson, R. K. Shoemaker, A. Miedaner, J. T. Muckerman, D. L. DuBois and M. R. DuBois, *Proc. Natl. Acad. Sci.*, 2007, **104**, 6951-6956.

(101) J. Y. Yang, R. M. Bullock, W. G. Shaw, B. Twamley, K. Fraze, M. R. DuBois and D. L. DuBois, *J. Am. Chem. Soc.*, 2009, **131**, 5935-5945.

(102) A. M. Appel, D. H. Pool, M. O'Hagan, W. G. Shaw, J. Y. Yang, M. R. DuBois and D. L. DuBois, *ACS Catal.*, 2011, **1**, 777-785.

(103) M. L. Helm, M. P. Stewart, R. M. Bullock, M. R. DuBois and D. L. DuBois, *Science*, 2011, **333**, 863-866.

(104) A. M. Appel, D. L. DuBois and M. R. DuBois, *J. Am. Chem. Soc.*, 2005, **127**, 12717-12726.

(105) H. I. Karunadasa, C. J. Chang and J. R. Long, *Nature*, 2010, **464**, 1329-1333.

(106) V. Grass, D. Lexa, J.-M. Savéant and *J. Am. Chem. Soc.*, 1997, **119**, 7526-7532.

(107) E. S. Donovan and G. A. N. Felton, *J. Organomet. Chem.*, 2012, **711**, 25-34.

Chapter 2

Biomimetics of the iron-only hydrogenase enzyme: Evaluation of $Fe_2(CO)_4\{\kappa^2\text{-}Ph_2PC(Me_2)PPh_2\}(\mu\text{-pdt})$ as a proton-reduction catalyst by experimental and computational methods

2.1. Introduction

In 2006, Hall and co-workers reported theoretical studies on the H-cluster active site of iron-only hydrogenases which suggested that asymmetry of the diiron centre is a desirable feature for a functional biomimetic [1]. Consequently, we [2-5] and others [6-20] have prepared a number of chelate complexes of the type $Fe_2(CO)_4(\kappa^2\text{-diphosphine})(\mu\text{-dithiolate})$ in which the diphosphine discriminates the two iron sites both sterically and electronically. In solution they exist in both dibasal (bb) and basal-apical (ba) forms which can interconvert slowly [2-4,6-9,16-18,22] (Scheme 2.1). In some instances the bridge isomer, $Fe_2(CO)_4(\mu\text{-diphosphine})(\mu\text{-dithiolate})$, is also accessible [3-5,21-25] and we have recently prepared and tested both bridge and chelate isomers of $Fe_2(CO)_4\{Ph_2PN(allyl)PPh_2\}(\mu\text{-pdt})$ (pdt = propanedithiolato) as proton reduction catalysts, with the chelate isomer showing superior catalytic properties [5].

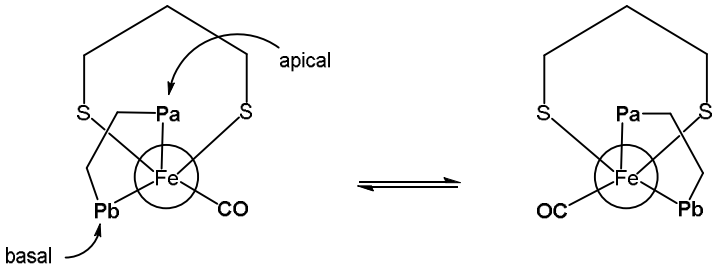

Scheme 2.1. Basal-apical ligand exchange.

In light of these results, we focussed our continuing efforts towards finding new functional biomimetics of the H-cluster active site on the preparation of new chelate complexes, $Fe_2(CO)_4(\kappa^2\text{-diphosphine})(\mu\text{-dithiolate})$. Earlier work carried out by our group showed that the small bite-angle diphosphine, bis(diphenylphosphino)methane (dppm), reacts with $Fe_2(CO)_6(\mu\text{-pdt})$ (**1.1**) to initially afford $Fe_2(CO)_5(\kappa^1\text{-dppm})(\mu\text{-pdt})$ which loses a further carbonyl upon heating to yield $Fe_2(CO)_4(\mu\text{-dppm})(\mu\text{-pdt})$ [3]. Small amounts of the chelate

isomer, $Fe_2(CO)_4(\kappa^2$-dppm)(μ-pdt), were also isolated in the first attempt of this reaction (carried out in toluene at *ca.* 110^{o}C) but we have since not been able to reproduce this result. It is known that alkyl substitution of one or more of the backbone protons in dppm results in the formation of ligands that are both more basic than dppm, while also giving a smaller bite angle and thus favouring chelate formation [26-40]. Both of these features were appealing to us for the preparation of readily protonated $Fe_2(CO)_4(\kappa^2$-diphosphine)(μ-pdt) complexes. While a number of backbone-functionalised dppm-derivatives have been reported, they are generally prepared "on metal" from coordinated dppm upon deprotonation of a backbone proton followed by quenching with electrophiles [28-31]. Such ligands are not easily prepared "off-metal" as they result from the nucleophilic substitution of dihaloalkanes, $RCHX_2$ or R_2CX_2, by the diphenylphosphide anion, Ph_2P^-. The latter is a poor nucleophile and both the steric and electronic changes to central carbon atom upon alkyl substitution make it less susceptible to nucleophilic attack. Two diphosphines that are accessible *via* this route are the methyl-substituted derivatives, 1,1′-bis(diphenylphosphino)ethane, $Ph_2PCH(Me)PPh_2$ [28] and 2,2′-bis(diphenylphosphino)propane, $Ph_2PC(Me_2)PPh_2$ [28]. The former can be isolated in moderate yields and is relatively air-stable, while the latter is formed in lower yields and is highly oxygen sensitive, presumably reflecting its greater basicity. Both diphosphines are known to favour chelate complexes [28-40] and thus we have attempted to prepare hydrogenase biomimetics containing these ligands. We herein detail the successful synthesis of $Fe_2(CO)_4\{\kappa^2$-$Ph_2PC(Me_2)PPh_2\}$(μ-pdt) (**2.1**) together with electrocatalytic proton reduction studies.

2.2. Results and discussion

2.2.1. Synthesis and structural characterization of $Fe_2(CO)_4\{\kappa^2$-$Ph_2PC(Me_2)PPh_2\}$(μ-pdt) (2.1). Reaction of equimolar amounts of $Fe_2(CO)_6$(μ-pdt) (**1.1**) and $Ph_2PC(Me_2)PPh_2$ in MeCN with added $Me_3NO{\cdot}2H_2O$ (2.5 equiv) initially gave an orange solution which darkened rapidly, becoming nearly black after 30 min. The mixture was heated at 70 ^{o}C for a further 4 h and after work-up afforded the target chelate complex $Fe_2(CO)_4\{\kappa^2$-$Ph_2PC(Me_2)PPh_2\}$(μ-pdt) (**2.1**) in 63% yield (Scheme 2.2).

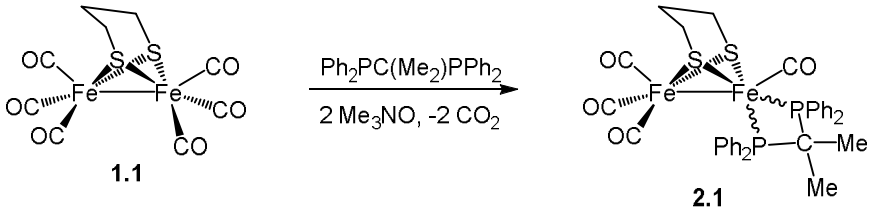

Scheme 2.2. Synthesis of $Fe_2(CO)_4\{\kappa^2\text{-}Ph_2PC(Me_2)PPh_2\}(\mu\text{-pdt})$ (**2.1**).

Analysis of the $^{31}P\{^1H\}$ NMR spectrum of the reaction mixture after *ca*. 30 min showed a prominent pair of doublets at 7.6 and 37.2 ppm (J_{PP} 67.5 Hz), which we tentatively assign to intermediate $Fe_2(CO)_5\{\kappa^1\text{-}Ph_2PC(Me_2)PPh_2\}(\mu\text{-pdt})$ (**2A**), this being supported by the observation of small absorptions at 2045 and 1981 cm^{-1} in the IR spectrum. Thus it seems that the reaction proceeds in an analogous manner to that observed for dppm [3]. A $^{31}P\{^1H\}$ NMR spectrum in $CDCl_3$ of the crude reaction mixture after 4 h also showed a small resonance at 86.9 ppm associated with the bridging isomer (see later) but this was formed in < 3 % yield. Complex **2.1** can be easily characterised by IR spectroscopy showing carbonyl absorptions at 2018vs, 1949s and 1896 cm^{-1}. An X-ray crystal structure was undertaken the results of which are displayed in Figure 2.1 and its caption. The most interesting feature is the dibasal arrangement of the diphosphine (**2.1bb** in Scheme 2.3) with P(1) lying *trans* to S(1) and P(2) *trans* to S(2) [P(1)–Fe(1)–S(1) 163.23(2), P(2)–Fe(1)–S(2) 156.11(2)^o], while the carbonyl occupies the apical site lying approximately *trans* to the metal-metal vector [C(1)–Fe(1)–Fe(2) 146.19(6)^o]. The diphosphine subtends a bite angle of 74.53(2)^o, which is identical to that of 74.55(4)^o in the analogous dppm-derivative [3], but some 3^o greater than observed in related bis(diphenylphosphino)amine complexes [2,5]. The angle at the backbone carbon in **2.1** of 90.54(7)^o is significantly smaller than that of 93.5(2)^o in $Fe_2(CO)_4(\kappa^2\text{-dppm})(\mu\text{-pdt})$ [3] as a result of the *gem*-dimethyl effect [26-27].

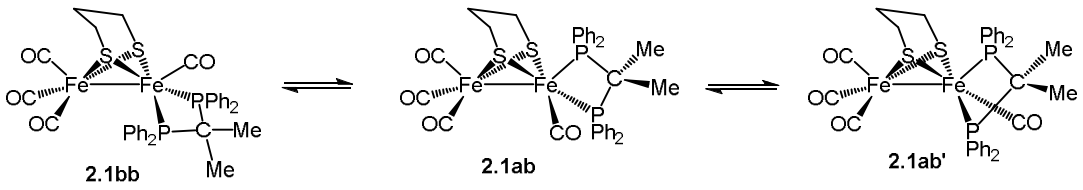

Scheme 2.3. Dibasal and apical-basal isomers of $Fe_2(CO)_4\{\kappa^2\text{-}Ph_2PC(Me_2)PPh_2\}(\mu\text{-pdt})$ (**2.1**).

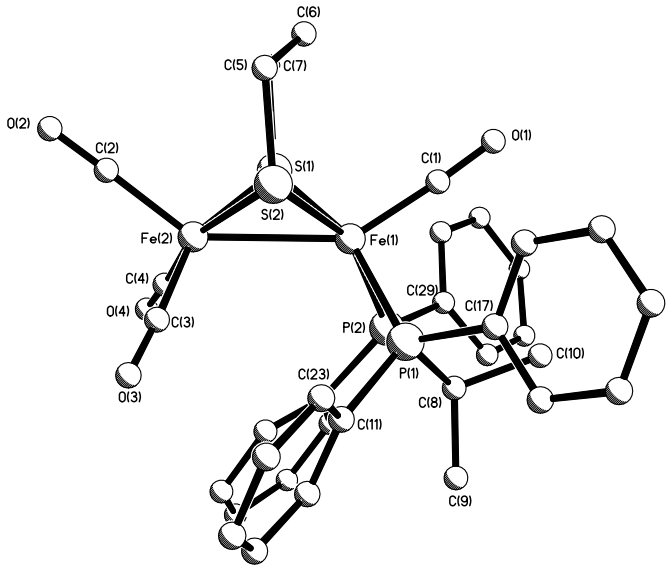

Figure 2.1. Molecular structure of $Fe_2(CO)_4\{\kappa^2\text{-}Ph_2PC(Me_2)PPh_2\}(\mu\text{-pdt})$ (**2.1bb**) with selected bond lengths (Å) and angles (°): Fe(1)–Fe(2) 2.6062(6), Fe(1)–P(1) 2.2348(6), Fe(1)–P(2) 2.2273(6), Fe(1)–S(1) 2.2270(6), Fe(1)–S(2) 2.2370(5), Fe(2)–S(1) 2.2543(6), Fe(2)–S(2) 2.2706(6), Fe(1)–C(1) 1.747(2), P(1)–Fe(1)–Fe(2) 112.79(2), P(2)–Fe(1)–Fe(2) 108.42(2), C(1)–Fe(1)–Fe(2) 146.19(6), P(1)–Fe(1)–P(2) 74.53(2), P(1)–C(8)–P(2) 90.54(7), P(1)–Fe(1)–S(1) 163.23(2), P(2)–Fe(1)–S(2) 156.11(2), Fe(1)–Fe(2)–C(3) 106.64(6), Fe(1)–Fe(2)–C(4) 108.14(6).

2.2.2. DFT calculations to probe the relative energies and interconversion of dibasal and basal-apical isomers. In the solid state $Fe_2(CO)_4\{\kappa^2\text{-}Ph_2PC(Me_2)PPh_2\}(\mu\text{-pdt})$ exists as the dibasal isomer **2.1bb**, however, in solution dibasal (**2.1bb**) and apical-basal (**2.1ab**) isomers co-exist (Scheme 2.3) as seen by the presence of two singlets in the $^{31}P\{^1H\}$ NMR spectrum at 52.4 and 77.2 ppm in CD_2Cl_2 (50.8 and 75.5 ppm in $CDCl_3$) in an approximate 2:1 ratio. The $^{31}P\{^1H\}$ NMR chemical shift was assigned to the isomers assuming that the dibasal isomer (which is the only isomeric form found in the solid-state) is the predominant species in solution. The ^1H NMR spectrum is also more complicated than might at first be expected as both isomers have inequivalent methyl groups (all coupling to phosphorus) and either four (dibasal) or six (basal-apical) different protons on the dithiolate backbone. Such isomerism is common in complexes of this type [2-4,6-9,16-18,22] with the apical-basal isomer generally being preferred. For example in the dppp analogue of **2.1**, namely $Fe_2(CO)_4\{\kappa^2\text{-}Ph_2P(CH_2)_3PPh_2\}(\mu\text{-pdt})$ the ratio of apical-basal to dibasal isomers is 12:1 [4], although we recently found that for the small bite-angle diphosphine complexes $Fe_2(CO)_4\{\kappa^2\text{-}Ph_2PN(R)PPh_2\}(\mu\text{-pdt})$ the dibasal isomer predominated in solution [5]. Isomers are generally distinguished on the basis of ^{31}P NMR chemical shifts, the apical-

basal resonance being seen at lower field [5]. We have carried out DFT calculations and the apical-basal isomer **2.1ab** was computed to lower in energy by *ca*. 2 kJ mol^{-1} than the dibasal form **2.1bb**; on the basis of this energy difference we predict a K_{eq} of 2.3 which is opposite to the 2:1 ratio of **2.1bb**:**2.1ab** found by ^{31}P NMR spectroscopy. The calculations were carried out in gaseous state and the additional factors such as solvent interaction that need to be considered in solution were not included in computation, which we assume would improve the precision of the results. In solution at room temperature, a single phosphorus resonance is observed for both isomers. While a single ^{31}P resonance for **2.1bb** is consistent with the formulated structure having idealized C_s symmetry, the observation of a single phosphorus resonance for **2.1ab** supports the rapid equilibration of the diphosphine ligand about the $Fe(CO)P_2$ centre of **2.1ab** (Scheme 2.4). DFT calculations confirm a low-energy path (42.3 kJ mol^{-1}) for the interconversion of **2.1ab** to **2.1ab′** through a tripodal rotation at the $Fe(CO)P_2$ centre. The activation barrier is sufficiently low and precludes the observation of distinct apical and basal ^{31}P resonances for this isomer. There is no evidence for the interconversion of **2.1ab/ab′** and **2.1bb** as both sets of signals are sharp at room temperature and remain so upon heating to 90°C and DFT calculations give a free energy of activation of 98.7 kJ mol^{-1} (Scheme 2.5), confirming that the two isomers do not interconvert under the conditions of electrochemical or protonation experiments (see later). The relatively large energy barrier for the isomerization involving **2.1ab/ab′** to **2.1bb** may be traced to the transition structure **TS_bb_ab′** that requires the adoption of a rotated structure where one of the Ph_2P moieties is situated in an axial position opposite to the pdt ligand. This conformation is energetically unfavourable and places the axial Ph_2P moiety in close contact with the iron-iron bond and the adjacent $Fe(CO)_3$ moiety. This phenomenon is not unlike that reported for the complexes $Fe_2(CO)_4\{\kappa^2\text{-}Ph_2PN(R)PPh_2\}(\mu\text{-pdt})$ [5].

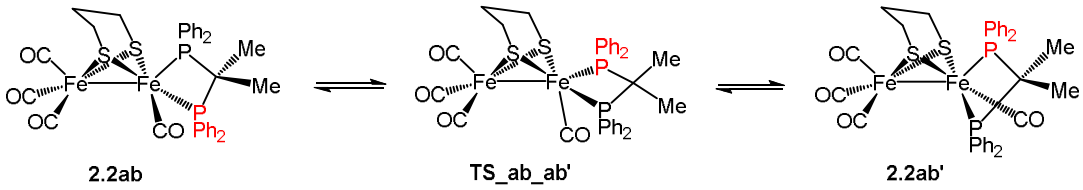

Scheme 2.4. Low energy pathway for the interconversion of **2ab** and **2ab′**.

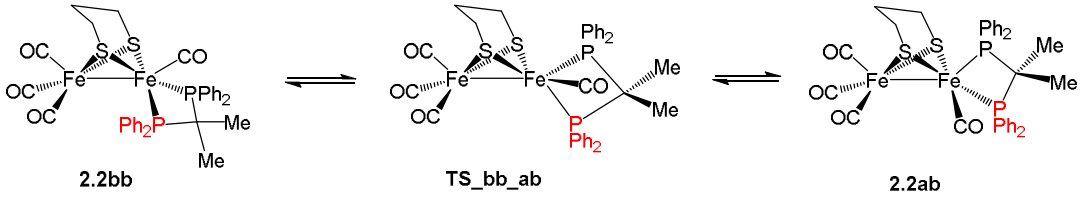

Scheme 2.5. High energy pathway for the possible interconversion of **2ab** and **2bb**.

2.2.3. Thermolysis of 2.1: Synthesis and structural characterization of $Fe_2(CO)_4\{\mu$-$Ph_2PC(Me_2)PPh_2\}(\mu$-pdt) (2.2) and DFT studies. In recent work we showed that heating chelate complexes $Fe_2(CO)_4\{\kappa^2$-$Ph_2PN(R)PPh_2\}(\mu$-pdt) in toluene resulted in their slow (10-14 h) but clean conversion to the bridged isomers $Fe_2(CO)_4\{\mu$-$Ph_2PN(R)PPh_2\}(\mu$-pdt) [5]. After heating a toluene solution of **2.1** for 8 h it initially appeared that there was no change as shown by IR spectroscopy, but careful inspection of the $^{31}P\{^1H\}$ NMR spectrum revealed the appearance of a small new singlet resonance at *ca.* 69 ppm. Subsequent heating for 30 h resulted in the growth of this resonance and concomitant decrease in intensity of those associated with **2.1**. After this time work-up of the reaction mixture lead to the isolation of the bridged isomer $Fe_2(CO)_4\{\mu$-$Ph_2PC(Me_2)PPh_2\}(\mu$-pdt) (**2.2**) in 70% yield (Scheme 2.6). Characterisation was straightforward, the IR spectrum being particularly informative, consisting of four absorptions at 1984m, 1952s, 1916m and 1895sh cm^{-1} being typical of a complex of the type $Fe_2(CO)_4(\mu$-diphosphine$)(\mu$-dithiolate) [3-5,21-25], while the $^{31}P\{^1H\}$ NMR spectrum in CD_2Cl_2 consisted only of a singlet at 89.0 ppm. In order to compare the structure of **2.2** with that of the chelated isomer a single crystal X-ray diffraction experiment was carried out, the results of which are summarised in Figure 2.2 and its caption.

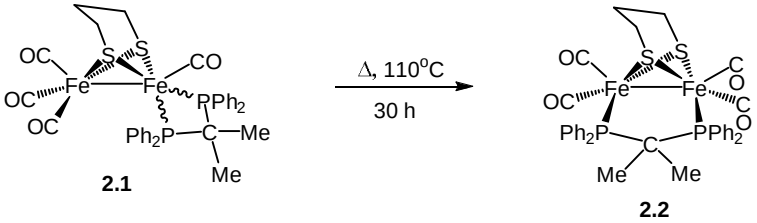

Scheme 2.6. Synthesis of $Fe_2(CO)_4\{\mu$-$Ph_2PC(Me_2)PPh_2\}(\mu$-pdt) (**2.2**).

Movement of the diphosphine from a chelate to bridge disposition results in only very minor changes to the $Fe_2S_2P_2$ core of the molecule. Thus, iron-sulphur and iron-phosphorus bond lengths remain virtually unchanged, while the iron-iron bond length decreases by 0.08 Å (*ca.* 3%). The biggest change between the two isomers is seen in the angles subtended

at the backbone carbon of the 2,2′-bis(diphenylphosphino)propane ligand, for example the P(1)–C(8)–P(2) angle increases from 90.54(7)° in **2.1** to 107.7(1)° in **2.2**; a change of around 20% and suggesting that this ligand is quite flexible. As far as we are aware there are only two other examples of crystallographically characterised complexes containing a bridging 2,2′-bis(diphenylphosphino)propane ligand [33,41]. Thus, Higgins and co-workers in the heterobimetallic complex, $CpRu(\mu\text{-}CO)_2\{\mu\text{-}Ph_2PC(Me_2)PPh_2\}RhCl_2$ [33], which has a P–C–P bond angle of 109.9(7)°, while we have recently characterised $Os_3(CO)_{10}\{\mu\text{-}Ph_2PC(Me_2)PPh_2\}$ with a P–C–P bond angle of 111.0(3)° [41].

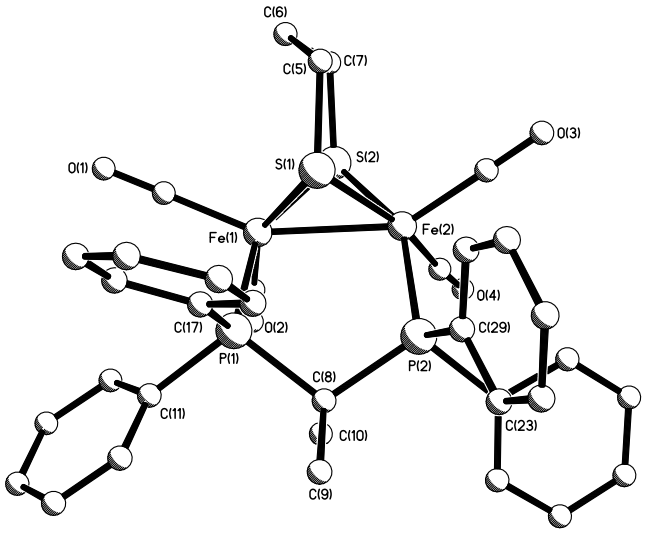

Figure 2.2. Molecular structure of $Fe_2(CO)_4\{\mu\text{-}Ph_2PC(Me_2)PPh_2\}(\mu\text{-pdt})$ (**2.2**)·CH_2Cl_2 with selected bond lengths (Å) and angles (°): Fe(1)–Fe(2) 2.5179(6), Fe(1)–P(1) 2.2352(8), Fe(1)–P(2) 2.2518(8), Fe(1)–S(1) 2.2481(8), Fe(1)–S(2) 2.2508(8), Fe(2)–S(1) 2.2600(8), Fe(2)–S(2) 2.2517(8), P(1)–Fe(1)–Fe(2) 96.96(3), P(2)–Fe(2)–Fe(1) 97.00(3), C(1)–Fe(1)–Fe(2) 154.4(1), C(3)–Fe(2)–Fe(1) 147.3(1), P(1)–C(8)–P(2) 107.7(1), P(1)–Fe(1)–S(2) 152.17(3), P(2)–Fe(2)–S(2) 149.18(3).

Formation of **2.2** upon heating the chelate isomers **2.1** suggests that the former is thermodynamically preferred. This was a surprise to us and seems to go against the accepted chelating ability of 2,2′-bis(diphenylphosphino)propane [32-40]. In order to probe this further, we have carried out DFT calculations and the data reveal that **2.2** lies *ca*. 2.9 and 2.0 kJ mol^{-1} lower in enthalpy than **2.1bb** and **2.1ab**, respectively. This confirms that **2.1** is the kinetic product from the reaction of **1.1** with 2,2′-bis(diphenylphosphino)propane. Theoretical investigations showed that unsymmetrically substituted diiron-dithiolate complexes, $Fe_2(CO)_4L_2(\mu\text{-dithiolate})$, favour the so-called "*rotated*" geometry where a CO

ligand asymmetrically bridges the iron-iron vector [1]. DFT analysis of CO substitution by PMe_3 in related complexes, namely $Fe_2(CO)_4(\kappa^2$-dppv)(μ-dithiolate) [dppv = bis(diphenylphosphino)ethylene], showed that the rotation of the $Fe(CO)_3$ group to form a bridging CO in the transition state is assisted by the electron-richness of the Fe(CO)(dppv) fragment [16]. With this in mind, a plausible route for the isomerisation process is shown in Scheme 2.7. This involves migration of a carbonyl from one iron to another *via* a semi-bridging mode with followed by rapture of an iron-phosphorus bond to generate the 32-electron complex, $Fe_2(CO)_4\{\kappa^1$-$Ph_2PC(Me_2)PPh_2\}$(μ-pdt). In the latter, once the coordinated diphenylphosphino moiety is in a basal site, then second phosphine can bridge across to the other iron centre to afford **2.2**. A similar route has been proposed for the Electron-transfer-catalyzed (ETC) isomerisation of $Fe_2(CO)_4(\kappa^2$-dppe)(μ-dithiolate) [8]. However, we can not rule out the possibility of an iron-sulphur bond scission during CO migration, a process we previously proposed for related amino-diphosphine complexes [5]. Attempts to differentiate between these two processes both experimentally and by DFT calculation have been unsuccessful.

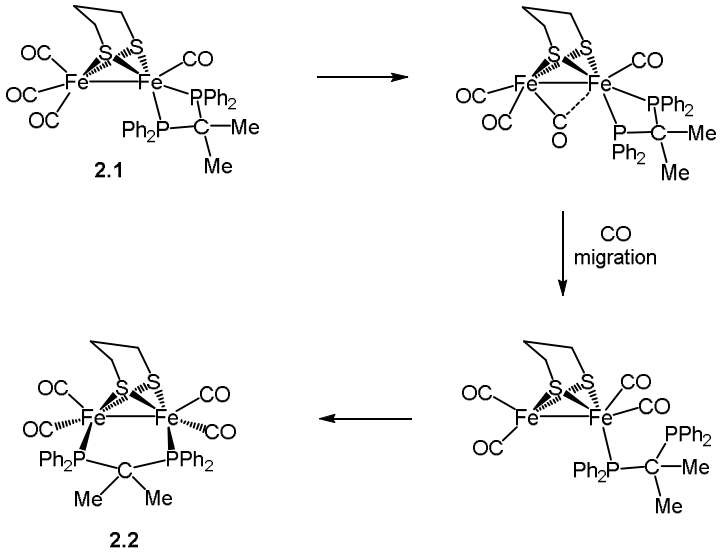

Scheme 2.7. Proposed mechanism for the conversion of **2.1** to **2.2**.

2.2.4. Synthesis and structural characterization of $[Fe_2(CO)_4(\mu$-H)$\{\kappa^2$-$Ph_2PC(Me_2)PPh_2\}$(μ-pdt)$][BF_4]$ (2.3). Many biomimetic models of the iron-only hydrogenase enzyme can bind to a proton and this protonation is a key step in the electrocatalytic proton reduction by the model systems. Thus, we next assessed the proton binding ability of **2.1** and **2.2**. Addition of $HBF_4{\cdot}Et_2O$ to a dichloromethane solution of **2.2** resulted only in the slow decomposition of the starting material in an analogous fashion to

behaviour noted for $Fe_2(CO)_4(\mu\text{-dppm})(\mu\text{-pdt})$ [3]. In contrast, addition of $HBF_4{\cdot}Et_2O$ to $Fe_2(CO)_4\{\kappa^2\text{-}Ph_2PC(Me_2)PPh_2\}(\mu\text{-pdt})$ (**2.1**) resulted in the immediate formation of basal-apical $[Fe_2(CO)_4(\mu\text{-H})\{\kappa^2\text{-}Ph_2PC(Me_2)PPh_2\}(\mu\text{-pdt})][BF_4]$ (**2.3ab**) which slowly (*ca.* 4 h) converted into the dibasal isomer $[Fe_2(CO)_4(\mu\text{-H})\{\kappa^2\text{-}Ph_2PC(Me_2)PPh_2\}(\mu\text{-pdt})][BF_4]$ (**2.3bb**) upon standing (Scheme 2.8). These transformations were easily followed by a combination of NMR and IR spectroscopy. Thus, upon initial addition of $HBF_4{\cdot}Et_2O$ a colour change from red-orange to blue-green occurred and in the IR spectrum absorptions attributed to **2.1** were replaced by bands at 2093vs, 2044s and 1982br cm^{-1} associated with **2.3ab**. Monitoring the same reaction by NMR spectroscopy in CD_2Cl_2 showed the immediate loss of all signals associated with **2.1** and formation of a hydride signal at δ –15.50 (dd, J 18.4, 4.4 Hz) in the ^1H NMR spectrum and two doublets at 68.7 and 60.1 ppm (J_{PP} 62.0 Hz) in the $^{31}P\{^1H\}$ NMR spectrum. Over time both of these signals diminished to be replaced by a triplet at δ –10.78 (t, J 19.2 Hz) and a singlet at 55.8 ppm associated with **2.3bb**. Similarly in the IR spectrum, adsorptions associated with **2.3ab** gradually diminished to be replaced by those at 2097vs, 2048s, 2035s and 1964s cm^{-1} attributed to **2.3bb**.

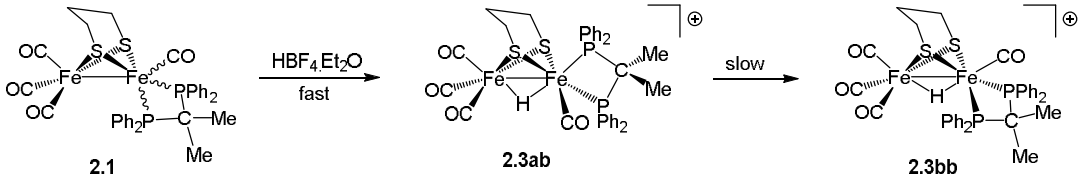

Scheme 2.8. Reaction $Fe_2(CO)_4\{\kappa^2\text{-}Ph_2PC(Me_2)PPh_2\}(\mu\text{-pdt})$ (**2.1**) with $HBF_4{\cdot}Et_2O$.

An X-ray diffraction study of **2.3bb** was undertaken, the results of which are summarised in Figure 2.3 and its caption. The complex co-crystallises with a disordered molecule of dichloromethane and no intermolecular interactions exist between either the solvent and the BF_4^- anion and the diiron cation. The diiron units in **2.1bb** and **2.3bb** are remarkably similar, showing that protonation across the iron-iron vector does not significantly perturb the system; the iron-iron bond length of 2.602(1) Å in **2.3bb** being within error the same as that seen in **2.1bb**. Other bond lengths also do not vary significantly upon protonation, while the angles subtended by the bite-angle of the diphosphine of 74.04(4)^o and also the angle subtended at the backbone carbon [P(1)–C(8)–P(2) 90.9(2)^o] are almost the same as those found in **2.1bb**. The largest metric changes between the two structures are the bond angles

subtended by the basal carbonyl and phosphine groups to the iron-iron bond, all values being greater in **2.3bb** as a result of the extra room required to accommodate the bridging hydride. For example, Fe(1)–Fe(2)–C(3) and Fe(1)–Fe(2)–C(4) bond angles of 119.3(2) and 110.7(2)^{o} in **2.3bb** are significantly expanded with respect to those of 106.64(6) and 108.14(6)^{o} respectively in **2.1bb**. A further noteworthy feature of both **2.1bb** and **2.3bb** is the orientation of the dithiolate backbone, the central methylene group being orientated towards the more bulky Fe(CO)(diphosphine) moiety.

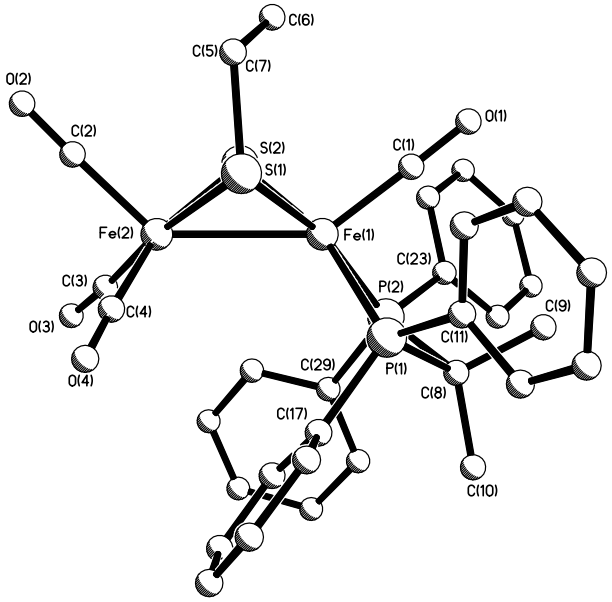

Figure 2.3. Molecular structure of the diiron cation in $[Fe_2(CO)_4(\mu\text{-}H)\{\kappa^2\text{-}Ph_2PC(Me_2)PPh_2\}(\mu\text{-}pdt)][BF_4].0.5CH_2Cl_2$ (**2.3bb**).$0.5CH_2Cl_2$ with selected bond lengths (Å) and angles (^{o}): Fe(1)–Fe(2) 2.602(1), Fe(1)–P(1) 2.226(1), Fe(1)–P(2) 2.254(1), Fe(1)–S(1) 2.251(1), Fe(1)–S(2) 2.251(1), Fe(2)–S(1) 2.269(1), Fe(2)–S(2) 2.273(1), Fe(1)–C(1) 1.756(4), P(1)–Fe(1)–Fe(2) 114.51(4), P(2)–Fe(1)–Fe(2) 119.55(4), C(1)–Fe(1)–Fe(2) 142.5(1), P(1)–Fe(1)–P(2) 74.04(4), P(1)–C(8)–P(2) 90.9(2), P(1)–Fe(1)–S(2) 165.22(5), P(2)–Fe(1)–S(1) 166.61(5), Fe(1)–Fe(2)–C(3) 119.3(2), Fe(1)–Fe(2)–C(4) 110.7(2).

The clean and rapid protonation of both **2.1ab** and **2.1bb** to give **2.3ab** is somewhat surprising as the two isomers do not interconvert rapidly at room temperature. Further the absence of **2.3bb** immediately after protonation suggests that this proceeds *via* a common intermediate which is clearly not **2.3bb**. In previous work with an analogue of **2.1**, namely $Fe_2(CO)_4\{\kappa^2\text{-}Ph_2P(CH_2)_3PPh_2\}(\mu\text{-}pdt)$, a similar situation was observed i.e. the mixture of apical-basal and dibasal isomers (12:1) immediately converted to apical-basal $[Fe_2(CO)_4(\mu\text{-}H)\{\kappa^2\text{-}Ph_2P(CH_2)_3PPh_2\}(\mu\text{-}pdt)][BF_4]$ upon addition of $HBF_4{\cdot}Et_2O$ [4]. Here when we

carried out the protonation at –90°C, we observed the intermediate formation of a third isomer containing a terminal hydride. Unfortunately all attempts to observe a similar low-temperature species upon protonation of **2.1** were unsuccessful. However, it seems reasonable to suggest that a common intermediate is also found here, protonation of both **2.1ab** and **2.1bb** initially yielding $[HFe_2(CO)_4\{\kappa^2\text{-}Ph_2PC(Me_2)PPh_2\}(\mu\text{-pdt})][BF_4]$ (**2.3tH**). The structure of **2.3tH** is not known but by analogy to the dppp-chemistry the hydride is most probably attached to the iron which is chelated by the diphosphine occupying both the basal sites with a carbonyl at apical position [4]. We further note that as found by ourselves [4] and others [7] for the analogous dppp-hydride, apical-basal $[Fe_2(CO)_4(\mu\text{-H})\{\kappa^2\text{-}Ph_2P(CH_2)_3PPh_2\}(\mu\text{-pdt})][BF_4]$, **2.3ab** is not deprotonated upon addition of strong bases, which shows that proton and ligand rearrangements are intramolecular.

2.2.5. Cyclic voltammetry studies of $Fe_2(CO)_4\{\kappa^2\text{-}Ph_2PC(Me_2)PPh_2\}(\mu\text{-pdt})$ (2.1) and $Fe_2(CO)_4\{\mu\text{-}Ph_2PC(Me_2)PPh_2\}(\mu\text{-pdt})$ (2.2). The CV of **2.1** in MeCN at scan rate 0.1 Vs^{-1} is shown in Figure 2.4. Two quasi-reversible oxidation waves are seen at $E_{1/2}$ = –0.19 V (ΔE = 110 mV) and $E_{1/2}$ = 0.04 V (ΔE = 80 mV), the reversibility of which is maintained at all scan rates, together with a further irreversible oxidation at E_p = 0.66 V. In the cathodic domain, two overlapping reductive features are observed at E_p = –2.16 V and E_p = –2.23 V together with a third quasi-reversible reduction at $E_{1/2}$ = –2.45 V (ΔE = 70 mV). The two overlapping reduction peaks also show some reversibility at all scan rates, becoming more separated at higher scan rates (≥0.25 V/s) (Figure 2.5). After reduction, a series of new oxidative features are observed between –2.0 to –1.3 V on the return scan, which are due to the oxidation of products formed upon first and second reductions. The plot of peak current (i_p) vs. square root of scan rate ($\sqrt{v}$) gives straight line for all primary oxidative and reductive processes, suggesting that all redox events of **2.1** are diffusion-controlled.

Schollhammer and Talarmin reported that the diiron-dithiolate complexes containing a chelating bis(diphenylphosphino)ethane (dppe) ligand undergo Electron-transfer-catalyzed (ETC) isomerisation upon one-electron reduction to form the symmetrical isomers in which the dppe bridged the iron-iron vector [8]. We did not see any evidence of such isomerisation for **2.1**. If **2.1** converted into **2.2** after reduction, then we would see peak(s) in the anodic region for **2** on the return scan, but we obtained identical CVs by sweeping the voltage in opposite directions (scanning anodic or cathodic region first)

even in slower scan rates. This suggests that **2.1** is not converting into **2.2** after reduction at least on voltammetric time frame. We interpret these data as resulting from the separate one-electron oxidation and reduction of the two geometric isomers of **2.1**, namely **2.1ab** and **2.1bb**. It is not possible to unambiguously assign individual oxidation and reduction waves to specific isomers and although DFT calculations shed some light on these processes.

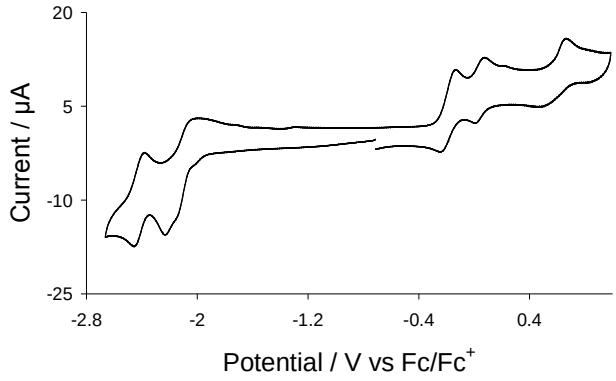

Figure 2.4. CV of $Fe_2(CO)_4\{\kappa^2\text{-}Ph_2PC(Me_2)PPh_2\}(\mu\text{-pdt})$ (**2.1**) in MeCN (0.5 mM solution, supporting electrolyte $[NBu_4][PF_6]$, scan rate 0.1 Vs^{-1}, glassy carbon electrode, potential vs Fc^+/Fc).

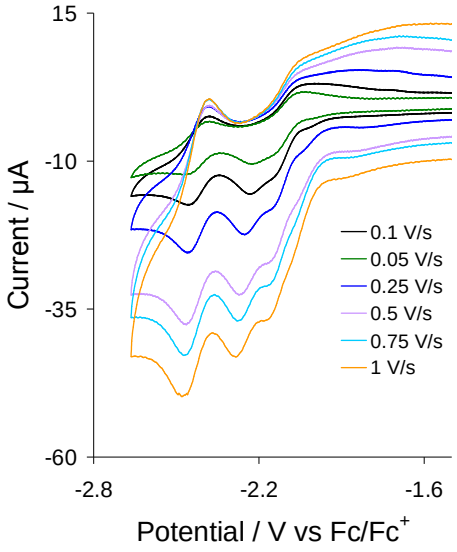

Figure 2.5. CVs of $Fe_2(CO)_4\{\kappa^2\text{-}Ph_2PC(Me_2)PPh_2\}(\mu\text{-pdt})$ (**2.1**) at various scan rates as shown in the legend (in MeCN, 0.5 mM solution, supporting electrolyte $[NBu_4][PF_6]$, glassy carbon electrode, potential vs Fc^+/Fc).

Thus, the HOMO of the dibasal isomer **2.1bb** is some 0.0033 Hartrees (0.09 eV, 8.7 kJ mol^{-1}) lower in energy than that in **2.1ab**. Thus we suggest that the first oxidation is

associated with electron loss from **2.1bb** and the second from **2.1ab**. Similarly, the LUMO of **2.1bb** lies 0.0042 Hartrees (0.11 eV, 11.0 $kJmol^{-1}$) higher in energy than that on **2.1ab** thus accounting for the two reduction waves and suggesting that the reduction at lower potential is associated with **2.1ab**. The later oxidative and reductive features presumably result from overlap of the separate waves from both isomers. As far as we are aware, the separate and distinguishable oxidation and reduction of dibasal and apical-basal isomers has not previously been noted [5,8,13-15]. The reversibility of the one-electron oxidation and reduction waves is also notable, being quite different from the behaviour noted for $Fe_2(CO)_4\{\kappa^2\text{-}Ph_2PN(allyl)PPh_2\}(\mu\text{-pdt})$ [5] for which both oxidation and reduction were irreversible at scan rates of 0.1 Vs^{-1}, the former showing some reversibility at 1 Vs^{-1} [5]. This suggests that both the mixed valence state complexes, Fe(II)-Fe(I) $[Fe_2(CO)_4\{\kappa^2\text{-}Ph_2PC(Me_2)PPh_2\}(\mu\text{-pdt})]^+$ (**2.1**$^+$) and Fe(I)-Fe(0) $[Fe_2(CO)_4\{\kappa^2\text{-}Ph_2PC(Me_2)PPh_2\}(\mu\text{-pdt})]^-$ (**2.1**$^-$) are reasonably long-lived. The latter is especially important with respect to the electrocatalytic reduction of protons and is considered in detail in the next section.

For comparison we have also studied the CV of the thermodynamically favoured bridge isomer **2.2** in MeCN as shown in Figure 2.6. Due to its low solubility in this solvent the sample had to be sonicated and heated in MeCN for some time to aid dissolution. Consequently, the precise concentration used was not determined, but nevertheless the data provide a useful comparison with those for **2.1**. The CV displays a reduction at E_p = –2.50 V and an oxidation at E_p = 0.74 V both of which show some reversibility at this scan rate (0.1 Vs^{-1}), however, neither improved when the scan rate was increased.

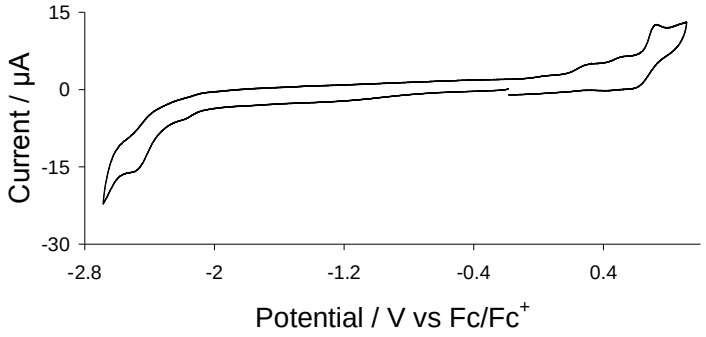

Figure 2.6. CV of $Fe_2(CO)_4\{\mu\text{-}Ph_2PC(Me_2)PPh_2\}(\mu\text{-pdt})$ (**2.2**) in MeCN (*ca.* 0.5 mM solution, supporting electrolyte $[NBu_4][PF_6]$, scan rate 0.1 Vs^{-1}, glassy carbon electrode, potential vs Fc^+/Fc).

2.2.6. Proton reduction catalysed by 2.1. The CVs of **2.1** recorded after addition of molar equivalents of $HBF_4 \cdot Et_2O$ are shown in Figure 2.7, which shows a positive shift of reduction potentials due to protonation of the initial complex. In light of the protonation studies discussed above, we conclude that under these conditions the major component of the electrochemical cell is apical-basal $[Fe_2(CO)_4(\mu\text{-}H)\{\kappa^2\text{-}Ph_2PC(Me_2)PPh_2\}(\mu\text{-}pdt)][BF_4]$ (**2.3ab**). The first and second reduction waves now appears at E_p = –1.58 V and E_p = –1.88 V, followed by a series of reductive features at more negative potentials. The peak current of these reduction waves increases consistently with addition of each molar equivalent of acid characteristic of electrocatalytic proton reduction by **2.1** at these potentials.

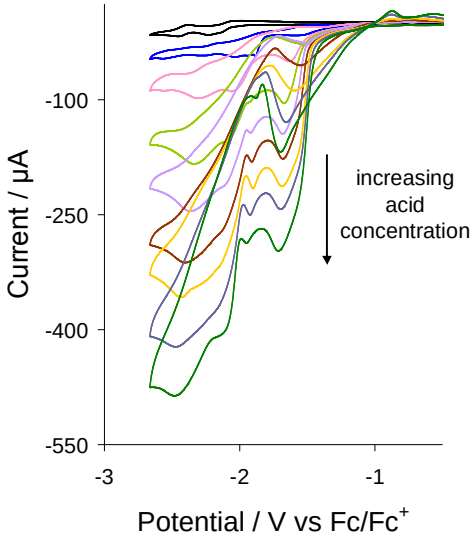

Figure 2.7. CVs of $Fe_2(CO)_4\{\kappa^2\text{-}Ph_2PC(Me_2)PPh_2\}(\mu\text{-}pdt)$ (**2.1**) in the absence of acid and in the presence of 1-7 and 9 molar equivalents of $HBF_4 \cdot Et_2O$ (0.5 mM solution, in acetonitrile, supporting electrolyte $[NBu_4][PF_6]$, scan rate 0.1 Vs^{-1}, glassy carbon electrode, potential vs Fc^+/Fc).

Two catalytic pathways have been probed by DFT as summarised in Scheme 2.9. All the species involved in those catalytic cycles have been found and fully optimized. Both result from the rapid protonation of **2.1** to afford the cationic hydride **2.3ab**. Since protonation studies show that there is no further proton addition to this species then it is assumed that the next step is a one electron reduction which takes place at around –1.58 V (Figure 2.7) to afford the neutral 35-electron hydride **$Fe_2(H)$**. At this point it is not clear whether a second protonation to give **$Fe_2(H_2)^+$**, or one electron reduction to yield **$Fe_2(H)^-$** occurs. Certainly, the basicity of **$Fe_2(H)$** should be roughly similar to that of **2.1ab** and thus

we expect this pathway to be favoured, and while reduction of **$Fe_2(H)$** occurs necessarily at a higher potential to that of **2.3ab** the precise value is not known. DFT calculations show that the 35-electron cationic dihydrogen species **$Fe_2(H_2)^+$** formed by protonation of the neutral hydride **$Fe_2(H)$** is able to release H_2 and gives the radical cation **$2.1ab^{\bullet+}$** which takes up an electron to regenerate **2.1**. The second pathway propagates *via* reduction of the neutral hydride **$Fe_2(H)$** to form **$Fe_2(H)^-$** which reacts with proton to generate the dihydride **$Fe_2(H_2)$**. This species undergoes a third protonation to form **$Fe_2(H)(H_2)^+$** which release H_2 and gives back the cationic hydride **2.3ab**. DFT calculations also show that **$Fe_2(H_2)^+$** can undergo reduction before release of H_2 to form the dihydride species **$Fe_2(H_2)$**. One complication to these catalytic pathways is the possible formation of **2.3bb** during the electrocatalysis. While we cannot completely rule this out, the relatively rapid scan speeds 0.1 Vs^{-1} utilised as compared with the rate of conversion of **2.3ab** to **2.3bb** ($t_{1/2}$ *ca.*1h) would suggest that the amount of **2.3bb** is always less than 1%.

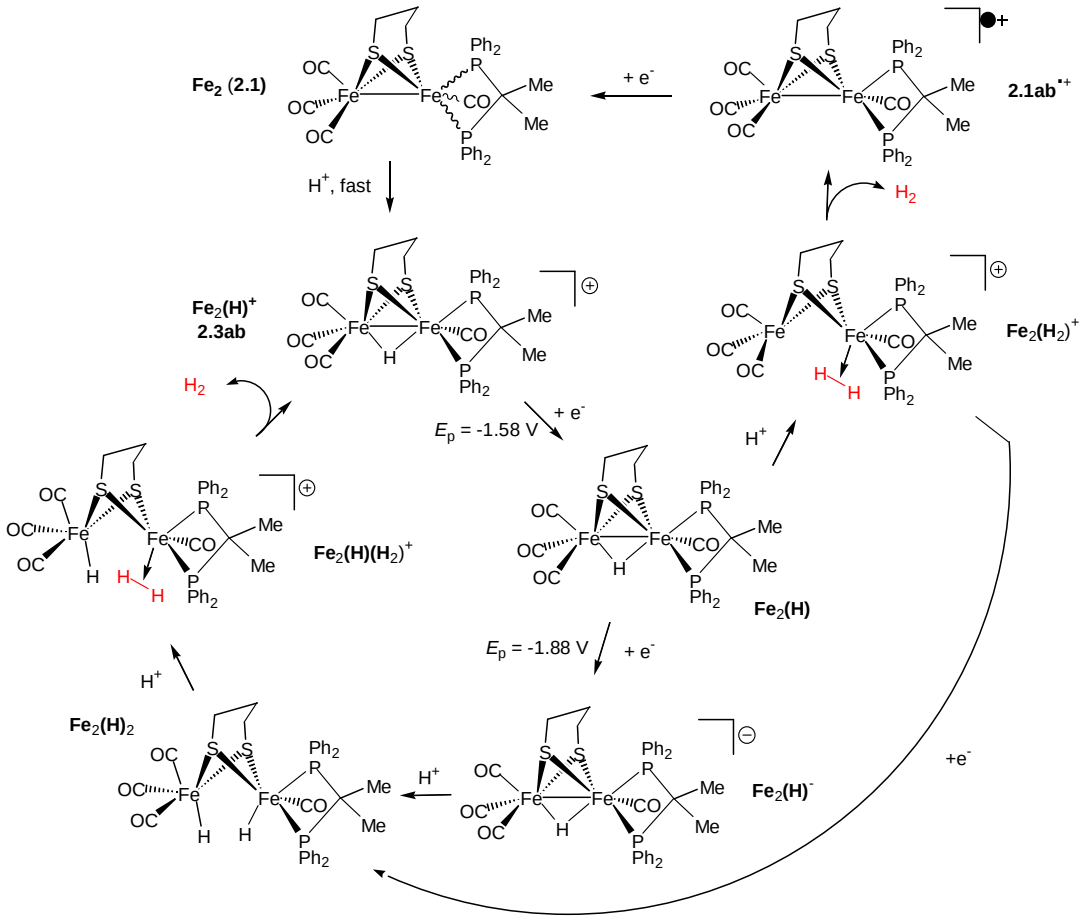

Scheme 2.9. DFT computed catalytic mechanism for the electrocatalytic proton reduction by $Fe_2(CO)_4\{\kappa^2$-$Ph_2PC(Me_2)PPh_2\}(\mu$-pdt) (**2.1**).

2.3. Summary and conclusions

This chapter details the synthesis, structure and thermal stability of the diphosphine chelate $Fe_2(CO)_4\{\kappa^2\text{-}Ph_2PC(Me_2)PPh_2\}(\mu\text{-pdt})$ (**2.1**) together with catalytic studies carried out to assess its proton reduction ability under electrochemical condition. $Me_3NO{\cdot}2H_2O$ initiated reaction between $Fe_2(CO)_6(\mu\text{-pdt})$ (**1.1**) and $Ph_2PC(Me_2)PPh_2$ gives **2.1** in moderate yield (63%) and the *in situ* spectroscopic data suggest that the reaction proceeds *via* the penta-carbonyl intermediate $Fe_2(CO)_5\{\kappa^1\text{-}Ph_2PC(Me_2)PPh_2\}(\mu\text{-pdt})$ (**2A**). X-ray structure shows that **2.1** prefers dibasal configuration in the solid-state while both dibasal and apical-basal isomers are found to exist in solution in an approximate 2:1 ratio. The apical-basal isomer **2.1ab** lies *ca*. 2 $kJmol^{-1}$ lower in energy than the dibasal form **2.1bb**, and they do not interconvert in solution at room temperature for which an activation barrier of 98.7 $kJ\ mol^{-1}$ has been calculated. Complex **2.1** slowly converts into the bridged isomer **2.2** upon heating and this provides support that the latter isomer is thermodynamically favoured. DFT calculations show that **2.2** lies *ca*. 2.9 and 2.0 $kJ\ mol^{-1}$ lower in energy than **2.1bb** and **2.1ab**, respectively. Complex **2.1** undergoes rapid protonation by $HBF_4{\cdot}Et_2O$ to afford initially basal-apical $[Fe_2(CO)_4(\mu\text{-H})\{\kappa^2\text{-}Ph_2PC(Me_2)PPh_2\}(\mu\text{-pdt})][BF_4]$ (**2.3ab**) which then slowly converts into the dibasal isomer $[Fe_2(CO)_4(\mu\text{-H})\{\kappa^2\text{-}Ph_2PC(Me_2)PPh_2\}(\mu\text{-pdt})][BF_4]$ (**2.3bb**) upon standing whereas **2.2** slowly decomposes in presence of $HBF_4{\cdot}Et_2O$. In both **2.3ab** and **2.3bb**, the hydride resides across the iron-iron bond and the protonation is believed to proceed *via* a terminal hydride species namely $[HFe_2(CO)_4\{\kappa^2\text{-}Ph_2PC(Me_2)PPh_2\}(\mu\text{-pdt})][BF_4]$ (**2.3tH**). The CV of **2.1** in MeCN shows separate redox features for both apical-basal and dibasal isomers leading to common intermediates while that of the bridge isomer displays single oxidative and reductive features. To our knowledge, **2.1** is the first phosphine-substituted diiron chelate that shows separate redox features for the dibasal and apical-basal isomers. Electrocatalytic studies carried out with **2.1** in presence of $HBF_4{\cdot}Et_2O$ shows that it catalyses proton reduction following chemically initiated CE route. An important finding is that it is the kinetic isomer **2.3ab** which is active in the catalytic cycle. DFT methods were applied to probe this mechanism which revealed that two interconnected catalytic pathways, namely CECE and CEECC, are operative during catalysis. This work thus provides further justification for the development of chelate complexes of the type $Fe_2(CO)_4(\kappa^2\text{-diphosphine})(\mu\text{-dithiolate})$ as viable proton reduction catalysts.

2.4. Experimental Section

2.4.1. General. All reactions were carried out using standard Schlenk-line techniques under N_2 and reaction solvents were purified on alumina columns. Work-up was done in air using standard bench reagents. The diphosphine $Ph_2PC(Me)_2PPh_2$ [28] and $Fe_2(CO)_6(\mu\text{-pdt})$ (**1.1**) [42] were prepared by standard procedures. NMR spectra were recorded on a Bruker AMX400 spectrometer and referenced internally to the residual solvent peak (^1H) or externally to $P(OMe)_3$ (^{31}P). Infrared spectra were recorded on a Nicolet 205 FT-IR spectrometer in a solution cell fitted with calcium fluoride plates, subtraction of the solvent absorptions being achieved by computation. Fast atom bombardment mass spectra were recorded on a VG ZAB-SE high resolution mass spectrometer and elemental analyses were performed in-house at UCL.

2.4.2. Synthesis of $Fe_2(CO)_4\{\kappa^2\text{-}Ph_2PC(Me_2)PPh_2\}(\mu\text{-pdt})$} (2.1). A mixture of **1.1** (0.20 g, 0.52 mmol), $Ph_2PC(Me_2)PPh_2$ (0.21 g, 0.52 mmol) and $Me_3NO.2H_2O$ (0.15 g, 0.14 mmol) were dissolved in MeCN (*ca.* 35 ml). The orange solution darkened rapidly and became black. After stirring for 4 h the solvent was removed under reduced pressure to give a dark red residue. This was washed with hexane (*ca.* 3 x 5 ml) in order to remove any unreacted **1.1** and diphosphine and the red residue was dried. This was extracted with diethylether (*ca.* 20 ml) and cooled to -10 ^oC to afford **2.1** (0.24 g, 63%) as brick red powder. Crystals suitable for X-ray diffraction were grown upon slow diffusion of hexanes into a concentrated CH_2Cl_2 solution. IR ν(CO)(CH_2Cl_2): 2018vs, 1949s, 1896m cm^{-1}. $^{31}P\{^1H\}$ NMR ($CDCl_3$): 75.5 (s), 50.8 (s); (CD_2Cl_2) 77.2 (s, **2.1ab**), 52.4 (s, **2.1bb**) ppm. ^1H NMR (CD_2Cl_2): δ 7.87 – 7.23 (m, 20H, Ph, **2.1ab** + **2.1bb**), 3.16 (d, J 6.3, 1H, CH_2, **2.1ab**), 2.42 (m, 4H, CH_2, **2.1bb**), 2.15 (br m, 5H, CH_2, **2.1ab**), 1.94 (brm, 2H, CH_2, **2.1bb**), 1.85 (t, J 12.2, 3H, Me, **2.1bb**), 1.82 (t, J 10.7, 3H, Me, **2.1ab**), 1.38 (t, J 10.8, 3H, Me, **2.1ab**), 1.34 (t, J 16.8, 3H, Me, **2.1bb**). Elemental analysis calc. for $Fe_2S_2P_2O_4C_{34}H_{32}$ (found): C 54.99 (55.08), H 4.31 (4.57).

Crystallographic data for **2.1bb**: red block, dimensions 0.36 × 0.16 × 0.13 mm^3, triclinic, space group *P*1bar, a = 10.625(2), b = 11.308(2), c = 15.007(3) Å, α = 86.626(3), β = 81.950(3), γ = 65.000(3)^o, V = 1618.0(5) $Å^3$, Z = 2, F(000) 764, d_{calc} = 1.524 g cm^{-3}, μ = 1.163 mm^{-1}. 13806 reflections were collected, 7330 unique [R(int) = 0.0271]. At convergence, R_1 = 0.0306, wR_2 = 0.0788 [$I > 2.0\sigma(I)$] and R_1 = 0.0337, wR_2 = 0.0804 (all data), for 525 parameters.

2.4.3. Synthesis of $Fe_2(CO)_4\{\mu\text{-}Ph_2PC(Me_2)PPh_2\}(\mu\text{-pdt})$ (2.2). A toluene solution (80 ml) of **2.1** (0.05 g, 0.67 mmol) was heated at reflux for approximately 30 h. After cooling to room temperature volatiles were removed on a rotary evaporator giving an oily red solid. This was washed with hexane (*ca.* 3 x 5 ml) to give a dry orange solid. The crude material was dissolved in a minimum amount of CH_2Cl_2 and layered with hexanes to afford large red crystals of **2.2** (0.035 g, 70%). IR ν(CO)(CH_2Cl_2): 1984m, 1952s, 1916m, 1895sh cm^{-1}. $^{31}P\{^1H\}$ NMR ($CDCl_3$): 86.9 (s); (CD_2Cl_2) 89.0 (s) ppm. ^1H NMR ($CDCl_3$) δ 8.02 – 6.79 (m, 20H, Ph), 2.13 (br, 4H, CH_2), 1.86 (br, 2H, CH_2), 1.65 (t, J 12.7, 3H, Me), 0.86 (m, 3H, Me). Elemental analysis calc. for $Fe_2S_2P_2O_4C_{34}H_{32}.CH_2Cl_2$ (found): C 48.92 (48.66), H 4.20 (4.23).

Crystallographic data for **2.2**·CH_2Cl_2: red block, dimensions 0.34 × 0.32 × 0.21 mm^3, monoclinic, space group $P2_1/n$, a = 12.100(2), b = 21.513(3), c = 13.203(2) Å, α = 90, β = 97.843(2), γ = 90°, V = 3404.7(9) $Å^3$, Z = 4, F(000) 1662, d_{calc} = 1.579 g cm^{-3}, μ = 1.226 mm^{-1}. 28679 reflections were collected, 8100 unique [R(int) = 0.0339]. At convergence, R_1 = 0.0492, wR_2 = 0.1369 [$I > 2.0\sigma(I)$] and R_1 = 0.0545, wR_2 = 0.1414 (all data), for 421 parameters.

2.4.4. Synthesis of $[Fe_2(CO)_4(\mu\text{-}H)\{\kappa^2\text{-}Ph_2PC(Me)_2PPh_2\}(\mu\text{-pdt})\}][BF_4]$ (2.3). To a CH_2Cl_2 (5 ml) of **2.1** (0.10 g, 0.13 mmol) was added a few drops of $HBF_4.Et_2O$. The mixture was swirled and the red- brown solution first turned blue, then purple and finally back to brown. The solution was stirred for 4 h and volatiles removed under vacuum to give a deep red oily solid. This was washed with a very small amount of Et_2O (to remove excess acid) and dried. Carefully layering a concentrated CH_2Cl_2 with Et_2O resulted in the slow formation of large red crystals of **2.3bb**. Data for **2.3bb**: IR ν(CO)(CH_2Cl_2): 2097vs, 2048s, 2035s, 1964s cm^{-1}. $^{31}P\{^1H\}$ NMR (CD_2Cl_2): 55.8 (s) ppm. ^1H NMR (CD_2Cl_2): δ 7.90 –7.32 (m, 20H, Ph), 3.09 (br, 2H, CH_2), 2.58 (br, 4H, CH_2), 2.19 (t, J 13.4, 3H, Me), 1.46 (t, J 17.1, 3H, Me), –10.78 (t, J 19.2 , 1H, μ-H). Elemental analysis calc. for $Fe_2S_2P_2O_4C_{34}H_{32}B_1F_4.0.5CH_2Cl_2$ (found): C 47.55 (47.86), H 3.79 (3.86). Data for **2.3ab**: IR ν(CO)(CH_2Cl_2): 2093vs, 2044s, 1982br cm^{-1}. $^{31}P\{^1H\}$ NMR (CD_2Cl_2): 68.7 (d, J 62.0), 60.1 (d, J 62.0) ppm. ^1H NMR (CD_2Cl_2) δ –15.50 (dd, J 18.4, 4.4, μ-H).

Crystallographic data for **2.3**·$0.5CH_2Cl_2$: red block, dimensions 0.16 × 0.14 × 0.13 mm^3, orthorhombic, space group *Pbca*, a = 11.273(3), b = 19.387(5), c = 33.773(8) Å, α = 90, β = 90, γ = 90°, V = 7381(3) $Å^3$, Z = 8, F(000) 3544, d_{calc} = 1.567 g cm^{-3}, μ = 1.116 mm^{-1}. 59991 reflections were collected, 8946 unique [R(int) = 0.0704]. At convergence, R_1 =

0.0712, wR_2 = 0.1712 [$I > 2.0\sigma(I)$] and R_1 = 0.0877, wR_2 = 0.1791 (all data), for 460 parameters. The structure was solved using the Patterson method.

2.5. References

(1) J. W. Tye, M. Y. Darensbourg and M. B. Hall, *Inorg. Chem.*, 2006, **45**, 1552-1559.

(2) F. I. Adam, G. Hogarth, I. Richards and B. E. Sanchez, *Dalton Trans.*, 2007, 2495-2498.

(3) F. I. Adam, G. Hogarth and I. Richards, *J. Organomet. Chem.*, 2007, **692**, 3957-3968.

(4) F. I. Adam, G. Hogarth, S. E. Kabir and I. Richards, *C. R. Chim.*, 2008, **11**, 890-905.

(5) S. Ghosh, G. Hogarth, N. Hollingsworth, K. B. Holt, I. Richards, M. G. Richmond, B. E. Sanchez and D. Unwin, *Dalton Trans.*, 2013, **42**, 6775-6792.

(6) J.-F. Capon, F. Gloaguen, F. Y. Pétillon, P. Schollhammer and J. Talarmin, *Eur. J. Inorg. Chem.*, 2008, 4671-4681.

(7) S. Ezzaher, J.-F. Capon, F. Gloaguen, F. Y. Pétillon, P. Schollhammer and J. Talarmin, *Inorg. Chem.*, 2007, **46**, 3426-3428.

(8) S. Ezzaher, J.-F. Capon, F. Gloaguen, F. Y. Pétillon, P. Schollhammer and J. Talarmin, *Inorg. Chem.*, 2007, **46**, 9863-9872.

(9) S. Ezzaher, J.-F. Capon, F. Gloaguen, N. Kervarec, F. Y. Pétillon, R. Pichon, P. Schollhammer and J. Talarmin, *C. R. Chim.*, 2008, **11**, 906-914.

(10) S. Ezzaher, J. -F. Capon, F. Gloaguen, F. Y. Pétillon, P. Schollhammer, J. Talarmin and N. Kervarec, *Inorg. Chem.*, 2009, **48**, 2-4.

(11) S. Ezzaher, J.-F. Capon, N. Dumontet, F. Gloaguen, F. Y. Pétillon, P. Schollhammer and J. Talarmin, *J. Electroanal. Chem.*, 2009, **626**, 161-170.

(12) S. Lounissi, J.-F. Capon, F. Gloaguen, F. Matoussi, F. Y. Pétillon, P. Schollhammer and J. Talarmin, *Chem. Commun.*, 2011, **47**, 878-880.

(13) D. Chouffai, G. Zampella, J.-F. Capon, L. De Gioia, A. Le Goff, F. Y. Pétillon, P. Schollhammer and J. Talarmin, *Organometallics*, 2012, **31**, 1082-1091.

(14) S. Lounissi, G. Zampella, J.-F. Capon, L. De Gioia, F. Matoussi, S. Mahfoudhi, F.Y. Pétillon, P. Schollhammer and J. Talarmin, *Chem.-Eur. J.*, 2012, **18**, 11123-11138.

(15) C. Greco, P. Fantucci, L. De Gioia, R. Suarez-Bertoa, M. Bruschi, J. Talarmin and P. Schollhammer, *Dalton Trans.*, 2010, **39**, 7320-7329.

(16) A. K Justice, G. Zampella, L. De Gioia, T. B. Rauchfuss, J. I. van der Vlugt and S. R. Wilson, *Inorg. Chem.*, 2007, **46**, 1655-1664.

(17) A. K Justice, T. B. Rauchfuss and S. R. Wilson, *Angew. Chem. Int. Ed.*, 2007, **46**, 6152-6154.

(18) N. Wang, M. Wang, T. Liu, T. Zhang, M. Darensbourg and L. Sun, *Inorg. Chem.*, 2008, **47**, 6948-6955.

(19) N. Wang, M. Wang, J. Liu, K. Jin, L. Chen and L. Sun, *Inorg. Chem.*, 2009, **48**, 11551-11558.

(20) L.-C. Song, W. Gao, X. Luo, Z.-X. Wang, X.-J. Sun and H.-B. Song, *Organometallics*, 2012, **31**, 3324-3332.

(21) L.-C. Song, C.-G. Li, J.-H. Ge, Z.-Y. Yang, H.-T. Wang, J. Zhang and Q.-M. Hu, *J. Inorg. Biochem.*, 2008, **102**, 1973-1979.

(22) W. Gao, J. Ekström, J. Liu, C. Chen, L. Eriksson, L. Weng, B. Åkermark and L. Sun, *Inorg. Chem.*, 2007, **46**, 1981-1991.

(23) X.-F. Liu and B.-S. Yin, *J. Coord. Chem.*, 2010, **63**, 4061-4067.

(24) F. Ridley, S. Ghosh, G. Hogarth, N. Hollingsworth, K. B. Holt and D. G. Unwin, *J. Electroanal. Chem.*, 2013, **703**, 14-22.

(25) G. Hogarth, S. E. Kabir and I. Richards, *Organometallics*, 2010, **29**, 6559-6568.

(26) M. E. Jung and G. Piizzi, *Chem. Rev.*, 2005, **105**, 1735-1766 and references therein.

(27) R. M. Beesley, C. K. Ingold and J. F. Thorpe, *J. Chem. Soc.*, 1915, 1080-1106.

(28) G. Hogarth and J. Kilmartin, *J. Organomet. Chem.*, 2007, **692**, 5655-5670.

(29) M. Filby, A. J. Deeming, G. Hogarth and M.-Y. Lee, *Can. J. Chem.*, 2006, **84**, 319-329.

(30) S. Al-Jibori and B. L. Shaw, *J. Chem. Soc., Chem. Commun.*, 1982, 286-287.

(31) S. Al-Jibori and B. L. Shaw, *Inorg. Chim. Acta*, 1983, **74**, 235-239.

(32) W. Hewertson and N. R. Watson, *J. Chem. Soc.*, 1962, 1490-1494.

(33) J. V. Barkley, J. C. Grimshaw, S. J. Higgins, P. B. Hoare, M. K. McCart and A. K. Smith, *J. Chem. Soc., Dalton Trans.*, 1995, 2901-2908.

(34) U. Anandhi, T. Holbert, D. Leung and P. R. Sharp, *Inorg. Chem.*, 2003, **42**, 1282-1295.

(35) J. S. Wiley and D. M. Heinekey, *Inorg. Chem.*, 2002, **41**, 4961-4966.

(36) J. V. Barkley, M. Ellis, S. J. Higgins and M. K. McCart, *Organometallics*, 1998, **17**, 1725-1731.

(37) M. Ferrer, A. Gutierrez, M. Mounir, L. Rodriguez, O. Rossell, M. Font-Bardia, P. Gomez-Sal, A. Martin and X. Solans, *Organometallics*, 2011, **30**, 3419-3429.

(38) J. A. van Rijn, M. A. Siegler, A. L. Spek, E. Bouwman and E. Drent, *Organometallics*, 2009, **28**, 7006-7014.

(39) C. S. Kraihanzel and P. K. Maples, *J. Organomet. Chem.*, 1976, **117**, 159-170.

(40) N. D. Reddy, P. E. Fanwick and R. A. Walton, *Inorg. Chim. Acta*, 2001, **314**, 189-193.

(41) J. C. Sarker, A. K. Raha, S. Ghosh, G. Hogarth, S. E. Kabir and M. G. Richmond, *J. Organomet. Chem.*, 2014, **750**, 49-58.

(42) A. Winter, L. Zsolnai and G. Huttner, *Z. Naturforsch.*, 1982, **37b**, 1430-1436.

Chapter 3

Hydrogenase biomimetics with redox active ligands: Catalytic proton reduction by $Fe_2(CO)_4(\kappa^2$-diamine)(μ-edt) (diamine = 2,2′-bipy, 1,10-phen)

3.1. Introduction

Recent focus in the synthesis of biomimetics of the active site of the iron-only hydrogenase enzyme centres on the incorporation of non-innocent ligands [1-11] onto the redox-active diiron centre such that communication between the two electrochemically active centres can be assessed [1-3] since it is such communication between the diiron and tetrairon sites in the so-called *H-cluster* [2,12-15] that controls the activity of the enzyme. In 2005, Pickett and co-workers reported a model $[Fe_4S_4(L)_3\{Fe_2(CH_3C(CH_2S)_3)(CO)_5\}]^{2-}$ {L = 1,3,5-tris(4,6-dimethyl-3-mercaptophenyl-thio)-2,4,6-tris(*p*-tolyl-thio)benzene} [2] in which the entire iron-sulphur framework of the active site of iron-only hydrogenase had been assembled. The {4Fe4S} site in this model catalysts was found to be easier to reduce than the {2Fe3S} site which can transfer the added electron to the later site [2] (Scheme 3.1).

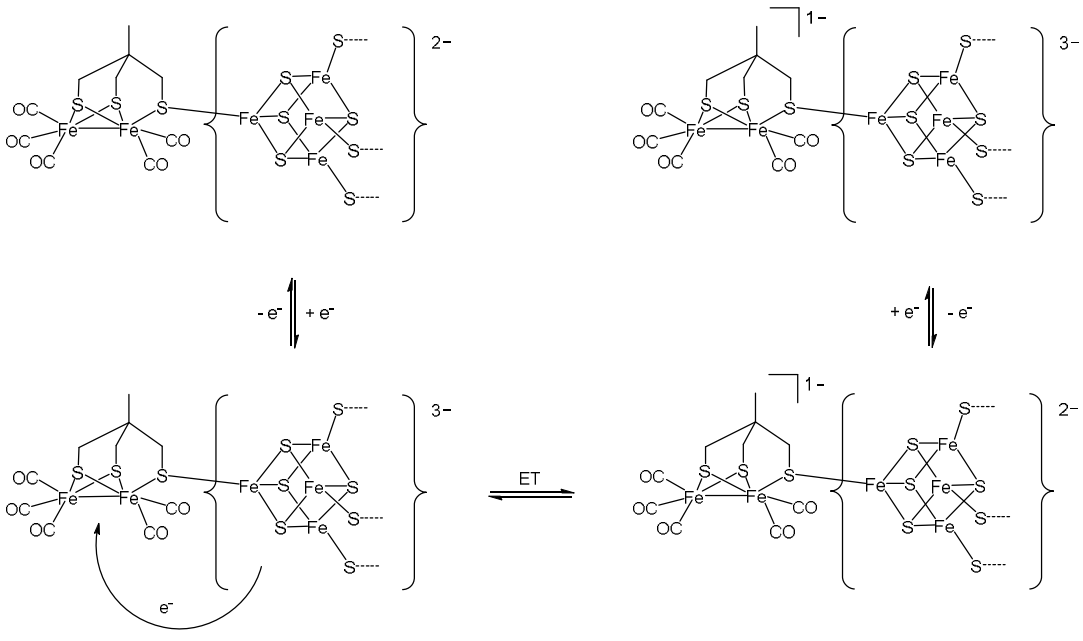

Scheme 3.1. Intramolecular electron transfer between {4Fe4S} and {2Fe3S} sites in $[Fe_4S_4(L)_3\{Fe_2(CH_3C(CH_2S)_3)(CO)_5\}]^{2-}$ {L = 1,3,5-tris(4,6-dimethyl-3-mercaptophenyl- thio)-2,4,6-tris(*p*-tolyl-thio)benzene} [2].

Reduction of the anchored cubane from $\{4Fe4S\}^{2+}$ to $\{4Fe4S\}^{+}$ has yet to be achieved in the natural system, although the neighbouring {4Fe4S} relay units can be reduced to this level [16]. This raises the question as to whether the anchored cubane switches between $\{4Fe4S\}^{2+}$ and $\{4Fe4S\}^{+}$ states during catalytic turnover in natural systems. Spectroscopic and theoretical studies carried out to date have suggested such electron transfer during turnover in the natural system [2,14,15]. Pickett's model catalyst can reduce protons at low over-potentials but its inherent frailty, as well as the structural intricacy, makes it practically irrelevant.

Consequently, simple redox-active non-innocent ligands have attracted much attention in recent years as surrogates of the anchored cubane cluster [1,4,8-11,17]. In this context, we have synthesized diiron biomimetics containing redox active diamine and diphosphine ligands and studied their electrochemical properties. In this chapter we consider biomimetic models containing diamines, with those based upon diphosphines being discussed in chapters 4 and 5.

2,2′-Bipyridine (2,2′-bipy) and 1,10-phenanthroline (1,10-phen) are non-innocent chelating agents that can coordinate with a wide-variety of metals in different oxidation states [18-20]. Thus 2,2′-bipyridine exists in three different oxidation levels namely the neutral 2,2′-bipy, the π-radical monoanion $(2,2'\text{-bipy})^{\cdot-}$ and the diamagnetic dianion $(2,2'\text{-bipy})^{2-}$, all of which have been characterised by X-ray crystallography [21-24], supporting metals across the periodic table [25-31] and with numerous applications [18,19,32-46]. For example, $[Ru(2,2'\text{-bipy})_3]^{2+}$ is the most widely studied one-electron photo-redox catalyst and has facilitated significant advances in energy storage, hydrogen and oxygen evolution from water and methane production from carbon dioxide [18,19,32-35]. The iron complex, $[Fe(1,10\text{-phen})_3]^{3+}$, is often used as a coordinatively saturated one-electron oxidant, a redox indicator and in model compounds of biologically active substances [36-46].

In 2007, Schollhammer and co-workers reported the first example of a biomimetic containing a chelating diamine, namely $Fe_2(CO)_4(\kappa^2\text{-}1,10\text{-phen})(\mu\text{-pdt})$ (**3.2-pdt**) [10] (pdt = $SCH_2CH_2CH_2S$) (Chart 3.1). Subsequent work found that this protonated upon addition of $HBF_4{\cdot}Et_2O$ to afford the bridging hydride complex, $[Fe_2(CO)_4(\kappa^2\text{-}1,10\text{-phen})(\mu\text{-H})(\mu\text{-pdt})][BF_4]$, which displayed poor thermal stability [8], while the related azadithiolate

complex, $Fe_2(CO)_4(\kappa^2$-1,10-phen)(μ-adt) (**3.2-adt**) (adt = $SCH_2N^iPrCH_2S$), undergoes protonation only at the bridgehead nitrogen [9]. More recently, Jones and co-workers reported a detailed study of the related 2,2′-bipyridine complex, $Fe_2(CO)_4(\kappa^2$-2,2′-bipy)(μ-pdt) (**3.1-pdt**) [11], which also protonates at the metal-metal bond upon addition of strong acids. The electrochemistry of the latter was probed, the reductive chemistry being interpreted in terms of two closely spaced one-electron processes, being associated with the diiron centre and the 2,2′-bipyridine ligand.

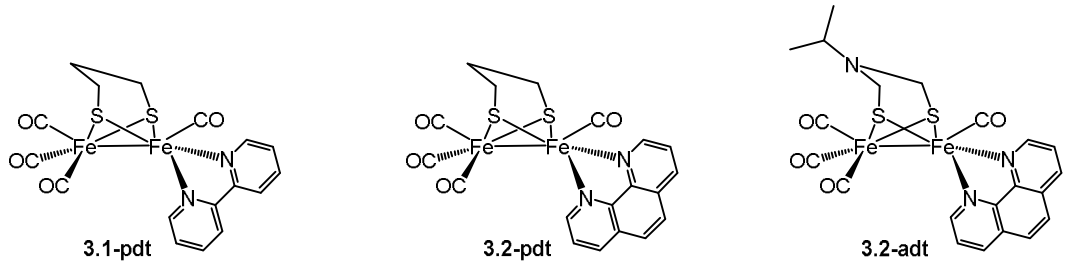

Chart 3.1. Biomimetic models of [FeFe]-hydrogenase containing diamine ligand [9-11].

The nature of the dithiolate backbone has a subtle impact on the reductive behaviour of dithiolate-bridged diiron complexes, $Fe_2(CO)_6$(μ-dithiolate), as evidenced by the variety of products that result from the transfer of one and two electrons into those compounds [47-56], but sometimes exerts significant influence on electrocatalytic pathway by regulating the proton transfer from solution to the diiron centre [8,9,11]. We thus sought to prepare $Fe_2(CO)_4(\kappa^2$-2,2′-bipy)(μ-edt) (**3.1-edt**) and $Fe_2(CO)_4(\kappa^2$-1,10-phen)(μ-edt) (**3.2-edt**) in order to compare their electrochemical properties and catalytic activity towards proton reduction with the analogous pdt-complexes.

3.2. Results and discussion

3.2.1. Synthesis and characterisation. The 2,2′-bipyridine complex, $Fe_2(CO)_4(\kappa^2$-2,2′-bipy)(μ-edt) (**3.1-edt**), was prepared upon refluxing an acetonitrile solution of $Fe_2(CO)_6$(μ-edt) (**1.3**) and a slight excess of 2,2′-bipyridine in the presence of $Me_3NO{\cdot}2H_2O$ being isolated after work-up as a dark green solid in 44% yield. In a similar manner the analogous 1,10-phenanthroline complex, $Fe_2(CO)_4(\kappa^2$-1,10-phen)(μ-edt) (**3.2-edt**), was prepared as a green solid in 32% yield (Scheme 3.2). Both are stable in the solid-state and in solution under an inert atmosphere but decompose over a few hours when solutions are left standing in air.

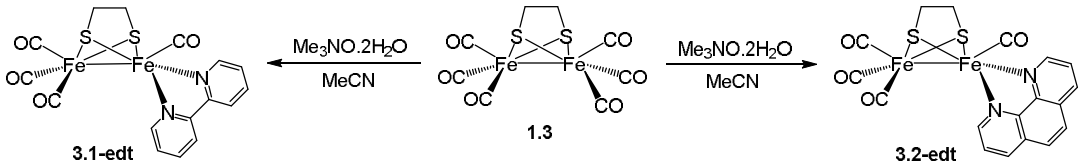

Scheme 3.2. Synthesis of $Fe_2(CO)_4(\kappa^2\text{-}2,2'\text{-bipy})(\mu\text{-edt})$ (**3.1-edt**) and $Fe_2(CO)_4(\kappa^2\text{-}1,10\text{-phen})(\mu\text{-edt})$ (**3.2-edt**).

The pair were characterized by X-ray crystallography, the results of which are summarised in Figure 3.1 and Table 3.1, the latter also giving selected metric parameters for related pdt and adt complexes. The crystallography of **3.1-edt** was straightforward and showed a single molecule which contained a plane of symmetry containing both irons and the apical carbonyls. For **3.2-edt,** there are four independent molecules in the asymmetric unit with only minor differences being noted between crystallographically independent molecules (Table 3.1). For each structure, the data were of sufficiently good quality to enable location of all hydrogen atoms from difference maps and these were refined isotropically. The two molecular structures are quite similar, the diamine binding in a chelating fashion and in a dibasal manner [9-11]. Iron-iron and iron-sulfur distances are unexceptional and do not differ significantly between the two. Iron-nitrogen bond lengths of 1.967(1) and 1.972(6) (av) Å in **3.1-edt** and **3.2-edt** respectively are slightly shorter than those in **3.1-pdt** [(av) 1.986(3) Å] [11] and **3.2-pdt** [1.990(3) Å] [10]. A more significant difference between edt and pdt complexes is seen in the Fe–Fe–N bond angles, those in the 1,10-phen complexes being around 5^o large in the pdt complex, a difference that might be due to the more sterically demanding nature of the pdt ligand. The central carbon-carbon bond of the 2,2′-bipyridine ligand in **3.1-edt** [1.464(3) Å] suggests that it is acting as a neutral diamagnetic ligand rather than a π-radical monoanion, the latter being associated with shorter carbon-carbon bonds between 1.41 – 1.43 Å [55,56].

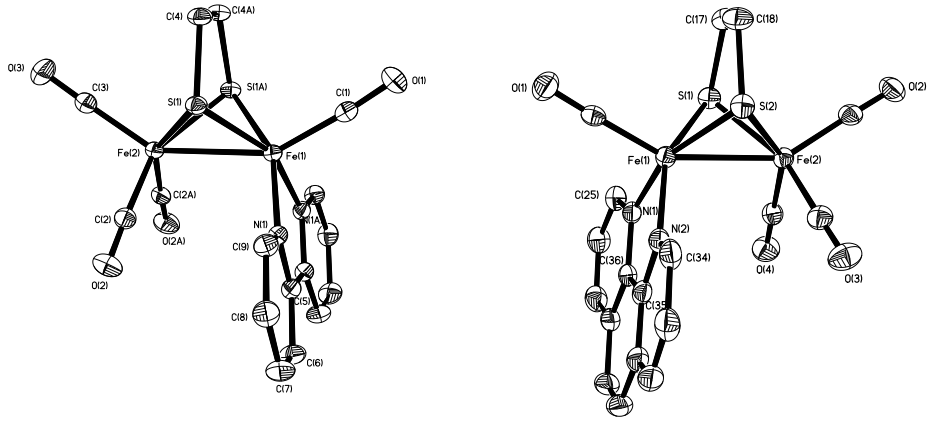

Figure 3.1. ORTEP plots (50% thermal ellipsoids) of $Fe_2(CO)_4(\kappa^2$-2,2′-bipy)(μ-edt) (**3.1-edt**) and one of the four independent molecules in the asymmetric unit of $Fe_2(CO)_4(\kappa^2$-1,10-phen)(μ-edt) (**3.2-edt**).

Table 3.1. Selected structural parameters for 2,2′-bipy and 1,10-phen complexes

Compound	**3.1-edt**	**3.1-pdt** [11]	**3.2-edt**	**3.2-pdt** [10]	**3.2-adt** [9]
Fe–Fe	2.5318(5)	2.5623(4)	2.5321(6) 2.5298(6) 2.5227(6) 2.5221(6)	2.5483(4)	2.5354(8)
Fe–N	1.967(1)	1.982(2) 1.990(2)	1.971(2) 1.987(2) 1.969(2) 1.972(2) 1.962(2) 1.976(2) 1.962(2) 1.977(2)	1.986(2) 1.993(2)	1.989(3) 1.983(3)
Fe–Fe–N	100.69(4)	107.95(4) 105.34(4)	99.67(2) 102.54(7) 99.99(7) 102.44(7) 99.93(7) 101.74(7) 99.06(7) 102.05(7)	105.33(4) 104.89(5)	102.76(9) 101.55(9)
N–Fe–N	81.41(8)	80.81(6)	81.7(1) 82.3(1) 82.4(1) 82.2(1)	81.71(7)	81.8(2)

While a single isomer is seen in the solid-state this is not the case for either **3.1-edt** or **3.2-edt** in solution. For **3.2-edt**, the aromatic region of the ^{1}H NMR spectrum shows the presence of a small amount of a second isomer in a *ca.* 30:1 ratio. Schollhammer also observed two isomers in the solution of **3.2-pdt** at low temperature due to the flipping of

bridgehead methylene unit of the pdt ligand [10]. Since such a route for isomerisation is not available for **3.1-edt** we assume that the second isomer is the apical-basal isomer (Chart 3.2) but cannot determine this unequivocally. In the case of **3.1-edt** the ratio of the two isomers in CD_2Cl_2 at 298 K is *ca.* 3.5:1. Some of the aromatic resonances overlap but the methylene region of the spectrum is quite clear and consists of four signals, two being associated with each isomer. Reducing the temperature to 223 K did not result in any significant difference in the ratio but some of the aromatic resonances separated making identification of individual protons more easy. For a basal-apical isomer, since the two nitrogen atoms are now inequivalent then, all of the aromatic protons should be different. We were not able to observe this and it may simply be that the resulting chemical shift differences are small. It is difficult to imagine any other type of isomerism occurring in this complex and consequently we attribute the smaller signals to a basal-apical isomer.

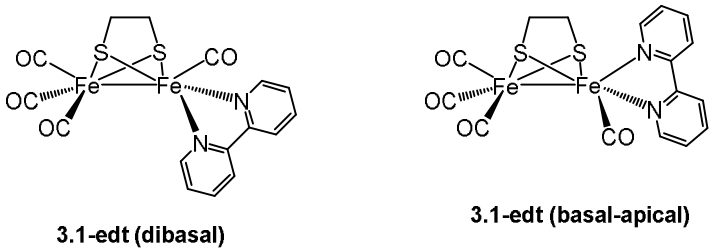

Chart 3.2. Dibasal and apical basal isomers of $Fe_2(CO)_4(\kappa^2\text{-}2,2'\text{-bipy})(\mu\text{-edt})$ (**3.1-edt**).

Evidence of isomers is also seen in the IR spectrum, which is more complex than that of **3.2-edt** specifically two high energy absorptions are seen at 2023 and 2010 cm^{-1}, the later being somewhat larger than the former. We can compare these values with that of 2010 cm^{-1} for **3.2-edt** and this allows us to further conclude that the absorption band at 2010 cm^{-1} in **3.1-edt** is associated with the dibasal isomer. In contrast, both IR and NMR data suggest only the presence of dibasal isomer in solution for **3.1-pdt** [11]. Unlike **3.1-edt**, the solution IR spectrum of **3.1-pdt** shows only three bands at 2007, 1937 and 1896 cm^{-1} characteristic for the dibasal isomer [11]. Given that IR frequencies are a measure of the amount of electron-density on the diiron centre this suggests that in the dibasal position the 2,2′-bipy ligand acts as a better σ-donor, creating a relatively electron-rich centre as compared to the basal-apical isomer. While as discussed in the previous chapter, related isomerism has been observed in diphosphine complexes of this type [57-59], this does not lead to significantly different NMR spectra. The difference observed here may be

important to later studies relating to the protonation and oxidation-reduction of the complex. For example, protonation and oxidation are likely to be more favourable for the relatively electron-rich dibasal isomer, while reduction may be favoured for the apical-basal isomer (see below).

3.2.2. Protonation studies. Schollhammer has shown that addition of $HBF_4 \cdot Et_2O$ to a dichloromethane solution of **3.2-pdt** at low temperatures results in formation of a bridging hydride complex, $[Fe_2(CO)_4(\mu\text{-}H)(\kappa^2\text{-}1,10\text{-phen})(\mu\text{-pdt})][BF_4]$ (**3.2H$^+$-pdt**) which has been crystallographically characterized [8], however this shows poor stability in solution at room temperature [8]. Similarly, Jones and co-workers have reported that **3.1-pdt** protonates upon addition of $HBF_4 \cdot Et_2O$ in acetonitrile to afford $[Fe_2(CO)_4(\mu\text{-}H)(\kappa^2\text{-}2,2'\text{-bipy})(\mu\text{-pdt})][BF_4]$ (**3.1H$^+$-pdt**) [11]. The behaviour of both **3.1-edt** and **3.2-edt** is very similar to that of their pdt analogues. Thus, addition of two equivalents of CF_3CO_2H to a dichloromethane solution of **3.1-edt** at room temperature was monitored by IR spectroscopy (Figure 3.2). Upon addition the colour of the solution immediately changed from green to red with complete loss of **3.1-edt** and the appearance of seven new absorptions at 2098, 2093, 2077, 2039, 2027, 1992 and 1973 cm^{-1}. Over a few minutes, the small absorption at 2077 cm^{-1} disappeared, while the other six bands remained, diminishing slowly over *ca.* 10 minutes. Very similar observations were noted for **3.2-edt** (Figure 3.3) with a transient absorption band at 2077 cm^{-1} also being noted. We also probed the behaviour of both **3.1-edt** and **3.2-edt** towards $HBF_4 \cdot Et_2O$. Addition of a slight excess of acid to a dichloromethane solution of **3.1-edt** at room temperature also lead to a rapid colour change with the formation of a new complex associated with IR bands at 2102, 2050 and 1990 cm^{-1}, while addition of the same acid to **3.2-edt** at room temperature resulted in the rapid appearance of three new absorptions in the IR spectrum at 2102, 2047 and 1989 cm^{-1} and over few minutes these were replaced by absorptions at 2108, 2063, 2048 and 2018 cm^{-1}. Thus it is clear that the diiron centre in both **3.1-edt** and **3.2-edt** is rapidly protonated by strong acids and the new absorption bands compare well with those of 2098, 2043 and 1985 cm^{-1} associated with **3.2H$^+$-pdt** [10] and 2098, 2044 and 1970 cm^{-1} for **3.1H$^+$-pdt** [11]. We attempted to follow the protonation of **3.1-edt** and **3.2-edt** by ^{1}H NMR spectroscopy, but did not see any signal after addition of acid even at –30°C. The resonances for the neutral complexes disappeared from the spectrum without any new resonance for the hydride species after addition of acid.

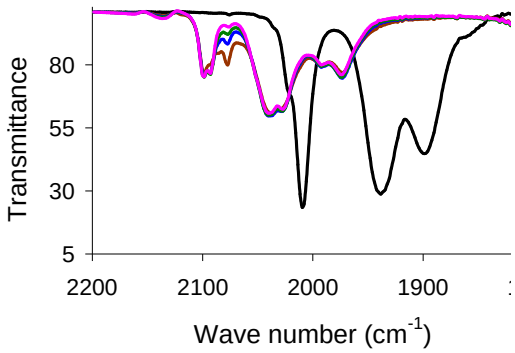

Figure 3.2. IR spectra of $Fe_2(CO)_4(\kappa^2$-2,2′-bipy)(μ-edt) (**3.1-edt**) in absence of acid (black) and after addition of two equivalents of CF_3CO_2H – after 1 min (brown), after 3 min (blue), after 5 min (green) and after 10 min (pink) – in CH_2Cl_2.

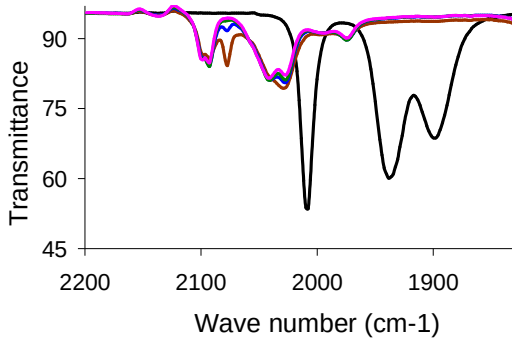

Figure 3.3. IR spectra of $Fe_2(CO)_4(\kappa^2$-1,10-phen)(μ-edt) (**3.2-edt**) in absence of acid (black) and after addition of two equivalents of CF_3CO_2H – after 1 min (brown), after 3 min (blue), after 5 min (green) and after 10 min (pink) – in CH_2Cl_2.

These observations are consistent with the formation of $[Fe_2(CO)_4(\mu$-H)$(\kappa^2$-2,2′-bipy)(μ-edt)$][BF_4]$ (**3.1H$^+$-edt**) and $[Fe_2(CO)_4(\mu$-H)$(\kappa^2$-1,10-phen)(μ-edt)$][BF_4]$ (**3.2H$^+$-edt**) (Scheme 3.3). The more complex nature of the IR spectra upon addition of CF_3CO_2H is associated with the existence of dibasal and basal-apical isomers of both **3.1H$^+$-edt** and **3.2H$^+$-edt**. Presumably the rate of conversion to the thermodynamically more stable isomer is acid dependent and thus with HBF_4 generation of a single isomer is rapid. The instability of all products has meant that we have been unable to determine which isomer is the most stable, but based on the crystal structure of dibasal $[Fe_2(CO)_4(\mu$-H)$(\kappa^2$-1,10-phen)(μ-pdt)$][BF_4].CH_2Cl_2.H_2O.BH_3$ (**3.2H$^+$-pdt**) [8], we favour this isomer. For the pdt complexes, the extra steric demands of the three atom backbone probably lead to the a relative destabilization of the apical-basal isomer.

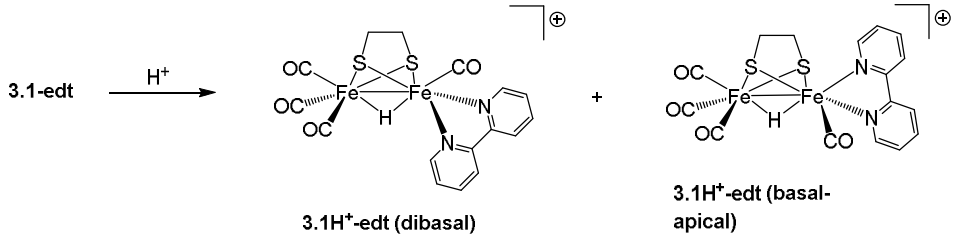

Scheme 3.3. Reaction of $[Fe_2(CO)_4(\kappa^2\text{-}2,2'\text{-bipy})(\mu\text{-edt})]$ (**3.1-edt**) with CF_3CO_2H.

We are unsure regarding the nature of the transient absorption band at 2077 cm^{-1} seen upon addition of CF_3CO_2H to both **3.1-edt** and **3.2-edt**. It is clearly associated with a protonated species being shifted *ca.* 60 cm^{-1} to higher wavenumbers with respect to the neutral complexes. From DFT calculations, Schollhammer and co-workers showed that the activation barriers towards protonation of dibasal **3.2-pdt** with $HBF_4{\cdot}Et_2O$ to give bridging or terminal hydride complexes were similar at 33.6 and 28.9 kcal mol^{-1} respectively [8]. Thus it seems possible that the transient species are terminal hydride complexes which either decompose or convert rapidly to bridging hydrides species.

3.2.3. Electrochemistry. The redox behaviour of $Fe_2(CO)_4(\kappa^2\text{-}2,2'\text{-bipy})(\mu\text{-edt})$ (**3.1-edt**) and $Fe_2(CO)_4(\kappa^2\text{-}1,10\text{-phen})(\mu\text{-edt})$ (**3.2-edt**) were studied in MeCN by cyclic voltammetry. Both show an irreversible reduction wave at E_p = –2.05 V, together with an irreversible oxidative wave at E_p = –0.18 V, showing that the nature of the diamine has little electronic impact upon the diiron core (Figure 3.4). Peak currents for **3.1-edt** are consistently larger than those for **3.2-edt** which we suggest is due to the larger diffusion coefficient of **3.1-edt** *vs.* **3.2-edt**. This is also observed for the free ligands (Figure 3.5) which show a single reduction wave at E_p = –2.63 V (2,2′-bipy) and E_p = –2.46 V (1,10-phen), respectively. Jones and co-workers investigated the electrochemistry of $Fe_2(CO)_4(\kappa^2\text{-}2,2'\text{-bipy})(\mu\text{-pdt})$ (**3.1-pdt**) under similar conditions and showed by controlled-potential coulometry that the irreversible reduction at E_p = –2.06 V is a two-electron process, and suggested that one electron is associated with the diiron centre and the second with the 2,2′-bipy ligand [11]. This is consistent with the reduction potentials of the free ligands which are expected to show a positive shift due to removal of electron density upon coordination to iron (Figure 3.5). The reductive peak currents for **3.1-edt** and **3.2-edt** are both much larger than the oxidative peak currents (i_{red} / i_{ox} = 1.5 for **3.1-edt** and i_{red} / i_{ox} = 2 for **3.2-edt**) also supporting this assumption. However, we can not rule out the possibility of both electrons going to the diiron centre at this point. DFT

calculations are ongoing in order to determine the electronic structure of both **3.1-edt** and **3.2-edt** and their radical anions which will give insight to the reductive process. No significant change has been observed on their CVs when the scan rate is varied (0.025 to 1 V/s).

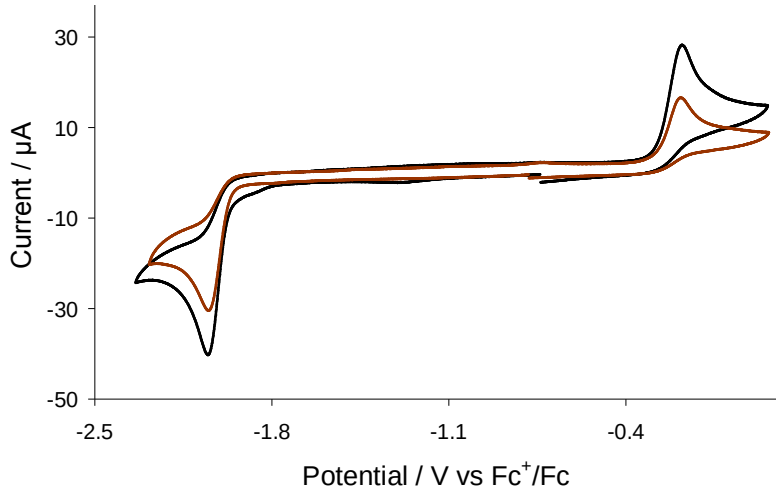

Figure 3.4. CVs of $Fe_2(CO)_4(\kappa^2$-2,2′-bpy)(µ-edt) (**3.1-edt**) (black) and $Fe_2(CO)_4(\kappa^2$-1,10-phen)(µ-edt) (**3.2-edt**) (brown) in MeCN (1 mM solution, supporting electrolyte $[NBu_4][PF_6]$, scan rate 0.1 Vs^{-1}, glassy carbon electrode, potential vs Fc^+/Fc).

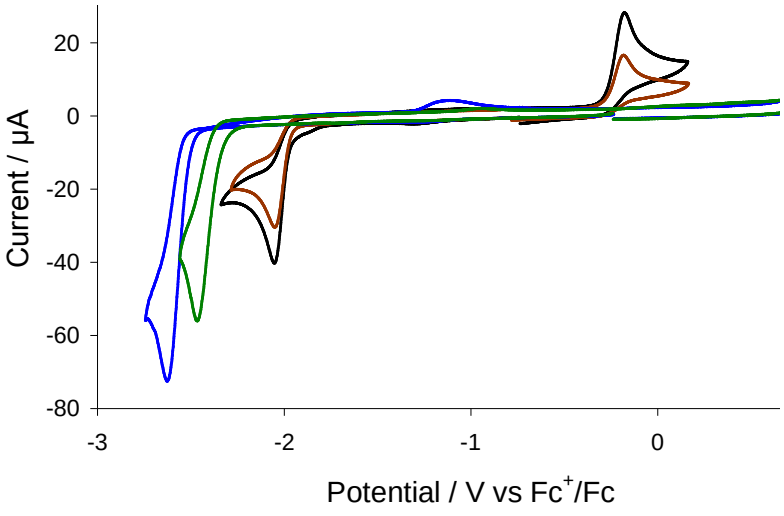

Figure 3.5. CVs of $Fe_2(CO)_4(\kappa^2$-bpy)(µ-edt) (**3.1-edt**) (black), $Fe_2(CO)_4(\kappa^2$-phen)(µ-edt) (**3.2-edt**) (brown), 2,2′-bipyridine (blue) and 1,10-phenanthroline (green) in MeCN (1 mM solution, supporting electrolyte $[NBu_4][PF_6]$, scan rate 0.1 Vs^{-1}, glassy carbon electrode, potential vs Fc^+/Fc).

The diiron centre in both **3.1-edt** and **3.2-edt** is oxidized irreversibly at E_p = –0.18 V. The nature of this oxidation process has been probed chemically using $[Cp_2Fe][BF_4]$ as the oxidant. Addition of one equivalent of $[Cp_2Fe][BF_4]$ to a dichloromethane solution of **3.1-edt** or **3.2-edt** at room temperature afforded an instant colour change, from dark green to orange for **3.1-edt** and from dark blue to yellow for **3.2-edt**, concomitant with the appearance of new IR bands at 2106, 2100, 2060, 2048, 2023 cm^{-1} and 2106, 2100, 2062, 2048, 2026 cm^{-1} associated with the formation of **3.1-edt**$^+$ and **3.2-edt**$^+$ respectively (Figure 3.6). The intensity of these bands relative to those of the starting materials is relatively low and all absorptions disappeared over a few minutes. This is consistent with the irreversible nature of the electrochemical oxidations. On the basis of the IR data we cannot fully assign the structures of these oxidized species but as the lowest energy absorptions are at 2023-2026 cm^{-1} it would appear that a semi-bridging carbonyl has not been generated.

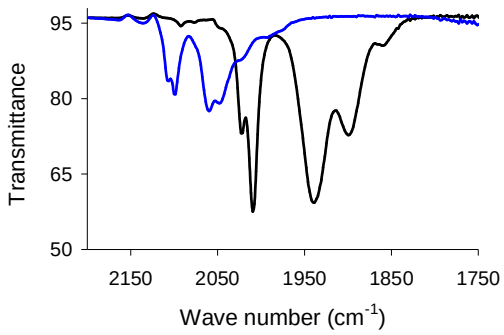

(a)

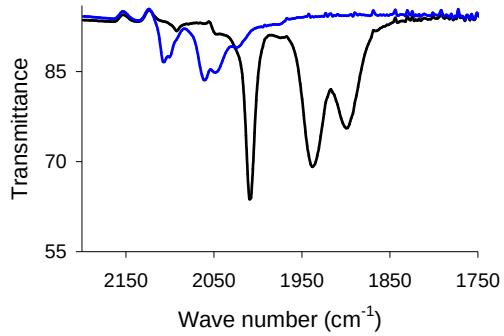

(b)

Figure 3.6. (a) IR spectra of $Fe_2(CO)_4(\kappa^2$-2,2′-bipy)(μ-edt) (**3.1-edt**) (black) and (blue) after addition of one equivalent of $[Cp_2Fe][BF_4]$ in CH_2Cl_2; (b) IR spectra of $Fe_2(CO)_4(\kappa^2$-1,10-phen)(μ-edt) (**3.2-edt**) (black) and (blue) after addition of one equivalent of $[Cp_2Fe][BF_4]$ in CH_2Cl_2.

3.2.4. Electrocatalytic studies. The electrocatalytic proton reduction by **3.1-edt** (Figure 3.7) and **3.2-edt** (Figure 3.8) was investigated in MeCN using CF_3CO_2H as the proton source. Attempts to study the catalysis using stronger acid *e.g.* $HBF_4{\cdot}Et_2O$ and *p*-toluenesulfonic acid (*p*-TsOH) which were used for catalytic study of **3.1-pdt** were unsuccessful as both **3.1-edt** and **3.2-edt** degrade rapidly in presence of these acids. Upon addition of one molar equivalent of acid, CVs of both show two new reduction peaks (at –1.68 and –1.89 V for **3.1-edt** and at –1.70 and –1.98 V for **3.2-edt**) in addition to the peak at –2.05 V. All three peaks grow with increasing acid concentration, which is characteristic of electrocatalytic proton reduction. However, the catalytic peak seen at the reduction potential of the neutral complexes (–2.05 V) disappears as the concentration of acid is increased (> 5 equivalents for **3.1-edt** and > 2 equivalents for **3.2-edt**). This is in contrast with the results obtained for **3.1-pdt**, for which the catalytic peak at the reduction potential of the neutral species was the prominent reduction feature throughout the experiment. This can be explained by comparing the rate of protonation of the edt and pdt complexes. Whilst **3.1-pdt** undergoes slow protonation in presence of strong acid $HBF_4{\cdot}Et_2O$ ($pK_a \approx 0.1$ in MeCN) [60], protonation of the edt complexes are relatively fast even in the presence of CF_3CO_2H ($pK_a \approx 12.7$ in MeCN) [60].

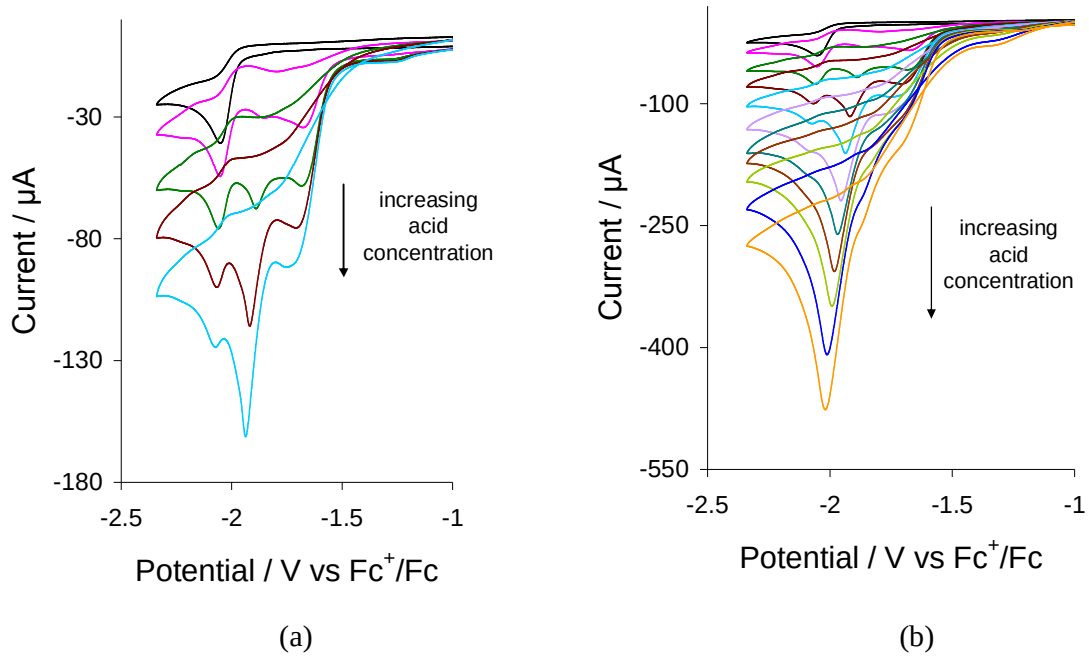

Figure 3.7. CVs of $Fe_2(CO)_4(\kappa^2\text{-}2,2'\text{-bipy})(\mu\text{-edt})$ (**3.1-edt**) - (a) upon addition of 1-4 equivalents of CF_3CO_2H, (b) upon addition of 1-10 equivalents of CF_3CO_2H (in MeCN, 1 mM solution, supporting electrolyte $[NBu_4][PF_6]$, scan rate 0.1 Vs^{-1}, glassy carbon electrode, potential vs Fc^+/Fc).

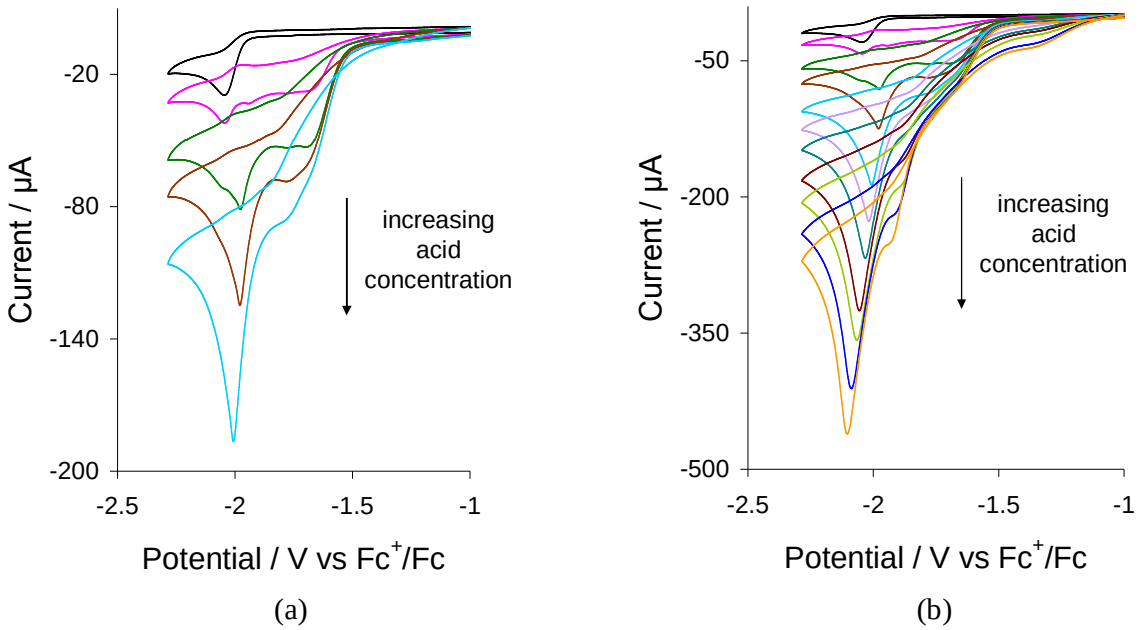

Figure 3.8. CVs of $Fe_2(CO)_4(\kappa^2$-1,10-phen)(µ-edt) (**3.2-edt**) - (a) upon addition of 1-4 equivalents of CF_3CO_2H, (b) upon addition of 1-10 equivalents of CF_3CO_2H (in MeCN, 1 mM solution, supporting electrolyte $[NBu_4][PF_6]$, scan rate 0.1 Vs^{-1}, glassy carbon electrode, potential vs Fc^+/Fc).

The first reduction peak in the CVs of **3.1-edt** and **3.2-edt** in presence of one equivalent of CF_3CO_2H appears *ca*. 0.35V more positive than the reduction potential of the neutral species and are due to the reduction of protonated species (**3.1H$^+$-edt** and **3.2H$^+$-edt**) which are responsible for the catalytic current at this potential. The current of the first reduction peak levels off at higher acid concentration and reaches a plateau after addition of five equivalents of acid, which indicates an acid-independent rate-limiting step such as the liberation of H_2 under these conditions. In contrast, the second reduction wave increases linearly with acid concentration indicating another proton reduction process at this potential (Figure 3.9).

The catalytic mechanism of **3.1-pdt** proposed by Jones and co-workers is shown in Scheme 3.4. Since **3.1-pdt** protonates slowly by strong acid ($HBF_4{\cdot}Et_2O$), they suggest that both **1H$^+$-pdt** and **1H-pdt** are the active electrocatalytic species in solution. Since both **3.1-edt** and **3.2-edt** undergo relatively rapid protonation even in the presence of CF_3CO_2H, we surmise that both follow a different, but relatively simple, mechanism for electrocatalytic proton reduction which is shown in Scheme 3.5.

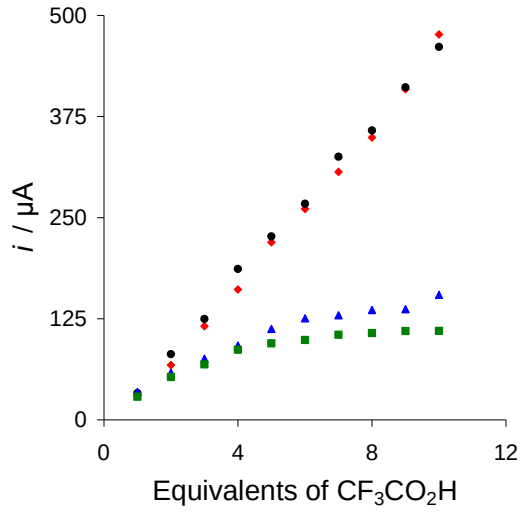

Figure 3.9. Plot of electrocatalytic peak current at potentials of the first and second catalytic waves *vs.* equivalents of CF_3CO_2H added for **3.1-edt** (blue triangle for the first wave and red diamonds for the second wave) and **3.2-edt** (green squares for the first wave and black circles for the second wave) [in MeCN, 1 mM solution, supporting electrolyte $[NBu_4][PF_6]$, scan rate 0.1 Vs^{-1}, glassy carbon electrode, potential vs Fc^+/Fc].

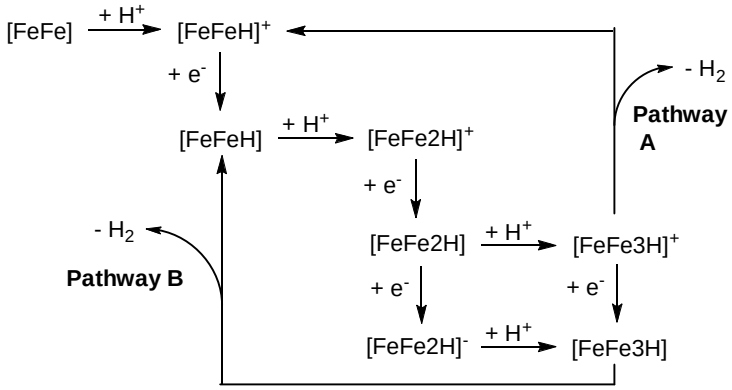

Scheme 3.4. Proposed mechanism for the electrocatalytic proton reduction by **3.1-pdt** [11].

According to this mechanism, hydrogen evolution at the first reduction potential takes place *via* an CECE mechanism (Pathway A, Scheme 3.5). The neutral complex undergoes protonation followed by reduction to form the neutral hydride species **[FeFeH]**. This then reacts with a second proton and releases H_2 to form **[FeFe]**$^+$ which takes up another electron to regenerate the catalyst. The neutral hydride species **[FeFeH]** can undergo a further reduction at a more negative potential before reacting with a

second proton, which accounts for the reduction of protons at the potential of second catalytic wave (Pathway B, Scheme 3.5).

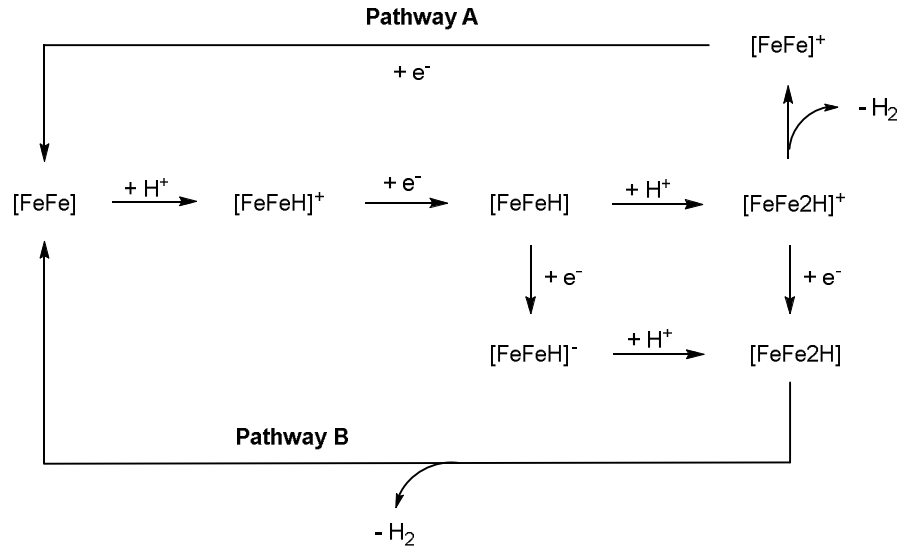

Scheme 3.5. Proposed mechanism for the electrocatalytic proton reduction by **3.1-edt** and **3.2-edt**.

Although spectroscopic data suggest rapid protonation of **3.1-edt** and **3.2-edt** by CF_3CO_2H, the CVs show that substantial amount of **3.1-edt** is present in solution at low acid concentrations and it undergoes complete protonation only after addition of 6 equivalents of acid in the electrochemical cell. In IR studies, which show instantaneous protonation of both the edt complexes after addition of 2 equivalents of CF_3CO_2H, we used *ca*. 5 times more concentrated solution of the edt complexes compared to the solution used for electrocatalytic study. This reflects that the rate of protonation of **3.1-edt** and **3.2-edt** also depends on concentration. Thus we cannot unequivocally say that **3.1-edt** follows the mechanism proposed in Scheme 3.5 throughout the experiment and it may follow the mechanism proposed by Jones at low acid concentrations. In contrast, **3.2-edt** shows a completely different CV after addition of 2 equivalents of acid and follows the same mechanism proposed by us throughout the experiment (at all acid concentrations). As proposed for **3.1-pdt**, we assume that both **3.1-edt** and **3.2-edt** follow the same EECC mechanism for the reduction of proton at the potential of neutral complexes (Scheme 3.6).

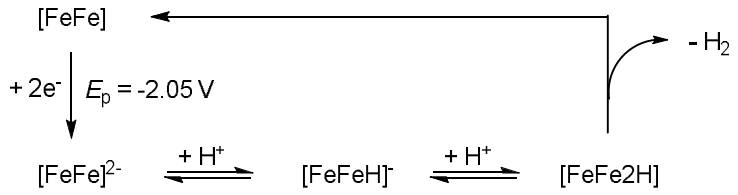

Scheme 3.6. Proposed mechanism for the catalytic event at the reduction potentials of neutral **3.1-edt** and **3.2-edt** during electrocatalytic proton reduction.

3.3. Summary and conclusions

Diiron chelates $Fe_2(CO)_4(\kappa^2$-2,2′-bipy)(μ-edt) (**3.1-edt**) and $Fe_2(CO)_4(\kappa^2$-1,10-phen)(μ-edt) (**3.2-edt**) were synthesised in moderate yield from the one pot reaction between the parent hexacarbonyl and corresponding diamine. Crystal structures of **3.1-edt** and **3.2-edt** show that the diamine occupies basal sites in the solid state, while both dibasal and apical-basal isomers are present in solution. This is in sharp contrast with that observed for their pdt analogue which exist only in dibasal form both in the solid-state and in solution [10,11]. We assume that in **3.1-pdt** and **3.2-pdt** the nonbonding interaction between the diamine ligand and the extra methylene group of the dithiolate backbone prevents formation of the apical-basal isomer. Both **3.1-edt** and **3.2-edt** readily protonate but the protonated products show limited stability. The protonated species **3.1H$^+$-edt** and **3.2H$^+$-edt** exist in both dibasal and apical-basal forms in presence of moderately strong acid (CF_3CO_2H), while a single isomer is observed when strong acid ($HBF_4{\cdot}Et_2O$) is used as the proton source indicating that the rate of conversion to the thermodynamically more stable isomer depends on the strength of acid.

Both **3.1-edt** and **3.2-edt** undergo irreversible oxidation and reduction in MeCN, the latter being proposed to be a two-electron process with one electron being associated with the diiron centre and the second with the 2,2′-bipy ligand [11]. The proton reduction ability of both complexes has been studied in MeCN using CF_3CO_2H as the proton source. These show that two interconnected catalytic cycles initiated by protonation at the diiron centre operates during catalysis. We propose a different mechanism for the edt complexes with respect to that proposed for **3.1-pdt** owing to their different rate of protonation. While **3.1H$^+$-pdt** and **3.1H-pdt** are the active electrocatalytic species due to the slow protonation of **3.1-pdt** by strong acids *e.g.* $HBF_4{\cdot}Et_2O$ ($pK_a \approx 0.1$ in MeCN) [60] and TsOH ($pK_a \approx 8.7$ in MeCN) [60], rapid protonation of **3.1-edt** and **3.2-edt** even by

moderately strong CF_3CO_2H ($pK_a \approx 12.7$ in MeCN) [60] suggests that they are the only active catalytic species during electrocatalytic proton reduction. This implies that the nature of the dithiolate backbone has significant influence in the electrocatalytic pathway for proton reduction by chelating diamine complexes.

3.4. Experimental section

3.4.1. General. Unless otherwise noted, all the reactions were carried out under a nitrogen atmosphere using standard Schlenk techniques. Reagent-grade solvents were dried using appropriate drying agents and distilled prior to use by standard methods. Infrared spectra were recorded on a Shimadzu FTIR 8101 or Nicolet 6700 FT-IR spectrophotometer. NMR spectra were recorded on a Bruker DPX 400 instrument. Elemental analyses were performed by Microanalytical Laboratories, University College London. Diiron complexes $Fe_2(CO)_6(\mu\text{-edt})$ (**1.3**) [61] was prepared by literature methods.

3.4.2. Synthesis of $Fe_2(CO)_4(\kappa^2\text{-}2,2'\text{-bipy})(\mu\text{-edt})$ (3.1-edt). To an acetonitrile solution (15 mL) of $Fe_2(CO)_6(\mu\text{-edt})$ (**1.3**) (100 mg, 0.269 mmol) was added 2,2′-bipyridine (42 mg, 0.269 mmol) and $Me_3NO{\cdot}2H_2O$ (37 mg, 0.333 mmol) and the mixture was heated at boiling temperature for 1 h. The reaction mixture was allowed to cool at room temperature and its volume was reduced to 3-4 mL by rotary evaporation under vacuum. The mixture was then passed through a short silica column (6 cm) using CH_2Cl_2 as eluent to remove unreacted Me_3NO and other undissolved materials. The solution was then transferred into a 100 mL round-bottomed flask and again concentrated to 3-4 mL. Addition of a layer of cold hexane over this solution and cooling at –20 ℃ for several days gave dark green crystals of $Fe_2(CO)_4(\kappa^2\text{-}2,2'\text{-bipy})(\mu\text{-edt})$ (**3.1-edt**) (56 mg, 44%). IR (ν(CO); CH_2Cl_2): 2023m, 2010vs, 1938vs, 1900m, 1859w cm^{-1}; ^1H NMR ($CDCl_3$): δ 8.87 (d, J 4.4, 2H, major), 8.31 (d, J 2.7, 2H, minor), 8.29 (d, J 8.4, 2H, minor), 8.11 (d, J 7.5, 2H, major), 7.93 (t, J 4.1, 2H, minor), 7.79 (t, J 4.5, 2H, major), 7.26 (brs, 2H, major + minor), 2.40 (apparent d, J 7.6, 2H, minor), 2.28 (apparent d, J 7.6, 2H, minor), 2.20 (apparent d, J 7.0, 2H, major), 2.05 (apparent d, J 7.0, 2H, major); Anal. calc. for $Fe_2N_2S_2O_4C_{16}H_{12}.0.5CH_2Cl_2$: C, 38.47, N, 5.44, H, 2.52; Found C, 38.93, N, 5.51, H, 2.42.

Crystallographic data for **3.1-edt**: dark green block, dimensions 0.34 × 0.14 × 0.11 mm^3, orthorhombic, space group *Pnma*, a = 13.015(1), b = 12.264(1), c = 10.759(1) Å, α = 90, β = 90, γ = 90°, V = 1717.4(3) $Å^3$, Z = 4, F(000) 952, d_{calc} = 1.826 g cm^{-3}, μ = 1.958 mm^{-1}. 13580 reflections were collected, 2191 unique [R(int) = 0.0308]. At convergence, R_1 = 0.0249, wR_2 = 0.0609 [$I > 2.0\sigma(I)$] and R_1 = 0.0268, wR_2 = 0.0618 (all data), for 151 parameters.

3.4.3. Synthesis of $Fe_2(CO)_4(\kappa^2$-1,10-phen)(μ-edt) (3.2-edt). An acetonitrile solution (15 mL) of $Fe_2(CO)_6$(μ-edt) (**1.3**) (100 mg, 0.269 mmol), 1,10-phenanthroline (49 mg, 0.272 mmol) and $Me_3NO{\cdot}2H_2O$ (37 mg, 0.333 mmol) was heated at boiling temperature for 1.5 h. A similar workup described as above gave dark green crystals of $Fe_2(CO)_4(\kappa^2$-1,10-phen)(μ-edt) (**3.2-edt**) (43 mg, 32%). IR (ν(CO); CH_2Cl_2): 2010vs, 1938s, 1900m cm^{-1}; ^{1}H NMR ($CDCl_3$): δ 9.14 (d, J 5.3, 2H, major), 8.63 (d, J 5.3, minor), 8.43 (d, J 7.8, minor), 8.30 (d, J 7.9, 2H, major), 8.06 (s, minor), 7.96 (s, 2H, major), 7.65 (dd, J 7.9, 5.3, 2H, major), 2.46 (m, minor), 2.26 (apparent dt, J 7.3, 5.0, 2H, major), 2.11 (apparent dt, J 7.4, 3.8, 2H, major); Anal. calc. for $Fe_2N_2S_2O_4C_{18}H_8.2CH_2Cl_2$: C, 36.03, N, 4.20, H, 2.40; Found C, 35.65, N, 4.69, H, 2.19.

Crystallographic data for **3.2-edt**: dark green block, dimensions 0.32 × 0.18 × 0.16 mm^3, triclinic, space group $P\bar{1}$, a = 10.6863(9), b = 18.224(2), c = 20.886(2) Å, α = 112.523(1), β = 101.945(1), γ = 92.294(1)°, V = 3643.6(5) $Å^3$, Z = 8, F(000) 2000, d_{calc} = 1.809 g cm^{-3}, μ = 1.850 mm^{-1}. 31408 reflections were collected, 16665 unique [R(int) = 0.0264]. At convergence, R_1 = 0.0426, wR_2 = 0.1242 [$I > 2.0\sigma(I)$] and R_1 = 0.0583, wR_2 = 0.1410 (all data), for 1009 parameters.

3.4.4. Protonation. 2 molar equivalents of CF_3CO_2H (0.8 μL) was added to a dichloromethane solution of **3.1-edt** (2.4 mg, 0.005 mmol) or **3.2-edt** (2.5 mg, 0.005 mmol) at room temperature. The resulted solution was then transferred into a solution IR cell fitted with calcium fluoride plates and a series of spectra were recorded as a function of time.

3.4.5. Oxidation. 1 molar equivalents of $[Cp_2Fe][BF_4]$ (1.4 mg, 0.005 mmol) was added to a dichloromethane solution of **3.1-edt** (2.4 mg, 0.005 mmol) or **3.2-edt** (2.5 mg, 0.005 mmol) at room temperature. The resulted solution was then transferred into a solution IR

cell fitted with calcium fluoride plates and a series of spectra were recorded as a function of time.

3.5. References

(1) J.M. Camara and T.B. Rauchfuss, *Nat. Chem.*, 2012, **4**, 26-30.

(2) C. Tard, X.M. Liu, S.K. Ibrahim, M. Bruschi, L. De Gioia, S.C. Davies, X. Yang, L.S. Wang, G. Sawers and C.J. Pickett, *Nature*, 2005, **433**, 610-613.

(3) C. Greco, *Inorg. Chem.*, 2013, **52**, 1901-1908.

(4) Y. Si, K. Charreteur, J.-F. Capon, F. Gloaguen, F.Y. Pétillon, P. Schollhammer and J. Talarmin, *J. Inorg. Biochem.*, 2010, **104**, 1038-1042.

(5) C. Gimbert-Suriñach, M. Bhadbhade and S. B. Colbran, *Organometallics*, 2012, **31**, 3480-3491.

(6) J.-F. Capon, F. Gloaguen, F. Y. Pétillon, P. Schollhammer and J. Talarmin, *Eur. J. Inorg. Chem.*, 2008, 4671-4681.

(7) C. Greco and L. De Gioia, *Inorg. Chem.*, 2011, **50**, 6987–6995.

(8) P.-Y. Orain, J.-F. Capon, F. Gloaguen, F.Y. Pétillon, P. Schollhammer, J. Talarmin, G. Zampella, L. De Gioia and T. Roisnel, *Inorg. Chem.*, 2010, **49**, 5003-5008.

(9) S. Ezzaher, P.-Y. Orain, J.-F. Capon, F. Gloaguen, F. Pétillon, T. Roisnel, P. Schollhammer and J. Talarmin, *Chem. Commun.*, 2008, 2547-2549.

(10) P.-Y. Orain, J.-F. Capon, N. Kervarec, F. Gloaguen, F. Pétillon, R. Pichon, P. Schollhammer and J. Talarmin, *Dalton Trans.*, 2007, 3754-3756.

(11) S. Roy, T.L. Groy and A. K. Jones, *Dalton Trans.*, 2013, **42**, 3843-3853.

(12) J. W. Peters, W. N. Lanzilotta, B. J. Lemon and L. C. Seefeldt, *Science*, 1998, **282**, 1853-1858.

(13) Y. Nicolet, C. Piras, P. Legrand, C. E. Hatchikian and J. C. Fontecilla-Camps, *Structure* 1999, **7**, 13-23.

(14) M. Bruschi, C. Greco, P. Fantucci and L. De Gioia, *Inorg. Chem.*, 2008, **47**, 6056-6071.

(15) D. E. Schwab, C. Tard, E. Brecht, J. W. Peters, C. J. Pickett and R. K. Szilagyi, *Chem. Commun.*, 2006, 3696-3698.

(16) C. V. Popescu and E. Munck, *J. Am. Chem. Soc.*, 1999, **121**, 7877-7884.

(17) Y.-C. Liu, C.-H. Lee, G.-H. Lee and M.-H. Chiang, *Eur. J. Inorg. Chem.*, 2011, 1155-1162.

(18) G. Chelucci and Randolph P. Thumme, *Chem. Rev.*, 2002, **102**, 3129-3170.

(19) P. G. Sammes and G. Yahioglu, *Chem. Soc. Rev.*, 1994, 327-334.

(20) C. V. Krishnan, C. Creutz, H. A. Schwarz and N. Sutin, *J. Am. Chem. Soc.*, 1983, **105**, 5617-5623.

(21) M. H. Chisholm, J. C. Huffman, I. P. Rothwell, P. G. Bradley, N. Kress and W. H. Woodruff, *J. Am. Chem. Soc.*, 1981, **103**, 4945-4947.

(22) E. Gore-Randall, M. Irwin, M. S. Denning and J. M. Goicoechea, *Inorg. Chem.*, 2009, **48**, 8304-8316.

(23) L. Echegoyen, A. DeCian, J. Fischer and J.-M. Lehn, *Angew. Chem. Int. Ed.*, 1991, **30**, 838-840.

(24) H. Bock, J.-M. Lehn, J.Pauls, S. Holl and V. Krenzel, *Angew. Chem. Int. Ed.*, 1999, **38**, 952-955.

(25) P. L. Bellavance, E. R. Corey, J. Y. Corey and G. W. Hey, *Inorg. Chem.*, 1977, **16**, 462-467.

(26) G. B. Nikiforov, H. W. Roesky, M. Noltemeyer and H.-G. Schmidt, *Polyhedron*, 2004, **23**, 561-566.

(27) M. Irwin, R. K. Jenkins, M. S. Denning, T. Krämer, F. Grandjean, G. J. Long, R. Herchel, J. E. McGrady and J. M. Goicoechea, *Inorg. Chem.*, 2010, **49**, 6160-6171.

(28) D. Roitershtein, Ã. Domingos, L. C. J. Pereira, J. R. Ascenso and N. Marques, *Inorg. Chem.*, 2003, **42**, 7666-7673.

(29) W. J. Evans and D. K. Drummond, *J. Am. Chem. Soc.*, 1989, **111**, 3329-3335.

(30) M. Schultz, J. M. Boncella, D. J. Berg, T. D. Tilley and R. A. Andersen, *Organometallics*, 2001, **21**, 460-472.

(31) S. J. Kraft, P. E. Fanwick and S. C. Bart, *Inorg. Chem.*, 2010, **49**, 1103-1110.

(32) K. Kalyanasundaram, *Coord. Chem. Rev.*, 1982, **46**, 159-244.

(33) A. Juris,V. Balzani, F. Barigelletti, S. Campagna, P. Belser and A. Von Zelewsky, *Coord. Chem. Rev.*, 1988, **84**, 84-277.

(34) P. Renaud and M. P. Sibi, Eds., *Radicals in Organic Synthesis*, Wiley-VCH, Weinheim, Germany, 2001.

(35) D. A. Nicewicz and D. W. C. MacMillan, *Science*, 2008, **322**, 77-80.

(36) J. H. Penn, R. C. Plants and A. Liu, *Chem. Commun.*, 1999, 2359-2360.

(37) G. Nord and O. Wernberg, *J. Chem. Soc., Dalton Trans.*, 1972, 866-868.

(38) G. Nord and O. Wernberg, *J. Chem. Soc., Dalton Trans.*, 1975, 845-849.

(39) M. Kimura and G. G. Wada, *Inorg. Chem.*, 1978, **17**, 2239-2242.

(40) J. Grodkowski, P. Neta, C. J. Schlesener and J. K. Kochi, *J. Phys.Chem.*, 1985, **89**, 4373-4378.

(41) R. Schmid, K. Kirchner and F. L. Dickert, *Inorg. Chem.*, 1988, **27**, 1530-1536.

(42) T. S. Lee, I. M. Kolthoff, D. L. Leussing, *J. Am. Chem. Soc.*, 1948, **70**, 2348-2352.

(43) J. E. Dickens, F. Basolo and H. M. Neumann, *J. Am. Chem. Soc.*, 1957, **79**, 1286-1290.

(44) D. W. Margerum, *J. Am. Chem. Soc.*, 1957, **79**, 2728-2733.

(45) B. R. James, J. R. Lyons and R. J. P. Williams, *Biochemistry*, 1962, **1**, 379-385.

(46) G. Nord, B. Pedersen and E. Bjergbakke, *J. Am. Chem. Soc.*, 1983, **105**, 1913-1919.

(47) J.-F. Capon, F. Gloaguen, P. Schollhammer and J. Talarmin, *J. Electroanal. Chem.*, 2006, **595**, 47.

(48) G. A. N. Felton, A. K. Vannucci, J. Chen, L. T. Lockett, N. Okumura, B. J. Pedro, U. I. Zakai, D. H. Evans, R. S. Glass and D. L. Lichtenberger, *J. Am. Chem. Soc.*, 2007, **129**, 12521-12530.

(49) J. Windhager, M. Rudolph, S. Bräutigam, H. Görls and W. Weigand, *Eur. J. Inorg. Chem.*, 2007, 2748-2760.

(50) J.-F. Capon, S. Ezzaher, F. Gloaguen, F. Y. Pétillon, P. Schollhammer, J. Talarmin, T. Davin, J. E. McGrady and K. W. Muir, *New J. Chem.*, 2007, **31**, 2052-2064.

(51) S. J. Borg, T. Behrsing, S. P. Best, M. Razavet, X. Liu and C. J. Pickett, *J. Am. Chem. Soc.*, 2004, **126**, 16988-16999.

(52) S. J. Borg, M. I. Bondin, S. P. Best, M. Razavet, X. Liu and C. J. Pickett, *Biochem. Soc. Trans.*, 2005, **33**, 3-6.

(53) I. Aguirre de Carcer, A. DiPasquale, A. L. Rheingold and D. M. Heinekey, *Inorg. Chem.*, 2006, **45**, 8000-8002.

(54) S. J. Borg, J. W. Tye, M. B. Hall and S. P. Best, *Inorg. Chem.*, 2007, **46**, 384-394.

(55) T. K. Mukhopadhyay, R. K. Feller, F. N. Rein, N. J. Henson, N. C. Smythe and J. C. Gordon, *Chem. Commun.*, 2012, **48**, 8670-8672.

(56) C. C. Scarborough and K. Wieghardt, *Inorg. Chem.*, 2011, **50**, 9773-9793.

(57) F. I. Adam, G. Hogarth, S. E. Kabir and I. Richards, *C.R. Chim.*, 2008, **11**, 890-905.

(58) S. Ezzaher, J.-F. Capon, F. Gloaguen, F. Y. Pétillon, P. Schollhammer and J. Talarmin, *Inorg. Chem.*, 2007, **46**, 3426-3428.

(59) A. K Justice, G. Zampella, L. De Gioia, T. B. Rauchfuss, J. I. van der Vlugt and S. R. Wilson, *Inorg. Chem.*, 2007, **46**, 1655-1664.

(60) K. Izutsu, *in Acid-Base Dissociation Constants in Dipolar Aprotic Solvents*, Blackwell Scientific Publications, Oxford, 1990.

(61) A. Winter, L. Zsolnai and G. Huttner, *Z. Naturforsch.*, 1982, **37b**, 1430-1436.

Chapter 4

Hydrogenase biomimetics containing redox-active ligands: Synthesis, structure and electrochemistry of $Fe_2(CO)_4(\mu\text{-edt})(\kappa^2\text{-bpcd})$ (bpcd = 4,5-bis(diphenylphosphino)-4-cyclopenten-1,3-dione)

4.1. Introduction

As detailed in the previous chapter, much of the current interest in the chemistry of hydrogenase biomimics centres around the incorporation of redox-active ligands [1-12] to the diiron centre such that the two redox systems can potentially act in a cooperative manner [1-3], much the same way as the diiron and tetrairon sites in the H-cluster of the iron-only hydrogenase enzyme are believed to do so [2,13-16]. Examples of such systems include the incorporation of conjugated diamines [8-11], quinones [12], ferrocene-based ligands [1,3,5-7] and diphosphines [4,7]. Diiron biomimics containing redox-active diamines have been discussed in detail in the previous chapter and ferrocene-based ligand will be discussed in Chapter 5. Here we will focus on diiron complexes bearing a redox-active diphosphine. Redox-active diphosphines have long attracted attention not only as a ligand in a variety of chemical transformation, but also their apparent, often deceptive, ability to stabilise metals in unusual oxidation states [17-19].

Diphosphines have been extensively utilised in hydrogenase biomimics as they are able to coordinate in a number of different ways to the diiron centre and their electron-donating and steric properties can be easily adjusted in order to fine-tune both the proton-binding ability [20-26] and redox-potential(s) [27-33] of the diiron centre. In general diphosphines are good σ-donor ligands and thus lead to an increase of electron-density at the diiron centre, which in turn facilitates proton binding. Conversely, their electron-donating ability leads to an increase in the reduction potential of the diiron centre and thus can increase the overpotential required for proton reduction. This is a key factor in the development of functional biomimetic catalysts as it is desirable to operate at low overpotentials. In a recent publication, Schollhammer and co-workers addressed this issue by coordinating the electron-withdrawing diphosphine, 2,3-bis(diphenylphosphino)maleic anhydride (bma), to a diiron centre [4]. The diphosphine

has a low-lying π^*-orbital delocalised over the maleic anhydride ring and thus $Fe_2(CO)_4(\kappa^2\text{-bma})(\mu\text{-pdt})$ (**4.1**) (Chart 4.1) is reduced at the relatively low potential of –1.10 V, a process which was shown to be primarily ligand-based. Unfortunately **4.1** does not catalytically reduce protons, behaviour attributed to poor proton-binding and a lack of electronic communication between redox centres [4]. A further factor which likely restricts the catalytic ability of **4.1** is the proton-induced ring-opening of the maleic anhydride ring [4].

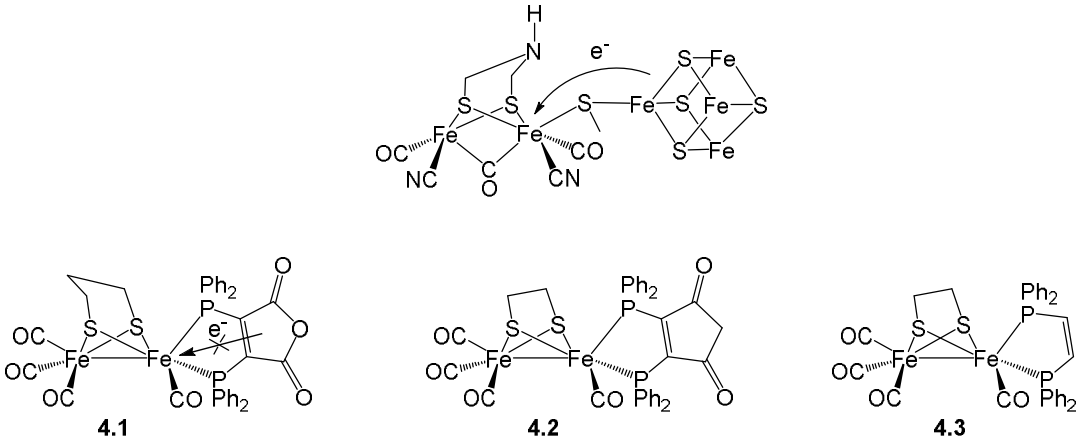

Chart 4.1. Structures of the [FeFe]-hydrogenase active site (top) and the biomimetic models **4.1**-**4.3** (right).

Bma is one of a number of diphosphines containing an electron-withdrawing backbone [34]. Closely related to bma is 4,5-bis(diphenylphosphino)-4-cyclopenten-1,3-dione (bpcd) [34] in which the backbone oxygen is replaced by a methylene group. While this slightly reduces the electron-withdrawing nature of the diphosphine [34], it also stabilises the backbone to addition of acid. Herein we describes the synthesis, structure and electrochemistry of $Fe_2(CO)_4(\kappa^2\text{-bpcd})(\mu\text{-edt})$ (**4.2**) which is able to act as a catalyst for the reduction of protons (Chart 4.1). In order to compare structural and electrochemical properties, we have also carried out electrochemistry and electrocatalysis with the analogous 1,2-bis(diphenylphosphino)ethene (dppv) complex $Fe_2(CO)_4(\kappa^2\text{-dppv})(\mu\text{-edt})$ (**4.3**) (Chart 4.1) [35].

4.2. Results and discussion

4.2.1. Synthesis and characterisation. The dppv complex $Fe_2(CO)_4(\kappa^2\text{-dppv})(\mu\text{-edt})$ (**4.3**) was prepared as previously reported by Rauchfuss upon reaction of dppv with the product of the reaction of $Fe_2(CO)_6(\mu\text{-edt})$ (**1.3**) and Me_3NO in MeCN [35]. Schollhammer and co-workers reported that a similar procedure utilising bma afforded only low yields of $Fe_2(CO)_5(Me_2NCH_2PPh_2)(\mu\text{-pdt})$ formed upon carbon-phosphorus bond cleavage [4]. Irradiating a toluene (or MeCN) solution of $Fe_2(CO)_6(\mu\text{-pdt})$ (**1.1**) and bma in the presence of $Me_3NO{\cdot}2H_2O$ did lead to the formation of $Fe_2(CO)_4(\kappa^2\text{-bma})(\mu\text{-pdt})$ (**4.1**) as a brown crystalline solid in 31% yield [4]. We tried a number of different methods to prepare $Fe_2(CO)_4(\kappa^2\text{-bpcd})(\mu\text{-edt})$ (**4.2**). All gave some product but none were high yielding. We found that heating a toluene solution of $Fe_2(CO)_6(\mu\text{-edt})$ (**1.3**), Me_3NO and bpcd proved to be the optimum synthesis of **4.2** being isolated as a green crystalline solid in 23% yield after work-up (Scheme 4.1). Interestingly all our attempts to prepare the analogous pdt-derivate $Fe_2(CO)_4(\kappa^2\text{-bpcd})(\mu\text{-pdt})$ either failed or gave a complex mixture from which the product could not be separated.

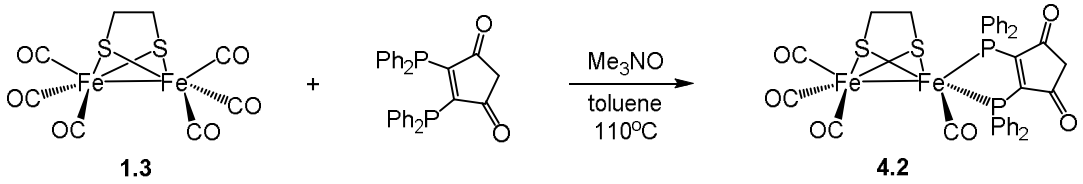

Scheme 4.1. Synthesis of $Fe_2(CO)_4(\kappa^2\text{-bpcd})(\mu\text{-edt})$ (**4.2**).

The IR spectrum of **4.2** shows a pair of low energy absorption bands at 1747 and 1716 cm^{-1} assigned to the carbonyls of the bpcd ligand, in addition to the expected metal-bound carbonyl bands at 2028, 1959 and 1921 cm^{-1}. These compare with values of 2029, 1960 and 1922 cm^{-1} for **4.1** [4] and 2023, 1953 and 1915 cm^{-1} for **4.3** [35] showing that the bma and bpcd ligands have a very similar effect of altering the electron-density on the metal centre available for back-bonding to the carbonyls. The room temperature $^{31}P\{^1H\}$ NMR spectrum of **4.2** consists of only a singlet at δ 84.0, showing that axial and basal sites are in rapid exchange. A similar situation was found for **4.1** [4]. The ^1H NMR spectrum of **4.2** is relatively uninformative and shows two doublets at δ 1.51 and 1.91 (J 7.6) and a quartet at δ 3.60 (J 76.8, 21.6), each integrating to 2H, attributed to the methylene protons of dithiolate and bpcd ligand together with resonances in the aromatic

region for phenyl protons. The solid-state structure of **4.2** was confirmed by X-ray analysis the results of which are summarised in Figure 4.1. The diphosphine occupies axial and basal sites akin to **4.1** [4] and **4.3** [35] and structural features of all three are very similar as shown in Table 4.1 which contains important structural parameters. The bite angle of the diphosphines vary slightly increases along the series such that dppv < bpcd < bma but the overall variation is only *ca.* 3° and should not lead to important differences in their structural behaviour. The metal-metal bond distance in **4.2** is almost identical to that of **4.3** within the experimental error but *ca.* 0.02 Å shorter than that observed in **4.1**. The basic structure does not deviate significantly upon using a more bulky bpcd instead of dppv.

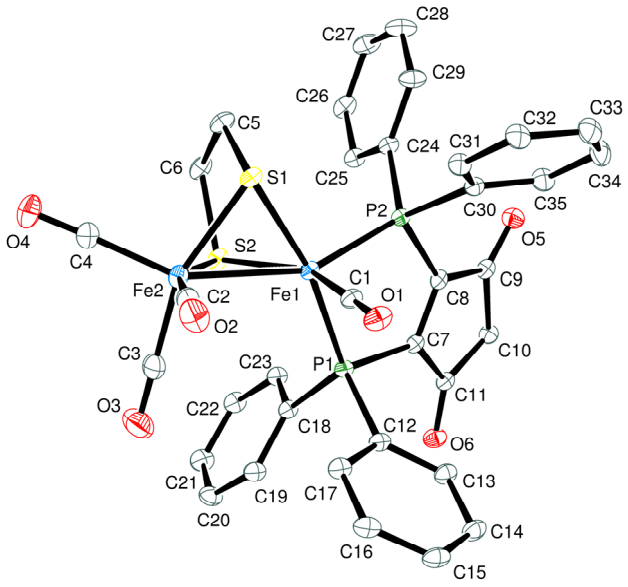

Figure 4.1. An ORTEP diagram of the molecular structure of $Fe_2(CO)_4(\kappa^2\text{-bpcd})(\mu\text{-edt})$ (**4.2**). Hydrogen atoms are omitted for clarity. Selected bond distances (Å) and angles (°): Fe(1)─Fe(2) 2.5289(5), Fe(1)─P(1) 2.2122(6), Fe(1)─P(2) 2.1917(7), Fe(1)─S(1) 2.2414(6), Fe(1)─S(2) 2.2508(6), Fe(2)─S(1) 2.2600(7), Fe(2)─S(2) 2.2651(6), P(1)─Fe(1)─P(2) 89.39(2), P(1)─Fe(1)─S(1) 168.33(3), P(2)─Fe(1)─S(1) 101.49(2), P(1)─Fe(1)─Fe(2) 112.21(2), P(2)─Fe(1)─Fe(2) 153.34(2).

Table 4.1. Selected metric parameters of **4.1-4.3**

	$Fe_2(CO)_4(\kappa^2\text{-bma})(\mu\text{-pdt})$ (**4.1**) [4]	$Fe_2(CO)_4(\kappa^2\text{-bpcd})(\mu\text{-edt})$ (**4.2**)	$Fe_2(CO)_4(\kappa^2\text{-dppv})(\mu\text{-edt})$ (**4.3**) [35]
Fe─Fe (Å)	2.5434(10)	2.5289(5)	2.5249(9)
ap Fe─P (Å)	2.1939(14)	2.1917(7)	2.1743(13)
ba Fe─P (Å)	2.2216(14)	2.2122(6)	2.2070(13)
P─Fe─P (°)	91.01(5)	89.39(2)	87.83(5)

4.2.2. Electrochemistry. The electrochemical behaviour of $Fe_2(CO)_4(\kappa^2\text{-bpcd})(\mu\text{-edt})$ (**4.2**) was studied by cyclic voltammetry in MeCN and Figure 4.2 shows the cyclic voltammogram (CV) of **4.2** together with that of $Fe_2(CO)_4(\kappa^2\text{-dppv})(\mu\text{-edt})$ (**4.3**) and free bpcd ligand. CVs of **4.3** and free bpcd ligand were recorded under similar conditions in order to understand the impact of bpcd on the elctrochemical behaviour of **4.2**. The CV of the free bpcd ligand shows two quasi-reversible reductions at $E_{1/2}$ = –1.35 V and $E_{1/2}$ = –2.15 V together with an irreversible oxidation at E_p = 0.85 V. No significant change was observed in the CVs when the scan rate was varied between 0.5 to 1 V/s. The cathodic region of the CV of **4.2** also shows two similar ligand-based reductive features which are now shifted to less negative potentials i.e., at $E_{1/2}$ = –1.08 V and $E_{1/2}$ = –1.94 V. These are followed by a third reversible reduction at $E_{1/2}$ = –2.27 V (i_{ox}/i_{red} ~ 1) and an irreversible reduction at E_p = –2.53 V, together with a small oxidative feature at E_p = –1.77 V on the return scan due to the oxidation of product formed after irreversible reduction.

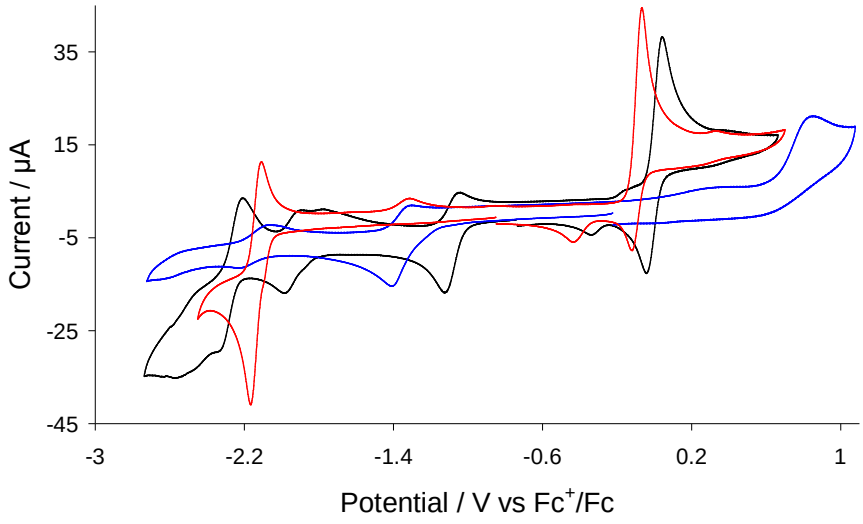

Figure 4.2. CVs of $Fe_2(CO)_4(\kappa^2\text{-bpcd})(\mu\text{-edt})$ (**4.2**) (black), $Fe_2(CO)_4(\kappa^2\text{-dppv})(\mu\text{-edt})$ (**4.3**) (red) and bpcd (blue) in MeCN (1 mM solution, supporting electrolyte $[NBu_4][PF_6]$, scan rate 0.1 V/s, glassy carbon electrode, potential vs Fc^+/Fc).

By way of contrast, **4.3** shows only a reversible reduction at $E_{1/2}$ = –2.14 V (i_{ox}/i_{red} ~ 0.56) which indicates that the third reduction of **4.2** is diiron-centred. The positive shift (*ca.* 0.25 V) of the first two reduction peaks (which are ligand-based) indicates that the $Fe_2(CO)_4$(edt) moiety acts in an electron-withdrawing capacity as to be expected for a carbonyl complex. The anodic region of the CV of **4.2** shows a quasi-reversible oxidation at $E_{1/2}$ = 0.00 V, together with a small reductive feature at E_p = –0.33 V on the return

scan. This oxidation event takes place at the diiron centre as its dppv analogue **4.3** shows a diiron-centred oxidation at a similar potential ($E_{1/2}$ = –0.10 V). The irreversible oxidative feature observed for the free ligand is not seen in the CV of **4.2** which we speculate is now shifted to more positive potential due to the electron-withdrawing nature of the $Fe_2(CO)_4$(edt) moiety. We have calculated the ground-state electronic structure of **4.2** using density functional theory (DFT) in order to get a better understanding of its redox behaviour, the results of which are shown in Figure 4.3. The HOMO is iron-iron bonding, whereas the LUMO is delocalized over the cyclopenten-1,3-dione ring which corroborate well with the experimental results as the oxidation occurred at the diiron centre, while the first two reductions are ligand-based.

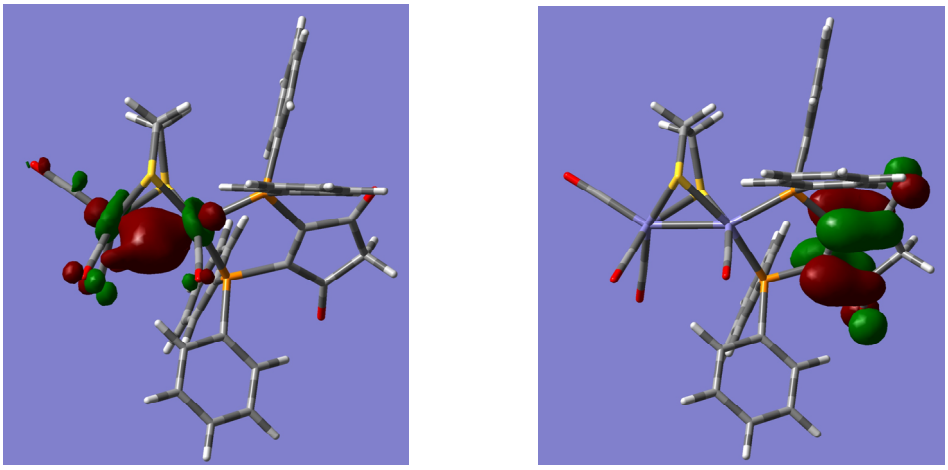

Figure 4.3. HOMO (left) and LUMO (right) of $Fe_2(CO)_4(\kappa^2$-bpcd)(μ-edt) (**4.2**) (calculations were carried out by collaborator).

4.2.3. Oxidation by [Cp_2Fe][BF_4]. As noted earlier, bpcd was introduced into the coordination sphere of **4.2** as a surrogate of [4Fe4S]-cluster with the hope that it can supply electron(s) to the diiron centre during catalysis, as performed by the later within the enzyme. To find out whether there is an electronic communication between the diiron centre and bpcd ligand or if the two centres simply act as separate redox entities, we chemically oxidized **4.2** using [Cp_2Fe][BF_4] and monitored the change in IR spectra over time (summarised in Figure 4.4). Two very weak absorption bands were observed at 2109 and 2087 cm^{-1} upon addition of one molar equivalent of [Cp_2Fe][BF_4] into a CH_2Cl_2 solution of **4.2** as a result of oxidation of the diiron centre. Within a few minutes these were replaced by a relatively low-energy weak absorption bands at 2053 cm^{-1} indicating that the loss of electron density at the diiron centre upon oxidation is now

compensated by electron-transfer from other parts of the molecule. We suggest that the coordinated bpcd ligand provides an electron to the diiron centre after oxidation *via* an intra-molecular electron transfer (ET) reaction as shown in Scheme 4.2.

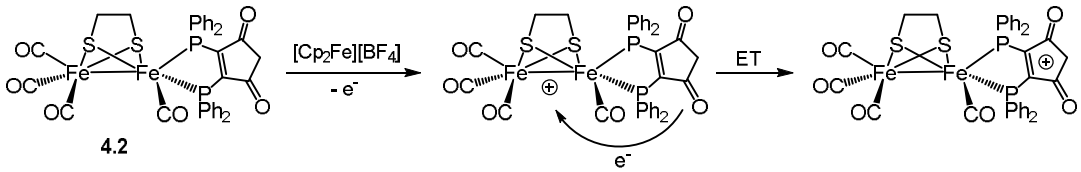

Scheme 4.2. Chemical oxidation of $Fe_2(CO)_4(\kappa^2$-bpcd)(μ-edt) (**4.2**) using $[Cp_2Fe][BF_4]$.

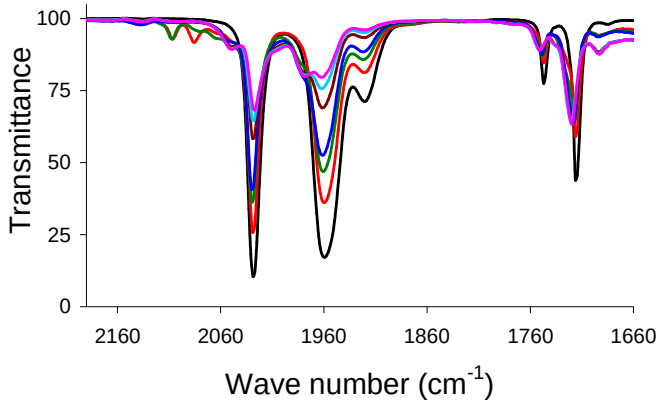

Figure 4.4. IR spectra of $Fe_2(CO)_4(\kappa^2$-bpcd)(μ-edt) (**4.2**) in CH_2Cl_2 upon addition of one equivalent of $[Cp_2Fe][BF_4]$ – without $[Cp_2Fe][BF_4]$ (black), upon addition of $[Cp_2Fe][BF_4]$ (red), after 2 min (green), after 4 min (blue), after 10 min (dark red), after 15 min (lavender), after 20 min (pink).

4.2.4. Reactions with acid. The interaction of acids with the diiron centre is one of the key steps in the catalytic cycle for proton reduction and is known to be complicated and varies from systems to system [9,10,20,36]. Simple diphosphine chelate complexes of the type $Fe_2(CO)_4(\kappa^2$-diphosphine)(μ-dithiolate) generally protonate rapidly upon addition of strong acids, proton addition occurring across the metal-metal bond with isomers sometimes being formed as a result of changes to the coordination environment of the diphosphine ligand [20,22-26]. Importantly, in most cases the diiron centre is sufficiently basic such that deprotonation, even upon addition of strong base, is unfavourable. In contrast to this behaviour, Schollhammer and co-workers reported that $Fe_2(CO)_4(\kappa^2$-bma)(μ-pdt) (**4.1**) was unreactive towards acids [4], although it seems likely that they actually observed a reversible acid-promoted ring-opening of the maleic anhydride ring.

As a reference point we first studied the protonation of **4.3** *via* IR and NMR spectroscopy. Complex **4.3** shows two new absorption bands at 2083 and 2052 cm^{-1} upon addition of two molar equivalents of CF_3CO_2H, together with absorption bands for the neutral species suggesting that protonation of **4.3** is kinetically slow (Figure 4.5a). The 60 cm^{-1} blue shift of the highest-energy absorption bands after addition of acid is indicative of protonation at the diiron centre. We could not detect any hydrides in the ^1H NMR spectrum of **4.3** at low acid concentration, but it displays a doublet at –15.99 ppm in the presence of excess CF_3CO_2H confirming protonation across the iron-iron bond (Figure 4.5b). The IR spectrum of **4.2** also shows two new high-energy absorption bands at 2109 and 2087 cm^{-1} upon addition of two molar equivalents of CF_3CO_2H consistent with protonation at diiron centre (Figure 4.6). However akin to oxidation, these bands were replaced by a relatively low-energy absorption at 2053 cm^{-1} within few minutes.

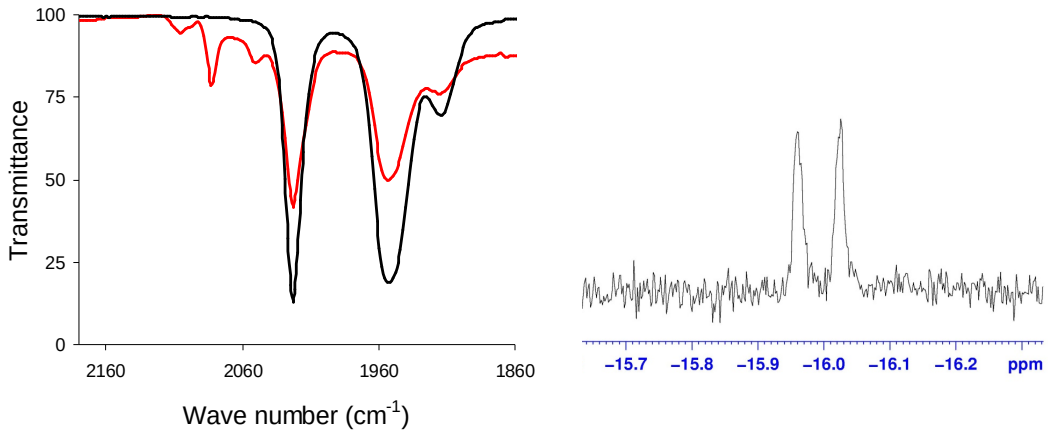

(a) (b)

Figure 4.5. (a) IR spectra of $Fe_2(CO)_4(\kappa^2$-dppv)(μ-edt) (**4.3**) in the absence of acid (black) and upon addition of two equivalent of CF_3CO_2H (red) in CH_2Cl_2; (b) Hydride region of the NMR spectrum of $Fe_2(CO)_4(\kappa^2$-dppv)(μ-edt) (**4.3**).

The IR spectra obtained in presence of acid are almost identical to those recorded during oxidation suggests that **4.2** undergoes oxidation in presence of acid. We did not see any hydride species in the ^1H NMR spectrum of **4.2** even in presence of excess CF_3CO_2H, the resonance for the neutral species faded slowly in presence of acid. At this point, we can not distinguish whether **4.2** reduces protons or the oxidation of the diiron centre takes place after protonation followed by an intra-molecular electron transfer from bpcd to the diiron centre (Scheme 4.3).

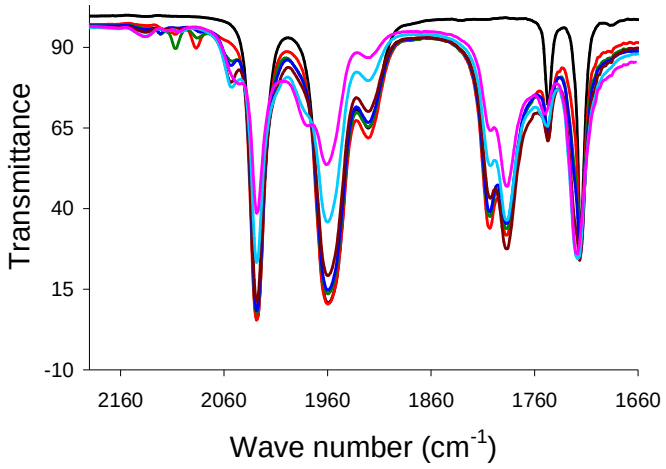

Figure 4.6. IR spectra of $Fe_2(CO)_4(\kappa^2\text{-bpcd})(\mu\text{-edt})$ (**4.2**) upon addition of two equivalent of CF_3CO_2H in CH_2Cl_2 – without CF_3CO_2H (black), upon addition of $[Cp_2Fe][BF_4]$ (red), after 2 min (green), after 4 min (blue), after 20 min (dark red), after 2 h (sky blue), after 8 h (pink).

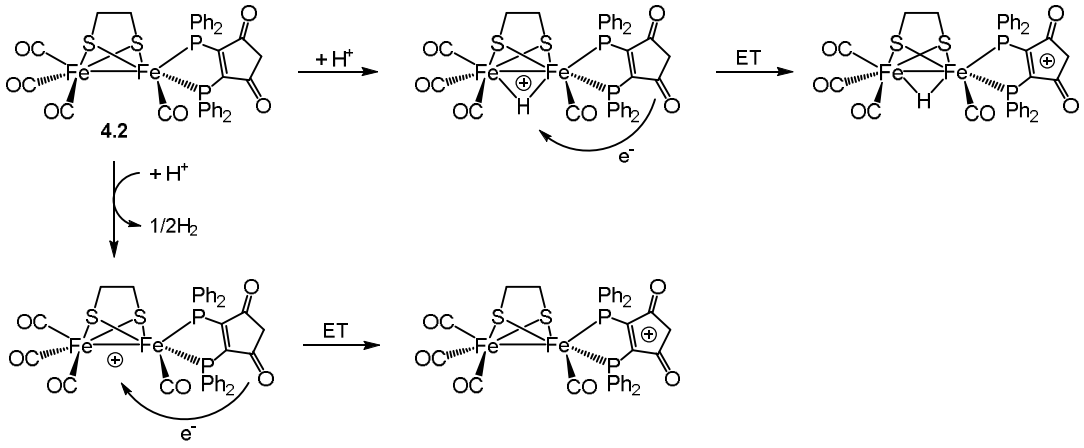

Scheme 4.3. Reaction of $Fe_2(CO)_4(\kappa^2\text{-bpcd})(\mu\text{-edt})$ (**4.2**) with acid.

4.2.5. Electrocatalytic proton reduction. As mentioned earlier, it was found that $Fe_2(CO)_4(\mu\text{-pdt})(\kappa^2\text{-bma})$ (**4.1**) did not act as a proton reduction catalyst. We have probed the ability of **4.2** to act as a proton reduction catalyst together with **4.3** in MeCN using CF_3CO_2H as the proton source. Figure 4.7 shows the CVs of **4.3** recorded upon sequential addition of 1-10 equivalents of acid. Since it undergoes slow protonation, no significant change was seen in the CV upon addition of 1 equivalent of acid but we saw a new reduction peak at E_p = –2.00 V upon addition of 2 equivalents of acid due to reduction of $[Fe_2(CO)_4(\mu\text{-H})(\kappa^2\text{-dppv})(\mu\text{-pdt})]^+$. The reduction peak of **4.3** at E_p = –2.15 V disappears after addition of 5 equivalents of acid showing complete protonation and we saw two distinct catalytic waves at E_p = –2.00 and –2.20 V at high acid

concentrations. A plausible mechanism is proposed to explain the catalytic waves shown by **4.3** at high acid concentration (shown in Scheme 4.4). According to this mechanism, after reduction of $[Fe_2(CO)_4(\mu\text{-}H)(\kappa^2\text{-}dppv)(\mu\text{-}pdt)]^+$ at E_p = –2.00 V the neutral hydride either reacts with a second proton at the same potential to release hydrogen or it may undergo a second reduction at E_p = –2.20 V before reacting with acid. Both process lead to the regeneration of catalyst thereby completing the catalytic cycle.

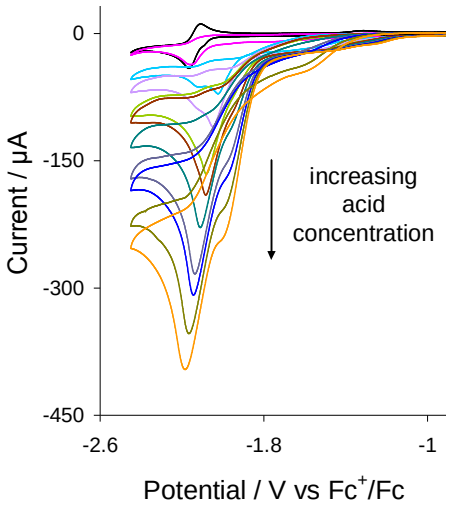

Figure 4.7. CVs of $Fe_2(CO)_4(\kappa^2\text{-}dppv)(\mu\text{-}edt)$ (**4.3**) in the absence of acid and in the presence of 1 to 10 molar equivalents of CF_3CO_2H (1 mM solution in acetonitrile, supporting electrolyte $[NBu_4][PF_6]$, scan rate 0.1 V/s, glassy carbon electrode, potential vs Fc^+/Fc).

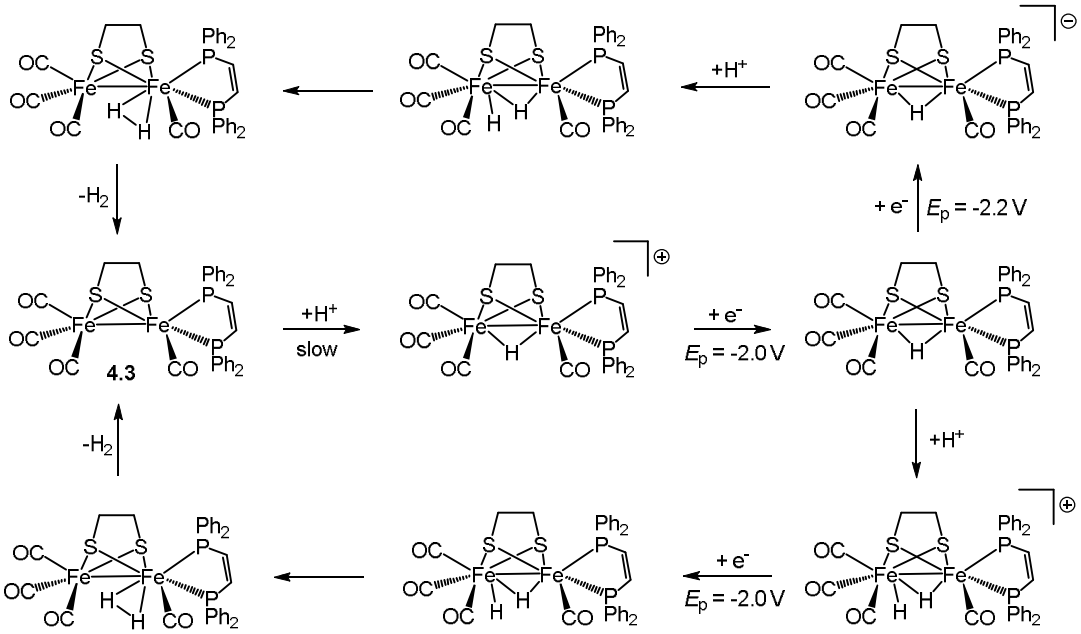

Scheme 4.4. Proposed mechanism for the electrocatalytic H_2 evolution by $Fe_2(CO)_4(\kappa^2\text{-}dppv)(\mu\text{-}edt)$ (**4.3**).

CVs of **4.2** recorded in presence of up to 10 equivalents of acid are shown in Figure 4.8 which show three distinct reductive features at E_p = –0.9, –2.1 and –2.3 V. The peak current of the first reductive process remains unchanged with respect to acid concentration, whereas that of the second and third reduction process increase as the concentration of acid is increased.

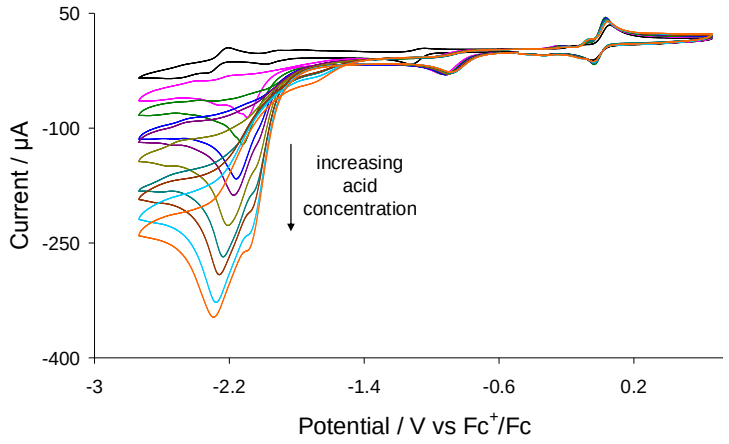

Figure 4.8. CVs of $Fe_2(CO)_4(\kappa^2$-bpcd)(µ-edt) (**4.2**) in the absence of acid and in the presence of 2 to 10 molar equivalents of CF_3CO_2H (1 mM solution in acetonitrile, supporting electrolyte $[NBu_4][PF_6]$, scan rate 0.1 V/s, glassy carbon electrode, potential vs Fc^+/Fc).

The increase in reduction current with acid concentration is characteristic of electrocatalytic proton reduction that confirms protonation of **4.2** in presence of acid. The ground-state electronic structure of protonated **4.2**, namely $[Fe_2(CO)_4(\mu$-H)$(\kappa^2$-bpcd)(µ-edt)$]^+$, shows that protonation of **4.2** across the iron-iron bond changes the HOMO (as expected), which is now mainly ligand-based but the LUMO is almost unaffected by this process (Figure 4.9). So, the first reductive process of $[Fe_2(CO)_4(\mu$-H)$(\kappa^2$-bpcd)(µ-edt)$]^+$ is also ligand based, which is now about 0.2 V more positive than that of **4.2**.

The neutral hydride species can not liberate hydrogen by reacting with a second proton so there is no increase in peak current at this potential as the concentration of acid is increased. This 35-electron species undergoes a second reduction at a more negative potential (E_p = –2.1 V) before (presumably) reacting with a second proton to release hydrogen as shown in Scheme 4.5. This anionic hydride can undergoes a further reduction at E_p = –2.3 V before reacting with proton which explains the second catalytic wave at this potential. A plot of catalytic limiting current against equivalents of acid (Figure 10) shows that both for **4.2** and **4.3** have similar catalytic efficiency.

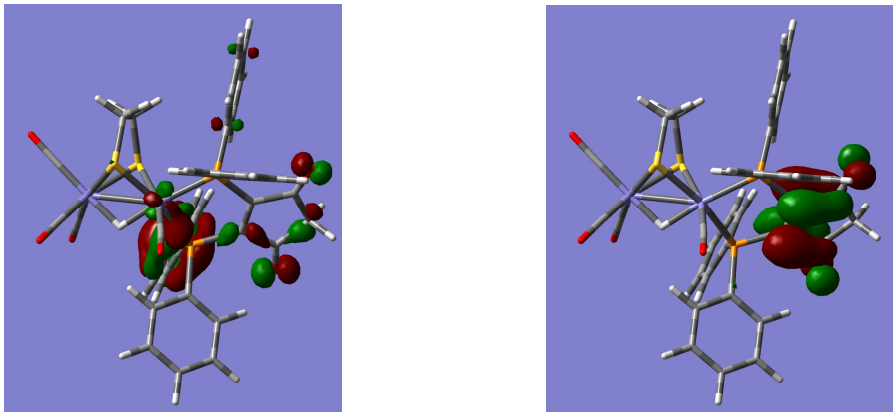

Figure 4.9. HOMO (left) and LUMO (right) of $[Fe_2(CO)_4(\mu\text{-}H)(\kappa^2\text{-}bpcd)(\mu\text{-}edt)]^+$ (calculations were carried out by collaborator).

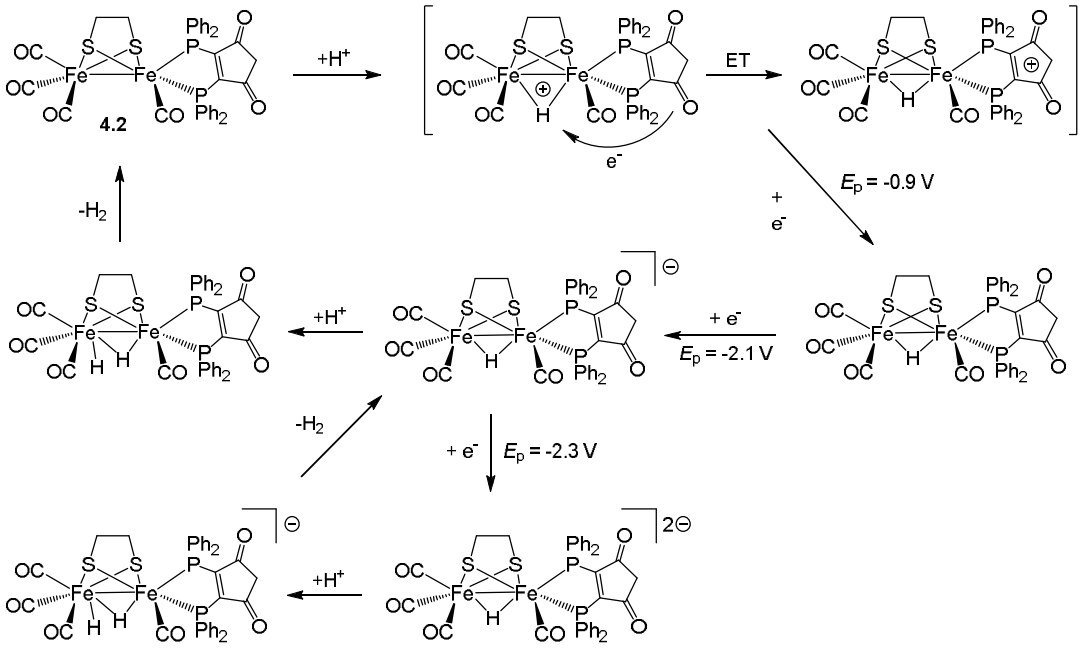

Scheme 4.5. Proposed mechanism for the electrocatalytic H_2 evolution by $Fe_2(CO)_4(\kappa^2\text{-}bpcd)(\mu\text{-}edt)$ (**4.2**).

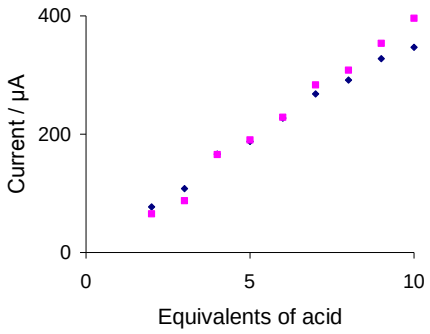

Figure 4.10. Plot of electrocatalytic peak current at potentials of the second catalytic waves *vs.* equivalents of CF_3CO_2H added for **4.2** (dark blue diamonds) and **4.3** (pink squares).

4.3. Summary and conclusions

The diiron biomimic, $Fe_2(CO)_4(\kappa^2\text{-bpcd})(\mu\text{-edt})$ (**4.2**), which contains a redox-active diphosphine (bpcd) has been prepared and studied as a catalyst for electrocatalytic proton reduction. The diphosphine adopts an axial-basal configuration in the solid-state but rapid exchange between these sites is observed in solution. Spectroscopic data suggests that chemical oxidation of **4.2** leads to intra-molecular electron-transfer from bpcd to the diiron core, which we believe is also the case during protonation. Complex **4.2** undergoes ligand-based reduction at a relatively mild potential ($E_{1/2}$ = –1.08 V) as supported by DFT calculations together with diiron-centred reductions at very negative potentials.

Electrocatalytic experiment in presence of CF_3CO_2H suggests that **4.2** is not catalytically active at mild potential ($E_{1/2}$ = –0.90 V) where ligand-based reduction of protonated species $[Fe_2(CO)_4(\mu\text{-H})(\kappa^2\text{-bpcd})(\mu\text{-edt})]^+$ takes place. The 35-electron neutral hydride $[Fe_2(CO)_4(\mu\text{-H})(\kappa^2\text{-bpcd})(\mu\text{-edt})]$ is not basic enough for second protonation. So, it undergoes a second reduction which takes place *ca.* –1.20 V more negative potential compared the first reductive process. At the moment we do not know the electronic structure of the 35-electron neutral hydride species, so can not unambiguously say whether this process is ligand-based or diiron-centred. DFT calculations are going on to shed light on this, so that we can reduce the gap between the ligand- and diiron-centred reduction processes. This can be done by further modification of the redox-active diphosphine so that the resultant catalyst will operate at mild potentials through delivery of electrons to the diiron centre *via* diphosphine.

4.4. Experimental Section

4.4.1. General. All reactions were carried out under a dry, oxygen-free nitrogen atmosphere using standard Schlenk techniques. Solvents were stored in alumina columns and dried with anhydrous engineering equipment, such that the water concentration was 5–10 ppm. $Fe_2(CO)_6(\mu\text{-edt})$ (**1.3**) [37], $Fe_2(CO)_4(\kappa^2\text{-dppv})(\mu\text{-edt})$ (**4.3**) [35] and 4,5-bis(diphenylphosphino)-4-cyclopenten-1,3-dione (bpcd) [34] were prepared according to the literature procedures. Infrared spectra were recorded using a Nicolet 6700 FT-IR spectrometer in a solution cell fitted with calcium fluoride plates, subtraction of the solvent absorptions being achieved by computation. NMR spectra were run on a Bruker

AMX400 instrument. All chemical shifts are reported in δ units with reference to the residual protons of the deuterated solvents for proton and to external $P(OMe)_3$ for ^{31}P chemical shifts. Preparative thin layer chromatography was carried out on 0.25 mm plates prepared from silica gel GHLF (UV254, Analtech).

4.4.2. Synthesis of $Fe_2(CO)_4(\kappa^2$-bpcd)(μ-edt) (4.2). An MeCN solution (20 mL) of $Fe_2(CO)_6$(μ-edt) (**1.3**) (50 mg, 0.134 mmol), bpcd (63 mg, 0.136 mmol) and Me_3NO (11 mg, 0.147 mmol) was heated to reflux for 2 h. The apparent red colour of the reaction mixture darkened during this period. The reaction mixture was then allowed to cool at room temperature. The solvent was removed under reduced pressure and the residue chromatographed by TLC on silica gel. Elution with hexane/CH_2Cl_2 (3:1, v/v) developed two bands on the TLC plate. The first band gave unconsumed $Fe_2(CO)_6$(μ-edt) (**1.3**) (4 mg) and the second band yielded $Fe_2(CO)_4(\kappa^2$-bpcd)(μ-edt) (**4.2**) (24 mg, 23%) as green crystals after recrystallization from hexane/CH_2Cl_2 at –4°C. Data for **4.2**: IR (νCO, CH_2Cl_2): 2028s, 1959s, 1921w, 1747w, 1716m cm^{-1}. ^1H NMR ($CDCl_3$): δ 7.96 (m, 4H), 7.52 (m, 6H), 7.43 (m, 2H), 7.38-7.30 (m, 8H), 3.60 (q, J 76.8, 21.6, 2H), 1.91 (d, J 7.6, 2H), 1.51 (d, J 7.6, 2H). $^{31}P\{^1H\}$ NMR ($CDCl_3$): δ 84.0 (s). Elemental analysis calc. for $C_{35}H_{26}Fe_2O_4P_2S_2$ (found): C 56.17 (56.51), H 3.50 (3.58).

Crystallographic data for $2Fe_2(CO)_4(\kappa^2$-bpcd)(μ-edt) (**4.2**)·CH_2Cl_2: red needle, dimensions 0.10 × 0.04 × 0.01 mm^3, monoclinic, space group $P\ 1\ 2_1/c\ 1$, a = 8.7205(1), b = 30.8866(5), c = 25.4645(6) Å, α = 90, β = 90.917(1), γ = 90°, V = 6857.9(2) $Å^3$, Z = 4, F(000) 3352, d_{calc} = 1.594 g cm^{-3}, μ = 2.516 mm^{-1}. 84633 reflections were collected, 20913 unique [R(int) = 0.0416]. At convergence, R_1 = 0.0448, wR_2 = 0.1063 [$I > 2.0\sigma(I)$] and R_1 = 0.0622, wR_2 = 0.1148 (all data), for 1082 parameters. The structure was solved by direct methods.

4.4.3. Synthesis of $Fe_2(CO)_4(\kappa^2$-dppv)(μ-edt) (4.3) [35]. A toluene (20 mL)solution of $Fe_2(CO)_6$(μ-edt) (**1.3**) (100 mg, 0.269 mmol) was treated with a MeCN solution (10 mL) of Me_3NO (22 mg, 0.293 mmol). After stirring for 10 min, the reaction mixture was treated with a toluene solution (10 mL) of dppv (120 mg, 0.303 mmol). The resultant mixture was stirred for 5 h and the solvent was then removed under vacuum. The residue was extracted into 5 mL of CH_2Cl_2 which gave $Fe_2(CO)_4(\kappa^2$-dppv)(μ-edt) (**4.3**) (134 mg, 70%) as red crystals after recrystallization from hexane/CH_2Cl_2 at –4°C. Data for **4.3**: IR (νCO, CH_2Cl_2): 2023vs, 1953s, 1915w cm^{-1}. ^1H NMR ($CDCl_3$): δ 8.14 (m, 1H), 7.99 (m,

5H), 7.54 (m, 6H), 7.35 (m, 6H), 7.23 (m, 4H), 1.91 (d, J 7.6, 2H), 1.81 (m, 2H), 1.30 (m, 2H). $^{31}P\{^{1}H\}$ NMR (CD_2Cl_2): δ 95.6 (s).

4.5. References

(1) J.M. Camara and T.B. Rauchfuss, *Nat. Chem.*, 2012, **4**, 26-30.

(2) C. Tard, X.M. Liu, S.K. Ibrahim, M. Bruschi, L. De Gioia, S.C. Davies, X. Yang, L.S. Wang, G. Sawers and C.J. Pickett, *Nature*, 2005, **433**, 610-613.

(3) C. Greco, *Inorg. Chem.*, 2013, **52**, 1901-1908.

(4) Y. Si, K. Charreteur, J.-F. Capon, F. Gloaguen, F.Y. Pétillon, P. Schollhammer and J. Talarmin, *J. Inorg. Biochem.*, 2010, **104**, 1038-1042.

(5) C. Gimbert-Suriñach, M. Bhadbhade and S. B. Colbran, *Organometallics*, 2012, **31**, 3480-3491.

(6) Y.-C. Liu, C.-H. Lee, G.-H. Lee and M.-H. Chiang, *Eur. J. Inorg. Chem.*, 2011, 1155-1162.

(7) C. Greco and L. De Gioia, *Inorg. Chem.*, 2011, **50**, 6987–6995.

(8) P.-Y. Orain, J.-F. Capon, F. Gloaguen, F.Y. Pétillon, P. Schollhammer, J. Talarmin, G. Zampella, L. De Gioia and T. Roisnel, *Inorg. Chem.*, 2010, **49**, 5003-5008.

(9) S. Ezzaher, P.-Y. Orain, J.-F. Capon, F. Gloaguen, F. Pétillon, T. Roisnel, P. Schollhammer and J. Talarmin, *Chem. Commun.*, 2008, 2547-2549.

(10) P.-Y. Orain, J.-F. Capon, N. Kervarec, F. Gloaguen, F. Pétillon, R. Pichon, P. Schollhammer and J. Talarmin, *Dalton Trans.*, 2007, 3754-3756.

(11) S. Roy, T.L. Groy and A. K. Jones, *Dalton Trans.*, 2013, **42**, 3843-3853.

(12) G. B. Hall, J. Chen, C. A. Mebi, N. Okumura, M. T. Swenson, S. E. Ossowski, U. I. Zakai, G. S. Nichol, D. L. Lichtenberger, D. H. Evans and R. S. Glass, *Organometallics*, 2013, **32**, 6605-6612.

(13) J. W. Peters, W. N. Lanzilotta, B. J. Lemon and L. C. Seefeldt, *Science*, 1998, **282**, 1853-1858.

(14) Y. Nicolet, C. Piras, P. Legrand, C. E. Hatchikian and J. C. Fontecilla-Camps, *Structure*, 1999, **7**, 13–23.

(15) M. Bruschi, C. Greco, P. Fantucci and L. De Gioia, *Inorg. Chem.*, 2008, **47**, 6056-6071.

(16) D. E. Schwab, C. Tard, E. Brecht, J. W. Peters, C. J. Pickett and R. K. Szilagyi, *Chem. Commun.*, 2006, 3696-3698.

(17) A. M. Allegier and C. A. Mirkin, *Angew. Chem. Int. Ed.*, 1998, **37**, 894-908.

(18) J. M. Camara and T. B. Rauchfuss, *J. Am. Chem. Soc.*, 2011, **133**, 8098-8101.

(19) K. S. Gan and T. S. A. Hor, In *Ferrocenes*, A. Togni and T. Hayashi, Eds., VCH, New York, 1995.

(20) F. I. Adam, G. Hogarth, S. E. Kabir and I. Richards, *C.R. Chim.*, 2008, **11**, 890-905.

(21) F. I. Adam, G. Hogarth and I. Richards, *J. Organomet. Chem.*, 2007, **692**, 3957-3968.

(22) S. Ghosh, G. Hogarth, N. Hollingsworth, K. B. Holt, I. Richards, M. G. Richmond, B. E. Sanchez and D. Unwin, *Dalton Trans.*, 2013, **42**, 6775-6792.

(23) S. Ezzaher, J.-F. Capon, F. Gloaguen, N. Kervarec, F. Y. Pétillon, R. Pichon, P. Schollhammer and J. Talarmin, *C.R. Chim.*, 2008, **11**, 906-914.

(24) C. Greco, P. Fantucci, L. De Gioia, R. Suarez-Bertoa, M. Bruschi, J. Talarmin and P. Schollhammer, *Dalton Trans.*, 2010, **39**, 7320-7329.

(25) J.-F. Capon, F. Gloaguen, F. Y. Pétillon, P. Schollhammer and J. Talarmin, *Eur. J. Inorg. Chem.*, 2008, 4671-4681.

(26) S. Ezzaher, J.-F. Capon, F. Gloaguen, F. Y. Pétillon, P. Schollhammer and J. Talarmin, *Inorg. Chem.*, 2007, **46**, 3426-3428.

(27) A. K Justice, T. B. Rauchfuss and S. R. Wilson, *Angew. Chem., Int. Ed.*, 2007, **46**, 6152-6154.

(28) S. Ezzaher, J.-F. Capon, F. Gloaguen, F. Y. Pétillon, P. Schollhammer and J. Talarmin, *Inorg. Chem.*, 2007, **46**, 9863-9872.

(29) S. Ezzaher, J. -F. Capon, F. Gloaguen, F. Y. Pétillon, P. Schollhammer, J. Talarmin and N. Kervarec, *Inorg. Chem.*, 2009, **48**, 2-4.

(30) S. Ezzaher, J.-F. Capon, N. Dumontet, F. Gloaguen, F. Y. Pétillon, P. Schollhammer and J. Talarmin, *J. Electroanal. Chem.*, 2009, **626**, 161-170.

(31) S. Lounissi, J.-F. Capon, F. Gloaguen, F. Matoussi, F. Y. Pétillon, P. Schollhammer and J. Talarmin, *Chem. Commun.*, 2011, **47**, 878-880.

(32) S. Lounissi, G. Zampella, J.-F. Capon, L. De Gioia, F. Matoussi, S. Mahfoudhi, F.Y. Pétillon, P. Schollhammer and J. Talarmin, *Chem.-Eur. J.*, 2012, **18**, 11123-11138.

(33) F. Ridley, S. Ghosh, G. Hogarth, N. Hollingsworth, K. B. Holt and D. Unwin, *J. Electroanal. Chem.*, 2013, **703**, 14-22.

(34) D. Fenske and H. J. Becher, *Chem. Ber.*, 1975, **108**, 2115-2123.

(35) A. K Justice, G. Zampella, L. De Gioia, T. B. Rauchfuss, J. I. van der Vlugt and S. R. Wilson, *Inorg. Chem.*, 2007, **46**, 1655-1664.

(36) S. Kaur-Ghumaan, L. Schwartz, R. Lomoth, M. Stein and S. Ott, *Angew. Chem. Int. Ed.*, 2010, **49**, 8033-8036.

(37) A. Winter, L. Zsolnai and G. Huttner, *Z. Naturforsch.*, 1982, **37B**, 1430-1436.

Chapter 5

Hydrogenase biomimetics: $Fe_2(CO)_4(\mu\text{-dppf})(\mu\text{-pdt})$ [dppf = 1,1′-bis(diphenylphosphino)ferrocene)] both a proton-reduction and hydrogen oxidation catalyst

5.1. Introduction

As detailed in previous chapters, the use of non-innocent ligands in the diiron biomimics acting as redox co-factors has intensified in recent years [1-12] with attempts to emulate the cooperative interaction between diiron and tetrairon sites in the active site of the enzyme [1-3,13-16]. Besides various redox-active ligand systems such as diamines [8-11], quinones [12] and diphosphines [4,7] that are usually incorporated as redox co-factor in the biomimetic models, ferrocene-based ligands are finding increasing use [1,3,5-7] due to their chemical inertness and well-defined redox properties[17]. For example, Chiang and co-workers have synthesized diphenylphosphinoferrocene substituted di- and tetra-iron biomimetics that can catalyse H_2 formation from acetic acid [6], whilst Colbran and co-workers have reported electrocatalytic proton reduction by ferrocenylphosphido-bridged diiron complexes (Chart 5.1) [5]. Although these model catalysts are able to catalyse proton reduction from various sources, no evidence for electronic communication between the diiron centre and ferrocene unit(s) has been seen.

Recent developments in hydrogenase biomimics suggest that H_2 activation can be favoured by the presence of a mild and chemically inert oxidant [18,19]. This concept was recently experimentally implemented by Camara and Rauchfuss [1,20] who utilised $(C_5Me_5)Fe(C_5Me_4CH_2PEt_2)$ (FcP*) as the intramolecular oxidant; the $Fe^{II/III}$ couple ($E_{1/2}$ = –0.59 V) of which lies closer to the H_2/H^+ couple *vs.* the Fc^+/Fc couple [1]. They showed that the dication of $Fe_2(CO)_3(\kappa^2\text{-dppv})(\kappa^1\text{-FcP*})\{\mu\text{-}SCH_2N(CH_2Ph)CH_2S\}$ (**5A**) cleaves H_2, being facilitated by an intramolecular electron-transfer in its doubly oxidised state, the electron transferring from the diiron unit to the pendent FcP* ligand i.e. switching from Fe(III)Fe(II)Fe(I) to Fe(II)Fe(II)Fe(II) (Scheme 5.1) [1]. In contrast, an analogue of **5A** in which FcP* is replaced by PMe_3 is catalytically inactive towards H_2 oxidation [1].

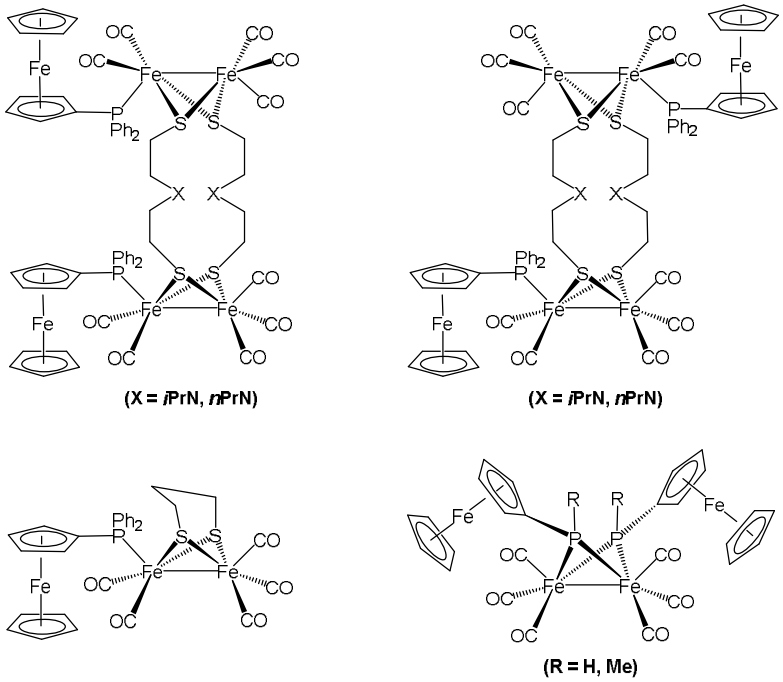

Chart 5.1. Diiron biomimics with ferrocene-based redox co-factor [5,6].

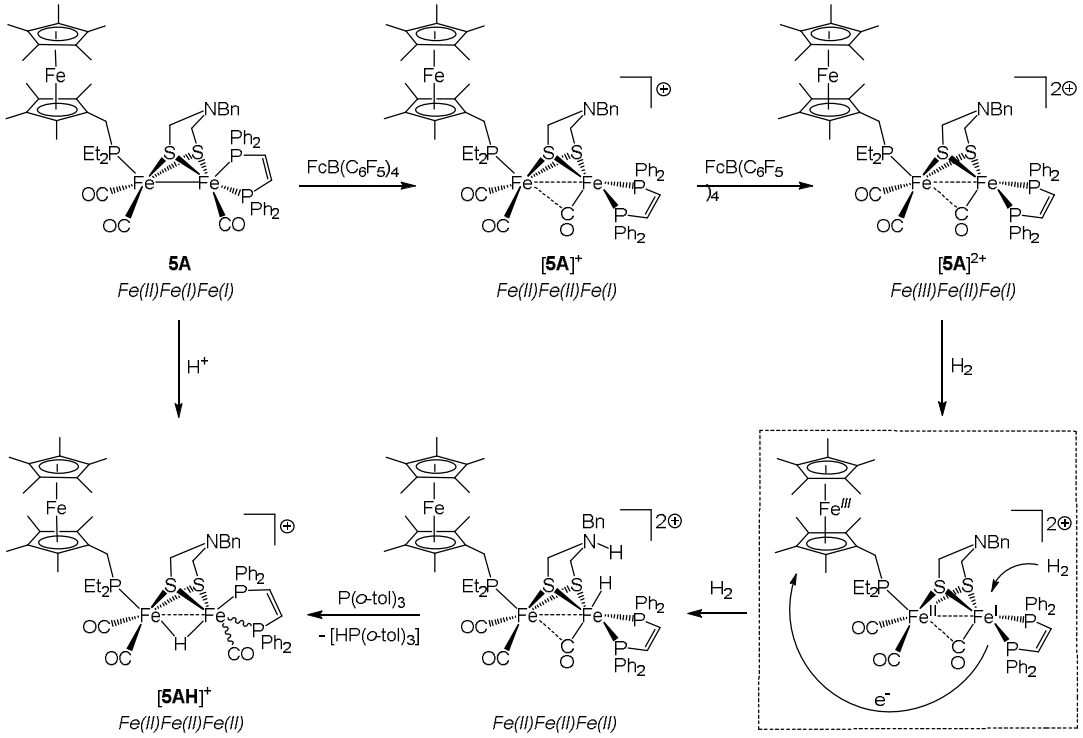

Scheme 5.1. Proposed mechanism for the electrocatalytic H_2 oxidation by $Fe(CO)_3(PMe_3)\{(C_5Me_5)Fe(C_5Me_4CH_2PEt_2)\}(\mu\text{-}SCH_2N(CH_2Ph)CH_2S\}$ (**5A**) [1].

The diphosphine 1,1′-bis(diphenylphosphino)ferrocene (dppf) has received much attention as a ligand in a variety of catalytic applications including electrocatalysis due to the redox-active ferrocene backbone and its flexible bite angle [21]. Being a metallocene, it has relatively high rate of electron-transfer [22-23] which makes its incorporation into redox catalysts attractive. It has also been proposed to influence the electron transfer properties of compounds to which it is attached [24]. Unlike ferrocene, the oxidative electrochemistry of dppf is complicated as its oxidation is not completely reversible due to the dimerisation of the oxidized species ($dppf^{+}$). This dimerisation is attributed to the presence of the lone pair of electrons on each phosphorus atom which can transfer an electron to the Fe(III) centre, thereby forming a phosphorus radical capable of dimerisation. This can be prevented by coordinating the dppf to a metal as the lone pair of electrons on each phosphorus atom is now occupied in metal-ligand bonding. Numerous studies have been carried out on dppf complexes, revealing that the Fe^{III}/Fe^{II} couple in these complexes is normally fully reversible and shows an anodic shift due to the inductive effect [25-24].

Despite the precedence of its use in redox catalysts, we were surprised that the electrocatalytic properties of biomimetic models containing a dppf ligand have yet to be reported. We thus set out to synthesize diiron biomimics bearing a dppf ligand and to study their electrocatalytic properties. As part of a preliminary study we herein describe $Fe_2(CO)_4(\mu\text{-dppf})(\mu\text{-pdt})$ (**5.1**) {pdt = $S(CH_2)_3S$} which we have shown is a catalyst for both proton reduction and H_2 oxidation.

5.2. Results and discussion

5.2.1. Synthesis and structure. Heating a toluene solution of equimolar amounts of $Fe_2(CO)_6(\mu\text{-pdt})$ (**1.1**) with dppf initially leads to formation of the linked tetranuclear complex $\{Fe_2(CO)_5(\mu\text{-pdt})\}_2(\mu,\kappa^1,\kappa^1\text{-dppf})$ [10] and unreacted dppf, which slowly rearranges to afford $Fe_2(CO)_4(\mu\text{-dppf})(\mu\text{-pdt})$ (**5.1**) in moderate yields (52%) as an air-stable orange solid (Scheme 5.2).

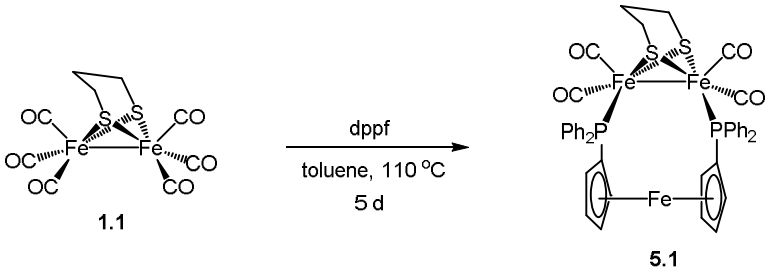

Scheme 5.2. Synthesis of $Fe_2(CO)_4$(μ-dppf)(μ-pdt) (**5.1**).

Characterisation of **5.1** was straightforward, most notably the IR spectrum in the carbonyl region consisted of four absorptions at 1986s, 1949vs, 1918s and 1896w cm^{-1} the pattern and relative intensity of which is characteristic of an $Fe_2(CO)_4$(μ-diphosphine)(μ-dithiolate) structure [28-39]. In the ^1H NMR spectrum four slightly broad singlet resonances of equal intensity between δ 4.93-4.01 are assigned to the cyclopentadienyl protons and three broad multiplets between δ 2.60-2.13 to the methylene groups of the dithiolate ligand. Single crystals of **5.1**·0.5 CH_2Cl_2 were grown upon slow diffusion of hexanes into a concentrated dichloromethane solution and the results of an X-ray diffraction study are summarised in Figure 5.1 and its caption.

The molecule contains the expected diiron core spanned by both diphosphine and dithiolate ligands and with each iron atom also supporting two terminal carbonyls. The Fe–Fe bond length of 2.6133(6) Å is significantly elongated as compared to related $Fe_2(CO)_4$(μ-diphosphine)(μ-pdt) complexes which typically range between 2.46 to 2.53 Å [28-39], although it is shorter than that of 2.6246(3) Å in $Fe_2(CO)_4${μ-$Ph_2P(CH_2)_4PPh_2$}(μ-pdt) [28] which also contains a highly flexible diphosphine backbone. Other hydrogenase biomimetics with relatively long iron-iron bonds include $Fe_2(CO)_2(\kappa^2$-$Ph_2PCH{=}CHPPh_2)_2$(μ-adt) (adt = SCH_2NHCH_2S) [Fe–Fe 2.6027(6) Å] [40]. Iron-sulphur bond lengths [range 2.2410(6)-2.2565(6) Å] are typical [28-39], while iron-phosphorus bonds lengths [Fe(1)–P(1) 2.2256(6), Fe(2)–P(2) 2.2679(6) Å] are again slightly longer than those found in related small-bite angle diphosphine complexes [28-39]. The dppf ligand lies *trans* to one of the sulphur atoms [P(1)–Fe(1)–S(1) 174.34(2), P(2)–Fe(2)–S(1) 167.79(2)°] and *cis* to the second [P(1)–Fe(1)–S(2) 90.77(2), P(2)–Fe(2)–S(2) 99.59(2)°]. Although in solution the molecule contains a plane of symmetry bisecting the iron-iron bond, in the solid-state this is not the case. Figure 5.1b highlights this showing that one cyclopentadienyl group lies above the $Fe_3S(1)$ plane and the second below it. Presumably

in solution this is readily inverted as a result of the well-established fluxionality of the dppf ligand [41,42].

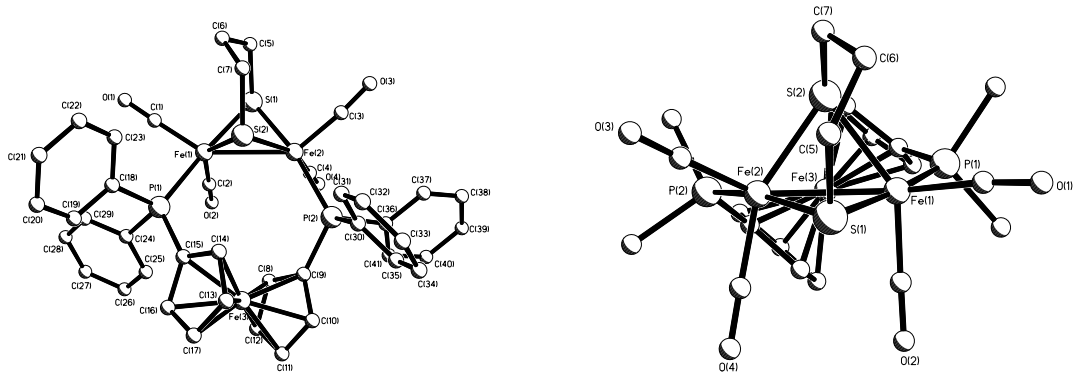

(a) (b)

Figure 5.1. Two views of the molecular structure of $Fe_2(CO)_4(\mu\text{-dppf})(\mu\text{-pdt})$ (**5.1**) (a) the full molecule and (b) with phenyl groups omitted for clarity. Selected bond lengths (Å) and angles (°): Fe(1)–Fe(2) 2.6133(6), Fe(1)–P(1) 2.2256(6), Fe(2)–P(2) 2.2679(6), Fe(1)–S(1) 2.2410(6), Fe(1)–S(2) 2.2540(6), Fe(2)–S(1) 2.2508(6), Fe(2)–S(2) 2.2565(6), P(1)–Fe(1)–Fe(2) 120.10(2), P(2)–Fe(2)–Fe(1) 118.65(2), P(1)–Fe(1)–S(1) 174.34(2), P(2)–Fe(2)–S(1) 167.79(2), P(1)–Fe(1)–S(2) 90.77(2), P(2)–Fe(2)–S(2) 99.59(2), C(2)–Fe(1)–Fe(2) 91.95(7), C(4)–Fe(2)–Fe(1) 101.73(7).

5.2.2. Protonation of $Fe_2(CO)_4(\mu\text{-dppf})(\mu\text{-pdt})$ (5.1). It is well-established that chelate complexes of the type $Fe_2(CO)_4(\kappa^2\text{-diphosphine})(\mu\text{-dithiolate})$ rapidly and cleanly protonate to afford stable hydrido-cations $[Fe_2(CO)_4(\mu\text{-H})(\kappa^2\text{-diphosphine})(\mu\text{-dithiolate})]^+$ [29,31,40,43,44], while in contrast isomeric species, $Fe_2(CO)_4(\mu\text{-diphosphine}(\mu\text{-dithiolate})$, with a bridging diphosphine are protonated only slowly by strong acids and generally form unstable species that cannot be easily characterised [28]. There are two exceptions to this. Thus, protonation of $Fe_2(CO)_4(\mu\text{-}Cy_2PCH_2PCy_2)(\mu\text{-pdt})$ by $HBF_4{\cdot}Et_2O$ occurs cleanly to afford $[Fe_2(CO)_4(\mu\text{-H})(\mu\text{-}Cy_2PCH_2PCy_2)(\mu\text{-pdt})][BF_4]$, which has been crystallographically characterised, protonation being favoured by the more electron-donating dicyclohexylphosphido groups [33]. The second example relates to $Fe_2(CO)_4\{\mu\text{-}Ph_2P(CH_2)_4PPh_2\}(\mu\text{-pdt})$, which unlike related species with fewer methylene groups in the backbone, also reacts rapidly with $HBF_4{\cdot}Et_2O$ to form a relatively stable cationic hydride [28]. The reason(s) for this different protonation behaviour of $Fe_2(CO)_4\{\mu\text{-}Ph_2P(CH_2)_4PPh_2\}(\mu\text{-pdt})$ are less clear as the diiron centres appear to have very similar basicities and we earlier attributed this behaviour to the more flexible nature of this diphosphine as shown by the relatively elongated iron-iron bond (see above). Given the

elongated nature of the iron-iron bond in **5.1**, this seemed to be a good opportunity to test this hypothesis. Indeed addition of a few drops of $HBF_4{\cdot}Et_2O$ to a dichloromethane solution of **5.1** resulted in the rapid and clean formation of the cationic-hydride $[Fe_2(CO)_4(\mu\text{-H})(\mu\text{-dppf})(\mu\text{-pdt})][BF_4]$ (**5.2**) (Scheme 5.3). Further, and unlike the related cationic-chelate complexes, addition of base leads to regeneration of the neutral complex. This suggests that while **5.1** is able to bind a proton, it is relatively weakly bound, which may be a useful feature for catalysis (see below).

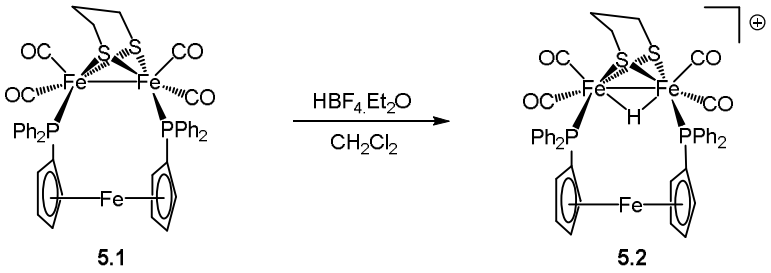

Scheme 5.3. Protonation of $Fe_2(CO)_4(\mu\text{-dppf})(\mu\text{-pdt})$ (**5.1**).

Characterisation of **5.2** was straightforward. In the IR spectrum the carbonyl absorptions now appear at 2058s, 2040s and 2002s cm^{-1} being shifted *ca.* 80 cm^{-1} to higher wavenumbers consistent with removal of significant electron-density form the diiron centre (Figure 5.2). The $^{31}P\{^1H\}$ NMR spectrum still only shows a singlet at 44.8 ppm, consistent with a bridging hydride and this is confirmed by the observation of a triplet at δ –12.40 (J_{PH} 17.6) associated with the hydride. Unfortunately we have been unable to grow crystals of **5.2** suitable for X-ray diffraction, all attempts leading to the formation of mixtures of **5.1** and **5.2**.

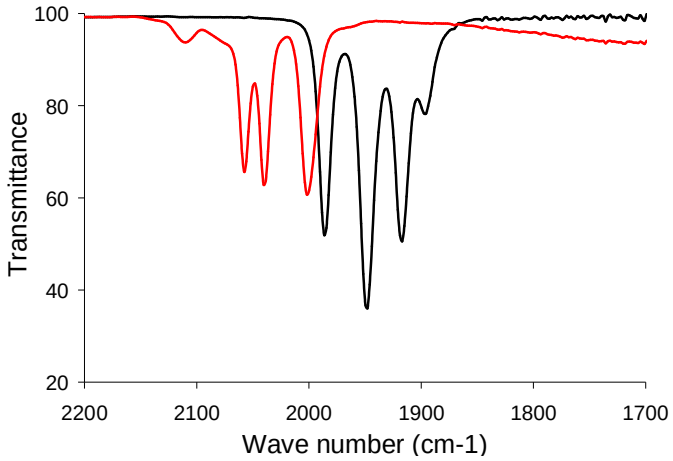

Figure 5.2. IR spectra of $Fe_2(CO)_4(\mu\text{-dppf})(\mu\text{-pdt})$ (**5.1**) (black) and **5.1** + 1 equiv. $HBF_4{\cdot}Et_2O$ (red) in CH_2Cl_2.

The major metric change upon protonation of chelate complexes $Fe_2(CO)_4(\kappa^2$-diphosphine)(μ-dithiolate) relates to the positions of the basal carbonyl ligand(s), the Fe–Fe–C(basal) bond angle increasing by *ca.* 8° on average, while the iron-iron bond length remains virtually unchanged [29,31,40,43,44]. Similarly with the only crystallographically characterised pair namely $Fe_2(CO)_4$(μ-$Cy_2PCH_2PCy_2$)(μ-pdt) and [$Fe_2(CO)_4$(μ-H)(μ-$Cy_2PCH_2PCy_2$)(μ-pdt)][BF_4] the iron-iron bond lengths are virtually identical [Fe–Fe 2.520 Å (av) over four independent molecules and 2.531(2) Å], while the basal carbonyls bend away from each other by *ca.* 12.5° [33]. Interestingly in **5.1** the Fe–Fe–C(basal) bond angles [C(2)–Fe(1)–Fe(2) 91.95(7), C(4)–Fe(2)–Fe(1) 101.73(7)°] vary by nearly 20° suggesting the these interactions are quite flexible. Further, given the longer iron-iron bond then they are likely to be less affected by the addition of a hydride as there is more space between the relatively bulky diphenylphosphino end groups. As mentioned above, the bis(diphosphine) complex $Fe_2(CO)_2(\kappa^2$-dppv)$_2$(μ-adt) has a relatively long metal-metal bond length [Fe–Fe 2.6027(6) Å] [40] although the analogous edt complex $Fe_2(CO)_2(\kappa^2$-dppv)$_2$(μ-edt) [Fe–Fe 2.5678(4) Å] [45] is less elongated. Unfortunately the structure of the analogous pdt complex has not been crystallographically determined but the corresponding hydride [$Fe_2(CO)_2$(μ-H)(κ^2-dppv)$_2$(μ-pdt)][BF_4] is characterised by an especially elongated iron-iron bond length of 2.6646(6) Å [46]. Further, Rauchfuss and co-workers have recently shown that the 35-electron complex, $Fe_2(CO)_2$(μ-H)(κ^2-dppv)$_2$(μ-pdt) [REF], formed upon one-electron reduction of [$Fe_2(CO)_2$(μ-H)(κ^2-dppv)$_2$(μ-pdt)][BF_4] and an intermediate in the catalytic proton reduction by $Fe_2(CO)_2(\kappa^2$-dppv)$_2$(μ-pdt), has an extremely long iron-iron bond [Fe–Fe 2.8030(5) Å] [46]. This possibly highlights the advantage of using hydrogenase biomimetics with highly flexible backbones as proton reduction catalysts. With this in mind, and also with the aim of understanding any possible relationship between the two different redox centres, we have undertaken a cyclic voltammetry study.

5.2.3. Electrochemistry. In order to asses the potential of **5.1** as a proton reduction and hydrogen oxidation catalyst, CVs were recorded in MeCN at various scan rates and Figure 5.3 shows the results. The complex undergoes an electrochemically reversible oxidation at $E_{1/2}$ = 0.05 V (ΔE = 60 mV) and a quasi-reversible oxidation at $E_{1/2}$ = 0.685 V (ΔE = 70 mV). The former is associated with the diiron centre being oxidized to a mixed-valence Fe(I)-Fe(II) state and the latter with the ferrocene moiety (see later). The reversibility of both oxidative processes is maintained at all scan rates, each originating from diffusion-controlled one-electron processes. The complex also shows two

overlapping irreversible reduction peaks at E_p = –2.10 V and E_p = –2.19 V which become separated at higher scan rates (≥0.25 V/s) (Fig. 2). Two small oxidation peaks are also observed at E_p = –1.80 V and E_p = –1.53 V on the return scan being due to the product formed in the reductive process, whilst the small reduction peak appeared at E_p = –0.35 V on the return scan is associated with the first oxidation product.

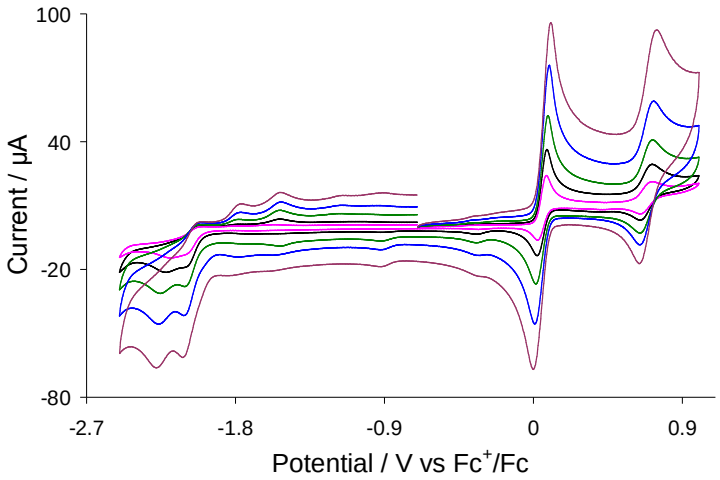

Figure 5.3. CVs of $Fe_2(CO)_4$(µ-dppf)(µ-pdt) (**5.1**) in MeCN (1 mM solution, supporting electrolyte $[NBu_4][PF_6]$, glassy carbon electrode, potential vs Fc^+/Fc) at scan rates 0.05 V/s (pink), 0.1 V/s (black), 0.25 V/s (green), 0.5 V/s (blue) and 1 V/s (plum).

That the first oxidation occurs from the diiron unit is shown upon addition of one molar equivalent of $FcPF_6$ (Fc = ferrocene) to a CH_2Cl_2 solution of **5.1** which results in the appearance of new absorption bands at 2044 and 2013 cm^{-1} in addition to the absorptions for **5.1** (Figure 5.4). As **5.1** first undergoes oxidation reversibly at $E_{1/2}$ = 0.05 V *vs.* Fc^+/Fc, Fc^+ does not results in stoichiometric oxidation of the complex as the oxidation potential of **5.1** is not sufficiently negative relative to the Fc^+/Fc couple. However the potentials are similar enough to allow the following equilibrium to be established:

$$Fc^+ + \mathbf{5.1} \rightleftharpoons Fc + \mathbf{5.1}^+$$

Thus conversion of some of **5.1** to $\mathbf{5.1}^+$ can be observed in the IR spectrum. The 60 cm^{-1} shift of the first ν_{CO} band to higher energy is indicative of localisation of the positive charge on the diiron centre, allowing assignment of the couple at 0.05 V *vs.* Fc^+/Fc to the oxidation of diiron centre rather than oxidation of the dppf ligand.

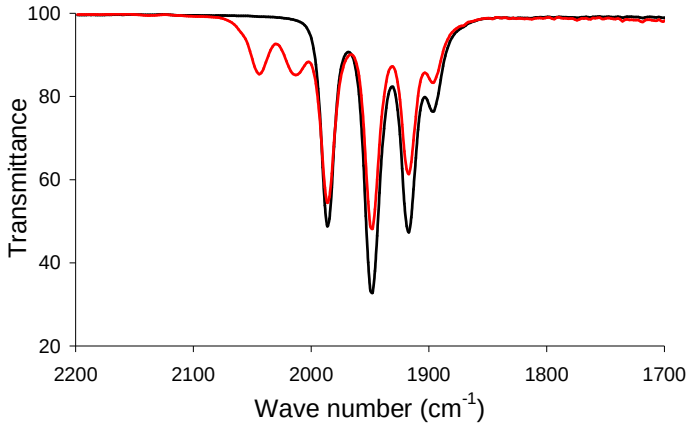

Figure 5.4. IR spectra of $Fe_2(CO)_4$(μ-dppf)(μ-pdt) (**5.1**) (black) and **5.1** + 1 equiv. $[Cp_2Fe][PF_6]$ (red) in CH_2Cl_2.

The second quasi-reversible oxidation is associated with the dppf ligand. Free dppf undergoes an irreversible oxidation at 0.20 V which becomes reversible and shifts to more positive potentials upon coordination to a metal centre [25-27]. The relative position of the second oxidative process *vs.* Fc^+/Fc and its excellent chemical reversibility (i_{Pa}/i_{Pc} ~ 1 at scan rate 0.1 Vs^{-1}) indicates that the process is associated with the $Fe^{II/III}$ couple of the ferrocene moiety. The ground-state electronic structures of **5.1** and the radical cation **5.1**$^+$ have been calculated by DFT to shed light on these oxidative processes, and the results corroborate well with the experimental observations (Figure 5.5). The HOMO of **5.1** is mainly the Fe–Fe bonding orbital, whereas that of **5.1**$^+$ is localised on ferrocene iron which suggest that the first oxidation of **5.1** occurs at the diiron centre, whilst the second oxidative event takes place at the ferrocene iron.

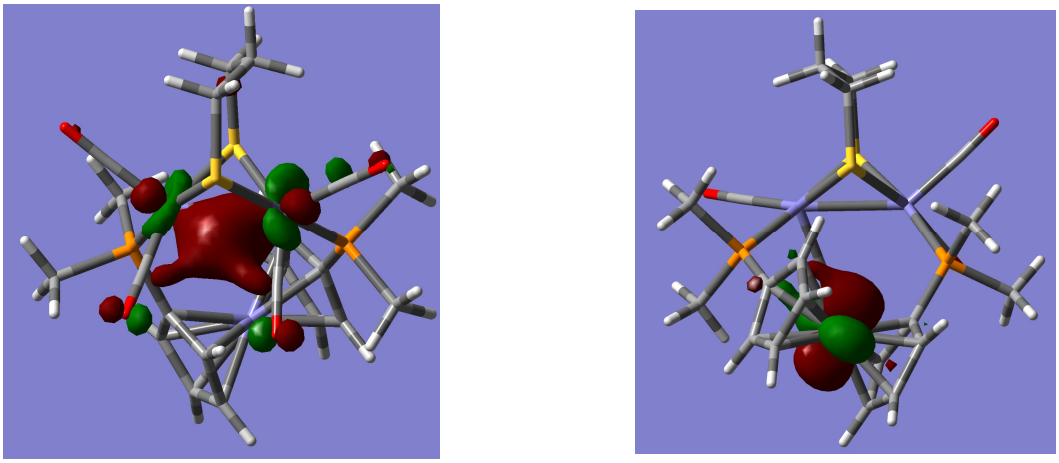

Figure 5.5. HOMO of **5.1** (left) and **5.1**$^+$ (right) – the phenyl groups on dppf were replaced by methyl groups to reduce computational time (calculations were carried out by collaborator).

5.2.4. Electrocatalytic proton reduction. Complex **5.1** was first tested as a proton reduction catalyst in the presence of $HBF_4{\cdot}Et_2O$ in MeCN. Figure 5.6 shows the CVs upon addition of between 1-10 equivalents of acid. A new reduction wave appears at E_p = –1.70 V upon addition of acid being associated with reduction of **5.2**, its height growing with increasing amounts of acid, being characteristic of electrocatalytic proton reduction [6]. At higher amounts of acid (≥7 molar equivalents) this wave splits into two distinct peaks possibly resulting from reduction of the putative cation $[HFe_2(CO)_4(\mu\text{-}H)(\mu\text{-dppf})(\mu\text{-pdt})]^+$ (Scheme 5.4). Another catalytic wave is also observed at E_p = –2.10 V which competes with the direct reduction of $HBF_4{\cdot}Et_2O$ by the glassy carbon electrode as this electrode becomes catalytically active beyond –2.00 V in presence of strong acids [47]. On the return scan a further reductive wave is seen at E_p = –1.55 V which also increases with acid concentration implying that a sufficiently stable species is generated in the depletion layer during catalysis on the forward scan which can release hydrogen by reducing at this potential [48]. Thus it appears that **5.1** enters into the catalytic cycle *via* a CE mechanism to generate the neutral paramagnetic complex $Fe_2(CO)_4(\mu\text{-}H)(\mu\text{-dppf})(\mu\text{-pdt})$ [49] which either protonates or undergoes a further reduction before second protonation to liberate hydrogen (Scheme 5.4). The peak heights of the oxidative processes do not change during the experiment showing the robustness of **5.1** under the operating conditions.

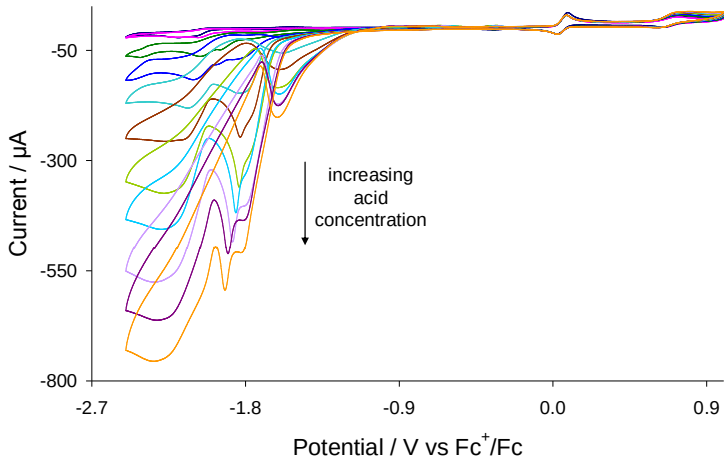

Figure 5.6. CVs of $Fe_2(CO)_4(\mu\text{-dppf})(\mu\text{-pdt})$ (**5.1**) in the absence of acid and in the presence of 1 to 10 molar equivalents of $HBF_4{\cdot}Et_2O$ (1 mM solution in MeCN, supporting electrolyte $[NBu_4][PF_6]$, scan rate 0.1 Vs^{-1}glassy carbon electrode, potential vs Fc^+/Fc).

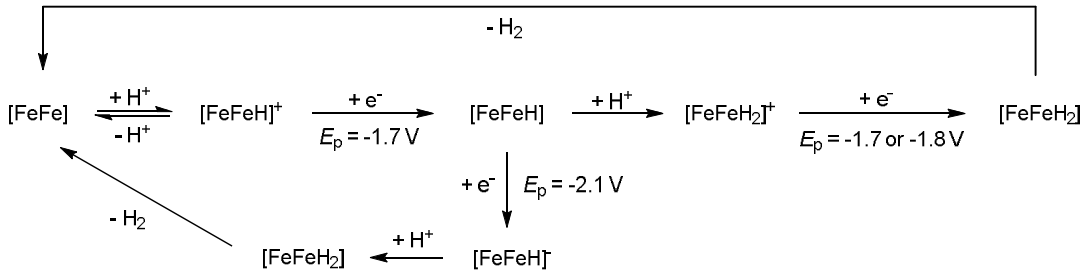

Scheme 5.4. Proposed mechanism for electrocatalytic proton reduction by $Fe_2(CO)_4$(μ-dppf)(μ-pdt) (**5.1**).

5.2.5. Electrocatalytic H_2 oxidation. That there is electronic communication between the diiron core and the ferrocene centre in **5A** (despite the presence of a methylene linker unit) prompted us to investigate the possibility of electronic communication between the two redox-active metal centres in **5.1**. Indeed we found that **5.1** catalytically cleaves H_2 in presence of a base (pyridine) in its $\mathbf{5.1}^{2+}$ state (Figure 5.7). Thus, addition of equimolar amount of pyridine to a MeCN solution of **5.1** under H_2 results in an increase of the oxidative peak current of the second oxidation process of **5.1** by 10 mA, which reaches 22 mA upon addition of 10 equivalents of pyridine. No such catalytic wave was observed when the same experiment was carried out in absence of base (Figure 5.8) or H_2 (Figure 5.9). Similarly either $Fe_2(CO)_4$(μ-$Ph_2PCH_2PPh_2$)(μ-pdt) [28,33] or $Fe_2(CO)_4${μ-$Ph_2P(CH_2)_4PPh_2$}(μ-pdt) [28], that has an iron-iron distance similar to **5.1**, does not show catalytic waves under the same conditions even when ferrocene is added. At this stage we do not have a clear view of the likely mechanism operating. It has been proposed [1] and examined theoretically [3] that $\mathbf{5A}^{2+}$ heterolytically cleaves H_2 to afford a terminal hydride and nitrogen-bound proton. This clearly cannot occur in the case of **5.1** and thus we tentatively propose the intermediate formation of a cationic dihydride as shown in Scheme 5.5.

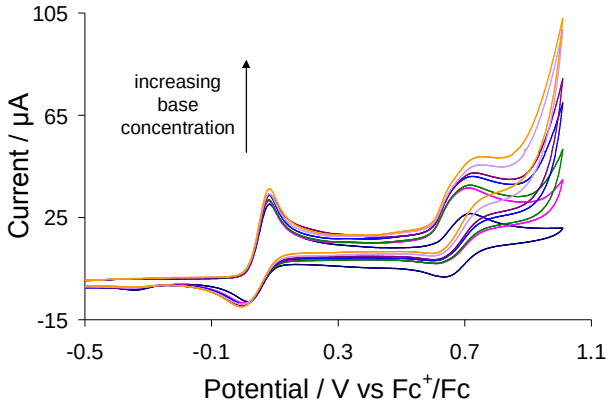

Figure 5.7. CVs of $Fe_2(CO)_4$(µ-dppf)(µ-pdt) (**5.1**) in the absence of pyridine and in the presence of 1 (pink), 2 (green), 4 (blue), 6 (violet), 8 (lavender) and 10 (light orange) molar equivalents of pyridine under H_2 atmosphere (1 mM solution in MeCN, supporting electrolyte $[NBu_4][PF_6]$, scan rate 0.1 Vs^{-1}, glassy carbon electrode, potential *vs* Fc^+/Fc).

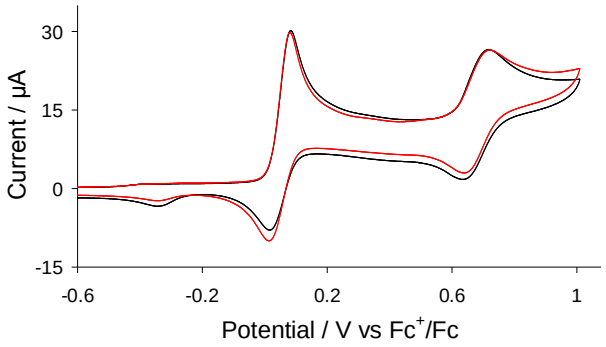

Figure 5.8. CVs of $Fe_2(CO)_4$(µ-dppf)(µ-pdt) (**5.1**) in the absence of hydrogen (black) and in the presence of hydrogen (red) (1 mM solution in MeCN, supporting electrolyte $[NBu_4][PF_6]$, scan rate 0.1 Vs^{-1}, glassy carbon electrode, potential *vs* Fc^+/Fc).

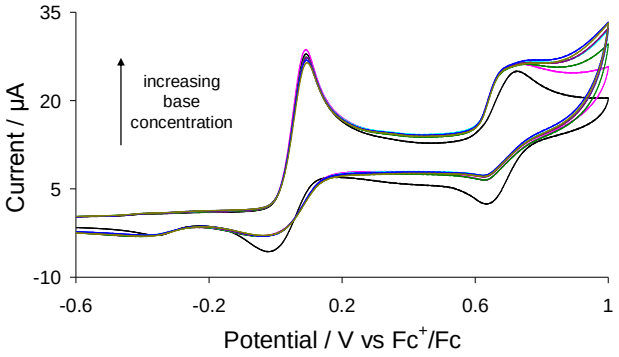

Figure 5.9. CVs of $Fe_2(CO)_4$(µ-dppf)(µ-pdt) (**5.1**) in the absence of pyridine and in the presence of 1, 2, 4, 6, 8 and 10 molar equivalents of pyridine (1 mM solution in MeCN, supporting electrolyte $[NBu_4][PF_6]$, scan rate 0.1 Vs^{-1}, glassy carbon electrode, potential *vs* Fc^+/Fc).

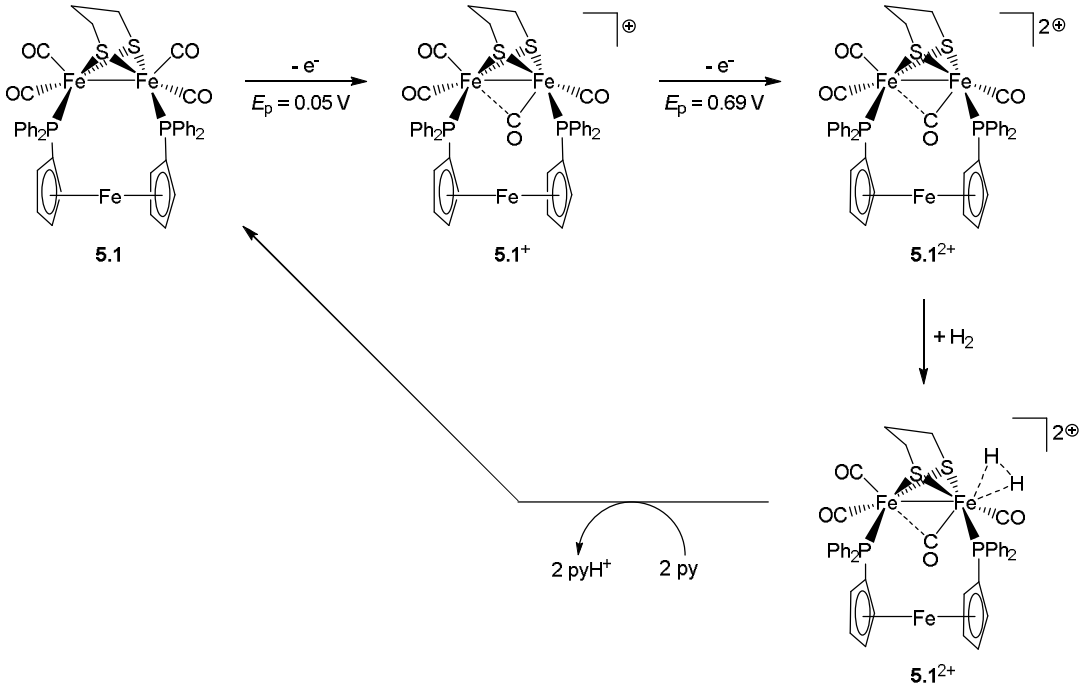

Scheme 5.5. Proposed mechanism for electrocatalytic H_2 oxidation by $Fe_2(CO)_4(\mu\text{-dppf})(\mu\text{-pdt})$ (**5.1**).

5.3. Summary and conclusions

The diiron biomimic $Fe_2(CO)_4(\mu\text{-dppf})(\mu\text{-pdt})$ (**5.1**) which contains a bridging dppf ligand has been synthesized and structurally characterized. Complex **5.1** reversibly protonates across the iron-iron bond to form the bridging hydride species $[Fe_2(CO)_4(\mu\text{-H})(\mu\text{-dppf})(\mu\text{-pdt})][BF_4]$ (**5.2**). It undergoes two irreversible reductions at the diiron centre together with two reversible oxidations. Experimental and theoretical studies show that the first oxidative process is centred at the diiron core whilst the second electron comes from the dppf iron. We have shown that **5.1** can catalyse both the reduction of protons and H_2 oxidation depending on the electrocatalytic environment. It catalyses H_2 formation from $HBF_4{\cdot}Et_2O$ whereas catalytically oxidizes H_2 in presence of pyridine.

We have also used $Fe_2(CO)_4(\mu\text{-}Ph_2PCH_2PPh_2)(\mu\text{-pdt})$ [28,33] and $Fe_2(CO)_4\{\mu\text{-}Ph_2P(CH_2)_4PPh_2\}(\mu\text{-pdt})$ [28] for electrocatalytic H_2 oxidation under similar conditions, but neither of them is catalytically active. The iron-iron distance in $Fe_2(CO)_4\{\mu\text{-}Ph_2P(CH_2)_4PPh_2\}(\mu\text{-pdt})$ [28] is similar to that of **5.1** which suggests that additional electronic influence of dppf plays key role during H_2 oxidation by the later. We assume that akin to **5A**, an intra-molecular electron transfer from the diiron centre to ferrocene

iron in **5.1** facilitates catalytic turnover for H_2 oxidation. We are currently developing a range of related biomimetics containing different secondary redox-active centres [50] and using density functional theory calculations in order to fully understand the electronic structure of **5.1**$^{2+}$ and the nature of the H_2 oxidation process.

5.4. Experimental

5.4.1. General. All reactions were carried out using standard Schlenk-line techniques under N_2 and reaction solvents were purified on alumina columns. Work-up was done in air using standard bench reagents. $Fe_2(CO)_6(\mu\text{-pdt})$ (**1.1**) [51] was prepared by standard procedures and dppf was purchased from Aldrich and used as supplied. NMR spectra were recorded on a Bruker AMX400 spectrometer and referenced internally to the residual solvent peak (^{1}H) or externally to $P(OMe)_3$ (^{31}P). Infrared spectra were recorded on a Nicolet 205 FT-IR spectrometer in a solution cell fitted with calcium fluoride plates, subtraction of the solvent absorptions being achieved by computation.

5.4.2. Synthesis of $Fe_2(CO)_4(\mu\text{-dppf})(\mu\text{-pdt})$ (5.1). A mixture of **1.1** (100 mg, 0.26 mmol) and dppf (140 mg, 0.26 mmol) in toluene (100 mL) was heated at reflux for 5 d resulting in a colour change from orange to red-brown. After cooling to room temperature, volatiles were removed under reduced pressure to give a dark oily red residue. This was washed with hexanes (3 × 5ml) and dried. Extraction into a minimum volume of dichloromethane followed by addition of hexanes and rotary evaporation gave $Fe_2(CO)_4(\mu\text{-dppf})(\mu\text{-pdt})$ (**5.1**) as a dry red solid (120 mg, 52%). Complex **5.1** can also be prepared upon heating a mixture of $\{Fe_2(CO)_5(\mu\text{-pdt})\}_2(\mu,\kappa^1,\kappa^1\text{-dppf})$ [39] and dppf in toluene over a similar period. The reaction time can be reduced significantly by conducting the reaction in refluxing xylene, but it leads to decrease in yield. This reaction when carried out in refluxing xylene affords **5.1** in only 11% yield (26 mg). IR ν(CO)(CH_2Cl_2): 1986s, 1949vs, 1918s 1896w cm^{-1}. ^{1}H NMR ($CDCl_3$): δ 8.01 (t, J 8.2, 2H, Ph), 7.67-6.99 (m, 18H, Ph), 4.93 (brs, 2H, CH), 4.46 (s, 2H, CH), 4.44 (s, 2H, CH), 4.01 (s, 2H, CH), 2.60 (br, 2H, CH_2), 2.31 (m, 2H, CH_2), 2.13 (br, 2H, CH_2). ^{31}P{^{1}H}NMR ($CDCl_3$): δ 51.3 (s) ppm. Elemental analysis calc. for $C_{41}H_{35}Fe_3O_4P_2S_2\cdot 0.5CH_2Cl_2$ (found): C 54.16 (53.41), H 3.81 (3.75).

Crystallographic data for $Fe_2(CO)_4(\mu\text{-dppf}\}(\mu\text{-pdt})$ (**5.1**).0.5CH_2Cl_2: red block, dimensions 0.38 × 0.32 × 0.16 mm, triclinic, space group *P1bar*, *a* = 9.737(2), *b* =

13.149(3), c = 16.654(3) Å, α = 99.609(3), β = 94.376(3), γ = 111.343(3)^{o}, V = 1936.1(7) Å^{3}, Z = 2, F(000) 944, d_{calc} = 1.588 g cm^{-3}, μ = 1.411 mm^{-1}. 16800 reflections were collected, 8886 unique [R(int) = 0.0333] of which 8134 were observed [$I > 2.0\sigma(I)$]. At convergence, R_1 = 0.0345, wR_2 = 0.0911 [$I > 2.0\sigma(I)$] and R_1 = 0. 0374, wR_2 = 0.0929 (all data), for 511 parameters.

5.4.3. Synthesis of [$Fe_2(CO)_4$(μ-H)(μ-dppf)(μ-pdt)][BF_4] (5.2). To a CH_2Cl_2 (50 mL) solution of **2** (50 mg, 0.06 mmol) was added a few drops of $HBF_4 \cdot Et_2O$. The mixture was stirred at room temperature for 20 min without any noticeable change. Volatiles were removed under reduced pressure and the resulting deep red oily solid washed with a small portion of Et_2O to remove excess acid. The remaining solid was dissolved in a minimum amount of CH_2Cl_2 which was then layered with hexanes. Slow mixing of the solutions afforded [$Fe_2(CO)_4$(μ-H)(μ-dppf)(μ-pdt)][BF_4] (**5.2**) (40 g, 73%) as a dry red solid. IR ν(CO)(CH_2Cl_2): 2058s, 2040s, 2002s cm^{-1}. ^{1}H NMR ($CDCl_3$): δ 8.11-7.33 (m, 20H, Ph), 4.74 (s, 2H, CH), 4.68 (s, 2H, CH), 4.49 (s, 2H, CH), 4.32 (s, 2H, CH), 2.86 (br, 2H, CH_2), 2.74 (m, 2H, CH_2), 2.48 (br, 2H, CH_2), –12.40 (t, J 17.6, 1H, μ-H). ^{31}P{^{1}H} NMR (CD_2Cl_2): δ 44.8 (s) ppm.

5.5. References

(1) J.M. Camara and T.B. Rauchfuss, *Nat. Chem.*, 2012, **4**, 26-30.

(2) C. Tard, X.M. Liu, S.K. Ibrahim, M. Bruschi, L. De Gioia, S.C. Davies, X. Yang, L.S. Wang, G. Sawers and C.J. Pickett, *Nature*, 2005, **433**, 610-613.

(3) C. Greco, *Inorg. Chem.*, 2013, **52**, 1901-1908.

(4) Y. Si, K. Charreteur, J.-F. Capon, F. Gloaguen, F.Y. Pétillon, P. Schollhammer and J. Talarmin, *J. Inorg. Biochem.*, 2010, **104**, 1038-1042.

(5) C. Gimbert-Suriñach, M. Bhadbhade and S. B. Colbran, *Organometallics*, 2012, **31**, 3480-3491.

(6) Y.-C. Liu, C.-H. Lee, G.-H. Lee and M.-H. Chiang, *Eur. J. Inorg. Chem.*, 2011, 1155-1162.

(7) C. Greco and L. De Gioia, *Inorg. Chem.*, 2011, **50**, 6987-6995.

(8) P.-Y. Orain, J.-F. Capon, F. Gloaguen, F.Y. Pétillon, P. Schollhammer, J. Talarmin, G. Zampella, L. De Gioia and T. Roisnel, *Inorg. Chem.*, 2010, **49**, 5003-5008.

(9) S. Ezzaher, P.-Y. Orain, J.-F. Capon, F. Gloaguen, F. Pétillon, T. Roisnel, P. Schollhammer and J. Talarmin, *Chem. Commun.*, 2008, 2547-2549.

(10) P.-Y. Orain, J.-F. Capon, N. Kervarec, F. Gloaguen, F. Pétillon, R. Pichon, P. Schollhammer and J. Talarmin, *Dalton Trans.*, 2007, 3754-3756.

(11) S. Roy, T.L. Groy and A. K. Jones, *Dalton Trans.*, 2013, **42**, 3843-3853.

(12) G. B. Hall, J. Chen, C. A. Mebi, N. Okumura, M. T. Swenson, S. E. Ossowski, U. I. Zakai, G. S. Nichol, D. L. Lichtenberger, D. H. Evans and R. S. Glass, *Organometallics*, 2013, **32**, 6605-6612.

(13) J. W. Peters, W. N. Lanzilotta, B. J. Lemon and L. C. Seefeldt, *Science*, 1998, **282**, 1853-1858.

(14) Y. Nicolet, C. Piras, P. Legrand, C. E. Hatchikian and J. C. Fontecilla-Camps, *Structure* **1999**, *7*, 13-23.

(15) M. Bruschi, C. Greco, P. Fantucci and L. De Gioia, *Inorg. Chem.*, 2008, **47**, 6056-6071.

(16) D. E. Schwab, C. Tard, E. Brecht, J. W. Peters, C. J. Pickett and R. K. Szilagyi, *Chem. Commun.*, 2006, 3696-3698.

(17) N. G. Connelly and W. E. Geiger, *Chem. Rev.*, 1996, **96**, 877-922.

(18) J. C. Gordon and G. J. Kubas, *Organometallics*, 2010, **29**, 4682-4701.

(19) C. Greco, G. Zampella, L. Bertini, M. Bruschi, P. Fantucci and L. De Gioia, *Inorg. Chem.*, 2007, **46**, 108-116.

(20) J. M. Camara and T. B. Rauchfuss, *J. Am. Chem. Soc.*, 2011, **133**, 8098-8101.

(21) K. S. Gan and T. S. A. Hor, In *Ferrocenes*, A. Togni and T. Hayashi (Eds.), VCH, New York, 1995.

(22) N. G. Connelly and W. E. Geiger, *Adv. Organomet. Chem.*, 1984, **23**, 1-93.

(23) D. L. DuBois, C. W. Eigenbrot, Jr., A. Miedaner and J. C. Smart, *Organometallics*, 1986, **5**, 1405-1411.

(24) R. T. Hembre, J. S. McQueen and V. W. Day, *J. Am. Chem. Soc.*, 1996, **118**, 798-803.

(25) C. Nataro, A. N. Campbell, M. A. Ferguson, C. D. Incarvito and A. L. Rheingold, *J. Organomet. Chem.*, 2003, **673**, 47-55 and references therein.

(26) G. Pilloni, B. Longato and B. Corain, *J. Organomet. Chem.*, 1991, **420**, 57-65.

(27) B. Corain, B. Longato, G. Favero, D. Ajò, G. Pilloni, U. Russo and F. R. Kreissl, *Inorg. Chim. Acta*, 1989, **157**, 259-266.

(28) F. I. Adam, G. Hogarth, S. E. Kabir and I. Richards, *C.R. Chim.*, 2008, **11**, 890-905.

(29) S. Ghosh, G. Hogarth, N. Hollingsworth, K. B. Holt, I. Richards, M. G. Richmond, B. E. Sanchez, D. Unwin, *Dalton Trans.*, 2013, **42**, 6775-6792.

(30) N. Wang, M. Wang, T. Liu, T. Zhang, M. Darensbourg and L. Sun, *Inorg. Chem.*, 2008, **47**, 6948-6955.

(31) N. Wang, M. Wang, J. Liu, K. Jin, L. Chen and L. Sun, *Inorg. Chem.*, 2009, **48**, 11551-11558.

(32) S. Ezzaher, J.-F. Capon, F. Gloaguen, F. Y. Pétillon, P. Schollhammer and J. Talarmin, *Inorg. Chem.*, 2007, **46**, 9863-9872.

(33) F. I. Adam, G. Hogarth and I. Richards, *J. Organomet. Chem.*, 2007, **692**, 3957-3968.

(34) L.-C. Song, H.-T. Wang, J.-H. Ge, S.-Z. Mei, J. Gao, L.-X. Wang, B. Gai, L.-Q. Zhao, J. Yan and Y.-Z. Wang, *Organometallics*, 2008**, 27**, 1409-1416.

(35) W. Gao, J. Ekström, J. Liu, C. Chen, L. Eriksson, L. Weng, B. Åkermark, L. Sun, *Inorg. Chem.*, 2007, **46**, 1981-1991.

(36) L.-C. Song, C.-G. Li, J.-H. Ge, Z.-Y. Yang, H.-T. Wang, J. Zhang and Q.-M. Hu, *J. Inorg. Biochem.*, 2008, **102**, 1973-1979.

(37) F. Ridley, S. Ghosh, G. Hogarth, N. Hollingsworth, K. B. Holt and D. G. Unwin, *J. Electroanal. Chem.*, 2013, **703**, 14-22.

(38) G. Hogarth, S. E. Kabir and I. Richards, *Organometallics*, 2010, **29**, 6559-6568.

(39) X.-F. Liu and B.-S. Yin, *J. Coord. Chem.*, 2010, **63**, 4061-4067.

(40) M. E. Carroll, B. E. Barton, T. B. Rauchfuss and P. J. Carroll, *J. Am. Chem. Soc.*, 2012, **134**, 18843-18852.

(41) D. Cauzzi, C. Graiff, C. Massera, G. Predieri, A. Tiripicchio and D. Acquotti, *J. Chem. Soc., Dalton Trans.*, 1999, 3515-3521.

(42) N. Begum, U. K. Das, M. Hassan, G. Hogarth, S. E. Kabir, E. Nordlander, M. A. Rahman and D. A. Tocher, *Organometallics*, 2007, **26**, 6462-6472.

(43) C. Greco, P. Fantucci, L. De Gioia, R. Suarez-Bertoa, M. Bruschi, J. Talarmin and P. Schollhammer, *Dalton Trans.*, 2010, **39**, 7320-7329.

(44) S. Ezzaher, J.-F. Capon, F. Gloaguen, F. Y. Pétillon, P. Schollhammer and J. Talarmin, *Inorg. Chem.*, 2007, **46**, 3426-3428.

(45) A. K. Justice, G. Zampella, L. D. Gioia and T. B. Rauchfuss, *Chem. Commun.*, 2007, 2019-2021.

(46) B. E. Barton and T. B. Rauchfuss, *Inorg. Chem.*, 2008, **47**, 2261-2263.

(47) G. A. N. Felton, R. S. Glass, D. L. Lichtenberger and D. H. Evans, *Inorg. Chem.*, 2006, **45**, 9181-9184.

(48) R. Mejia-Rodriguez, D. Chong, J. H. Reibenspies, M. P. Soriaga and M. Y. Darensbourg, *J. Am. Chem. Soc.*, 2004, **126**, 12004-12014.

(49) A. Jablonskyté, J. A. Wright, S. A. Fairhurst, J. N. T. Peck, S. K. Ibrahim, V. S. Oganesyan and C. J. Pickett, *J. Am. Chem. Soc.*, 2011, **133**, 18606-18609.

(50) O. R. Luca and R. H. Crabtree, *Chem. Soc. Rev.*, 2013, **42**, 1440-1459.

(51) A. Winter, L. Zsolnai and G. Huttner, *Z. Naturforsch.*, 1982, **37b**, 1430-1436.

Chapter 6

Electrocatalytic Proton Reduction by $Fe(CO)_2(\kappa^2\text{-dppv})(\kappa^1\text{-SR})_2$ (dppv = bis(diphenylphosphino)ethylene; R = C_6F_5, C_6H_5, $C_6H_4CH_3$-*p*)

6.1. Introduction

Besides tremendous resurging interest in the chemistry of dithiolato-bridged diiron complexes as models of the active site of [FeFe]-hydrogenase, complexes containing other base metals especially cobalt and nickel have also been widely investigated as potential electrocatalysts for proton reduction (Chapter 1). Almost all these cobalt and nickel complexes contain a single metal centre and are able to catalyse proton reduction at relatively mild overpotentials [1-24] when compared to diiron biomimics [25]. A number of these are also active in an aqueous medium [1,5-11,17], with some impressive turnover numbers being recently reported [21,22]. In comparison, little attention has been paid to mononuclear iron complexes [26-31], even though the iron-porphyrin complex, [(TPP)Fe(Cl)] (TPP = tetraphenylporphyrin), was found to catalyse proton reduction at reasonable catalytic rates as early as 1996 [26].

Recently, the proton reduction ability of mononuclear iron complexes has been tested by several groups [27-33]. Winkler and co-workers used fluorinated diglyoxime-iron complexes [27], whereas Artero and Fontecave used a cyclopentadienyl complex as catalyst [28]. Very recently an iron polypyridyl complex was found to catalyse hydrogen formation from aqueous solutions with a turnover frequency of up to 3000 s^{-1} [33]. The catalytic pathway(s) for all these 18-electron complexes is proposed to involve the loss of a coordinated ligand upon reduction to create a vacant coordination site in order to accommodate the incoming protons [27,28]. In contrast, the mononuclear iron catalysts developed by Ott and co-workers [29], which show close structural resemblance to the distal iron of the active site of [FeFe]-hydrogenase (Chart 6.1), work in a different manner. These octahedral complexes undergo reversible protonation, proposed to take place at sulphur. They show two catalytic waves with different turnover rates upon addition of acid, indicating that hydrogen production occurs *via* two pathways involving different oxidation states of the catalyst [29]. Mechanistic and theoretical studies support a mechanism according to which protonation at sulphur followed by an one-electron

reduction results in Fe–S bond scission to form a penta-coordinated iron(II) intermediate (Scheme 6.1).

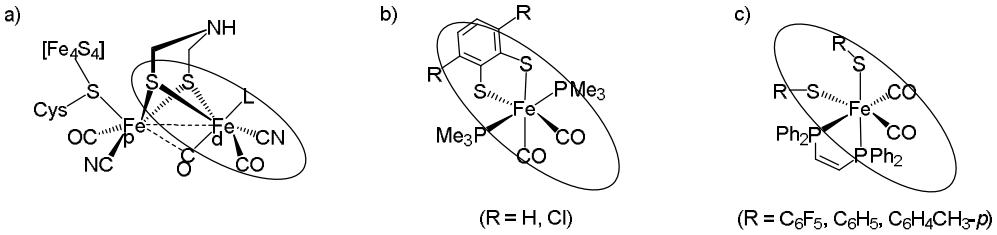

Chart 6.1. a) The active site of the [FeFe] H_2ases enzyme, b) model complexes studied by Ott [29] and c) model complexes studied by us (presented in this chapter). Structural similarities between the distal iron centre and the model complexes are highlighted.

This intermediate either protonates at metal centre and undergoes subsequent reduction at the same potential or reduces at a more negative potential followed by protonation at metal centre to give a neutral hydride species. Interaction between the basic iron-bound hydride and the acidic sulphur-bound hydrogen leads to the formation of molecular hydrogen and give back the catalyst thereby completing the catalytic cycle.

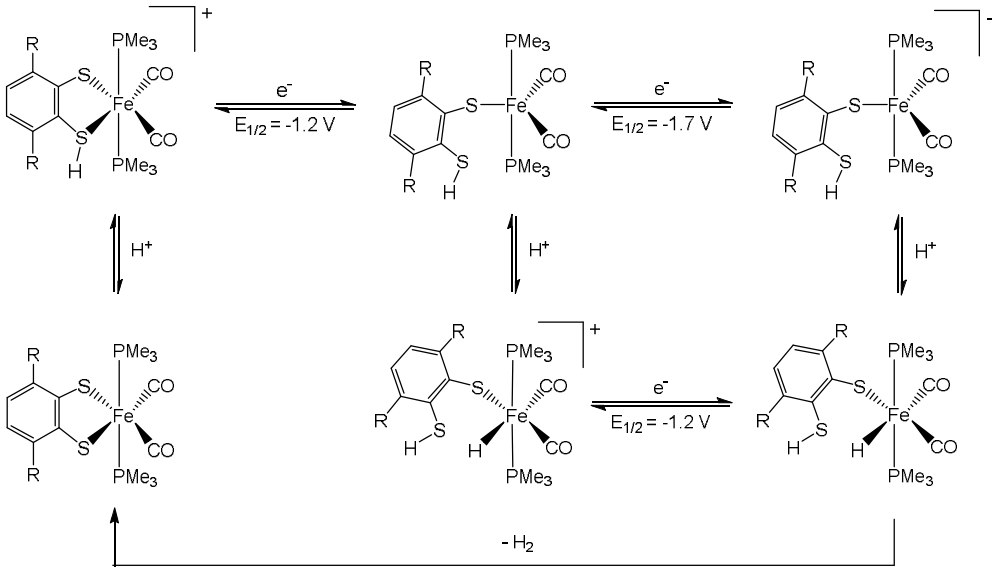

Scheme 6.1. Catalytic mechanism proposed for $Fe(CO)_2(PMe_3)_2(\kappa^2\text{-}SC_6H_2R_2S)$ (R = H, Cl) [29].

Since a vacant coordination site is necessary to reduce proton at the iron centre, a number of square-pyramidal 16-electron iron complexes have also been tested by Ott [30,31] and Jones [32] which will be discussed further in the following chapter. Recently, we have

reported electrocatalytic proton reduction by the diiron bis(thiolate) complex, $Fe_2(CO)_6(\mu\text{-}SC_6F_5)_2$ [34], and in an attempt to make the bis(diphenylphosphino)ethylene (dppv) chelate of this complex we serendipitously obtained mononuclear $Fe(CO)_2(\kappa^2\text{-dppv})(\kappa^1\text{-}SC_6F_5)_2$ (**6.1**). Complex **6.1** is structurally similar to $Fe(CO)_2(PMe_3)_2(\kappa^2\text{-}SC_6H_2R_2S)$, so we have decided to test its proton reduction ability together with that of the analogous phenyl- and *p*-tolyl-thiolate complexes, $Fe(CO)_2(\kappa^2\text{-dppv})(\kappa^1\text{-}SC_6H_5)_2$ (**6.2**) and $Fe(CO)_2(\kappa^2\text{-dppv})(\kappa^1\text{-}SC_6H_4CH_3\text{-}p)_2$ (**6.3**).

6.2. Results and discussion

6.2.1. Synthesis and characterisation. Complexes **6.1**-**6.3** were synthesized from direct reactions of the corresponding hexacarbonyl $Fe_2(CO)_6(\mu\text{-SR})_2$ and *cis*-1,2-bis(diphenylphosphino)ethylene (dppv) at elevated temperatures (Scheme 6.2). They are fairly air-stable in solid-state but decompose in solution when exposed to air. Air stability in solution decreases with increasing electron-donating ability of the thiolate, with **6.1** being the most stable.

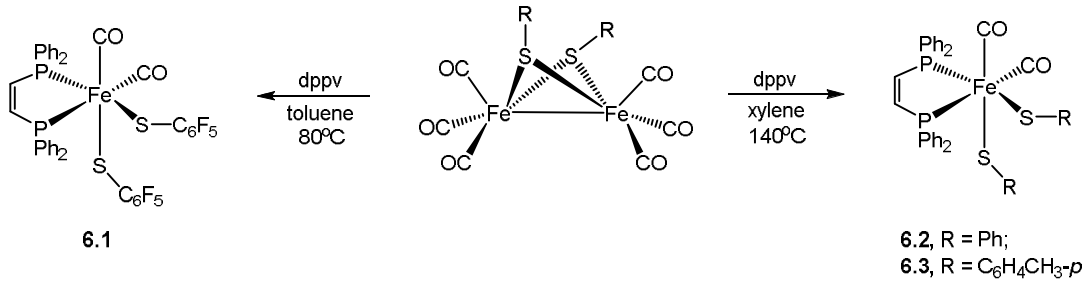

Scheme 6.2. Synthesis of $Fe(CO)_2(\kappa^2\text{-dppv})(\kappa^1\text{-SR})_2$ complexes (**6.1**-**6.3**).

IR spectra of **6.1**-**6.3** show two strong absorption bands in the carbonyl stretching region indicating that the carbonyl ligands are in *cis*-orientation relative to each other which is also confirmed by X-ray crystallography (see later). Their $^{31}P\{^1H\}$-NMR spectra indicate presence of two isomers in solution, with each consisting of two doublets and a singlet. Three isomers are possible for this type of complexes as shown in Chart 6.2. The major isomer is **6A** in which the two phosphorus atoms are non-equivalent being responsible for the appearance of two doublets in the $^{31}P\{^1H\}$-NMR spectrum. In both **6B** and **6C** phosphorus atoms are equivalent, thus we should expect a singlet in the $^{31}P\{^1H\}$-NMR spectrum for both. We assume that the minor isomer adopts **6B** configuration since **6C** is

electronically less favourable as the two strong π-acid ligands (carbonyls) are in *trans*-orientation which is most unlikely. The amount of the minor isomer (**6B**) increases with the electron-donating ability of the thiolate and the **6A**/**6B** ratio is found to be 20:1, 13:1 and 4:1 for **6.1**, **6.2** and **6.3**, respectively. VT NMR studies of **6.1** and **6.3** show that the isomeric ratio does not change with temperature.

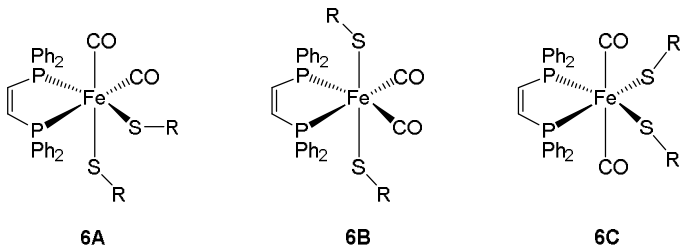

Chart 6.2. Three possible isomers of $Fe(CO)_2(\kappa^2\text{-dppv})(\kappa^1\text{-SR})_2$.

The solid-state structures of **6.1**-**6.3** show that they all have a similar structure and crystallise in the **6A** (Chart 6.2) isomeric form, which is also the predominant species in solution. Unfortunately disorders associated with residual solvent in **6.1** and the phenyl rings of the thiolate ligands in **6.2** lead to poor overall structural models which preclude a detailed discussion of structural parameters. Nevertheless, the structures provide sufficient information about the geometry of the molecule and the orientation of the ligands and are shown in Figures 6.1 and 6.2. In both, the iron adopts a distorted octahedral geometry with the carbonyls and thiolate ligands in mutually *cis*-orientations.

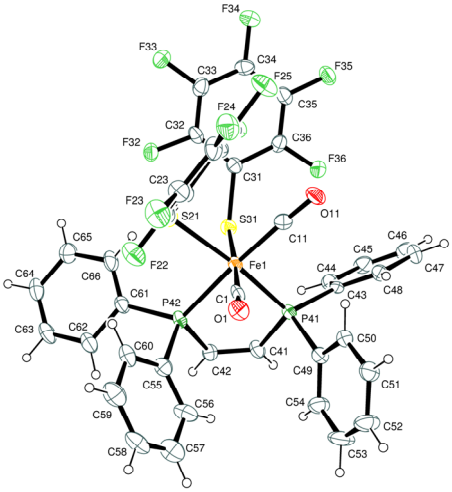

Figure 6.1. An ORTEP diagram of the molecular structure of $Fe(CO)_2(\kappa^2\text{-dppv})(\kappa^1\text{-SC}_6F_5)_2$ (**6.1**) showing 50% thermal ellipsoids.

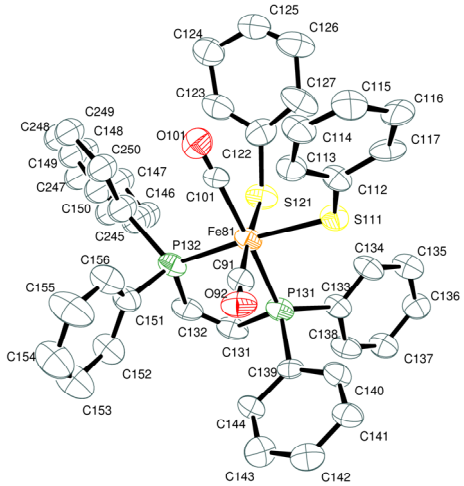

Figure 6.2. An ORTEP diagram of the molecular structure of $Fe(CO)_2(\kappa^2\text{-dppv})(\kappa^1\text{-SC}_6H_5)_2$ (**6.2**) showing 50% thermal ellipsoids.

We obtained a better quality crystal structure of **6.3** which is shown in Figure 6.3, with the caption containing selected bond lengths and angles. Complex **6.3** consists of a single iron atom coordinated by a *cis*-dppv, two carbonyls and two *p*-tolylthiolate ligands. Both the carbonyls and the thiolate ligands adopt *cis*-configuration. The coordination geometry around iron can be best described as a distorted octahedron, which is evident from the reduction of P–Fe–P chelate angle and expansion of the S–Fe–S angle from 90° in the idealized polyhedron to 86.33(2)° and 94.03(2)° respectively. The Fe–CO bond distance *trans* to the thiolate ligand [Fe(1)–C(1) 1.776(2) Å] is slightly shorter than that *trans* to phosphine Fe(1)–C(11) 1.798(3) Å] as the thiolate ligand is a better σ-donor than phosphine which improve back-bonding between iron and carbonyl. The Fe–P and Fe–S bond lengths in **6.3** are similar to those reported for related complexes [35].

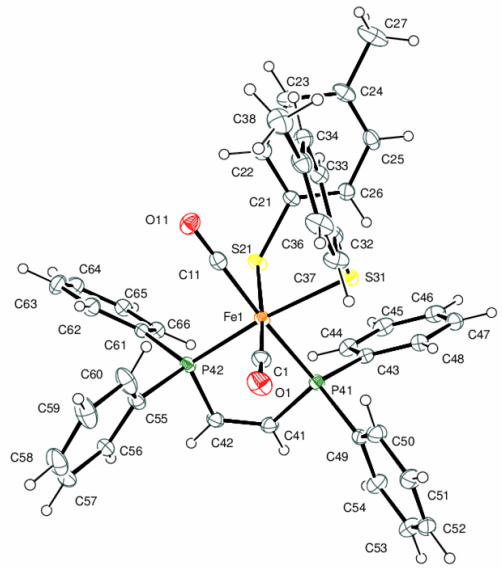

Figure 6.3. An ORTEP diagram of the molecular structure of $Fe(CO)_2(\kappa^2\text{-dppv})(\kappa^1\text{-}SC_6H_4CH_3\text{-}p)_2$ (**6.3**) showing 50% thermal ellipsoids. Selected bond lengths (Å) and angles(°): Fe(1)–C(1) 1.776(2), Fe(1)–C(11) 1.798(3), Fe(1)–P(41) 2.2756(7), Fe(1)–P(42) 2.2415(6), Fe(1)–S(21) 2.3722(5), Fe(1)–S(31) 2.3547(6), P(41)–Fe(1)–P(42) 86.33(2), S(21)–Fe(1)–S(31) 94.03(2), C(1)–Fe(1)–C(11) 93.60(10), C(1)–Fe(1)–P(41) 94.17(8), S(21)–Fe(1)–P(42) 85.58(2), S(21)–Fe(1)–C(1) 174.94(8), S(31)–Fe(1)–P(42) 172.68(3), C(11)–Fe(1)–P(41) 172.21(6).

6.2.2. Electrochemistry. The electrochemical response of **6.1**-**6.3** was monitored by cyclic voltammetry in MeCN. Complex **6.1** complex shows a quasi-reversible reduction at $E_{1/2}$ = –1.43 V followed by an irreversible reduction at E_p = –2.46 V (Figure 6.4). The reversibility of the first reduction does not improve when the scan rate is varied. It also

exhibits an oxidation at E_p = 0.80 V which shows some reversibility at slow scan rates (≤ 0.5 V/s). The related iron dithiolate complexes, $Fe(CO)_2(PMe_3)_2(\kappa^2\text{-}SC_6H_2R_2S)$ (R = H, Cl), show a reversible oxidation and two irreversible reductions in MeCN assigned to the $Fe^{II/III}$, $Fe^{II/I}$ and $Fe^{I/0}$ couples, respectively [29]. Likewise, we attributed the oxidation of **6.1** to the $Fe^{II/III}$ couple and the reductions to the $Fe^{II/I}$ and $Fe^{I/0}$ couples, respectively.

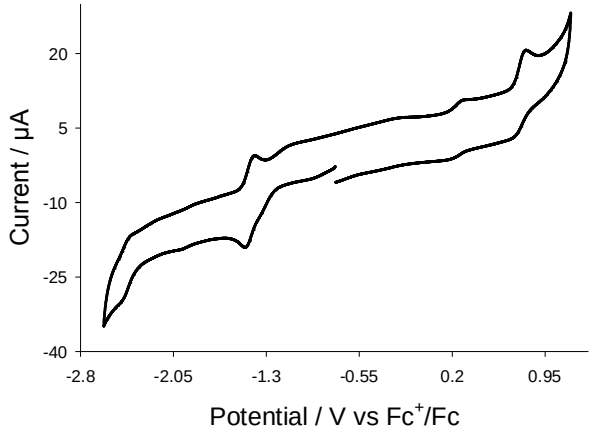

Figure 6.4. CV of $Fe(CO)_2(\kappa^2\text{-dppv})(\kappa^1\text{-}SC_6F_5)_2$ (**6.1**) in MeCN (0.5 mM solution, supporting electrolyte $[NBu_4][PF_6]$, scan rate 0.1 Vs^{-1}, glassy carbon electrode, potential vs Fc^+/Fc).

The CV of **6.2** shows a quasi-reversible reduction at $E_{1/2}$ = –1.55 V followed by a second reduction at E_p = –2.03 V (Figure 6.5). A small quasi-reversible reductive feature is also observed at $E_{1/2}$ = –2.34 V. The reversibility of the second reduction improved at higher scan rates (≥ 0.5 Vs^{-1}). The first oxidation of **6.2** occurs at E_p = –0.19 V, a *ca.* 1 V negative shift compared to the oxidation potential of **6.1**, which is followed by two more oxidations at E_p = 0.20 V and E_p = 0.45.

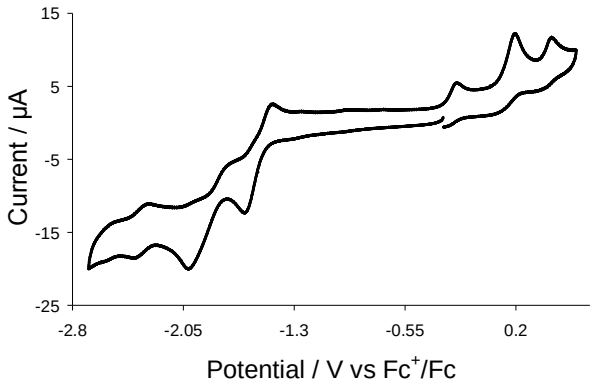

Figure 6.5. CV of $Fe(CO)_2(\kappa^2\text{-dppv})(\kappa^1\text{-SPh})_2$ (**6.2**) in MeCN (0.5 mM solution, supporting electrolyte $[NBu_4][PF_6]$, scan rate 0.1 Vs^{-1}, glassy carbon electrode, potential vs Fc^+/Fc).

Complex **6.3** undergoes a quasi-reversible reduction at $E_{1/2}$ = –1.49 V followed by two small irreversible reductive features at E_p = –2.05 and –2.27 V (Figure 6.6). It undergoes two irreversible oxidations at E_p = 0.06 and 0.69 V. No significant change was observed when the scan rate was varied.

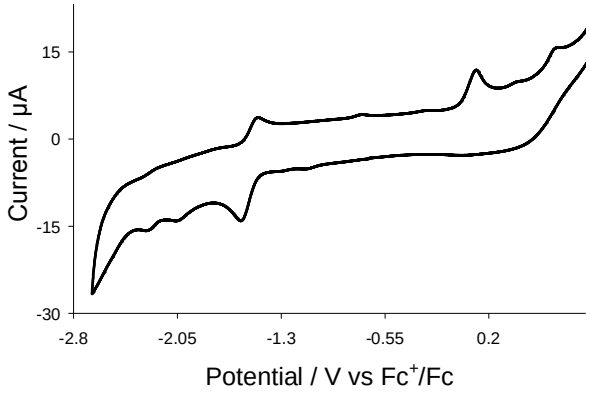

Figure 6.6. CV of $Fe(CO)_2(\kappa^2\text{-dppv})(\kappa^1\text{-}SC_6H_4CH_3\text{-}p)_2$ (**6.3**) in MeCN (0.5 mM solution, supporting electrolyte $[NBu_4][PF_6]$, scan rate 0.1 Vs^{-1}, glassy carbon electrode, potential vs Fc^+/Fc).

The CVs of **6.1**-**6.3** show that their redox response is highly sensitive to the nature of thiolate ligand. As expected, **6.1** with electron-withdrawing fluorine atoms in the thiolate moiety, reduces at least negative potential but its oxidation potential is the most positive. Although the redox features in their CVs are quite different from each other, all undergo a quasi-reversible reduction assigned to $Fe^{II/I}$ couple. CVs of **6.2** and **6.3** are relatively complex compared to that of **6.1** probably due to the increasing amount of *trans*-isomer (with respect to thiolate, **6B**, Chart 6.2) in solution.

6.2.3. Reactions with acid. The reactions of **6.1**-**6.3** with acid were carried out using $HBF_4{\cdot}Et_2O$. Addition of $HBF_4{\cdot}Et_2O$ to a CH_2Cl_2 solution of **6.1** at room temperature resulted in a colour change from red to yellow. Absorptions at 2037 and 1993 cm^{-1} for the neutral complex were replaced by two new features at 2062 and 2017 cm^{-1} (Figure 6.7). The small blue shift (25 cm^{-1}) of the highest energy absorption suggests that protonation has occurred at the sulphur atom(s) [29]. Within a few minutes these bands diminished with concomitant appearance of new absorptions at 2100, 2064 and 2024 cm^{-1} suggesting further structural change. The 63 cm^{-1} blue shift of the highest energy absorption observed for this species indicates that iron loses significant amount of electron-density during the process. We assume that after protonation at sulphur a penta-coordinated cationic species formed by loss of C_6F_5SH from $\mathbf{6.1H^+}$ (Scheme 6.3). The

trigonal bipyramidal complexes are generally fluxional in solution, so the resultant species may exhibit different isomeric forms in solution. As far as we are aware, there is no precedence of such cationic penta-coordinated species of iron reflecting the instability of this type of species. Protonation of **6.1** at sulphur is reversible as the original infrared spectrum can be recovered upon addition of PPh_3 to the protonated solution.

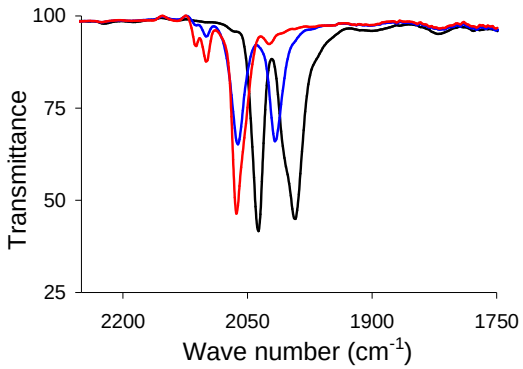

Figure 6.7. IR spectrum of $Fe(CO)_2(\kappa^2\text{-dppv})(\kappa^1\text{-}SC_6F_5)_2$ (**6.1**) in CH_2Cl_2 – in absence of acid (green), after addition of 2 equiv. of $HBF_4{\cdot}Et_2O$ (blue), after 5 min of acid addition (red).

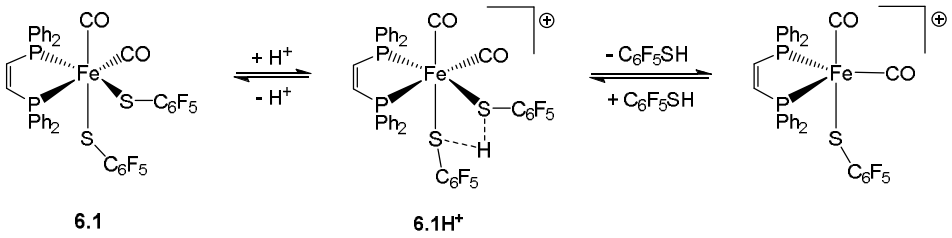

6.1 **6.1H⁺**

Scheme 6.3. Protonation of $Fe(CO)_2(\kappa^2\text{-dppv})(\kappa^1\text{-}SC_6F_5)_2$ (**6.1**) by $HBF_4{\cdot}Et_2O$.

Protonation of **6.2** is also accompanied by a colour change from red to yellow with the replacement of the absorptions at 2023 and 1978 cm^{-1} (for **6.2**) by three new absorptions at 2092, 2056 and 2019 cm^{-1} (Figure 6.8). In this case, we have not seen the absorption bands for $\mathbf{6.2H^+}$ which indicates that it is relatively unstable and loses C_6H_5SH after protonation much faster than $\mathbf{6.1H^+}$. Similar results were observed upon addition of $HBF_4{\cdot}Et_2O$ to CH_2Cl_2 solution of **6.3**; absorptions at 2020 and 1975 cm^{-1} were replaced by a new set at 2058, 2016 and 1990 cm^{-1}. Attempts to monitor protonation of these complexes *via* NMR spectroscopy were unsuccessful which we assume is due to the fluxionality and instability of the resulted penta-coordinated cationic species.

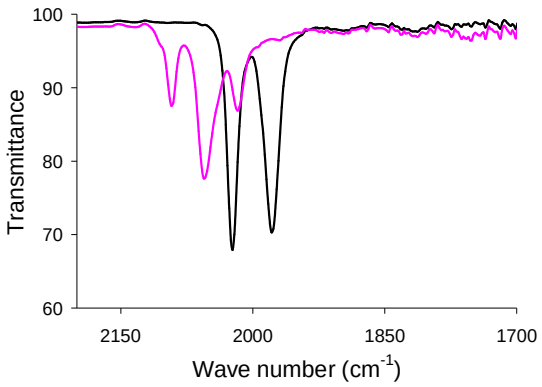

Figure 6.8. IR spectrum of $Fe(CO)_2(\kappa^2\text{-dppv})(\kappa^1\text{-}SC_6H_5)_2$ (**6.2**) in CH_2Cl_2 – in absence of acid (black) and after addition of 2 equiv. of $HBF_4{\cdot}Et_2O$ (pink).

6.2.4. Catalysis. Catalysis was carried out in MeCN using $HBF_4{\cdot}Et_2O$ as the proton source. The CV of **6.1** shows three new reduction peaks at E_p = –0.90, –1.25 V and –1.90 V upon addition of 1 molar equivalent of $HBF_4{\cdot}Et_2O$ (Figure 6.9). No oxidative wave is observed in the CV since the oxidation potential of **6.1** at E_p = 0.80 V is probably moved beyond the potential window of the solvent due to protonation at sulphur. The reduction potential of **6.1** also shows a *ca.* 0.5 V positive shift upon protonation. The peak current of the first reduction does not increase with the concentration of acid but that of the second and third waves increase sequentially as the concentration of acid is increased, characteristic of proton reduction at these potentials (Figure 6.10). The observation of two catalytic waves with distinct peak current suggests that hydrogen can be produced from the same acid *via* two pathways involving two different oxidation states of the catalyst [29].

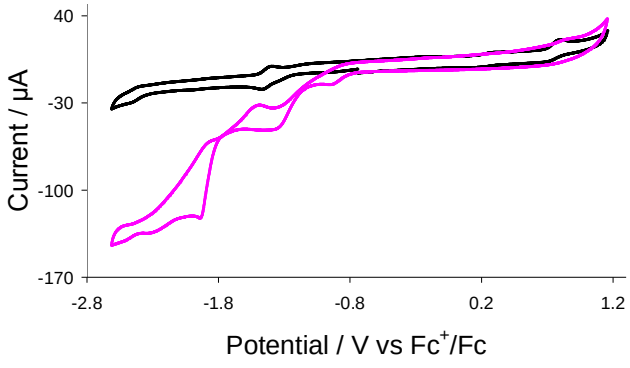

Figure 6.9. CVs of $Fe(CO)_2(\kappa^2\text{-dppv})(\kappa^1\text{-}SC_6F_5)_2$ (**6.1**) in the absence of acid (black) and in the presence of 1 molar equivalent of $HBF_4{\cdot}Et_2O$ (pink) (0.5 mM solution in acetonitrile, supporting electrolyte $[NBu_4][PF_6]$, scan rate 0.1 Vs^{-1}, glassy carbon electrode, potential vs Fc^+/Fc).

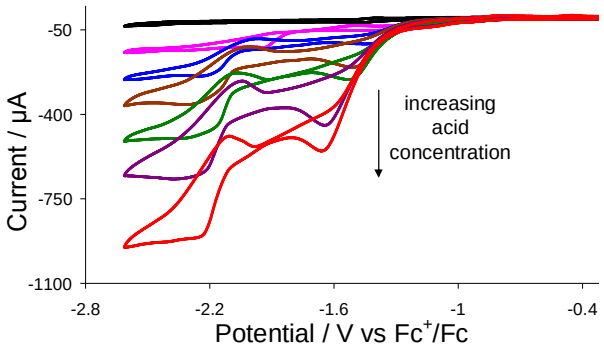

Figure 6.10. CVs of $Fe(CO)_2(\kappa^2\text{-dppv})(\kappa^1\text{-}SC_6F_5)_2$ (**6.1**) in the absence of acid (black) and in the presence of 1 (pink), 3 (blue), 5 (brown), 6 (green), 8 (violate) and 9 (red) molar equivalents of $HBF_4{\cdot}Et_2O$ (0.5 mM solution in acetonitrile, supporting electrolyte $[NBu_4][PF_6]$, scan rate 0.1 Vs^{-1}, glassy carbon electrode, potential vs Fc^+/Fc).

We proposed a plausible mechanism for electrocatalytic proton reduction by **6.1** as shown in Scheme 6.4 on the basis of spectroscopic and electrochemical data. The first step is the reversible protonation at sulphur followed by reduction at E_p = –0.90 V. This reduction is accompanied by loss of thiol to form **6.1B** [29], which reduces further at E_p = –1.25 V to give **6.1C**. The 17-electron penta-coordinated species **6.1B** has a vacant coordination site but it is not basic enough to bind a proton therefore undergoes a second reduction before reacting with acid. This explains why the height of the first reduction peak (E_p = –0.90 V) does not increase with acid concentration. Now the two electron reduced species **6.1C** can either protonate to form **6.1D** or undergoes a further reduction at E_p = –1.90 V to yield **6.1E** which protonates to give **6.1F**. Both **6.1D** and **6.1F** can release hydrogen *via* homolytic (bimolecular reaction, not shown in the mechanism) and/or heterolytic pathway that regenerate **6.1B** and **6.1C,** thereby completing the catalytic cycle. The peak height at the second catalytic wave increase more rapidly than that of the first wave indicating that the catalyst is more efficient at the potential of the second wave (Figure 6.11) akin to $Fe(CO)_2(PMe_3)_2(\kappa^2\text{-}SC_6H_2Cl_2S)$ [29].

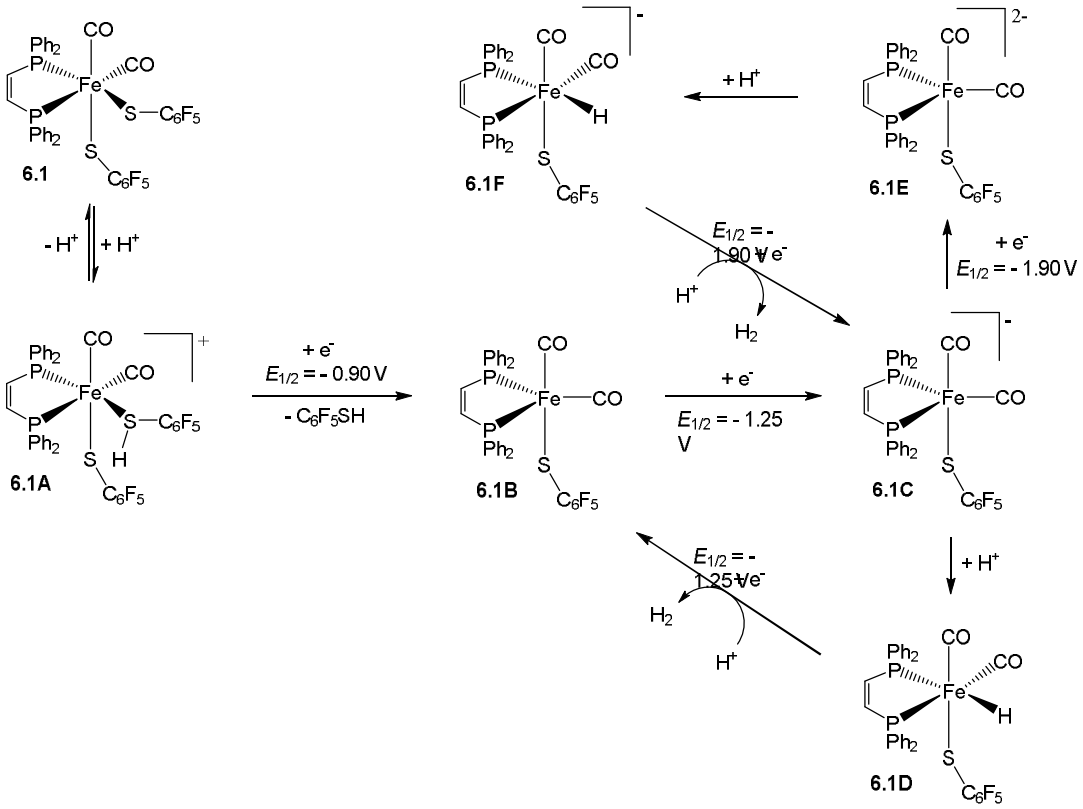

Scheme 6.4. Proposed catalytic mechanism for the electrocatalytic proton reduction by $Fe(CO)_2(\kappa^2\text{-dppv})(\kappa^1\text{-}SC_6F_5)_2$ (**6.1**).

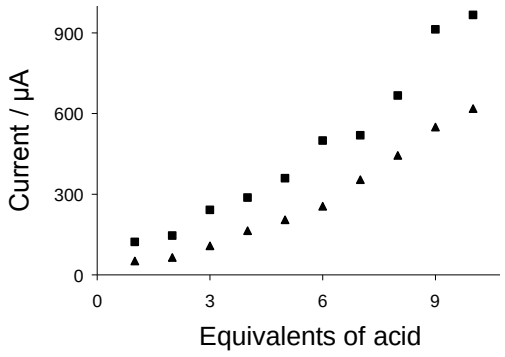

Figure 6.11. Plot of catalytic limiting current *vs.* equivalents of $HBF_4{\cdot}Et_2O$ added for $Fe(CO)_2(\kappa^2\text{-dppv})(\kappa^1\text{-}SC_6F_5)_2$ (**6.1**) at potentials of the first (triangles) and second (squares) catalytic waves.

Both **6.2** and **6.3** show quite similar catalysis in presence of $HBF_4{\cdot}Et_2O$ but with less resolve currents (Figure 6.12). Both of them show three new reduction peaks upon addition of 1 molar equivalent of $HBF_4{\cdot}Et_2O$ (at E_p = –1.15, –1.45 and –1.95 V for **6.2**; at E_p = –1.00, –1.40 and –2.00 V for **6.3**). Akin to **6.1**, the peak current of the second and third waves increase with the concentration of acid while that of the first wave remains constant throughout the experiment. Additional catalytic currents were also observed in

their CVs near the negative end of the potential window which we assume is due to direct reduction of $HBF_4 \cdot Et_2O$ by the glassy carbon electrode as it becomes catalytically active in presence of strong acids beyond –2 V. We assume that both **6.2** and **6.3** follow a similar catalytic mechanism as that proposed for **6.1**.

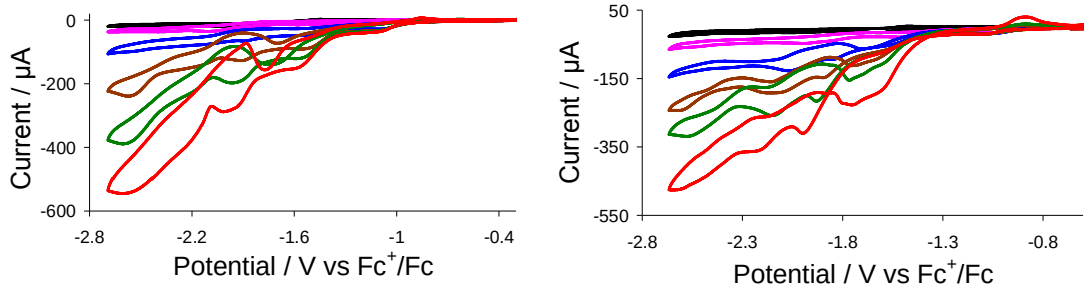

(a) (b)

Figure 6.12. CVs of (a) $Fe(CO)_2(\kappa^2\text{-dppv})(\kappa^1\text{-}SC_6H_5)_2$ (**6.2**) in the absence of acid (black) and in the presence of in presence of 1 (pink), 3 (blue), 5 (brown), 7 (green) and 9 (red) molar equivalents of $HBF_4 \cdot Et_2O$, (b) $Fe(CO)_2(\kappa^2\text{-dppv})(\kappa^1\text{-}SC_6H_4CH_3\text{-}p)_2$ (**6.3**) in the absence of acid (black) and in the presence of in presence of 1 (pink), 3 (blue), 5 (brown), 7 (green) and 9 (red) molar equivalents of $HBF_4 \cdot Et_2O$ (0.5 mM solution in acetonitrile, supporting electrolyte $[NBu_4][PF_6]$, scan rate 0.1 Vs^{-1}, glassy carbon electrode, potential vs Fc^+/Fc).

Plots of limiting current at the first catalytic wave against concentration of acid for **6.1**-**6.3** (Figure 6.13) show that the catalytic efficiency of **6.1** is far better than that of **6.2** and **6.3** as the limiting current observed for the later two complexes are almost negligible compared to that of **6.1**. Usually the limiting current (catalytic efficiency) increases as the basicity of the metal centre is increased. The opposite trend observed for this series is probably related to the instability of these complexes in presence of $HBF_4 \cdot Et_2O$. As discussed in the previous section, the loss of a thiol after protonation at sulphur is relatively fast for **6.2** and **6.3** as compared to **6.1**, which also explains the unresolved catalytic currents observed in the CVs of **6.2** and **6.3**.

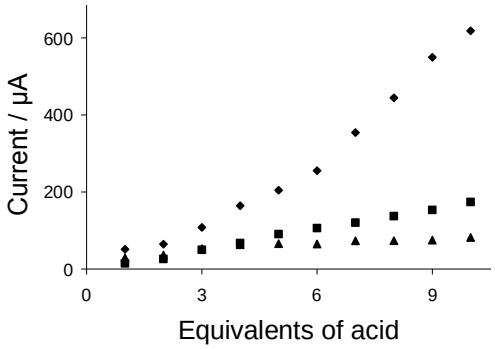

Figure 6.13. Plot of catalytic limiting current at potentials of first catalytic wave *vs.* equivalents of $HBF_4{\cdot}Et_2O$ added for $Fe(CO)_2(\kappa^2\text{-dppv})(\kappa^1\text{-}SC_6F_5)_2$ (**6.1**) (diamonds), $Fe(CO)_2(\kappa^2\text{-dppv})(\kappa^1\text{-}SC_6H_5)_2$ (**6.2**) (squares) and $Fe(CO)_2(\kappa^2\text{-dppv})(\kappa^1\text{-}SC_6H_4CH_3\text{-}p)_2$ (**6.3**) (triangles).

6.3. Summary and conclusions

The mononuclear iron(II) bis(thiolate) complexes (**6.1**-**6.3**) have been synthesized and tested for electrocatalytic proton reduction. The crystal structures show that the thiolate ligands adopt a *cis*-configuration in the solid-state, but exist in both *cis*- and *trans*-configuration in solution. Each of them undergoes a quasi-reversible reduction at relatively mild potential compared to the corresponding hexacarbonyl [34,36] from which they were prepared. All protonate at sulphur upon addition of acid and lose a thiolate ligand as thiol.

All three catalyze proton reduction at mild potentials. The catalytic efficiency of **6.1** is better than **6.2** and **6.3** which we attribute due to the greater stability of **6.1** in presence of acid. Electrochemical data reveals that a penta-coordinated 17-electron species, $Fe(CO)_2(dppv)(\kappa^1\text{-SR})$, generated *in situ* by reduction and concomitant loss of a thiolate ligand is the actual catalytic species. Akin to the related iron dithiolate complexes $Fe(CO)_2(PMe_3)_2(\kappa^2\text{-}SC_6H_2R_2S)$ reported by Ott and co-workers [29], each shows two catalytic waves involving two oxidation states of iron but the catalytic mechanism of these iron(II) bis(thiolate) complexes (**6.1**-**6.3**) is significantly different from that of $Fe(CO)_2(PMe_3)_2(\kappa^2\text{-}SC_6H_2R_2S)$. In Ott's complexes, the chelating dithiolate ligand remains bonded to the iron throughout the catalytic cycle and the presence of PMe_3 ligands make the iron centre more basic compared to **6.1**-**6.3**, so the penta-coordinated 17-electron species $Fe(CO)_2(PMe_3)_2(\kappa^1\text{-}SC_6H_2R_2SH)$ are able to reacts with proton which is not seen for **6.1**-**6.3**.

6.4. Experimental

6.4.1. General. All reactions were carried out under a dry, oxygen-free nitrogen atmosphere using standard Schlenk techniques. Solvents were stored in alumina columns and dried with anhydrous engineering equipment, such that the water concentration was 5–10 ppm. Metal carbonyls and all other reagents were purchased from various commercial chemical companies and used without further purification. Preparative thin layer chromatography was carried out on 0.25 mm plates prepared from silica gel GHLF (UV254, Analtech). Infrared spectra were recorded using a Nicolet 205 FT-IR or Nicolet 6700 FT-IR spectrometer in a solution cell fitted with calcium fluoride plates, subtraction of the solvent absorptions being achieved by computation. NMR spectra were run on a Bruker AMX400 instrument.

6.4.2. Synthesis of $Fe(CO)_2(\kappa^2\text{-dppv})(\kappa^1\text{-}SC_6F_5)_2$ (6.1). A toluene (30 mL) solution of $Fe_2(CO)_6(\mu\text{-}SC_6F_5)_2$ (100 mg, 0.147 mmol) and dppv (59 mg, 0.149 mmol) was heated at 80-85°C for 24 h. The reaction mixture was cooled to room temperature and filtered. Volatiles were removed under reduced pressure and the residue redissolved in toluene. A layer of hexane was added to the toluene solution before being kept at room temperature under nitrogen for crystallization which gave red crystals of $Fe(CO)_2(\kappa^2\text{-dppv})(\kappa^1\text{-}SC_6F_5)_2$ (**6.1**) (36 mg, 27%). Spectroscopic and analytical data for **6.1**: IR (νCO, CH_2Cl_2): 2037 s, 1993 s cm^{-1}. ^1H NMR ($CDCl_3$): δ 8.08 (m, 2H), 7.99 (m, 1H), 7.92 (m, 3H), 7.71 (m, 2H), 7.51 (m, 10H), 7.31 (m, 4H). $^{31}P\{^1H\}$-NMR ($CDCl_3$): major isomer: δ 81.0 (d, J = 22.2 Hz), 58.5 (d, J = 22.2 Hz); minor isomer: δ 77.9 (s). Elemental analysis calc. for $C_{40}H_{22}F_{10}Fe_1O_2P_2S_2$ (found): C 53.00 (51.34), H 2.45 (2.45).

Crystallographic data for **6.1**: red plate, dimensions 0.004 × 0.004 × 0.001 mm^3, monoclinic, space group $P2_1/c$, a = 10.665(6), b = 15.197(9), c = 25.547(16) Å, α = 90, β = 99.200(6), γ = 90°, V = 4087(4) $Å^3$, Z = 4, F(000) 1824, d_{calc} = 1.473 g cm^{-3}, μ = 0.629 mm^{-1}. 23195 reflections were collected, 7138 unique [R(int) = 0.1894]. At convergence, R_1 = 0.0930, wR_2 = 0.2187 [$I > 2.0\sigma(I)$] and R_1 = 0.1338, wR_2 = 0.2545 (all data), for 515 parameters.

6.4.3. Synthesis of $Fe(CO)_2(\kappa^2\text{-dppv})(\kappa^1\text{-}SC_6H_5)_2$ (6.2). A xylene (25 mL) solution of $Fe_2(CO)_6(\mu\text{-}SC_6H_5)_2$ (150 mg, 0.301 mmol) and dppv (300 mg, 0.757 mmol) was heated to reflux for 1 h. The solvent was removed under reduced pressure and the residue

separated by TLC on silica gel. Elution with hexane/CH_2Cl_2 (1:3, v/v) developed two bands on TLC plates. The slower moving band afforded $Fe(CO)_2(\kappa^2$-dppv)$(\kappa^1$-$SC_6H_5)_2$ (**6.2**) (18 mg, 8%) as red crystals after recrystallization from diethylether at –30°C while the contents of the faster moving band were too small for characterization. Data for **6.2**: IR (νCO, CH_2Cl_2): 2023 s, 1978 s cm^{-1}. ^{1}H NMR ($CDCl_3$): δ 8.10 (m, 1H), 8.25 (m, 1H), 7.88 (m, 3H), 7.69 (m, 3H), 7.51-7.33 (m, 18H), 7.03 (m, 4H), 6.90 (m, 2H). $^{31}P\{^1H\}$-NMR ($CDCl_3$): major isomer: δ 80.8 (d, J 22.6), 61.1 (d, J 22.6); minor isomer: δ 74.1 (s). Elemental analysis calc. for $C_{40}H_{32}FeO_2P_2S_2$ (found): C 66.12 (65.04), H 4.44 (4.51).

Crystallographic data for **6.2**: red block, dimensions 0.04 × 0.04 × 0.04 mm^3, monoclinic, space group $P2_1/n$, a = 11.60 (1), b = 34.74(4), c = 19.35(2) Å, α = 90, β = 106.292(13), γ = 90°, V = 7489(16) $Å^3$, Z = 4, F(000) 3008, d_{calc} = 1.289 g cm^{-3}, μ = 0.632 mm^{-1}. 34061 reflections were collected, 7745 unique [R(int) = 0.0628]. At convergence, R_1 = 0.1452, wR_2 = 0.4340 [$I > 2.0\sigma(I)$] and R_1 = 0.1593, wR_2 = 0.4478 (all data), for 792 parameters.

6.4.4. Synthesis of $Fe(CO)_2(\kappa^2$-dppv)$(\kappa^1$-$SC_6H_4CH_3$-*p*$)_2$ (6.3). A xylene solution (20 mL) of $Fe_2(CO)_6(\mu$-$SC_6H_4CH_3$-*p*$)_2$ (100 mg, 0.190 mmol) and dppv (189 mg, 0.477 mmol) was heated to reflux for 1 h. The solvent was removed under reduced pressure and the residue chromatographed by TLC on silica gel. Elution with hexane/CH_2Cl_2 (1:3, v/v) developed two bands on TLC plates. The second band afforded $Fe(CO)_2(\kappa^2$-dppv)$(\kappa^1$-$SC_6H_4CH_3$-*p*$)_2$ (**6.3**) (7 mg, 5%) as red crystals after recrystallization from diethylether at –30°C while the contents of the first band were too small for characterization. Data for **6.3**: IR (νCO, CH_2Cl_2): 2020 s, 1975 s cm^{-1}. ^{1}H NMR ($CDCl_3$): major isomer: δ 8.13 (m, 1H), 7.89 (m, 2H), 7.70 (m, 2H), 7.39 (m, 20H), 7.13 (d, J 8, 2H), 6.90 (d, J 8, 1H), 6.83 (d, J 8, 1H), 6.73 (d, J 8, 1H), 2.34 (s, 6H). $^{31}P\{^1H\}$-NMR ($CDCl_3$): major isomer: δ 80.6 (d, J 21.1), 61.0 (d, J 21.1); minor isomer: δ 74.4 (s). Elemental analysis calc. for $C_{42}H_{36}FeO_2P_2S_2$ (found): C 66.84 (65.71), H 4.82 (4.91).

Crystallographic data for **6.3**: red plate, dimensions 0.04 × 0.04 × 0.001 mm^3, monoclinic, space group $P2_1/n$, a = 12.8737(3), b = 17.3484(4), c = 16.2313(4) Å, α = 90, β = 90.288(2), γ = 90°, V = 3625.02(15) $Å^3$, Z = 4, F(000) 1568, d_{calc} = 1.383 g cm^{-3}, μ = 0.656 mm^{-1}. 39824 reflections were collected, 10490 unique [R(int) = 0.0620]. At convergence, R_1 = 0.0469, wR_2 = 0.1043 [$I > 2.0\sigma(I)$] and R_1 = 0.0700, wR_2 = 0.1159 (all data), for 444 parameters.

6.4.5. Protonation. 2 molar equivalents of $HBF_4 \cdot Et_2O$ (0.680 μL) was added to a dichloromethane solution containing 0.005 mmol of the complex to be examined (**6.1**, **6.2**, **6.3**) at room temperature. The resulted solution was then transferred into a solution IR cell fitted with calcium fluoride plates and a series of spectra were recorded as a function of time.

6.5. References

(1) S. Losse, J. G. Vos and S. Rau, *Coord. Chem. Rev.*, 2010, **254**, 2492-2504.

(2) V. Artero and M. Fontecave, *Coord. Chem. Rev.*, 2005, **249**, 1518-1535.

(3) J.-M. Savéant, *Chem. Rev.*, 2008, **108**, 2348-2378.

(4) J. L. Dempsey, B. S. Brunschwig, J. R. Winkler and H. B. Gary, *Acc. Chem. Res.*, 2009, **42**, 1995-2004.

(5) J. P. Bigi, T. E. Hanna, W. H. Harman, A. Chang and C. J. Chang, *Chem. Commun.*, 2010, **46**, 958-960.

(6) Y. Sun, J. P. Bigi, N. A. Piro, M. L. Tang, J. R. Long and C. J. Chang, *J. Am. Chem. Soc.*, 2011, **133**, 9212-9215.

(7) B. D. Stubbert, J. C. Peters and H. B. Gray, *J. Am. Chem. Soc.*, 2011, **133**, 18070-18073.

(8) C. C. L. McCrory, C. Uyeda and J. C. Peters, *J. Am. Chem. Soc.*, 2012, **134**, 3164-3170.

(9) C.-F. Leung, Y.-Z. Chen, H.-Q. Yu, S.-M. Yiu, C.-C. Ko and T.-C. Lau, *Int. J. Hydrogen Energy*, 2011, **36**, 11640-11645.

(10) W. R. McNamara, Z. Han, P. J. Alperin, W. W. Brennessel, P. L. Holland and R. Eisenberg, *J. Am. Chem. Soc.*, 2011, **133**, 15368-15371.

(11) P. Connolly and J. H. Espenson, *Inorg. Chem.*, 1986, **25**, 2684-2688.

(12) J. W. M. Singh, T. Baine, S. Kudo, S. Tian, X. A. N. Ma, H. Zhou, N. J. De Yonker, T. C. Pham, J. C. Bollinger, D. L. Baker, B. Yan, C. E. Webster and X. Zhao, *Angew. Chem. Int. Ed.*, 2012, **51**, 5941-5944.

(13) L. A. Berben and J. C. Peters, *Chem. Commun.*, 2010, **46**, 398-400.

(14) M. R. DuBois and D. L. DuBois, *Acc. Chem. Res.*, 2009, **42**, 1974-1982.

(15) O. Pantani, E. Anxolabéhère-Mallart, A. Aukauloo and P. Millet, *Electrochem. Commun.*, 2007, **9**, 54-58.

(16) P.-A. Jacques, V. Artero, J. Pécaut and M. Fontecave, *Proc. Natl. Acad. Sci.*, 2009, **106**, 20627-20632.

(17) B. J. Fisher and R. Eisenberg, *J. Am. Chem. Soc.*, 1980, **102**, 7361-7363.

(18) A. Begum, G. Moula and S. Sarkar, *Chem. Eur. J.*, 2010, **16**, 12324-12327.

(19) D. L. DuBois and R. M. Bullock, *Eur. J. Inorg. Chem.*, 2011, 1017-1027.

(20) A. D. Wilson, R. H. Newell, M. J. McNevin, J. T. Muckerman, M. R. DuBois and D. L. DuBois, *J. Am. Chem. Soc.*, 2006, **128**, 358-366.

(21) A. L. Goff, V. Artero, B. Jousselme, P. D. Tran, N. Guillet, R. Métayé, A. Fihri, S. Palacin and M. Fontecave, *Science*, 2009, **326**, 1384-1387.

(22) M. L. Helm, M. P. Stewart, R. M. Bullock, M. R. DuBois and D. L. DuBois, *Science*, 2011, **333**, 863-866.

(23) A. M. Appel, D. H. Pool, M. O'Hagan, W. G. Shaw, J. Y. Yang, M. R. DuBois and D. L. DuBois, *ACS Catal.*, 2011, **1**, 777-785.

(24) Z. Han, L. Shen, W. W. Brennessel, P. L. Holland and R. Eisenberg, *J. Am. Chem. Soc.*, 2013, **135**, 14659-14669.

(25) G. A. N. Felton, C. A. Mebi, B. J. Petro, A. K. Vannucci, D. H. Evans, R. S. Glass and D. L. Lichtenberger, *J. Organomet. Chem.*, 2009, **694**, 2681-2699.

(26) I. Bhugun, D. Lexa and J.-M. Saveánt, *J. Am. Chem. Soc.*, 1996, **118**, 3982-3983.

(27) M. J. Rose, H. B. Gray and J. R. Winkler, *J. Am. Chem. Soc.*, 2012, **134**, 8310-8313.

(28) V. Artero and M. Fontecave, *C. R. Chimie*, 2008, **11**, 926-931.

(29) S. Kaur-Ghumaan, L. Schwartz, R. Lomoth, M. Stein and S. Ott, *Angew. Chem. Int. Ed.*, 2010, **49**, 8033-8036.

(30) M. Beyler, S. Ezzaher, M. Karnahl, M.-P. Santoni, R. Lomoth and S. Ott, *Chem. Commun.*, 2011, **47**, 11662-11664.

(31) A. Orthaber, M. Karnahl, S. Tschierlei, D. Streich, M. Stein and S. Ott, *Dalton Trans.*, 2014, **43**, 4537-4549.

(32) S. Roy, S. K. S. Mazinani, T. L. Groy, L. Gan, P. Tarakeshwar, V. Mujica and A. K. Jones, *Inorg. Chem.*, 2014, **53**, 8919-8929.

(33) G. P. Connor, K. J. Mayer, C. S. Tribble and W. R. McNamara, *Inorg. Chem.*, 2014, 53, 5408-5410.

(34) F. Ridley, S. Ghosh, G. Hogarth, N. Hollingsworth, K. B. Holt, D. G. Unwin, *J. Electroanal. Chem.*, 2013, **703**, 14-22.

(35) J. Takács, L. Markó and L. Párkányi, *J. Organomet. Chem.*, 1989, 361, 109-116.

(36) D. Chong, I. P. Georgakaki, R. Mejia-Rodriguez, J. Sanabria-Chinchilla, M. P. Soriaga and M. Y. Darensbourgh, *Dalton Trans.*, 2003, 4158-4163.

Chapter 7

Electrocatalytic proton reduction by the coordinatively and electronically unsaturated square-pyramidal Fe(II) complex Fe(CO)(κ^2-dppn)(κ^2-tbt)

7.1. Introduction

As detailed in the previous chapter, research on mononuclear iron complexes as electrocatalysts for the reduction of protons has been spurred on primarily by the development of efficient catalysts based on mononuclear cobalt and nickel complexes, in addition to biomimetic dithiolate-bridged diiron complexes [1-8]. Unlike diiron biomimics which can accommodate a proton across Fe–Fe bond, coordinatively saturated mononuclear iron complexes do not contain a free coordination site for proton binding so that it can be reduced electrocatalytically at the metal centre [2-5]. Hence a feature of all those catalysts is the initial loss of a ligand through reduction to create a vacant coordination site for binding proton. To circumvent this problem, coordinatively unsaturated square-pyramidal iron complexes have recently been used as catalysts by Ott [6,7] and Jones [8] (Chart 7.1). These iron complexes are also electronically unsaturated (16-electron) and can be easily prepared in moderate to good yields from one pot reaction between $FeCl_2$ and a chelating diphosphine and dithiol in presence of CO.

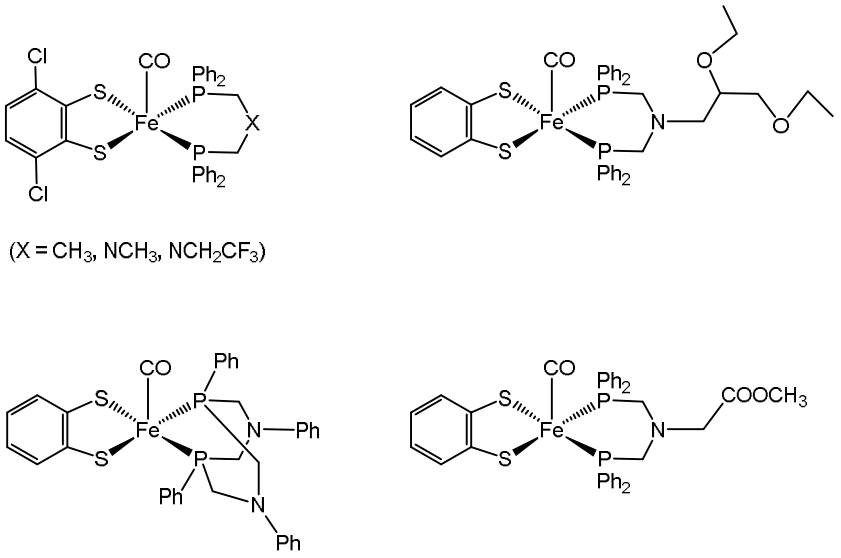

Chart 7.1. Square-pyramidal iron complexes used as electrocatalysts for the reduction of protons [6-8].

Electrocatalytic studies show that square-pyramidal iron complexes can catalyse proton reduction at relatively mild potentials and are robust with respect to degradation during catalysis [6-8]. Moreover, catalytic hydrogen formation is achieved using a wide range of acids and, depending on the strength of acid used, these complexes have been found to follow different mechanisms, a feature akin to diiron biomimics [6]. For instance, in presence of weak acids such as AcOH, catalysis starts with metal-based reduction followed by protonation, whereas the catalytic reaction proceeds *via* initial ligand protonation by strong acids followed by a metal-centred reduction which lead to the formation of a hydride intermediate to generate hydrogen.

The diphosphine 1,1′-bis(diphenylphosphino)naphthalene (dppn) has attracted considerable interest as a chelating ligand due to its rigid naphthalene backbone [9-23]. It has been found to stabilise cationic metal species [23], possibly *via* additional electronic influence of the highly delocalised naphthalene backbone that is not possible for related diphosphines with rigid backbones such as 1,2-bis(diphenylphosphino)ethylene. During our investigations on dithiolate-bridged diiron chelate complexes, we found that in addition to the expected diiron chelate $Fe_2(CO)_4(\kappa^2\text{-dppn})(\mu\text{-tdt})$ (**7.1**), a small amount of square-pyramidal $Fe(CO)(\kappa^2\text{-dppn})(\kappa^2\text{-tdt})$ (**7.2**) is also formed from the reaction between $Fe_2(CO)_6(\mu\text{-tdt})$ and dppn. The highly delocalized nature of bonding in this complex involving both the chelating ligands and iron makes it significantly different from those studied by Ott [6,7] and Jones [8] which prompted us to investigate its electrocatalytic properties.

7.2. Results and discussion

7.2.1. Synthesis and structure. The $Me_3NO{\cdot}2H_2O$ initiated reaction between $Fe_2(CO)_6(\mu\text{-tdt})$ and dppn in MeCN at 80°C afforded the expected asymmetrically substituted binuclear product $Fe_2(CO)_4(\kappa^2\text{-dppn})(\mu\text{-tdt})$ (**7.1**) (35%) [24], together with smaller amounts of the 16-electron mononuclear complex $Fe(CO)(\kappa^2\text{-dppn})(\kappa^2\text{-tdt})$ (**7.2**) (12%) (Scheme 7.1). Characterisation of **7.2** was made primarily on the basis of the crystal structure as shown in Figure 7.1. The complex co-crystallises with a molecule of chloroform and two short interactions between the hydrogen of chloroform and a sulphur (2.668 Å) and carbon (2.857 Å) of the dithiolate ligand are present within the unit cell.

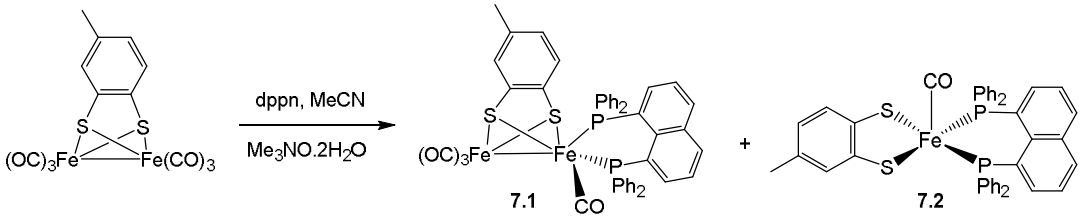

Scheme 7.1. Synthesis of Fe(CO)(κ^2-dppn)(κ^2-tdt) (**7.2**).

Complex **7.2** favours square-pyramidal geometry over trigonal-bipyramidal arrangement in the solid state with the carbonyl ligand in apical position. The diphosphine and dithiolate ligands constitute the base of the pyramid and lie mutually *trans*. Metric parameters are very similar to those of related square-pyramidal complexes reported by Ott [6,7] and Jones [8]. Theoretical studies [7] show that simple monodentate phosphines favour hexa-coordinate complexes in reaction with dithiolate-bridged diiron complexes as the loss of CO from these octahedral complexes is energetically unfavourable, whereas the use of strongly chelating diphosphines leads to selective formation of penta-coordinate square-pyramidal complexes.

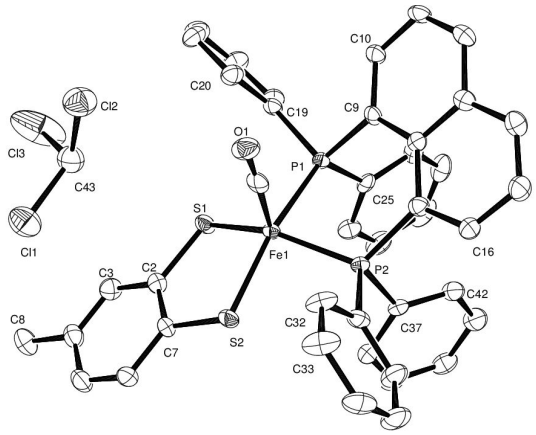

Figure 7.1. An ORTEP diagram of the molecular structure of Fe(CO)(κ^2-dppn)(κ^2-tdt) (**7.2**). Hydrogen atoms are omitted for clarity. Selected bond distances (Å) and angles (º): Fe(1)─P(1) 2.2043(7), Fe(1)─P(2) 2.1943(7), Fe(1)─S(1) 2.1887(7), Fe(1)─S(2) 2.2034(7), Fe(1)─C(1) 1.723(3), P(1)─Fe(1)─P(2) 87.97(3), S(1)─Fe(1)─S(2) 88.99(3), P(1)─Fe(1)─S(1) 88.09(3), P(2)─Fe(1)─S(2) 88.60(3), P(1)─Fe(1)─S(2) 166.57(3), P(2)─Fe(1)─S(1) 152.59(3), C(1)─Fe(1)─P(1) 90.62(9), C(1)─Fe(1)─P(2) 93.60(2), C(1)─Fe(1)─S(1) 113.57(2), C(1)─Fe(1)─S(2) 102.56(9).

Spectroscopic data of **7.2** are generally in accord with the solid-state structure. The IR spectrum shows single carbonyl absorption at 1918 cm^{-1}, being similar to those observed

for related complexes reported by Ott [6,7] and Jones [8]. On the basis of the solid-state structure, the two phosphorus atoms of the dppn ligand would be expected to be inequivalent, but the $^{31}P\{^{1}H\}$ NMR spectrum shows only a singlet at 67.9 ppm at room temperature. Complexes with square-pyramidal geometry are generally fluxional in solution and switch between square-pyramidal (**7.2**$_{sp}$) and trigonal-bipyrimidal (**7.2**$_{tbp}$) geometries *via* Berry pseudo-rotation. We assume that this exchange makes the phosphorus atoms equivalent in solution on NMR timescale. DFT calculations are ongoing in order to calculate the energy difference between **7.2**$_{sp}$ and **7.2**$_{tbp}$ and shed light on the exchange process [7]. Recent theoretical studies on a related square-pyramidal complex, carried out by Ott and co-workers, reveal that the energy difference between these conformers in solution is small (*ca*. 6.6 kcalmol^{-1}) with the square-pyramidal conformer being lower in energy [7].

7.2.2. Electrochemistry. The redox chemistry of **7.2** was studied by cyclic voltammetry in both CH_2Cl_2 and a 1:1 mixture of CH_2Cl_2/MeCN since the complex is sparingly soluble in MeCN. The CV of **7.2** in CH_2Cl_2 at 0.1 V/s shows a reversible reduction at $E_{1/2}$ = –1.54 V (i_{an}/i_{ca} ~ 1) and an irreversible oxidation at E_p = 0.57 V (Figure 7.2). The irreversibility of the oxidative wave is expected since the basicity of the Fe(III) centre is not sufficient to bind CO, which likely dissociates after oxidation. A reductive feature has also been observed at E_p = –0.23 V on the return scan due to the reduction of product generated upon irreversible oxidation. The oxidative wave of **7.2** shows some reversibility at higher scans rates (≥ 5 V/s) and the linear i_p vs $\sqrt{v}$ plots indicating that both the reductive and oxidative processes are diffusion controlled.

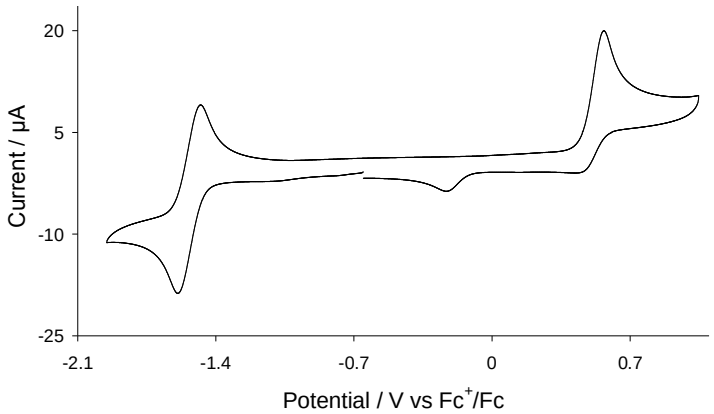

Figure 7.2. CV of Fe(CO)(κ^2-dppn)(κ^2-tdt) (**7.2**) in CH_2Cl_2 (1 mM solution, supporting electrolyte $[NBu_4][PF_6]$, scan rate 0.1 Vs^{-1}, glassy carbon electrode, potential vs Fc^+/Fc)

The CV of **7.2** shows some further redox features in a 1:1 mixture of CH_2Cl_2/MeCN (Figure 7.3). The first reduction now appears at $E_{1/2}$ = –1.68 V (i_{an}/i_{ca} ~ 0.7) and is again reversible. A second irreversible reduction wave is observed at E_p = –2.21 V. Two oxidative waves are seen, a reversible oxidation at $E_{1/2}$ = 0.22 V (i_{ca}/i_{an} ~ 0.8) followed by an irreversible wave at E_p = 0.52 V and a small reductive feature is observed on the return scan at E_p = –0.47 V which is associated with the irreversible oxidative wave at E_p = 0.52 V. The $Fe^{II/III}$ couple becomes reversible in MeCN, possibly due to the coordination of MeCN to $\mathbf{7.2}^+$ to form $[Fe(CO)(NCMe)(\kappa^2\text{-dppn})(\kappa^2\text{-tdt})]^+$ which is sufficiently basic to stabilize the CO ligand. The second irreversible oxidation wave belongs to the oxidation of this solvated species. No additional features were observed when scan rate was varied between 0.025 to 0.5 V/s and the peak current of the reversible processes exhibit linear relationship with the square root of scan rate suggesting that both processes are controlled by diffusion.

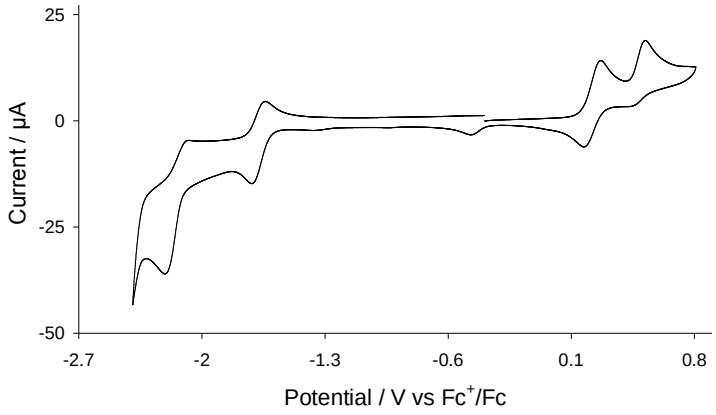

Figure 7.3. CV of $Fe(CO)(\kappa^2\text{-dppn})(\kappa^2\text{-tdt})$ (**7.2**) in a 1:1 mixture of CH_2Cl_2/MeCN (1 mM solution, supporting electrolyte $[NBu_4][PF_6]$, scan rate 0.1 Vs^{-1}, glassy carbon electrode, potential vs Fc^+/Fc).

We have calculated the ground state electronic structure of **7.2** in order to get insight into the redox processes, and the preliminary results indicate complexity in its redox chemistry. Hence, we extended our calculations on radical ions to shed more light on this which is currently ongoing. The HOMO of **7.2** is delocalized over iron, one sulphur and the tolyl ring, whereas the LUMO is primarily delocalized over the naphthalene backbone of dppn with a very small contribution from iron (Figure 7.4). Although the HOMO is delocalized, we assume that the one-electron oxidation corresponds to $Fe^{II/III}$ couple as observed in related square-pyramidal complex studied by Jones [8], but the first reduction occurs at the naphthalene ring of dppn.

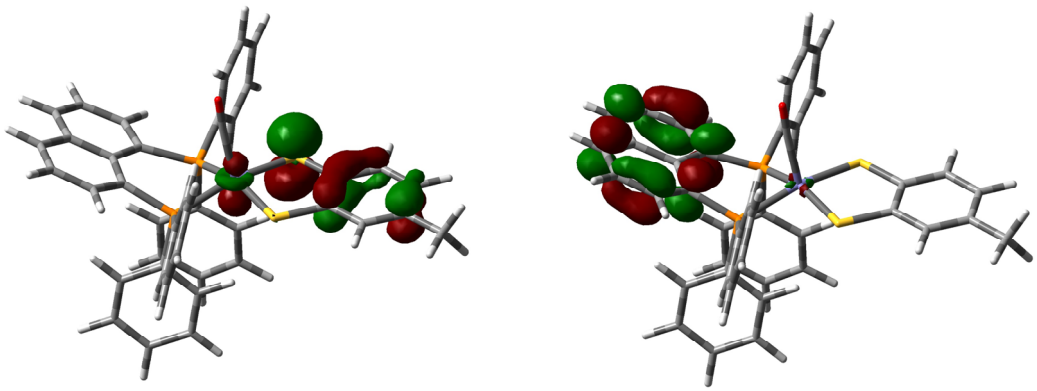

Figure 7.4. HOMO (left) and LUMO (right) of Fe(CO)(κ^2-dppn)(κ^2-tdt) (**7.2**) (calculations were carried out by collaborator).

The HOMO-LUMO gap observed in 1:1 mixture of CH_2Cl_2/MeCN (1.90 V) is *ca*. 0.2 V smaller than that in CH_2Cl_2 (2.11 V) which is expected due to the coordinating nature of MeCN. Further MeCN is more efficient in stabilizing ionic species than CH_2Cl_2 and reduces the energy required for ionization. Whilst this is the case in oxidative chemistry of **7.2** i.e. the first oxidation potential in MeCN is *ca* 0.35 V less positive than that in CH_2Cl_2, the opposite scenario is observed during reduction i.e. the first reduction potential of **1** in MeCN is *ca*. 0.15 V more negative than that in CH_2Cl_2.

Since **7.2** is formally a 16-electron square-pyramidal complex, there is the possibility that a two-electron donor (in this case MeCN) can interact with the central iron through the missing vertex of the octahedron, which will lead to further stabilization of the neutral complex in solution. During reduction this interaction has to be overcome (along with other energy barriers) which will shift the reduction potential to more negative values as compared to that in CH_2Cl_2 where such secondary interaction is not possible. For the same reason, oxidation of **7.2** in MeCN is relatively easier compared to CH_2Cl_2 as electron loss can be compensated better in MeCN through secondary interactions with the solvent. Since the iron centre formally gains extra electron density from this interaction, which in turn strengthens the Fe–C back-bonding, it will have an impact on the IR absorption of the carbonyl ligand. The IR spectrum of **7.2** shows single absorption at 1914 cm^{-1} in MeCN as compared to 1918 cm^{-1} in CH_2Cl_2 and the 4 cm^{-1} decrease in wavenumber in MeCN suggests that such interaction is present in MeCN solution of **7.2**.

7.2.3. Catalysis. Although **7.2** is not protonated by a range of acids, it was nevertheless found to be an efficient proton reduction catalyst. The catalytic ability of **7.2** was tested in a 1:1 mixture of CH_2Cl_2/MeCN using CF_3CO_2H as the proton source, Figure 7.5a shows CVs obtained after addition of 1-7 molar equivalents of acid. Upon addition of CF_3CO_2H, two new reduction peaks were observed at E_p = –1.60 and –1.70 V, the first of which we assume corresponds to the reduction of **7.2** to **7.2**$^-$ as the reduction potential often displays a slight positive shift in presence of acid. At lower acid concentrations, the peak height of the first reduction was smaller than that of the second, but the peak height of the former increases as the concentration of acid is increased and surpassed the later when 10 molar equivalents of CF_3CO_2H is added to the solution (Figure 7.5b). At higher acid concentration both peaks merge to form a single catalytic wave (Figure 7.5b).

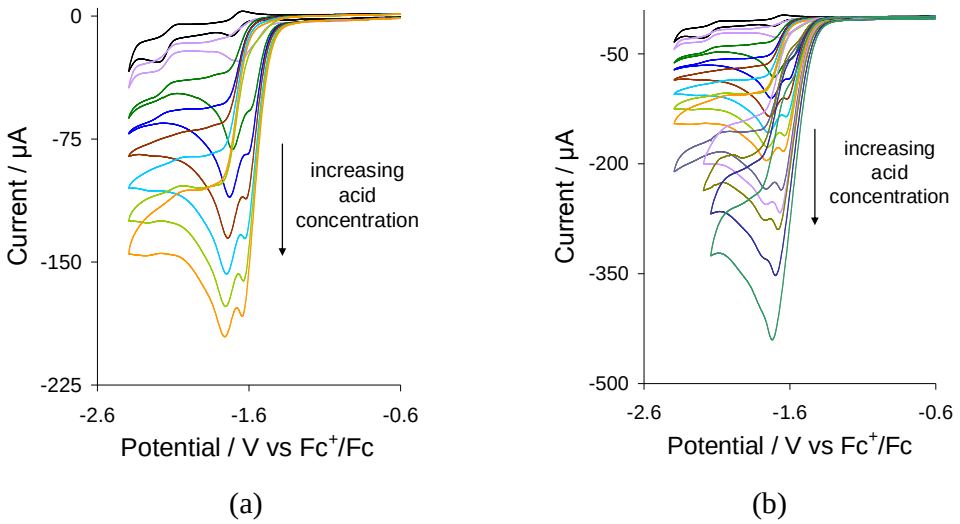

Figure 7.5. CVs of Fe(CO)(κ^2-dppn)(κ^2-tdt) (**7.2**) – (a) in the absence acid and in the presence of 1-7 molar equivalents of CF_3CO_2H, (b) in the absence acid and in the presence of 1-7, 9, 10, 12, 16 and 20 molar equivalents of CF_3CO_2H (in 1:1 mixture of CH_2Cl_2/MeCN, 1 mM solution, supporting electrolyte $[NBu_4][PF_6]$, scan rate 0.1 Vs^{-1}, glassy carbon electrode, potential vs Fc^+/Fc).

Since **7.2** does not protonate by CF_3CO_2H, we propose an EC mechanism as shown in Scheme 7.2. Proton reduction by **7.2** commences *via* reduction at E_p = –1.60 V, which generates **7.2**$^-$**,** and this is likely followed by rapid protonation to yield HFe(CO)(κ^2-dppn)(κ^2-tdt) (**7.2H**). Although DFT calculations suggest that the reduction of **7.2** is dppn-centred, we assume that the HOMO of the radical anion is (at least partially) based on iron which is necessary for metal protonation. This species either protonates at the same potential to give **7.2H$_2$**$^+$, which liberates hydrogen after taking a second electron,

thus following an ECCE mechanism (pathway A) or it may undergo a further reduction at E_p = –1.70 V before protonation to generate hydrogen *via* ECEC mechanism (pathway B). The small difference between the reduction potential of **7.2** and **7.2H** (0.1 V) as compared to that between **7.2** and **7.2**$^-$ (~ 0.5 V) can be understood by considering the molecular geometry and electronic structure of them. Since **7.2H** is a 17-electron octahedral complex it is expected to be reduced at lower potentials than square-pyramidal **7.2**$^-$. The CVs also suggest that protonation of **7.2H** is slow at low acid concentrations and pathway B dominates hydrogen production, but as the concentration of acid is increased the equilibrium is shifted to right and pathway A becomes dominant.

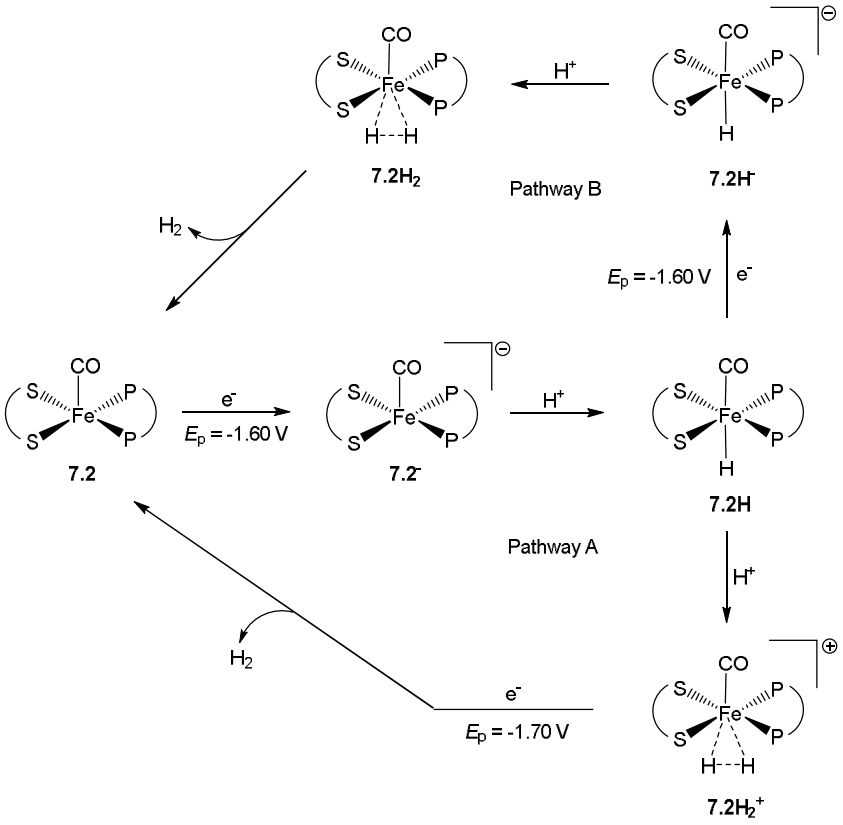

Scheme 7.2. Catalytic mechanism proposed for Fe(CO)(κ^2-dppn)(κ^2-tdt) (**7.2**).

From the above discussion it is clear that **7.2** follows a different mechanism for electrocatalytic proton reduction than other square-pyramidal iron catalysts previously reported [6-8]. In order to develop this issue further we need a more detailed understanding of the electronic structure and molecular geometry of **7.2**, its radical anion (**7.2**$^-$) and the neutral hydride (**7.2H**). DFT calculations are currently ongoing to shed light on this as well as to validate the proposed mechanism.

7.3. Summary and conclusions

The coordinatively and electronically unsaturated square-pyramidal Fe(II) complex, Fe(CO)(κ^2-dppn)(κ^2-tbt) (**7.2**), has been synthesised and structurally characterised by single crystal X-ray diffraction analysis. It adopts square-pyramidal geometry in the solid-state but is fluxional in solution. Complex **7.2** has been studied by cyclic voltammetry in different solvents which reveal that its electrochemical response can be greatly influenced by the nature of solvent. Electrocatalytic studies show that it can catalyze hydrogen formation from CF_3CO_2H at relatively mild potential, but follows a different mechanism with respect to those proposed for related square-pyramidal complexes [6-8]. Theoretical studies are going on to shed light on this difference as well as to understand the structural changes taking place during catalysis.

7.4. Experimental

7.4.1. General. Unless otherwise stated, all manipulations were carried out under a nitrogen atmosphere using standard Schlenk techniques. Reagent-grade solvents were dried using appropriate drying agents and distilled prior to use by standard methods. Infrared spectra were recorded on a Shimadzu FTIR 8101 spectrophotometer. NMR spectra were recorded on a Bruker DPX 400 instrument. Elemental analysis was performed by Microanalytical Laboratories, University College London. $Fe_2(CO)_6$(μ-tdt) was prepared according to a published procedure [25].

7.4.2. Synthesis of Fe(CO)(κ^2-dppn)(κ^2-tdt) (7.2). An MeCN solution (15 mL) of $Fe_2(CO)_6$(μ-tdt) (100 mg, 0.23 mmol), $Me_3NO{\cdot}2H_2O$ (18 mg, 0.23 mmol) and dppn (114 mg, 0.23 mmol) was heated to reflux for 1 h. The reaction mixture was then allowed to cool at room temperature. The solvent were removed by rotary evaporation under reduced pressure and the residue chromatographed by TLC on silica gel. Elution with hexane/CH_2Cl_2 (4:1, v/v) developed two bands. The green band gave Fe(CO)(κ^2-dppn)(κ^2-tdt) (**7.2**) (20 mg, 12%) as dark green crystals, while the red band gave $Fe_2(CO)_4$(κ^2-dppn)(μ-tdt) (**7.1**) (70 mg, 35 %) [24] as deep red crystals after recrystallization from hexane/CH_2Cl_2 at 4^{o}C.

Data for **7.1** [24]: IR (νCO)(CH_2Cl_2): 2021s, 1950m, 1907w cm^{-1}. ^1H NMR ($CDCl_3$): δ 8.12 (d, J 8.0, 2H), 7.92 (d, J 8.0, 1H), 7.88 (s, 1H), 7.48 (m, 13H), 6.89 (m, 3H), 6.66 (m, 9H), 2.34 (3H, s). $^{31}P\{^1H\}$ NMR ($CDCl_3$): 69.5 (s) ppm.

Data for **7.2**: Anal. calc. for $C_{42}H_{32}FeOP_2S_2$ (found): C 68.67 (70.31), H 4.39 (4.66). IR (νCO)(CH_2Cl_2): 1918s cm^{-1}. ^1H NMR ($CDCl_3$): δ 8.16 (d, J 7.04 Hz, 2H), 7.96 (d, J 8.08 Hz, 2H), 7.91 (s, 1H), 7.58-7.51 (m, 14H), 6.95 (m, 3H), 6.69 (m, 8H), 2.37 (s, 3H). $^{31}P\{^1H\}$ NMR ($CDCl_3$): δ 67.9 (s) ppm.

Crystallographic data for **7.2**: green needle, dimensions 0.27 × 0.11 × 0.05 mm^3, monoclinic, space group $P2_1/c$, a = 15.78693(2), b = 13.69981(2), c = 18.0806(2) Å, α = 90, β = 102.5994(2), γ = 90°, V = 3816.27(8) $Å^3$, Z = 4, F(000) 1760.5, d_{calc} = 1.4863 g cm^{-3}, μ = 7.192 mm^{-1}. 12821 reflections were collected, 7172 unique [R(int) = 0.0364]. At convergence, R_1 = 0.0433, wR_2 = 0.1061 [$I > 2.0\sigma(I)$] and R_1 = 0.0531, wR_2 = 0.1149 (all data), for 469 parameters.

7.5. References

(1) I. Bhugun, D. Lexa and J.-M. Saveánt, *J. Am. Chem. Soc.*, 1996, **118**, 3982-3983.

(2) M. J. Rose, H. B. Gray and J. R. Winkler, *J. Am. Chem. Soc.*, 2012, **134**, 8310-8313.

(3) V. Artero and M. Fontecave, *C. R. Chimie*, 2008, **11**, 926-931.

(4) G. P. Connor, K. J. Mayer, C. S. Tribble and W. R. McNamara, *Inorg. Chem.*, 2014, **53**, 5408-5410.

(5) S. Kaur-Ghumaan, L. Schwartz, R. Lomoth, M. Stein and S. Ott, *Angew. Chem. Int. Ed.*, 2010, **49**, 8033-8036.

(6) M. Beyler, S. Ezzaher, M. Karnahl, M.-P. Santoni, R. Lomoth and S. Ott, *Chem. Commun.*, 2011, **47**, 11662-11664.

(7) A. Orthaber, M. Karnahl, S. Tschierlei, D. Streich, M. Stein and S. Ott, *Dalton Trans.*, 2014, **43**, 4537-4549.

(8) S. Roy, S. K. S. Mazinani, T. L. Groy, L. Gan, P. Tarakeshwar, V. Mujica and A. K. Jones, *Inorg. Chem.*, 2014, **53**, 8919-8929.

(9) R. D. Jackson, S. James, A. G. Orpen and P. G. Pringle, *J. Organomet. Chem.*, 1993, **458**, C3-C4.

(10) V. W.-W. Yam and S. W.-K. Choi, *J. Chem. Soc., Dalton Trans.*, 1996, 4227-4232.

(11) S. L. James, A. G. Orpen and P. G. Pringle, *J. Organomet. Chem.*, 1996, **525**, 299-301.

(12) V. W.-W. Yam, C.-L. Chan, S. W.-K. Choi, K. M.-C. Wong, E. C.-C. Cheng, S.-C. Yu, P.-K. Ng, W.-K. Chan and K.-K. Cheung, *Chem. Commun.*, 2000, **1**, 53-54.

(13) V. W.-W. Yam, C.-K. Li, C.-L. Chan and K.-K. Cheung, *Inorg. Chem.*, 2001, **40**, 7054-7058.

(14) J.-E. Song, B.-O. Kim and Y. Ha, *Mater. Sci. Eng. C*, 2004, **24**, 191-194.

(15) M. I. Bruce, P. A. Humphrey, S. Okucu, R. Schmutzler, B. W. Skelton and A. H. White, *Inorg. Chim. Acta*, 2004, **357**, 1805-1812.

(16) M. I. Bruce, P. A. Humphrey, R. Schmutzler, B. W. Skelton and A. H. White, *J. Organomet. Chem.*, 2004, **689**, 2415-2420.

(17) W. H. Watson, S. Kandala and M. G. Richmond, *J. Organomet. Chem.*, 2007, **692**, 968-975.

(18) V. N. Nesterov, W. H. Watson, S. Kandala and M. G. Richmond, *Polyhedron*, 2007, **26**, 3602-3608.

(19) S. E. Kabir, F. Ahmed, S. Ghosh, M. R. Hassan, M. S. Islam, A. Sharmin, D. A. Tocher, D. T. Haworth, S. V. Lindeman and T. A. Siddiquee, *J. Organomet. Chem.*, 2008, **693**, 2657-2665.

(20) S. Ghosh, G. Hogarth, S. E. Kabir, A. L. Miah, L. Salassa, S. Sharmin and C. Garino, *Organometallics*, 2009, **28**, 7047-7052.

(21) A. Rahaman, F. R. Alam, S. Ghosh, D. A. Tocher, M. Haukka, S. E. Kabir, E. Nordlander, G. Hogarth, *J. Organomet. Chem.*, 2014, **751**, 326-335.

(22) A. Rahaman, S. Ghosh, D. G. Unwin, S. Basak-Modi, K. B. Holt, S. E. Kabir, E. Nordlander, M. G. Richmond and G. Hogarth, *Organometallics*, 2014, **33**, 1356-1366.

(23) J. M. Camara and T. B. Rauchfuss, *J. Am. Chem. Soc.*, 2011, **133**, 8098-8101.

(24) S. Rana, *PhD thesis*, 2005, Jahangirnagar University.

(25) R. B. King, *J. Am. Chem. Soc.*, 1963, **85**, 1584-1587.

Chapter 8

Electrocatalytic proton reduction catalysed by the tetrairon-oxo cluster $[Fe_4(CO)_{10}(\kappa^2\text{-dppn})(\mu_4\text{-O})]^{2-}$ [dppn = 1,1′-bis(diphenylphosphino)naphthalene]

8.1. Introduction

In contrast to the multitude of contributions focused on model complexes of the active site of the [FeFe]-hydrogenase enzyme [1-5], the ability of non-enzyme-related iron complexes to catalyse proton reduction has been relatively neglected. Iron-containing low valent clusters are potentially useful in this respect as the highly delocalised nature of the bonding within the cluster core can give rise to low reduction potentials and stable reduced species [6-13]. Thus, metal carbonyl clusters have been shown to undergo a wide-range of reversible redox transformations and in some cases up to a significant number of stable redox states are accessible [14-20]. Berben and co-workers have recently reported that the tetrairon clusters $[NEt_4][Fe_4(CO)_{12}(\mu_4\text{-N})]$ [21,22] and $[NEt_4]_2[Fe_4(CO)_{12}(\mu_4\text{-C})]$ [22] are both efficient catalysts for proton reduction (Chart 8.1). Further, replacing the cation(s) with sodium leads to formation of water-soluble species which are able to generate hydrogen from aqueous acidic solutions [22]. Such clusters are potentially interesting catalysts as they are (in theory) able to bind hydrogen atoms to both electropositive metal centres (hydridic) and the (relatively) electronegative main group elements (acidic). Such binding is believed to be important in hydrogenases [23] and other catalytic processes [24-28] whereby acidic and hydridic hydrogens are held in close proximity (Chart 8.2).

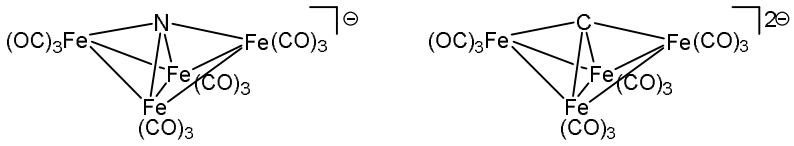

Chart 8.1. Tetrairon nitrido- and carbido- clusters tested as proton reduction catalyst [21,22].

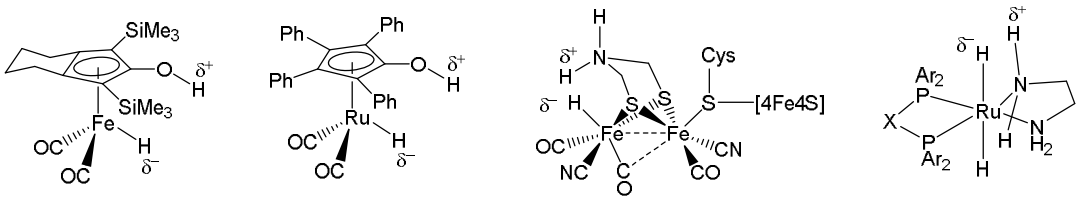

Chart 8.2. Catalysts employing the co-coordination of acidic and hydridic hydrogen atoms [24-28].

Low valent transition metal clusters containing oxo ligands are relatively rare as the latter is considered to be a *hard* π-donor ligand, while the cluster core is best stabilised by *soft* π-acceptor ligands [29-39]. For iron the most notable example of such an oxo cluster is $[Fe_3(CO)_9(\mu_3\text{-}O)]^{2-}$, which is formed in high yields from the reaction of oxygen with $[Fe_3(CO)_{11}]^{2-}$ [40-43]. In 2009 we reported the synthesis and crystal structure of the novel tetrairon-oxo cluster, $Fe_4(CO)_{10}(\kappa^2\text{-dppn})(\mu_4\text{-}O)$ (**8.1**) (dppn = 1,8-bis(diphenylphosphino)naphthalene), formed in low yields from the reaction of dppn with $Fe_3(CO)_{12}$ (Scheme 8.1) [44]. This cluster is seemingly closely related to both of the isoelectronic clusters $[Fe_4(CO)_{12}(\mu_4\text{-}N)]^-$ [45-48] and $[Fe_4(CO)_{12}(\mu_4\text{-}C)]^{2-}$ [49-53], although DFT calculations suggested that it was best considered as a Lewis acid-base pair of $[Fe_3(CO)_9(\mu_3\text{-}O)]^{2-}$ and $[Fe(CO)(\kappa^2\text{-dppn})]^{2+}$ [44], since the binding of the oxo ligand to the butterfly array of metal atoms was rather unsymmetrical. In contrast, both $[Fe_4(CO)_{12}(\mu_4\text{-}N)]^-$ [45-48] and $[Fe_4(CO)_{12}(\mu_4\text{-}C)]^{2-}$ [49-53] have approximate C_2-symmetry with the main-group atom binding equally to both wingtip metal atoms.

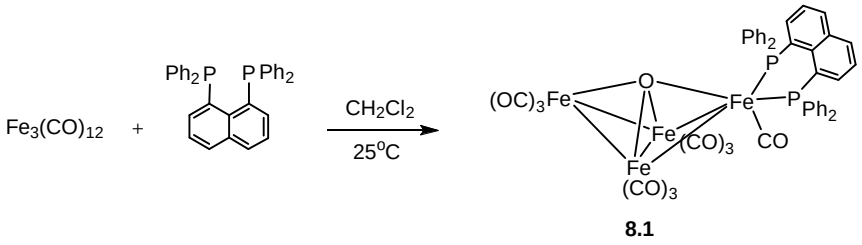

8.1

Scheme 8.1. Synthesis of $Fe_4(CO)_{10}(\kappa^2\text{-dppn})(\mu_4\text{-}O)$ (**8.1**) [44].

Oxo cluster **8.1** thus seemed a potentially useful candidate for assessment as a proton reduction catalyst as reduction may lead to scission of the oxo-Lewis acid interaction leaving a three-coordinate oxo ligand and an iron(0) centre, the former generating a site for an acidic hydrogen and the latter for a hydridic hydrogen ion. Herein we provide details of the electrochemistry of **8.1** and show that, while in its neutral or singly reduced state it is not active for proton reduction, upon addition of two electrons the generated

cluster dianion $[Fe_4(CO)_{10}(\kappa^2\text{-dppn})(\mu_4\text{-O})]^{2-}$ (**8.1**$^{2-}$) is an active proton reduction catalyst. Further we have used DFT calculations to probe the nature of **8.1**$^{2-}$ and protonated derivatives leading to the development of a mechanistic overview of its operation *via* two different but inter-related catalytic cycles.

8.2. Results and discussion

8.2.1. Protonation studies. In our earlier work [44] we detailed preliminary studies on the protonation of $Fe_4(CO)_{10}(\kappa^2\text{-dppn})(\mu_4\text{-O})$ (**8.1**) using $HBF_4{\cdot}Et_2O$ ($pK_a \approx 0.1$ in MeCN) [54] which resulted in the rapid (1-2 min) decolourization of the red solution with concomitant disappearance of all carbonyl bands. In order to try and develop conditions where **8.1** may be able to electrocatalyse the reduction of protons we screened its stability to a range of acids, monitoring this by IR spectroscopy. These results showed that it was stable in CH_2Cl_2 solution upon addition of excess Cl_2HCCO_2H ($pK_a \approx 13.2$ in MeCN) [54] and CF_3CO_2H ($pK_a \approx 12.7$ in MeCN) [54] as monitored by IR spectroscopy. Further the lack of any discernable changes to the IR spectrum in both cases (even after 2 h) indicated its inertness towards these acids in this solvent (Figure 8.1). Thus we conclude that **8.1** is stable in the presence of acids with pK_as above 12.

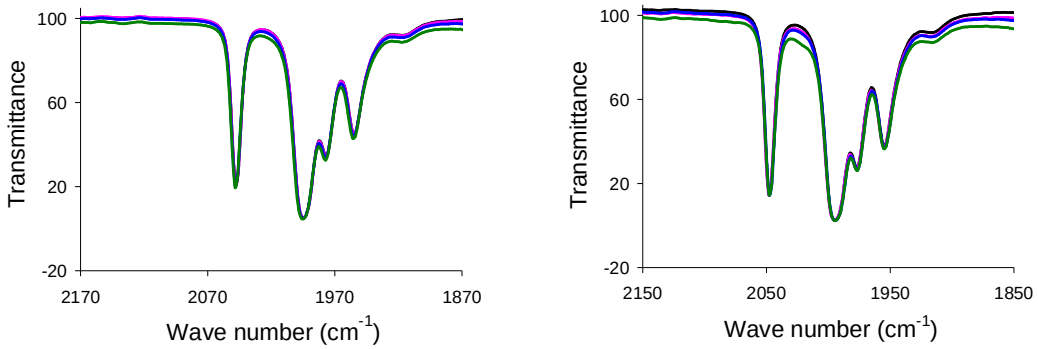

Figure 8.1. IR spectra of $Fe_4(CO)_{10}(\kappa^2\text{-dppn})(\mu_4\text{-O})$ (**8.1**) in the absence of (black) and in the presence of 1 (pink), 3 (blue) and 5 (green) molar equivalents of Cl_2HCCO_2H (a) and CF_3CO_2H (b) in CH_2Cl_2.

8.2.2. Electrochemistry. The electrochemical response of **8.1** was studied by cyclic voltammetry (CV) in both CH_2Cl_2 and a 1:1 mixture of CH_2Cl_2/MeCN (since the electrocatalytic proton reduction by **8.1** was carried out in CH_2Cl_2/MeCN). Unfortunately we were unable to record good quality CVs in pure MeCN due to the poor solubility of

8.1 in this solvent. The CV of **8.1** recorded in CH_2Cl_2 at scan rate 0.1 V/s is shown in Figure 8.2. In the cathodic region it shows a reversible reduction at $E_{1/2}$ = –1.02 V, followed by a second irreversible reduction E_p = –1.59 V. The first reductive response remains unchanged at all scan rates, while the reversibility of the second reductive process improves at higher scan rates (≥0.5 V/s). The CV also shows a reversible oxidation in the anodic domain at $E_{1/2}$ = 0.74 V, which remains unchanged at all scan rates. All redox responses originate from the diffusion controlled solution process as shown by the linear i_p vs $\sqrt{v}$ plots. We assume all the redox events observed in the CV of **8.1** involved one electron similar to those found in the related tetrairon nitride and carbide clusters [21,22]. These observations are consistent with formation of $[Fe_4(CO)_{10}(\kappa^2\text{-dppn})(\mu_4\text{-O})]^-$ (**8.1**$^-$) and $[Fe_4(CO)_{10}(\kappa^2\text{-dppn})(\mu_4\text{-O})]^+$ (**8.1**$^+$) which are stable within the timeframe of the experiment, and the dianion $[Fe_4(CO)_{10}(\kappa^2\text{-dppn})(\mu_4\text{-O})]^{2-}$ (**8.1**$^{2-}$) which has more limited stability, but nevertheless can be stable within the timeframe of the electrocatalytic transformations (see below).

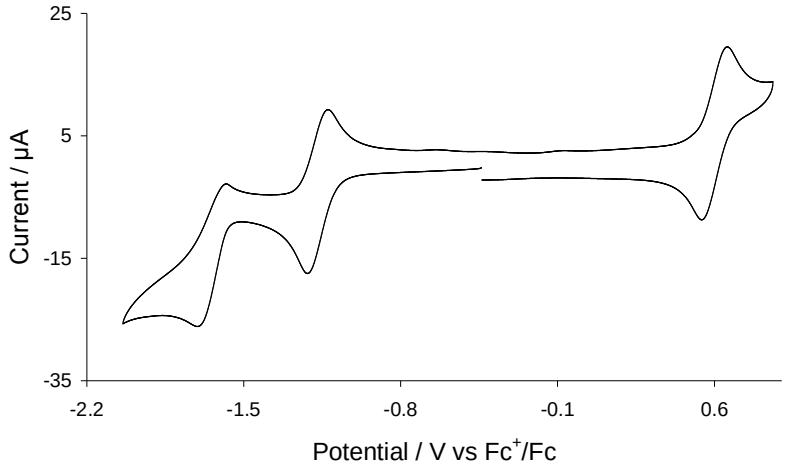

Figure 8.2. CV of $Fe_4(CO)_{10}(\kappa^2\text{-dppn})(\mu_4\text{-O})$ (**8.1**) in CH_2Cl_2 (1 mM solution, supporting electrolyte $[NBu_4][PF_6]$, scan rate 0.1 Vs^{-1}, glassy carbon electrode, potential vs Fc^+/Fc).

The CV of **8.1** in a 1:1 mixture of CH_2Cl_2/MeCN is shown in Figure 8.3. The cathodic region shows similar reductive features to those observed in CH_2Cl_2, namely a reversible reduction at $E_{1/2}$ = –1.26 V followed by an irreversible process at E_p = –1.78 V. In contrast, the anodic region is quite different from that observed in CH_2Cl_2 and shows a large irreversible oxidative wave at E_p = 0.45 V. Overall the redox responses in CH_2Cl_2/MeCN mixture appear at *ca.* 0.25 V more negative values than in CH_2Cl_2 alone. A new reduction peak is also seen at E_p = –1.46 V in CH_2Cl_2/MeCN when the anodic

region is scanned first due to the reduction of product formed upon irreversible oxidation. The height of this grows faster than the other reduction peaks as the scan rate is increased together with the appearance of an oxidative feature at E_p = –0.35 V on the return scan which is associated with this new reductive process. The linear dependence of i_p against $\sqrt{v}$ shows all these redox events are diffusion controlled.

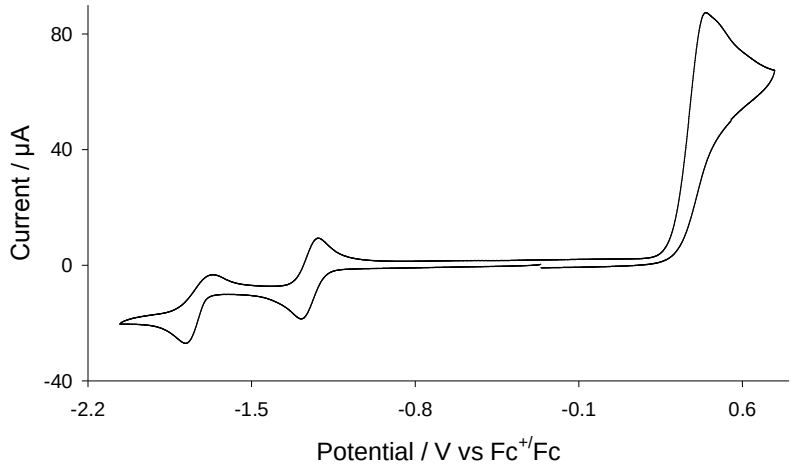

Figure 8.3. CV of $Fe_4(CO)_{10}(\kappa^2\text{-dppn})(\mu_4\text{-O})$ (**8.1**) in a 1:1 mixture of CH_2Cl_2/MeCN (1 mM solution, supporting electrolyte $[NBu_4][PF_6]$, scan rate 0.1 Vs^{-1}, glassy carbon electrode, potential vs Fc^+/Fc).

These observations are summarised in Scheme 8.2. Both the monoanion **8.1**$^-$ and monocation **8.1**$^+$ are stable in CH_2Cl_2 solutions, while in the presence of MeCN, **8.1**$^+$ is clearly unstable and presumably degrades to species which are oxidised at lower potentials than **8.1** giving rise to the relatively large current observed. The dianion **8.1**$^{2-}$ has some stability in CH_2Cl_2 and when MeCN is added this does not change significantly suggesting that MeCN does not coordinate to this cluster.

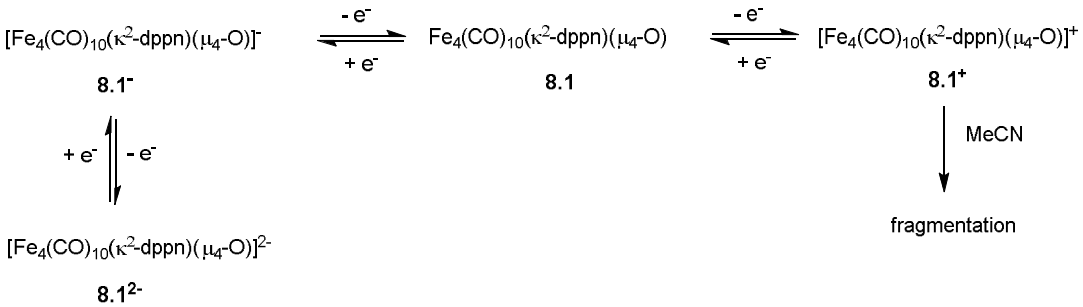

Scheme 8.2. Redox-states of $Fe_4(CO)_{10}(\kappa^2\text{-dppn})(\mu_4\text{-O})$ (**8.1**).

The results of these studies compare well with those of Diego Rail and Berben on the isoelectronic nitride cluster $[NEt_4][Fe_4(CO)_{12}(\mu_4\text{-N})]$ [21] when studied in MeCN. This

shows a reversible one-electron reduction at –1.23 V vs SCE and a second irreversible reduction at –1.6 V vs SCE associated with generation of $[Fe_4(CO)_{12}(\mu_4\text{-}N)]^{2-}$ and $[Fe_4(CO)_{12}(\mu_4\text{-}N)]^{3-}$ respectively. Given the different solvents used in the two studies it is not easy to compare reduction potentials directly, although it is perhaps not surprising that the oxo cluster, with its lower charge and more electronegative main-group element, reduce at somewhat lower potentials than the nitride cluster. A perhaps more significant difference is the enhanced stability of $\mathbf{8.1}^{2-}$ over $[Fe_4(CO)_{12}(\mu_4\text{-}N)]^{3-}$ and this could be important regarding the proposed addition of two-electrons leading to Fe–O bond scission and the creation of vacant coordination sites on both atoms. One somewhat unexpected difference between the two clusters relates to their oxidation behaviour, with $\mathbf{8.1}^{+}$ showing significant stability in the absence of MeCN. Berben and co-workers recorded CVs of $[Fe_4(CO)_{12}(\mu_4\text{-}N)]^{-}$ in MeCN [21] and water [22] and in both no stable oxidation product resulted. This may be simply a result of the strongly coordinating nature of both of these solvents.

8.2.3. Electrocatalysis. All electrocatalytic testing was carried out in a 1:1 mixture of CH_2Cl_2/MeCN. While the cation $\mathbf{8.1}^{+}$ is unstable in this medium, both the $\mathbf{8.1}^{-}$ and $\mathbf{8.1}^{2-}$ are stable on the electrochemical timeframe. Proton reduction catalysis was first tested with the relatively week acid, Cl_2HCCO_2H (pK_a ≈ 13.2 in MeCN). Figure 8.4 shows the CVs upon addition of up to 10 equivalents of acid to 1:1 mixture of CH_2Cl_2/MeCN solution of **8.1**.

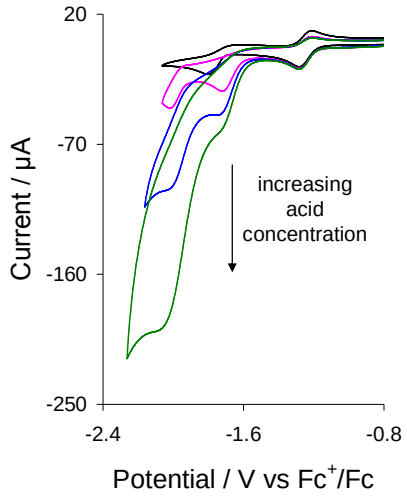

Figure 8.4. CVs of $Fe_4(CO)_{10}(\kappa^2\text{-dppn})(\mu_4\text{-}O)$ (**8.1**) in the absence and presence of 1, 4 and10 equivalents of Cl_2HCCO_2H (in a 1:1 mixture of CH_2Cl_2/MeCN, 1 mM solution, supporting electrolyte $[NBu_4][PF_6]$, scan rate 0.1 Vs^{-1}, glassy carbon electrode, potential vs Fc^{+}/Fc).

The second reduction peak shows *ca*. 70 mV positive shift with a increase of peak current upon addition of acid. The height of this peak grows slowly as the concentration of acid is increased which is characteristic of electrocatalytic proton reduction. A new catalytic peak is also seen at E_p = –2.00 V which increases sharply with acid concentration, but the catalysis becomes competitive at this potential due to the direct reduction of Cl_2HCCO_2H by the electrode.

In order to enhance the catalytic performance of **8.1** we carried out catalysis in presence of the relatively strong CF_3CO_2H. Figure 8.5 shows the CVs upon addition of between 1-10 equivalents of CF_3CO_2H. Akin to the catalytic event(s) observed with Cl_2HCCO_2H, **8.1** triggers a catalytic wave at its second reduction potential upon addition of CF_3CO_2H together with a second catalytic wave at E_p = –2.0 V but with well-resolved current. However, in this case the acid is not seen to reduce at the electrode within the potential range at which catalysis takes place and thus all catalytic current are attributed to the reduction of protons by **8.1**. The catalytic current of the second wave is almost double than that of the first wave, and the current obtained with CF_3CO_2H is also much better higher than that with Cl_2HCCO_2H, as might be expected for a stronger acid. The height of the oxidation peak remains unchanged upon addition of 10 equivalents CF_3CO_2H indicating no sign of degradation during catalysis.

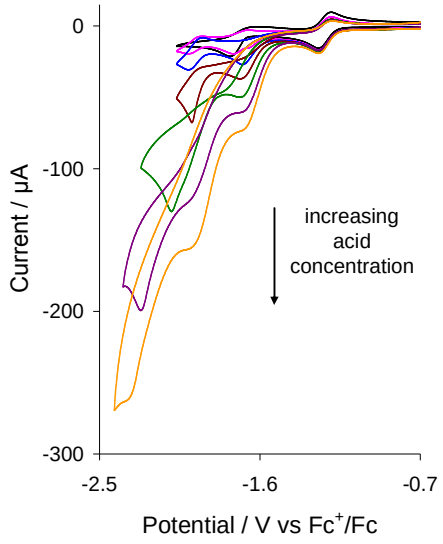

Figure 8.5. CVs of $Fe_4(CO)_{10}(\kappa^2\text{-dppn})(\mu_4\text{-O})$ (**8.1**) in the absence and presence of 1, 2, 3, 5, 8 and 10 equivalents of CF_3CO_2H (in a 1:1 mixture of CH_2Cl_2/MeCN, 1 mM solution, supporting electrolyte $[NBu_4][PF_6]$, scan rate 0.1 Vs^{-1}, glassy carbon electrode, potential vs Fc^+/Fc).

8.2.4. Density functional theory (DFT) calculations. In order to understand the structural consequences of electron addition to **8.1** and also in an attempt to identify likely protonation sites in order to support a clear mechanistic scheme for proton reduction, we have carried out a series of DFT calculations on **8.1** and **8.1**$^{2-}$. Initially we sought to reproduce the ground state structure of **8.1** as elucidated by X-ray crystallography [44]. Calculations show that in the ground state the hinge Fe–Fe bonding orbital is the major component of the HOMO while the LUMO is delocalised over all five atoms constituting the trigonal-bipyramidal core of the cluster and the naphthalene ring (Figure 8.6). After two-electron reduction, the HOMO of the reduced species (**8.1**$^{2-}$) looks similar to the LUMO of neutral **8.1**, and the LUMO is now localized over the naphthalene ring and adjacent iron (Figure 8.7).

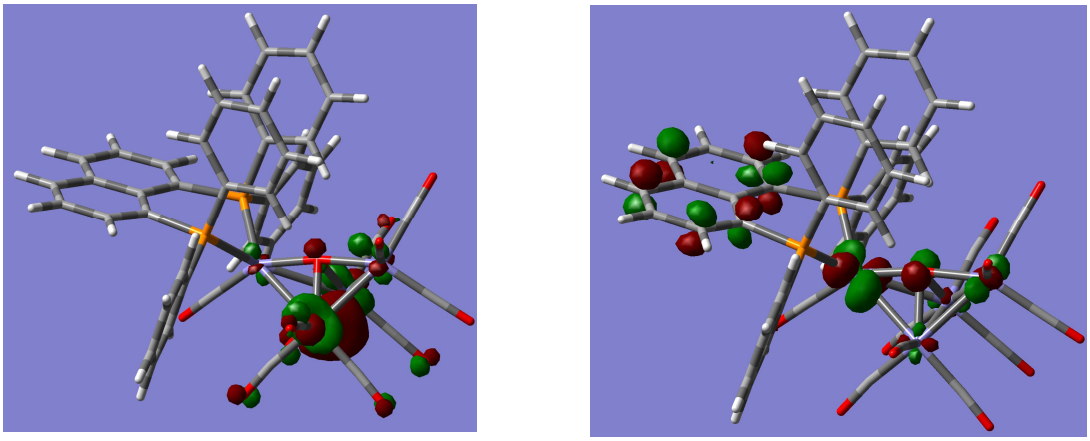

HOMO **LUMO**

Figure 8.6. HOMO and LUMO of $Fe_4(CO)_{10}(\kappa^2\text{-dppn})(\mu_4\text{-O})$ (**8.1**) (calculations were carried out by collaborator).

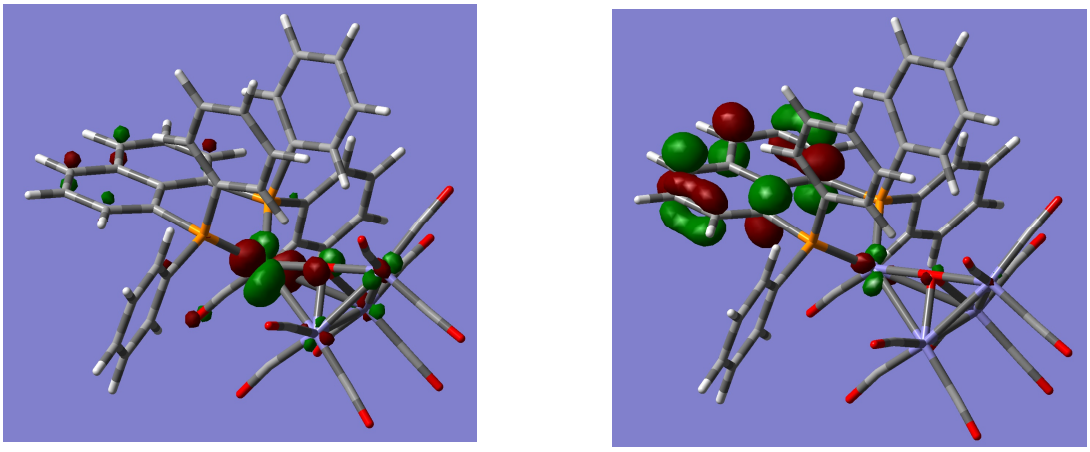

HOMO **LUMO**

Figure 8.7. HOMO and LUMO of $[Fe_4(CO)_{10}(\kappa^2\text{-dppn})(\mu_4\text{-O})]^{2-}$ (**8.1**$^{2-}$) (calculations were carried out by collaborator).

Analysis of atomic charges (Table 8.1) reveals that in **8.1**$^{2-}$ the negative charge is mainly accumulated on the iron atom directly bonded to dppn ligand. The Wiberg bond index for Fe_1–Fe_2 and Fe_1–Fe_3 bonds are 0.28 and 0.29 respectively in **8.1** and 0.13 in **8.1**$^{2-}$ (Table 8.1), the latter value is 46% smaller than those vectors in the neutral cluster, which suggests that these two bond weaken considerably after two-electron reduction. The value for the Fe_1–O(oxo) bonds also decrease from 0.61 (in **8.1**) to 0.45 (in **8.1**$^{2-}$) while the change in the indices for other three Fe–O(oxo) bonds are insignificant. Overall, two-electron reduction of **8.1** promotes the expansion of the trigonal-pyramid containing the dppn-substituted iron center and does not lead to scission of any of the Fe–O(oxo) bonds.

Table 8.1. Selected natural charges and Wiberg bond indices for clusters **8.1** and **8.1**$^{2-}$.[a]

Species	8.1	8.1^{2-}
Atomic Charge		
Fe_1	–0.62	–0.80
Fe_2	–1.26	–1.22
Fe_3	–1.26	–1.22
Fe_4	–1.10	–1.23
P_1	1.31	1.23
P_2	1.30	1.23
O(oxo)	–0.37	–0.44
Wiberg bond index		
Fe_1–Fe_2	0.28	0.13
Fe_1–Fe_3	0.29	0.13
Fe_2–Fe_3	0.52	0.49
Fe_2–Fe_4	0.44	0.45
Fe_3–Fe_4	0.44	0.45
Fe_1–P_1	0.73	0.68
Fe_3–P_2	0.73	0.68
Fe_1–O(oxo)	0.61	0.45
Fe_2–O(oxo)	0.51	0.54
Fe_3–O(oxo)	0.52	0.55
Fe_4–O(oxo)	0.59	0.55

[a]Atom numbers for species **8.1** and **8.1**$^{2-}$ are based on the numbering sequence for the structure depicted below:

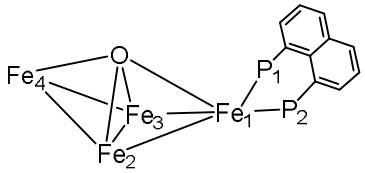

8.4.5. Mechanistic considerations. Berben and co-workers have addressed the mechanism of proton reduction with $[Fe_4(CO)_{12}(\mu_4\text{-N})]^-$ as a pre-catalyst both in MeCN [21] and in aqueous solutions [22]. The major features of the catalysis do not vary significantly with changes in solvent and an ECCE mechanism is favoured (Scheme 8.3). Thus, $[Fe_4(CO)_{12}(\mu_4\text{-N})]^-$ is not catalytically active, nor does it bind protons strongly.

Thus in MeCN, catalysis occurs at the potential of the one-electron reduced species, $[Fe_4(CO)_{12}(\mu_4\text{-}N)]^{2-}$, showing that this is a key catalytic intermediate. This cluster protonates readily to afford $[Fe_4(CO)_{12}(\mu_4\text{-}N)H]^-$ and it is protonation of this species to give $[Fe_4(CO)_{12}(\mu_4\text{-}N)H_2]$ which is rate-limiting, with subsequent reduction and loss of hydrogen being facile. This is in accord with their experimental observation that the strength of the acid is a key factor in the rate of the hydrogen evolution reaction [21]. In water, a similar reaction scheme is proposed [22] and here $[Fe_4(CO)_{12}(\mu_4\text{-}N)H]^-$ was directly observed *via* its oxidation to yield $HFe_4(CO)_{12}(\mu_4\text{-}N)$. Berben and co-workers did not attempt to identify proton binding sites or delineate structural changes to the cluster upon reduction.

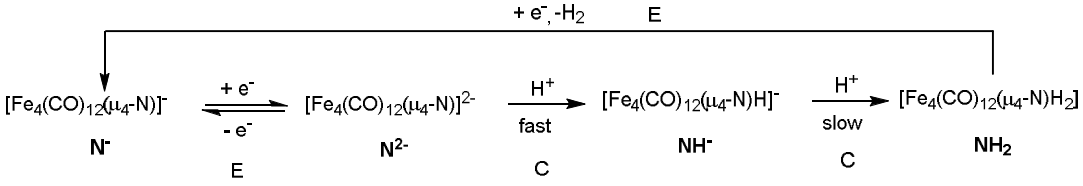

Scheme 8.3. Electrocatalytic proton reduction by $[Fe_4(CO)_{12}(\mu_4\text{-}N)]^-$.

In contrast, when $[Fe_4(CO)_{12}(\mu_4\text{-}C)]^{2-}$ was employed as a pre-catalyst in water a significantly different mechanistic scheme for proton reduction was seen (Scheme 8.4). Now protonation of the dianion was coupled with protonation to afford $[Fe_4(CO)_{12}(\mu_4\text{-}C)H]^{2-}$ which in turn undergoes a second proton-coupled electron transfer to afford $[Fe_4(CO)_{12}(\mu_4\text{-}C)H_2]^{2-}$ with liberation of hydrogen closing the catalytic cycle [22].

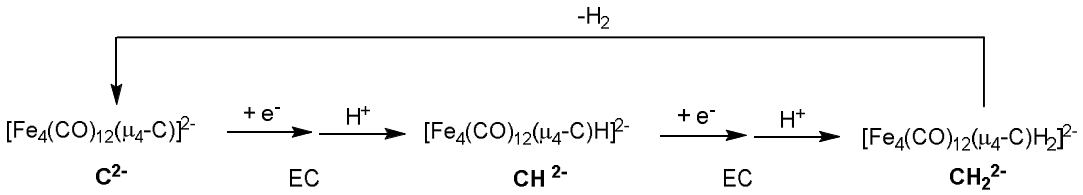

Scheme 8.4. Electrocatalytic proton reduction by $[Fe_4(CO)_{12}(\mu_4\text{-}C)]^{2-}$.

On the basis of the electrochemical and electrocatalytic results when **8.1** is used as a pre-catalyst we propose that two interlinked catalytic cycles are operating, the relative rates of which are dependent upon acid type and concentration (Scheme 8.5).

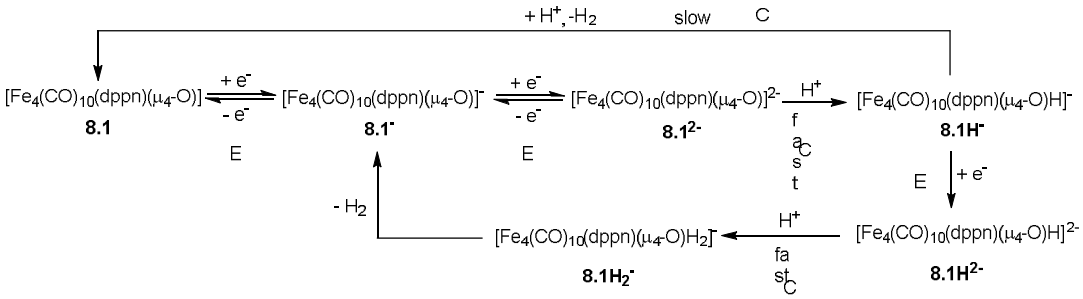

Scheme 8.5. Electrocatalytic proton reduction by $[Fe_4(CO)_{10}(\kappa^2\text{-dppn})(\mu_4\text{-O})]$ (**8.1**).

Thus, it is clear from both Figures 8.4 and 8.5 that $[Fe_4(CO)_{10}(\kappa^2\text{-dppn})(\mu_4\text{-O})]^-$ (**8.1**$^-$) is not catalytically active and that two catalytic process operate on at the approximate reduction potential of **8.1**$^-$ which clearly involves formation of $[Fe_4(CO)_{10}(\kappa^2\text{-dppn})(\mu_4\text{-O})]^{2-}$ (**8.1**$^{2-}$) and the second which takes place at around –2.0 V, a potential that is not associated with any unprotonated tetrairon-oxo species. In order to account for these observations we suggest that protonation of **8.1**$^{2-}$ is rapid and generates $[Fe_4(CO)_{10}(\kappa^2\text{-dppn})(\mu_4\text{-O})H]^-$ (**8.1H**$^-$) which can then either undergo a second protonation to afford $Fe_4(CO)_{10}(\kappa^2\text{-dppn})(\mu_4\text{-O})H_2$ (**8.1H$_2$**) (not shown) and either this event or loss of hydrogen is rate-limiting to regenerate **8.1** *via* an overall EECC mechanism. Given the slow rate of protonation of **8.1H**$^-$ it has a life-time long enough to undergo a further reduction to generate **8.1H**$^{2-}$ a process which occurs at *ca.* –2 V. Protonation of **8.1H**$^{2-}$ is then expected to be relatively rapid with loss of hydrogen resulting in generation of **8.1**$^-$. Thus, this overall process proceeds *via* an ECEC mechanism. That the rate of protonation of **8.1H**$^-$ is the determining factor regarding the relative amounts of hydrogen generated by each cycle is supported by experiments using different acids. Thus with the relatively weak acid Cl_2HCCO_2H (pK_a = 13.2) the current from the lower potential process does not vary significantly upon addition of excess acid, while that associated with the second process does. In contrast, with CF_3CO_2H (pK_a = 12.7) both processes increase notably upon successive addition of acid although the rate of increase of the ECEC process (at –2.0 V) is faster than that for the EECC cycle.

Since two-electron reduction leads to expansion of one of the trigonal-pyramids of **8.1** instead of Fe–O(oxo) or Fe–Fe bond scission, it is difficult to identify the proton binding site in **8.1**$^{2-}$. To identify this and also to understand the structural changes taking place during catalysis, we probed the EECC catalytic cycle by DFT calculations. These show

that protonation takes place at the dppn-bound iron in **8.1**$^{2-}$, with concomitant cleavage of one of the wingtip-hinge Fe–Fe bonds (Figure 8.8a), to form **8.1H**$^{-}$. The negative charge is mainly accumulated on the dppn-bound iron atom in **8.1**$^{2-}$, as shown by the atomic charge analysis which also supports this protonation behaviour (Table 8.1). The second wingtip-hinge Fe–Fe bond involving this iron is also found to be significantly longer after protonation with a bond distance of 2.761 Å as compared to the average wingtip-hinge Fe–Fe bond distance of 2.650 Å in **8.1**. However, the Wiberg bond index suggests a weak bonding interaction between these two iron atoms. The second protonation lead to the formation of a hydrogen complex, **8.1H$_2$**, in which hydrogen is bonded to the dppn-bound iron atom (Figure 8.8b). This species releases hydrogen and regenerates **8.1** *via* the 62-electron cluster **8.1′** which has an open Fe–Fe edge as shown in Scheme 8.6. Cluster **8.1′** can either undergo two-electron reduction to regenerate the dianion **8.1**$^{2-}$ or undergo bond closure to regenerate the starting cluster **8.1**, and the energy difference between **8.1** and **8.1′** is only *ca*. 2 kcalmol^{-1} in the gas phase (Figure 8.9).

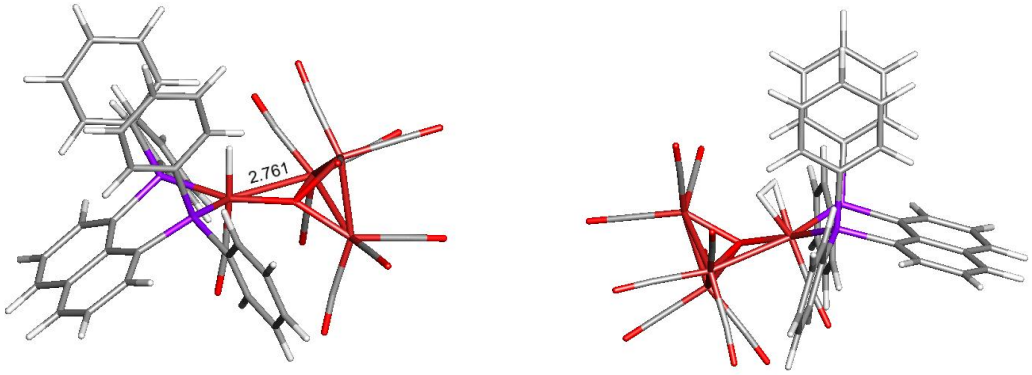

(a) (b)

Figure 8.8. B3LYP-optimized structure of $[Fe_4(CO)_{10}(\kappa^2\text{-dppn})(\mu_4\text{-O})H]^-$ (**8.1H**$^-$) and $Fe_4(CO)_{10}(\kappa^2\text{-dppn})(\mu_4\text{-O})H_2$ (**8.1H$_2$**) (calculations were carried out by collaborator).

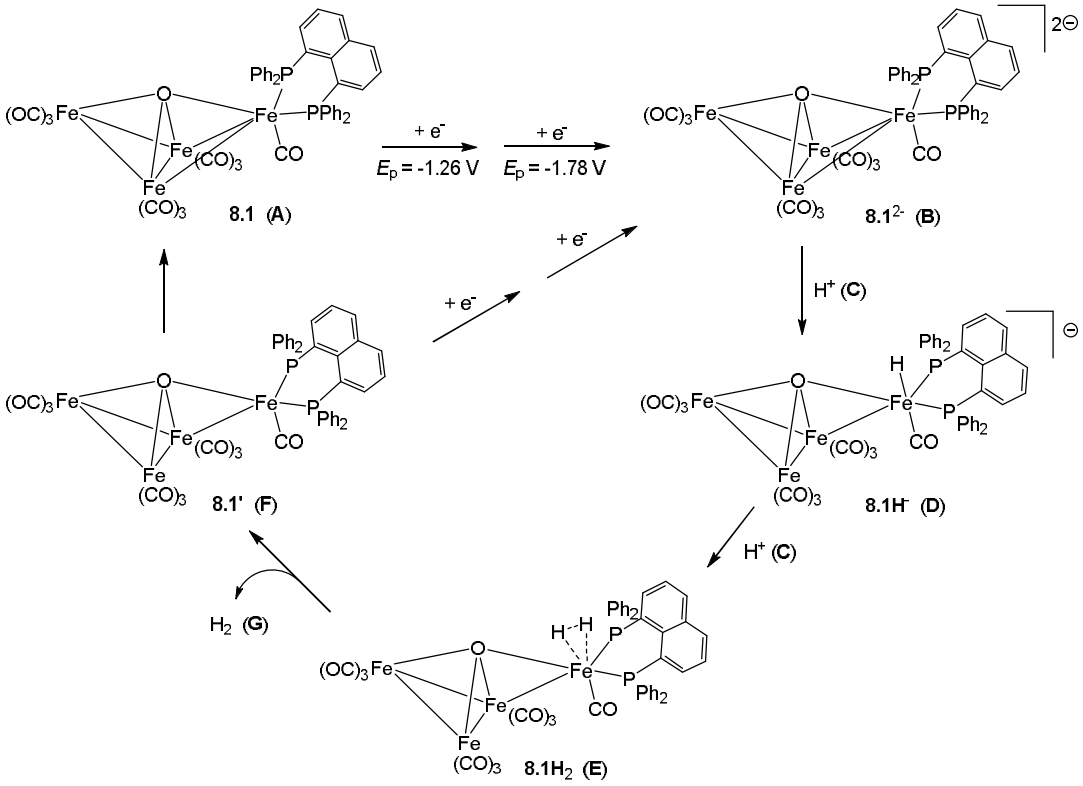

Scheme 8.6. Proposed mechanism for electrocatalytic proton reduction by **8.1**.

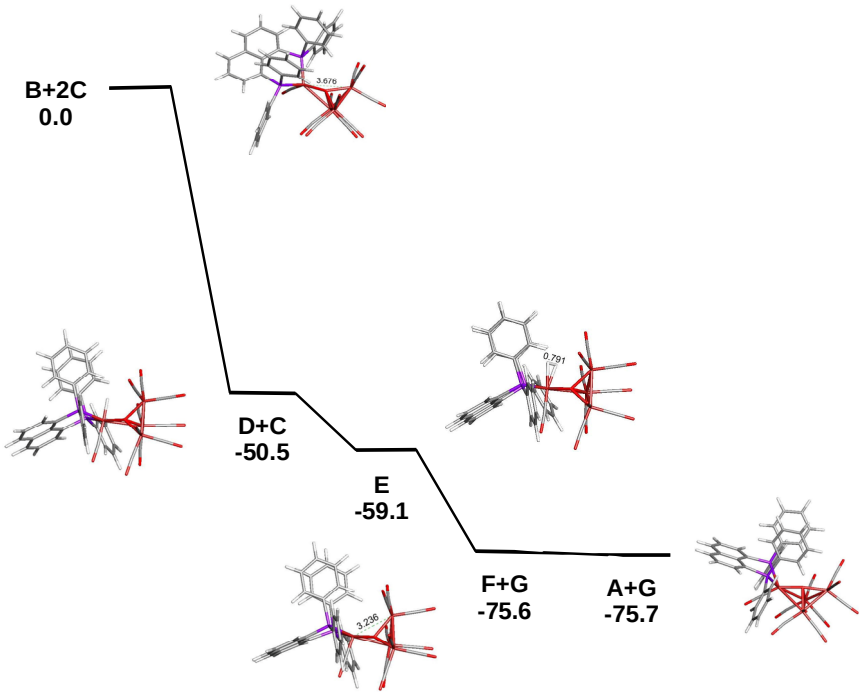

Figure 8.9. B3LYP-optimized structures and free energy surface for the reaction of the dianion **8.1**$^{2-}$ (**B**) with H^+ (**C**). Energy values are in kcalmol^{-1} with respect to **B**+**2C**. The optimized structure of the liberated H_2 (**G**) that accompanies **8.1′** (**F**) and **8.1** (**A**) is not shown (calculations were carried out by collaborator).

8.3. Summary and conclusions

The tetrairon-oxo cluster $Fe_4(CO)_{10}(\kappa^2\text{-dppn})(\mu_4\text{-O})$ (**8.1**) has been studied as a proton reduction catalyst. The cluster contains a trigonal bipyramidal core consists of an oxygen and four iron atoms. Acidification studies show that **8.1** is stable in presence of acid with pK_a >12 but does not undergo protonation. It degrades rapidly in presence of strong acid such as $HBF_4{\cdot}Et_2O$ (pK_a ≈ 0.1 in MeCN). The cluster undergoes two sequential one-electron reductions to generate $\mathbf{8.1}^-$ and $\mathbf{8.1}^{2-}$ respectively which are stable on the voltammetric timescale. The oxidised species $\mathbf{8.1}^+$ is also stable in CH_2Cl_2 but undergoes fragmentation (probably by reacting with MeCN) when 1:1 mixture of CH_2Cl_2/MeCN was used as solvent. Electrocatalytic studies carried out in presence of Cl_2HCCO_2H and CF_3CO_2H show that **8.1** becomes catalytically active at its second reduction potential with the catalytic current depending on acid strength. At least two competitive catalytic cycles are involved in the proton reduction event by **8.1** leading to two distinct catalytic waves in presence of acid.

DFT calculations carried out to identify the proton binding site and structural changes during catalysis show that the cluster remains intact after two-electron reduction. One of the trigonal pyramids expand by this process instead of Fe–Fe or Fe–O(oxo) bond cleavage, the latter being highly expected since **8.1** was best described as a Lewis acid-base pair of $[Fe_3(CO)_9(\mu_3\text{-O})]^{2-}$ and $[Fe(CO)(\kappa^2\text{-dppn})]^{2+}$ [44]. Cluster $\mathbf{8.1}^{2-}$ protonates at the wingtip iron bonded to dppn with concomitant rapture of one of the wingtip-hinge Fe–Fe bonds. Overall results suggest that the $[Fe_3(CO)_9(\mu_3\text{-O})]^{2-}$ moiety acts as a bidentate ligand to $[Fe(CO)(\kappa^2\text{-dppn})]^{2+}$ fragment where the catalysis takes place and the oxygen atom has no direct role in the catalysis, although its electronegativity probably serves to stabilise generated anionic species.

8.4. Experimental Section

8.4.1. General. IR spectra were recorded using a Nicolet 6700 FT-IR spectrometer in a solution cell fitted with calcium fluoride plates, subtraction of the solvent absorptions being achieved by computation.

8.4.1. Preparation of $Fe_4(CO)_{10}(\kappa^2$-dppn)(μ_4-O) (8.1) [44]**.** To a CH_2Cl_2 solution (20 mL) of $Fe_3(CO)_{12}$ (200 mg, 0.397 mmol) was added dppn (148 mg, 0.299 mmol) and the mixture was stirred under nitrogen for 24 h at room temperature. The solvent was removed under vacuum and the residue separated by TLC on silica gel. Elution with hexane/CH_2Cl_2 (2:1, v/v) developed three bands. The first gave a small amount of unreacted $Fe_3(CO)_{12}$, while the contents of the second was too small for complete characterization. The third band yielded $Fe_4(CO)_{10}(\kappa^2$-dppn)(μ_4-O) (**8.1**) (31 mg, 10%) as deep red crystals after recrystallization from hexane/CH_2Cl_2 at 4°C.

8.4.2. Computational details. DFT calculations were performed with the Gassian09 package of programs [55]. The calculations were carried out with the B3LYP functional, which utilizes the Becke three-parameter exchange functional (B3) [56] combined with the correlation functional of Lee, Yang, and Parr (LYP) [57]. The iron atoms were described by Stuttgart-Dresden effective core potentials (ecp) and an SDD basis set, while the 6-31+G(d') basis set was employed for the remaining atoms.

The geometries reported for all species were fully optimized and the analytical Hessian afforded only positive eigenvalues for each ground-state structure. The computed frequencies were used to make zero-point and thermal corrections to the electronic energies, and the reported free energies are quoted in kcal/mol relative to the specified standard. The computed frequencies were used to make zero-point and thermal corrections to the electronic energies.

In order to evaluate the thermodynamics for proton reduction, the solvation energy of proton [$\Delta G_{solv}(H^+)$] was determined in dichloroethane (DCE) using the known pK_a of phenol (19.6) and the following equation:

$$\Delta G_{solv}(H^+) = \Delta G_{solv}(HA) - \Delta G_{solv}(A^-) + 2.303RTpK_a$$

The effect of DCE solvent on all iron-containing species was calculated using the polarizable continuum model (PCM) through single-point calculations of the gas-phase optimized geometry. The resulting solvation free energy was appropriately added to the ΔG_{gas} to yield ΔG_{solv}. Use of DCE in place of DCM as the solvent was dictated by the availability of the pK_a data for a wide variety of acid-base equilibria in the former solvent [58]. Standard-state corrections were added to all species to convert concentrations from 1 atm to 1 M, as outlined in the treatise by Cramer [59].

The Wiberg bond indices were computed using Weinhold's natural bond orbital (NBO) program, as executed by Gaussian 09 [60,61]. The geometry-optimized structures were drawn with the *JIMP*2 molecular visualization and manipulation program [62,63].

8.5. References

(1) I. P. Georgakaki, L. M. Thomson, E. J. Lyon, M. B. Hall and M. Y. Darensbourg, *Coord. Chem. Rev.*, 2003, **238-239**, 255-266.

(2) D. J. Evans and C. J. Pickett, *Chem. Soc. Rev.*, 2003, **32**, 268-275.

(3) T. B. Rauchfuss, *Inorg. Chem.*, 2004, **43**, 14-26.

(4) L. Sun, B. Åkermark and S. Ott, *Coord. Chem. Rev.*, 2005, **249**, 1653-1663.

(5) X. Liu, S.K. Ibrahim, C. Tard and C.J. Pickett, *Coord. Chem. Rev.*, 2005, **249**, 1641-1652.

(6) S. Ghosh, G. Hogarth, K. B. Holt, S. E. Kabir, A. Rahaman and D. G. Unwin, *Chem. Commun.*, 2011, **47**, 11222-11224.

(7) A. Rahaman, S. Ghosh, D. G. Unwin, S. Basak-Modi, K. B. Holt, S. E. Kabir, E. Nordlander, M. G. Richmond and G. Hogarth, *Organometallics*, 2014, **33**, 1356-1366.

(8) Z. Li, X. Zeng, Z. Niu and X. Liu, *Electrochimica Acta*, 2009, **54**, 3638-3644.

(9) J. Yeo, M. H. Cheah, M. I. Bondin and S. P. Best, *Aust. J. Chem.*, 2012, **65**, 241-253.

(10) W. Gao, J. Sun, M. Li, T. Åkermark, K. Romare, L. Sun, B. Åkermark, *Eur. J. Inorg. Chem.*, 2011, 1100-1105.

(11) C. A. Mebi, K. E. Brigance and R. B. Bowman, *J. Braz. Chem. Soc.*, 2012, **23**, 186-189.

(12) M. H. Cheah, C. Tard, S. J. Borg, X. Liu, S. K. Ibrahim, C. J. Pickett and S. P. Best, *J. Am. Chem. Soc.*, 2007, **129**, 11085-11092.

(13) C. Tard, X. Liu, D. L. Hughes and C. J. Pickett, *Chem. Commun*., 2005, 133-135.

(14) S. R. Drake, *Polyhedron*, 1990, **9**, 455-474.

(15) G. Longoni, C. Femoni, M. C. Iapalucci and P. Zanello, in *Metal Clusters in Chemistry*, Eds. P. Braunstein, L. A. Oro and P. R. Raithby, 1999, **2**, 1137-1158.

(16) G. Hogarth, S. E. Kabir and E. Nordlander, *Dalton Trans.*, 2010, **39**, 6153-6174.

(17) T. M. Bockman and J. K. Kochi, *J. Am. Chem. Soc.*, 1987, **109**, 7725-7735.

(18) Q. Zhao, T. D. Harris and T. A. Betley, *J. Am. Chem. Soc.*, 2011, **133**, 8293-8306.

(19) R. J. H. Clark, P. J. Dyson, D. G. Humphrey and B. F. G. Johnson, *Polyhedron*, 1998, **17**, 2985-2991.

(20) M. P. Cifuentes, M. G. Humphrey and G. A. Heath, *Inorg. Chim. Acta*, 1997, **259**, 273-280.

(21) M. D. Rail and L. A. Berben, *J. Am. Chem. Soc.*, 2011, **133**, 18577-18579.

(22) A. D. Nguyen, M. D. Rail, M. Shanmugam, J. C. Fettinger and L. A. Berben, *Inorg. Chem.*, 2013, **52**, 12847-12854.

(23) H.J. Fan and M.B. Hall, *J. Am. Chem. Soc.*, 2001, **123**, 3828-3829.

(24) C. P.Casey and H. Guan, *J. Am. Chem. Soc.*, 2007, **129**, 5816-5817.

(25) R. Noyori and T. Ohkuma, *Angew. Chem. Int. Ed.*, 2001, **40**, 40-73.

(26) T. Ikariya, K. Murata and R. Noyori, *Org. Biomol. Chem.*, 2006, **4**, 393-406.

(27) Y. Shvo, D. Czarkie, Y. Rahamim and D. F. Chodosh, *J. Am. Chem. Soc.*, 1986, **108**, 7400-7402.

(28) C. P. Casey, S. W. Singer, D. R. Powell, R. K. Hayashi and M. Kavana, *J. Am. Chem. Soc.*, 2001, **123**, 1090-1100.

(29) J. Y. Park, J. R. Shapley, C. Bueno, J. W. Ziller and M. R. Churchill, *Organometallics*, 1988, **7**, 2307-2316.

(30) L. Xu and K. H. Whitmire, *Organometallics*, 2002, **21**, 2581-2583.

(31) J.-H. Gong, D.-K. Hwang, C.-W. Tsay, Y. Chi, S.-M. Peng and G.-H. Lee, *Organometallics*, 1994, **13**, 1720-1727.

(32) M. R. Churchill, C. Bueno, J. T. Park and J. R. Shapley, *Inorg. Chem.*, 1984, **23**, 1017-1021.

(33) Y. Chi, L. Hwang, G.-H. Lee and S.-M. Peng, *J. Chem. Soc., Chem. Commun.*, 1988, 1456-1457.

(34) Y. Chi, J. R. Shapley, J. Ziller and M. R. Churchill, *Organometallics*. 1987, **6**, 301-307.

(35) R. J. Goudsmit, B. F. G. Johnson, J. Lewis, P. R. Raithby and K. H. Whitmire, *J. Chem. Soc., Chem. Commun.*, 1983, 246-247.

(36) G. Lavigne, N. Lugan and J.-J. Bonnet, *Nouv. J. Chim.*, 1981, **5**, 423-425.

(37) Md. D. H. Sikder, S. Ghosh, S. E. Kabir, G. Hogarth and D. A. Tocher, *Inorg. Chim. Acta*, 2011, **376**, 170-174.

(38) C.K. Schauer and D.F. Shriver, *Angew. Chem., Int. Ed.*, 1987, **26**, 255-256.

(39) C. K. Schauer, S. Harris, M. Sabat, E. J. Voss and D. F. Shriver, *Inorg. Chem.*, 1995, **34**, 5017-5028.

(40) A. Ceriotti, L. Resconi, F. Demartin, G. Longoni, M. Manassero and M. Sansoni, *J. Organomet. Chem.*, 1983, **249**, C35-C37.

(41) C. Femoni, M.C. Iapalucci, G. Longoni, S. Zacchini and E. Zazzaroni, *Dalton Trans.*, 2007, 2644-2651.

(42) V. G. Albano, C. Castellari, C. Femoni, M. C. Iapalucci, G. Longoni, M. Monari, M. Rauccio and S. Zacchini, *Inorg. Chim. Acta*, 1999, **291**, 372-379.

(43) L. A. Poliakova, S. P. Gubin, O. A. Belyakova, Y. V. Zubavichus and Y. L. Slovokhotov, *Organometallics*, 1997, **16**, 45274530.

(44) S. Ghosh, G. Hogarth, S. E. Kabir, A. L. Miah, L. Salassa, S. Sultana and C. Garino, *Organometallics*, 2009, **28**, 7047-7052.

(45) D. E. Fjare and W. L. Gladfelter, *Inorg. Chem.*, 1981, **20**, 3533-3539.

(46) D. E. Fjare and W. L. Gladfelter, *J. Am. Chem. Soc.*, 1981, **103**, 1572-1574.

(47) P. Zanello, F. Laschi, A. Cinquantini, R. D. Pergola, L. Garlaschelli, M. Cucco, F. Demartin and T. R. Spalding, *Inorg. Chim. Acta*, 1994, **226**, 1-8.

(48) M. Tachikawa, J. Stein, E. L. Muetterties, R. G. Teller, M. A. Beno, E. Gebert and J. M. Williams, *J. Am. Chem. Soc.*, 1980, **102**, 6648-6649.

(49) J. H. Davies, M. A. Beno, J. M. Williams, J. Zimmie, M. Tachikawa and E. L. Muetterties, *Proc. Natl. Acad. Sci. U.S.A.*, 1981, **78**, 668-671.

(50) J. S. Bradley, G. B. Ansell, M. E. Leonowicz and E. W. Hill, *J. Am. Chem. Soc.*, 1981, **103**, 4968-4970.

(51) S. Harris, M. L. Blohm and W. L. Gladfelter, *Inorg. Chem.*, 1989, **28**, 2290-2297.

(52) M. Tachikawa and E.L. Muetterties, *J. Am. Chem. Soc.*, 1980, **102**, 4541-4542.

(53) M. A. Beno, J. M. Williams, M. Tachikawa and E. L. Muetterties, *J. Am. Chem. Soc.*, 1980, **102**, 4542-4544.

(54) K. Izutsu, *in Acid-Base Dissociation Constants in Dipolar Aprotic Solvents*, Blackwell Scientific Publications, Oxford, 1990.

(55) M. J. Frisch *et al.*, Gaussian 09, Revision E.01, Gaussian, Inc., Wallingford, CT, USA, 2009.

(56) A. D. Becke, *J. Chem. Phys.*, 1993, **98**, 5648-5652.

(57) C. Lee, W. Yang and R. G. Parr, *Phys. Rev. B*, 1988, **37**, 785-789.

(58) E. Raamat, K. Kaupmees, G. Ovsjannikov, A. Trummal, A. Kütt, J. Saame, I. Koppel, I. Kaljurand, L. Lipping, T. Rodima, V. Pihl, I. A. Koppel and I. Leito, *J. Phys. Org. Chem.*, 2013, **26**, 162-170.

(59) C. J. Cramer, *Essentials of Computational Chemistry*, 2nd Ed.; Wiley: Chichester, UK, 2004, p. 378-379.

(60) A. E. Reed, L. A. Curtiss and F. Weinhold, *Chem. Rev.*, 1988, **88**, 899-926.

(61) K. B. Wiberg, *Tetrahedron*, 1968, **24**, 1083-1096.

(62) JIMP2, version 0.091, a free program for the visualization and manipulation of molecules: M. B. Hall and R. F. Fenske, *Inorg. Chem.*, 1972, **11**, 768-775.

(63) J. Manson, C. E. Webster and M. B. Hall, Texas A&M University, College Station, TX, 2006: http://www.chem.tamu.edu/jimp2/index.html.

Chapter 9

Electrocatalytic proton reduction by thiolate-capped triiron hydride clusters $Fe_3(CO)_9(\mu_3\text{-}SR)(\mu\text{-}H)$ (R = ^{i}Pr, ^{t}Bu)

9.1. Introduction

As detailed in the previous chapter, while the development of iron-based electrocatalysts for H_2 evolution almost entirely centres around the structural mimics of the active site of [FeFe]-hydrogenase enzyme, [1-5] researchers are beginning to explore alternate iron sources such as low-valent clusters. The proton reduction ability of non-enzyme-related iron complexes has been relatively neglected, even though the first report of electrocatalytic proton reduction by an iron complex dated back to 1996 when Saveánt and co-workers reported electrocatalytic proton reduction by the Fe porphyrin complex, [(TPP)Fe(Cl)] (TPP = tetraphenylporphyrin), at reasonable catalytic rates [6]. More recently, as discussed in Chapters 6 and 7, mononuclear catalysts based on single iron atom have been developed by several groups [7-16] that can catalyze proton reduction more efficiently compared to the most structural biomimics of the enzyme [16].

Low-valent iron clusters have attracted attention as potential electrocatalysts due to the presence of highly delocalised bonding in their core that often leads to low reduction potentials and stable reduced species. In addition to the tetrairon clusters [17,18] discussed in the previous chapter, the sulphide-capped triiron cluster $Fe_3(CO)_9(\mu_3\text{-}S)_2$ (**9A**) [19,20] and it 1,2-bis(diphenylphosphino)ethylene (dppv) derivative $Fe_3(CO)_5(\kappa^2\text{-}dppv)_2(\mu_3\text{-}S)_2$ [21] have also been tested as proton reduction catalysts (Chart 9.1). Cluster **9A** undergoes two sequential one-electron reductions and exhibits catalytic wave in presence of acid. This cluster does not react with acid and the strength of the latter plays an important role in catalysis as the cluster becomes an active catalysts at the first reduction potential in presence of $HBF_4{\cdot}Et_2O$ [19], whereas it takes two electrons before reacting with CH_3CO_2H [20]. In contrast, the dppv derivative, $Fe_3(CO)_5(\kappa^2\text{-}dppv)_2(\mu_3\text{-}S)_2$, protonates by strong acid such as $HBF_4{\cdot}Et_2O$ and displays catalytic event initiated by protonation [21]. Recently, we also investigated a bis(diphenylphosphino)methane (dppm) derivative of **9A** and its selenide- and telluride-derivatives (Chart 9.1) and found that the chalcogenides exert a significant influence on their redox response and electrochemical properties [22].

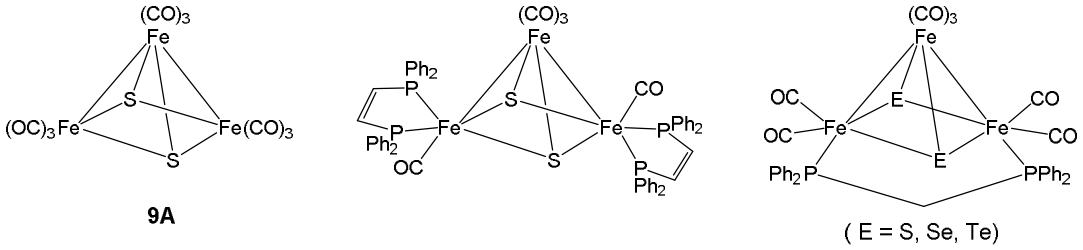

Chart 9.1. Sulphido-capped triiron clusters tested as proton reduction catalysts [19-22].

Cluster $Fe_3(CO)_9(\mu_3\text{-}S)_2$ (**9A**) follows a relatively complex mechanism during electrocatalytic proton reduction in presence of strong acid such as $HBF_4{\cdot}Et_2O$ as it partially loses CO after one-electron reduction to form **9A–CO** which is also catalytically active [19]. It has been proposed that three different catalytically active species are responsible for proton reduction within the investigated potential range (between –1.6 and –0.5 V) as shown in Scheme 9.1. The first catalytic wave around –1.0 V is assigned to **9A** while the second wave around –1.3 is comprised of contribution from both **9A–CO** and the doubly protonated species **$H_2$9A**. In contrast, **9A** follows a simple EECC mechanism during H_2 formation from weak acids e.g. CH_3CO_2H [20].

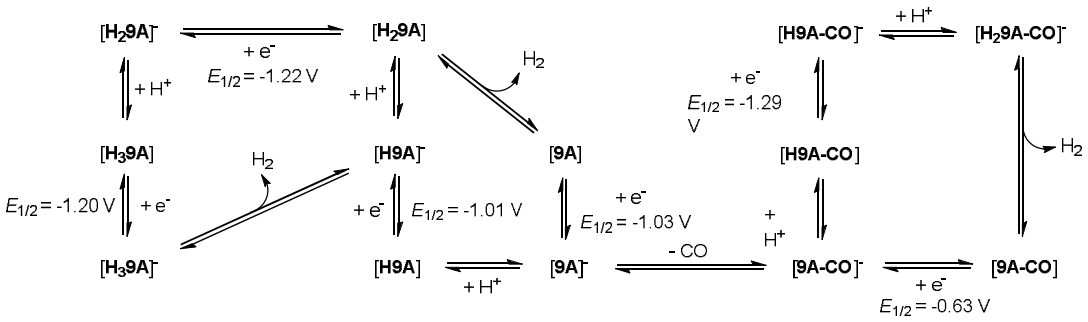

Scheme 9.1. Proposed mechanism for electrocatalytic proton reduction by $Fe_3(CO)_9(\mu_3\text{-}S)_2$ (**9A**) in presence of $HBF_4{\cdot}Et_2O$ [19].

Thus thiolate-capped low-valent triiron clusters are potentially interesting candidates for electrocatalytic proton reduction and a number of such triiron clusters have been reported [23-27]. As part of a preliminary study we have tested two clusters, namely $Fe_3(CO)_9(\mu_3\text{-}S^iPr)(\mu\text{-}H)$ (**9.1**) and $Fe_3(CO)_9(\mu_3\text{-}S^tBu)(\mu\text{-}H)$ (**9.2**), as proton reduction catalysts and found that both are capable of reducing protons at their monoanionic state. DFT

calculations have also been carried out in order to understand the nature of radical anion and protonated derivatives to shed light on the catalytic cyclic.

9.2. Results and discussion

9.2.1. Syntheses. Clusters **9.1** and **9.2** were first synthesized by Beer and Haines in 1970 from the direct reaction between equimolar amount of $Fe_3(CO)_{12}$ and RSH (R = ^{i}Pr, ^{t}Bu) at 80°C (Scheme 9.2). They also found that the use of excess thiol leads to the fragmentation of the trinuclear framework to give primarily $Fe_2(CO)_6(\mu\text{-SR})_2$ [23]. The use of less bulky thiol always results in the formation of only $Fe_2(CO)_6(\mu\text{-SR})_2$ [23]. Both clusters were characterised by spectroscopic data [23], and later by X-ray crystallography [26,27].

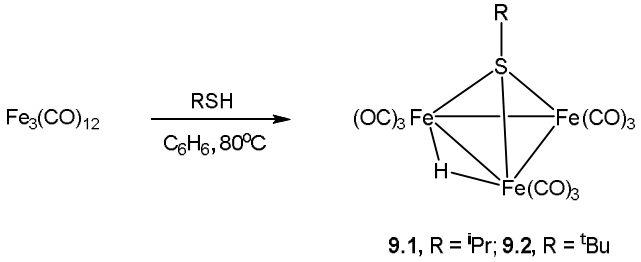

Scheme 9.2. Synthesis of $Fe_3(CO)_9(\mu_3\text{-S}^{i}\text{Pr})(\mu\text{-H})$ (**9.1**) and $Fe_3(CO)_9(\mu_3\text{-S}^{t}\text{Bu})(\mu\text{-H})$ (**9.2**).

Earlier diffraction data for **9.1** and **9.2** were collected at room temperature and we thus collected a low temperature data set for **9.1,** an ORTEP diagram generated from the new data is shown in Figure 9.1. Although we obtained a different polymorph, metric parameters are very similar to those reported earlier by Bau *et. al.* [26]. The molecule consists of an isosceles triangle of three irons [Fe(1)─Fe(2) 2.6874(5), Fe(1)─Fe(3) 2.6380(5) and Fe(2)─Fe(3) 2.6365(5) Å] coordinated by nine carbonyls, a face-capping isopropyl thiolate ligand and a bridging hydride. The carbonyls are evenly distributed among three irons and the thiolate ligand asymmetrically caps one face of the metal triangle [Fe(1)─S(1) 2.1411(7), Fe(2)─S(1) 2.1446(6) and Fe(3)─S(1) 2.1198(7) Å]. The hydride was located from a difference map which spans across the longest Fe─Fe vector and lie on the opposite face of the metallic plane with respect to the thiolate ligand. The OC─Fe─Fe angles along this edge opens up significantly due to hydride disposition [C(1)─Fe(1)─Fe(2) 105.44(8) and C(4)─Fe(2)─Fe(1) 106.07(9)°] as expected. The ^{1}H NMR spectrum of **9.1** shows a high-field singlet at –23.76 ppm indicating the presence of

a bridging hydride within the molecule in addition to a septet and a doublet at 4.20 and 1.70 ppm, respectively, with an intensity ratio of in 1:7, which are attributed to the methine and methyl protons of the isopropyl thiolate ligand.

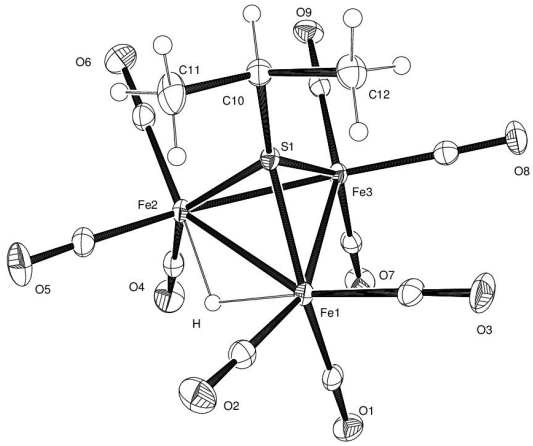

Figure 9.1. An ORTEP diagram of the molecular structure of $Fe_3(CO)_9(\mu_3\text{-}S^iPr)(\mu\text{-}H)$ (**9.1**). Selected bond distances (Å) and angles (º): Fe(1)─Fe(2) 2.6874(5), Fe(1)─Fe(3) 2.6380(5), Fe(2)─Fe(3) 2.6365(5), Fe(1)─S(1) 2.1411(7), Fe(2)─S(1) 2.1446(6), Fe(3)─S(1) 2.1198(7), Fe(1)─Fe(2)─Fe(3) 59.396(12), Fe(2)─Fe(1)─Fe(3) 59.341(12), Fe(2)─Fe(3)─Fe(1) 61.263(12), Fe(1)─S(1)─Fe(2) 77.67(2), Fe(2)─S(1)─Fe(3) 76.37(2), Fe(3)─S(1)─Fe(1) 76.50(2), S(1)─Fe(1)─Fe(2) 51.226(17), S(1)─Fe(1)─Fe(3) 51.108(19), S(1)─Fe(2)─Fe(1) 51.386(18), C(1)─Fe(1)─Fe(2) 105.44(8), C(4)─Fe(2)─Fe(1) 106.07(9), C(2)─Fe(1)─Fe(2) 102.29(8), C(5)─Fe(2)─Fe(1) 101.80(9).

9.2.2. Protonation and electrochemistry. Since protonation is a key step in the electrocatalytic proton reduction, clusters **9.1** and **9.2** were treated with a range of acids [CH_3CO_2H (p$K_a \approx 22.3$), CF_3CO_2H (p$K_a \approx 12.7$) and $HBF_4{\cdot}Et_2O$ (p$K_a \approx 0.1$)] in CH_2Cl_2 for protonation [28]. IR spectroscopic data shows that they do not react with these acids and are stable in these acidic solutions even in presence of air. Thus, IR spectra of both **9.1** and **9.2** recorded in presence of excess $HBF_4{\cdot}Et_2O$ do not show any discernable change after several hours of standing. CVs of **9.1** and **9.2** recorded in CH_2Cl_2 at a scan rate of 0.1 V/s are shown in Figure 9.2. Both display a quasi-reversible reduction wave in the cathodic region together with a large irreversible oxidative wave in the anodic domain. The reversibility of the reductive process of both clusters improves with scan rate, whilst the oxidative process remains irreversible at all scan rates (0.025 to 1 V/s) (Figure 9.3). The linear plot obtained by plotting reductive peak currents against square root of scan rates indicates that the reductive feature of both clusters originates from the diffusion controlled solution process.

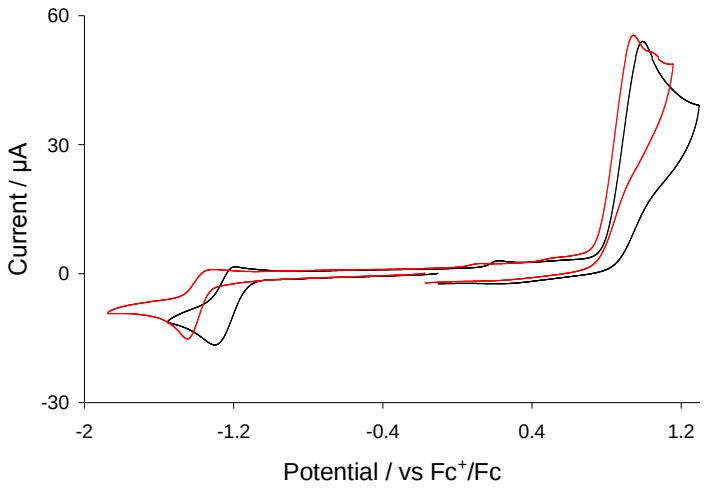

Figure 9.2. CVs of $Fe_3(CO)_9(\mu_3\text{-}S^iPr)(\mu\text{-}H)$ (**9.1**) (black) and $Fe_3(CO)_9(\mu_3\text{-}S^tBu)(\mu\text{-}H)$ (**9.2**) (red) in CH_2Cl_2 (1 mM solution, supporting electrolyte $[NBu_4][PF_6]$, scan rate 0.1 Vs^{-1}, glassy carbon electrode, potential vs Fc^+/Fc).

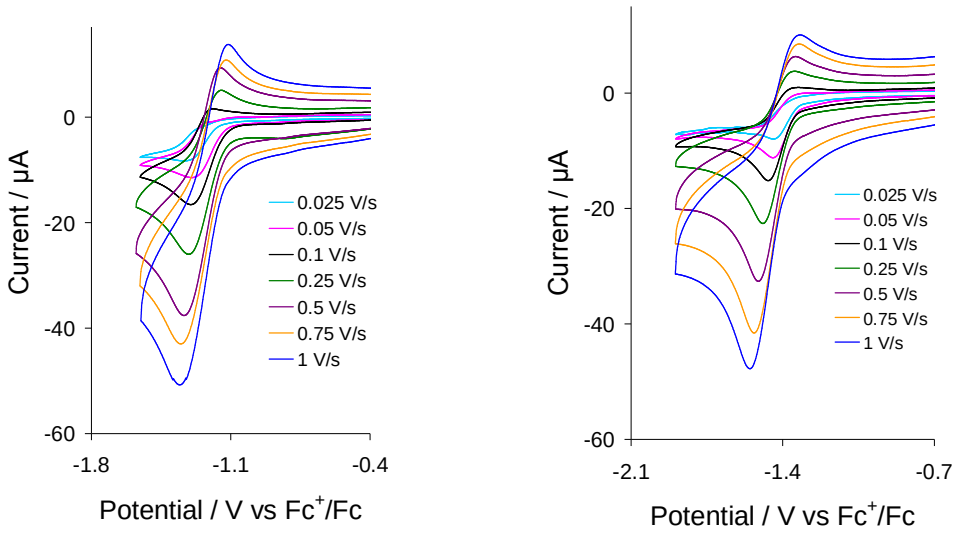

Figure 9.3. CVs of $Fe_3(CO)_9(\mu_3\text{-}S^iPr)(\mu\text{-}H)$ (**9.1**) (a) and $Fe_3(CO)_9(\mu_3\text{-}S^tBu)(\mu\text{-}H)$ (**9.2**) (b) at various scan rates as shown in the legend (in CH_2Cl_2, 1 mM solution, supporting electrolyte $[NBu_4][PF_6]$, scan rate 0.1 Vs^{-1}, glassy carbon electrode, potential vs Fc^+/Fc).

The reduction potential of **9.2** shows 160 mV negative shift due to presence of an additional methyl group on the thiolate ligand ($E_{1/2}$ = –1.24 V for **9.1** and $E_{1/2}$ = –1.40 V for **9.2**), while it has little effect on the oxidation potential ($E_{1/2}$ = 0.99 V for **9.1** and $E_{1/2}$ = 0.93 V for **9.2**). The peak current of the anodic wave of the reductive process observed on the return scan at scan rate 0.1 V/s is *ca.* 50% compared to that of the cathodic wave

on the forward scan (i_{an}/i_{ca} ~ 0.5 for both **9.1** and **9.2**) suggesting the radical anion has limited stability on the CV timescale. In order to get a better understanding on the redox processes of **9.1** and **9.2** we have calculated the ground state electronic structure of the related hypothetical cluster $Fe_3(CO)_9(\mu_3\text{-SMe})(\mu\text{-H})$ (**9.3**). The LUMO of **9.3** is spread over all three iron atoms and is anti-bonding in nature (Figure 9.4) which suggests that its reduction would simply expand the metal triangle. Hence reduction should show full chemical reversibility (i_{an}/i_{ca} ~ 1), but the experimentally observed results indicate that a secondary chemical process takes place after reduction. As a result we extended our calculations to the radical anion $\mathbf{9.3}^-$ (Figure 9.5) and found that it is a 49-electron open cluster with two formal iron-iron bonds i.e. one electron reduction of **9.3** leads to the cleavage of one of the non-hydride-bridged iron-iron bonds. We assume that a similar iron-iron bond scission step followed the reduction of **9.1** and **9.2** which is responsible for the poor chemical reversibility of the process at slow scan rates (Scheme 9.3). The major component of HOMO in $\mathbf{9.3}^-$ is located on the terminal iron bonded to hydride making it a credible site for proton binding during catalysis (see later).

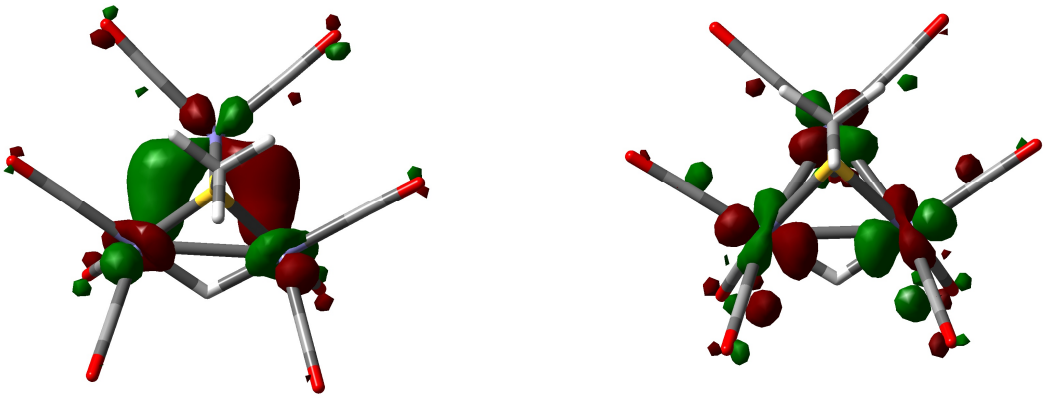

HOMO **LUMO**

Figure 9.4. HOMO and LUMO of $Fe_3(CO)_9(\mu_3\text{-SMe})(\mu\text{-H})$ (**9.3**) (calculations were carried out by collaborator).

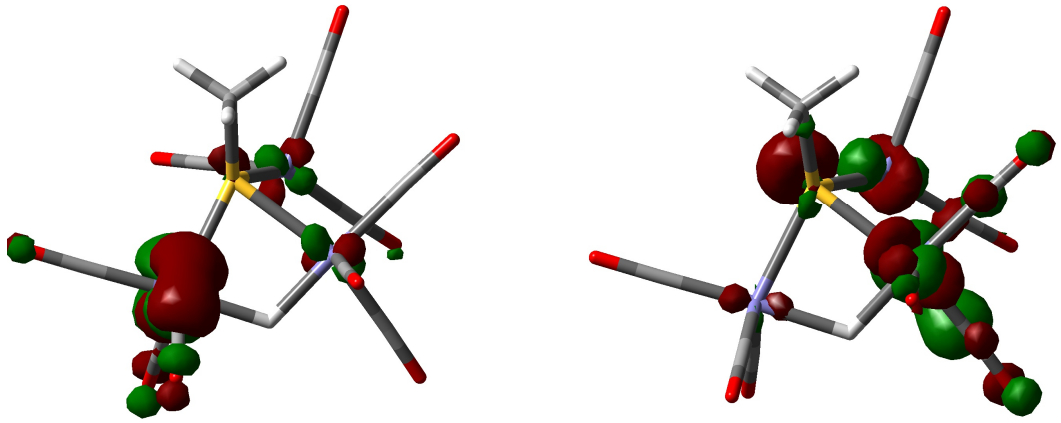

Figure 9.5. HOMO and LUMO of $[Fe_3(CO)_9(\mu_3\text{-SMe})(\mu\text{-H})]^-$ (**9.3**$^-$) (calculations were carried out by collaborator).

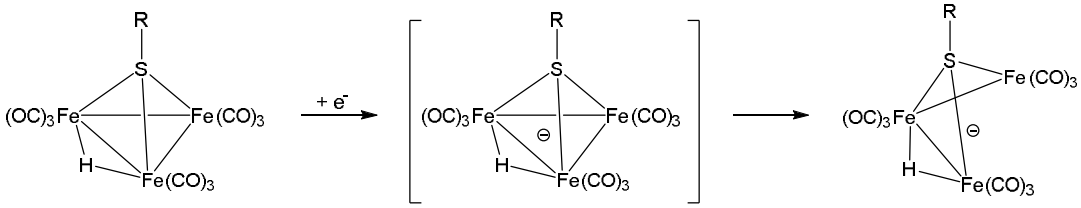

Scheme 9.3. Reduction of $Fe_3(CO)_9(\mu_3\text{-SR})(\mu\text{-H})$ and the following chemical process.

9.2.3. Electrocatalysis. Electrocatalytic testing of **9.1** and **9.2** were carried out in CH_2Cl_2 in presence of CF_3CO_2H and $HBF_4{\cdot}Et_2O$. Both clusters induce catalytic waves at their first reduction potential in presence of acid (Figures 9.6 and 9.7). The catalytic current obtained for **9.1** is marginally greater than that of **9.2** which levels off at higher acid concentrations (Figure 9.8a). The limiting current is also higher for $HBF_4{\cdot}Et_2O$ compared to that for CF_3CO_2H indicating that the rate of catalysis is dependent on acid strength (Figure 9.8b).

Since both clusters do not protonate by the acids used as proton source, we propose an ECEC mechanism for H_2 evolution as shown in Scheme 9.4 (process I). The catalysis is commenced by reduction followed by a protonation to form $H_2Fe_3(CO)_9(\mu_3\text{-SR})$. We assume that this 49-electron open cluster (since one-electron reduction results in iron-iron bond scission) cannot release hydrogen, so it undergoes a further reduction to form 50-electron, $[H_2Fe_3(CO)_9(\mu_3\text{-SR})]^-$. The latter release hydrogen and forms $[Fe_3(CO)_9(\mu_3\text{-}$

SR)]$^-$ which then reacts with a proton to regenerate the starting cluster. The anion $[Fe_3(CO)_9(\mu_3\text{-}SR)]^-$ can also be accessed by deprotonating $Fe_3(CO)_9(\mu_3\text{-}SR)(\mu\text{-}H)$ with a base e.g. *n*-C_4H_9Li or C_5H_5Na, and forms a stable salt [27].

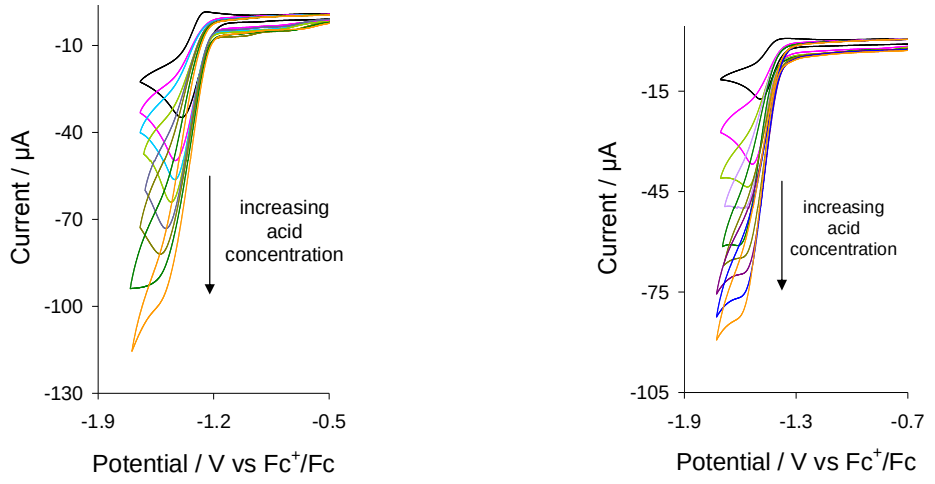

(a) (b)

Figure 9.6. (a) CVs of $Fe_3(CO)_9(\mu_3\text{-}S^iPr)(\mu\text{-}H)$ (**9.1**) in the absence and presence of 1, 2, 3, 5, 6, 8 and 10 molar equivalents of CF_3CO_2H; (b) CVs of $Fe_3(CO)_9(\mu_3\text{-}S^tBu)(\mu\text{-}H)$ (**9.2**) in the absence and presence of 1, 2, 3, 4, 5, 6, 8 and 10 molar equivalents of CF_3CO_2H (in CH_2Cl_2, 1 mM solution, supporting electrolyte $[NBu_4][PF_6]$, scan rate 0.1 Vs^{-1}, glassy carbon electrode, potential vs Fc^+/Fc).

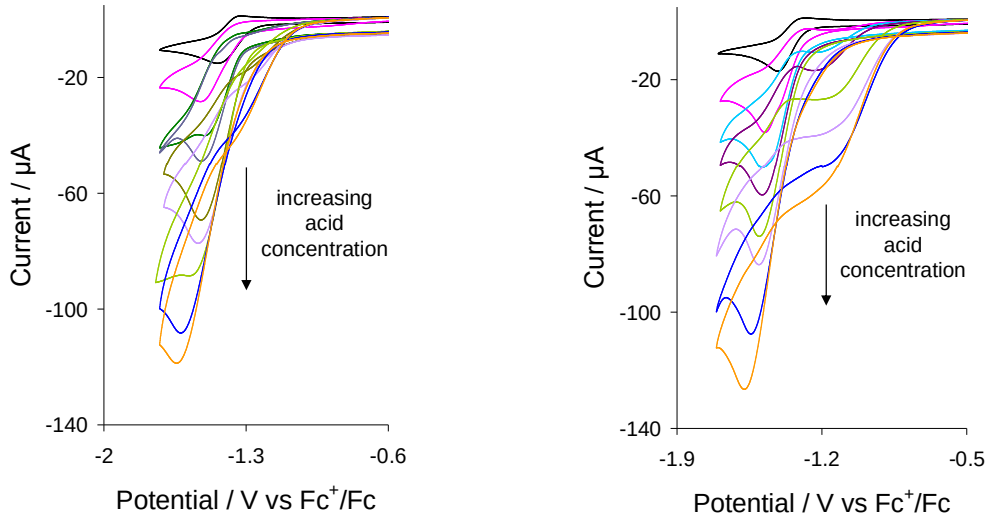

(a) (b)

Figure 9.7. (a) CVs of $Fe_3(CO)_9(\mu_3\text{-}S^iPr)(\mu\text{-}H)$ (**9.1**) in the absence and presence of 1, 2, 3, 4, 6, 8 and 10 molar equivalents of $HBF_4{\cdot}Et_2O$; (b) CVs of $Fe_3(CO)_9(\mu_3\text{-}S^tBu)(\mu\text{-}H)$ (**9.2**) in the absence and presence of 1, 3, 4, 6, 7, 8, 9 and 10 molar equivalents of $HBF_4{\cdot}Et_2O$ (in CH_2Cl_2, 1 mM solution, supporting electrolyte $[NBu_4][PF_6]$, scan rate 0.1 Vs^{-1}, glassy carbon electrode, potential vs Fc^+/Fc).

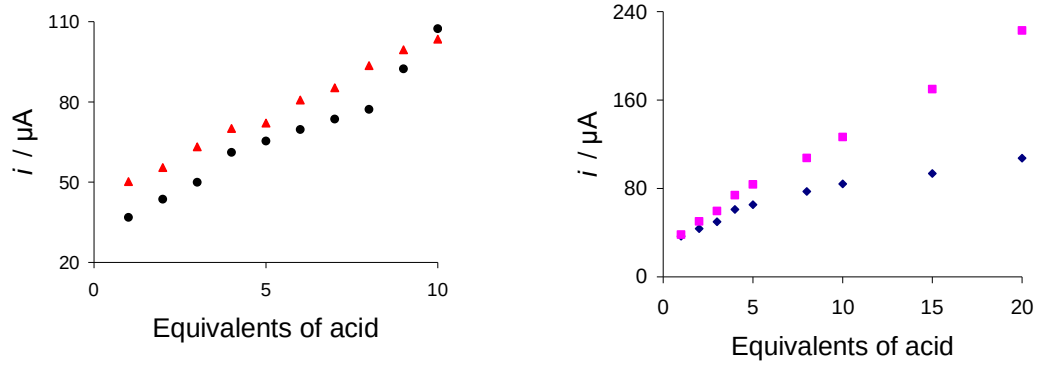

(a) (b)

Figure 9.8. (a) Plot of catalytic limiting current *vs.* equivalents of CF_3CO_2H added for $Fe_3(CO)_9(\mu_3\text{-}S^iPr)(\mu\text{-}H)$ (**9.1**) (red triangles) and $Fe_3(CO)_9(\mu_3\text{-}S^tBu)(\mu\text{-}H)$ (**9.2**) (black circles); (b) Plot of catalytic limiting current *vs.* equivalents of CF_3CO_2H (black diamonds) and $HBF_4{\cdot}Et_2O$ (pink squares) added for $Fe_3(CO)_9(\mu_3\text{-}S^tBu)(\mu\text{-}H)$ (**9.2**).

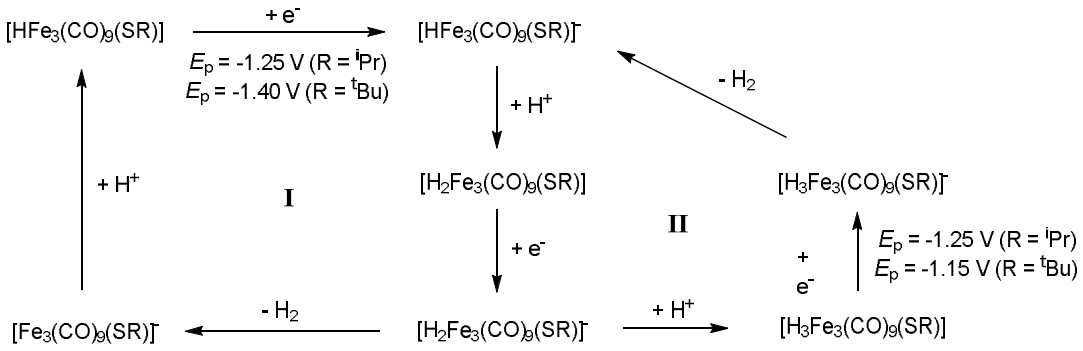

Scheme 9.4. Proposed mechanism for electrocatalytic proton reduction by $Fe_3(CO)_9(\mu_3\text{-}SR)(\mu\text{-}H)$.

The CV of both clusters show a build-up of reduction current on the return scan in presence of $HBF_4{\cdot}Et_2O$ (*ca.* –1.25 V for **9.1** and *ca.* –1.15 V for **9.2**). This suggests that a more easily reducible product or intermediate is formed during catalysis, possibly *via* a slow chemical reaction, that is sufficiently stable to build-up in solution and migrate back to the electrode for reduction at a more positive potential [29]. We assume that the release of hydrogen from $[H_2Fe_3(CO)_9(\mu_3\text{-}SR)]^-$ is slow, and it undergoes further protonation in presence of strong acid $HBF_4{\cdot}Et_2O$ to form $H_3Fe_3(CO)_9(\mu_3\text{-}SR)$ which release hydrogen on the return scan as shown by process II in Scheme 9.4. The absolute structures of various species involved in the proposed mechanism is not known except the radical anion $[HFe_3(CO)_9(\mu_3\text{-}SR)]^-$ and deprotonated anion $[Fe_3(CO)_9(\mu_3\text{-}SR)]^-$. DFT calculations are ongoing to reveal the structural details of those species as well as to validate the proposed mechanism. A rough estimation of the catalytic efficiency shows

that thiolate-capped **9.1** and **9.2** are better catalysts than the sulphide-capped **9A**. Li *et al.* obtained only *ca.* 20 μA catalytic current at the first catalytic wave after addition of 9 equivalents of $HBF_4 \cdot Et_2O$ using 4.1 mM catalyst, whereas we obtained *ca.* 100 μA catalytic current after addition of same amount of $HBF_4 \cdot Et_2O$ using 1 mM catalysts.

9.3. Summary and conclusions

The thiolate-capped triiron clusters, $Fe_3(CO)_9(\mu_3\text{-}S^iPr)(\mu\text{-}H)$ (**9.1**) and $Fe_3(CO)_9(\mu_3\text{-}S^tBu)(\mu\text{-}H)$ (**9.2**), have been tested as electrocatalysts for the reduction of proton. The CVs of these clusters show that their reduction potential is significantly influenced by the substituents on the thiolate-backbone. For both clusters, a relatively slow chemical process takes place after reduction which is found to be an iron-iron bond scission as revealed by theoretical investigations. They do not protonate by a wide range of acid and are stable in acidic solution. Both clusters are catalytically active toward proton reduction at their reduction potentials and can catalyse H_2 formation from CF_3CO_2H and $HBF_4 \cdot Et_2O$ following an ECEC mechanism. An additional CECE process is also proposed for H_2 formation from $HBF_4 \cdot Et_2O$. The catalytic efficiency of both clusters depend on acid strength (pH of the solution) as higher catalytic current was obtained when $HBF_4 \cdot Et_2O$ was used as the proton source.

9.4. Experimental

9.4.1. General. All the reactions were carried out under a nitrogen atmosphere using standard Schlenk techniques unless otherwise stated. Reagent-grade solvents were dried using appropriate drying agents and distilled prior to use by standard methods. Infrared spectra were recorded on a Nicolet 6700 FT-IR spectrophotometer. NMR spectra were recorded on a Bruker DPX 400 instrument. $Fe_3(CO)_9(\mu_3\text{-}S^iPr)(\mu\text{-}H)$ (**9.1**) and $Fe_3(CO)_9(\mu_3\text{-}S^tBu)(\mu\text{-}H)$ (**9.2**) were prepared according to a published procedure [23].

9.4.2. Preparation of $Fe_3(CO)_9(\mu_3\text{-}S^iPr)(\mu\text{-}H)$ (9.1). A benzene solution (20 mL) of $Fe_3(CO)_{12}$ (200 mg, 0.398 mmol) and isopropylthiol (48 μL, 0.512 mmol) was heated to reflux for 1 h. The reaction mixture was then allowed to cool at room temperature and the volatiles removed under vacuum. The residue was chromatographed by TLC on silica gel. Elution with pet ether (40-60) developed five bands on the TLC plate. The first two

bands gave two isomers of $Fe_2(CO)_6(\mu\text{-}S^iPr)_2$ [23] as the major products. The third band gave unconsumed $Fe_3(CO)_{12}$ while the fourth band afforded $Fe_3(CO)_9(\mu_3\text{-}S^iPr)(\mu\text{-}H)$ (**9.1**) (10 mg, 5%) as deep red crystals after recrystallization from hexane/CH_2Cl_2 at 4°C. Spectroscopic data for **9.1**: IR (νCO, CH_2Cl_2): 2083m, 2046s, 2022s, 2006s, 1954w cm^{-1}. ^1H NMR ($CDCl_3$): δ 4.20 (sep, J 20.4, 13.6, 6.8, 1H), 1.70 (d, J 6.4, 6H), –23.76 (s, 1H). Crystallographic data for **9.1**: red block, dimensions 0.55 × 0.43 × 0.25 mm^3, triclinic, space group *P* 1, a = 7.7272(4), b = 8.5059(4), c = 14.0708(5) Å, α = 89.748(3), β = 88.451(4), γ = 73.011(4)°, V = 884.14(7) $Å^3$, Z = 2, F(000) 494.6, d_{calc} = 1.8622 g cm^{-3}, μ = 884.14(7) mm^{-1}. 8397 reflections were collected, 4178 unique [R(int) = 0.0330]. At convergence, R_1 = 0.0340, wR_2 = 0.0710 [$I > 2.0\sigma(I)$] and R_1 = 0.0422, wR_2 = 0.0782 (all data), for 231 parameters.

9.4.3. Preparation of $Fe_3(CO)_9(\mu_3\text{-}S^tBu)(\mu\text{-}H)$ (9.2). A benzene solution (20 mL) of $Fe_3(CO)_{12}$ (200 mg, 0.398 mmol) and *tert*-butylthiol (128 μL, 1.127 mmol) was heated to reflux for 1 h. A similar work up and chromatographic separation developed five bands on the TLC plate. The first two bands gave two isomers of $Fe_2(CO)_6(\mu\text{-}S^tBu)_2$ [23] as the major products. The third band gave unconsumed $Fe_3(CO)_{12}$ while the fourth band afforded $Fe_3(CO)_9(\mu_3\text{-}S^tBu)(\mu\text{-}H)$ (**9.2**) (24 mg, 12%) as deep red crystals after recrystallization from hexane/CH_2Cl_2 at 4°C. Spectroscopic data for **9.2**: IR (νCO, CH_2Cl_2): 2083m, 2046s, 2023s, 2008s, 1950w cm^{-1}. ^1H NMR ($CDCl_3$): δ 1.75 (s, 9H), –23.71 (s, 1H).

9.5. References

(1) I. P. Georgakaki, L. M. Thomson, E. J. Lyon, M. B. Hall and M. Y. Darensbourg, *Coord. Chem. Rev.*, 2003, **238-239**, 255-266.

(2) D. J. Evans and C. J. Pickett, *Chem. Soc. Rev.*, 2003, **32**, 268-275.

(3) T. B. Rauchfuss, *Inorg. Chem.*, 2004, **43**, 14-26.

(4) L. Sun, B. Åkermark and S. Ott, *Coord. Chem. Rev.*, 2005, **249**, 1653-1663.

(5) X. Liu, S.K. Ibrahim, C. Tard and C.J. Pickett, *Coord. Chem. Rev.*, 2005, **249**, 1641-1652.

(6) J. W. Peters, W. N. Lanzilotta, B. J. Lemon and L. C. Seefeldt, *Science*, 1998, **282**, 1853-1858.

(7) Y. Nicolet, C. Piras, P. Legrand, C. E. Hatchikian and J. C. Fontecillacamps, *Structure*, 1999, **7**, 13-23.

(8) S. Shima, E. J. Lyon, R. K. Thauer, B. Mienert and E. Bill, *J. Am. Chem. Soc.*, 2005, 127, 10430-10435.

(9) S. Shima, O. Pilak, S. Vogt, M. Schick, M. S. Stagni, W. Meyer-Klaucke, E. Warkentin, R. K. Thauer and U. Ermler, *Science*, 2008, **321**, 572-575.

(10) A. Volbeda, M. H. Charon, C. Piras, C. E. Hatchikian, M. Frey and J. C. Fontecillacamps, *Nature*, 1995, 373, 580-587.

(11) I. Bhugun, D. Lexa and J.-M. Savéant, *J. Am. Chem. Soc.* 1996, **118**, 3982-3983.

(12) S. Kaur-Ghumaan, L. Schwartz, R. Lomoth, M. Stein, S. Ott, *Angew. Chem., Int. Ed.*, 2010, **49**, 8033-8036.

(13) L. Schwartz, P. S. Singh, L. Eriksson, R. Lomoth, S. Ott, *C. R. Chim.*, 2008, **11**, 875-889.

(14) M. Beyler, S. Ezzaher, M. Karnahl, M.-P. Santoni, R. Lomoth and S. Ott, *Chem. Commun.*, 2011, **47**, 11662-11664.

(15) A. Orthaber, M. Karnahl, S. Tschierlei, D. Streich, M. Stein and S. Ott, *Dalton Trans.*, 2014, **43**, 4537-4549.

(16) M. J. Rose, H. B. Gray and J. R. Winkler, *J. Am. Chem. Soc.*, 2012, **134**, 8310-8313.

(17) M. D. Rail and L. A. Berben, *J. Am. Chem. Soc.*, 2011, **133**, 18577-18579.

(18) A. D. Nguyen, M. D. Rail, M. Shanmugam, J. C. Fettinger and L. A. Berben, *Inorg. Chem.*, 2013, **52**, 12847-12854.

(19) Z. Li, X. Zeng, Z. Niu and X. Liu, *Electrochimica Acta*, 2009, **54**, 3638-3644.

(20) C. A. Mebi, K. E. Brigance and R. B. Bowman, *J. Braz. Chem. Soc.*, 2012, **23**, 186-189.

(21) W. Gao, J. Sun, M. Li, T. Åkermark, K. Romare, L. Sun, B. Åkermark, *Eur. J. Inorg. Chem.*, 2011, 1100-1105.

(22) A. Rahaman, S. Basak-Modi, S. Ghosh, G. Hogarth, E. Nordlander, manuscript in preparation.

(23) J. A. de Beer and R. J. Haines, *J. Organomet. Chem.*, 1970, **24**, 757-767.

(24) L.-R. Frank and A. Winter, *J. Organomet. Chem.*, 1987, **335**, 249-253.

(25) J. Takács and L. Markó, *J. Organomet. Chem.*, 1983, 247, 223-225.

(26) R. Bau, B. Don, R. Greatrex, R. J. Haines, R. A. Love and R. D. Wilson, *Inorg. Chem.*, 1975, 14, 3021-3025.

(27) A. Winter, L. Zsolnai and G. Huttner, *Chem. Ber.*, 1982, 115, 1286-1304.

(28) All pK_a values reported here were measured in MeCN; K. Izutsu, *in Acid-Base Dissociation Constants in Dipolar Aprotic Solvents*, Blackwell Scientific Publications, Oxford, 1990.

(29) R. Mejia-Rodriguez, D. Chong, J. H. Reibenspies, M. P. Soriaga and M. Y. Darensbourg, *J. Am. Chem. Soc.*, 2004, **126**, 12004-12014.

Chapter 10

Electrocatalytic proton reduction by $M_3(CO)_9(\mu_3\text{-ampy})(\mu\text{-H})$ (M = Fe, Ru; ampy = 2-aminopyridinates)

10.1. Introduction

As discussed in Chapters 8 and 9, the use of low valent iron clusters as electrocatalysts for proton reduction is promising. Such clusters often show low reduction potentials and stable anions, owing to the highly delocalised nature of bonding within their core, essential characteristics for a good electrocatalyst [1-8]. Our strategy to design cluster-based electrocatalysts involves the inclusion of a main group electronegative element into the cluster core to facilitate interaction between acidic and hydridic hydrogens, a key step in the catalytic cycle of [FeFe]-hydrogenase [9,10]. In the enzyme, the iron-bound basic hydride reacts with the nitrogen-bound acidic proton to form H_2 during proton reduction as shown in Scheme 1.1 (also in Chart 10.1b) [10]. This nitrogen is located in the middle of azadithiolato bridge, so is flexible and can shuttle protons to and from the iron centre during catalysis. It is also part of a proton channel that also includes four residual amino acids and a crystallographically characterized water molecule. This channel relays protons from the active site to the surface of the enzyme and vice versa [11-14].

Following this strategy, we first examined the proton reduction ability of the tetrairon-oxo cluster $Fe_4(CO)_{10}(\kappa^2\text{-dppn})(\mu_4\text{-O})$ (**8.1**) which contains an electronegative oxygen atom in the cluster core (Chapter 8). The dianion of **8.1** is an active catalyst, although theoretical studies reveal that oxygen has no direct role in the catalysis. Later we improvised our strategy and placed a basic hydride within the catalyst as in the thiolato-capped triiron clusters $Fe_3(CO)_9(\mu_3\text{-SR})(\mu\text{-H})$ (**9.1**, R = ^{i}Pr; **9.2**, R = ^{t}Bu) (Chapter 9) and found that their radical anions can catalyse proton reduction. DFT calculations reveal that the interaction between iron-bound hydride and sulphur-bound proton is a key step in proton reduction by these thiolato-capped clusters.

The successful implementation of this strategy has prompted us to investigate cluster that already contain acidic and hydridic hydrogens in close proximity within the cluster sphere. The trimetallic 2-aminopyrimidinate clusters are ideal candidates for this study as

they contain a metal-bound basic hydride and nitrogen-bound acidic (relatively) hydrogen in close proximity (Chart 10.1). Unlike the active site, the bridging nitrogen in these clusters is rigid, so to facilitate interaction between acidic and hydridic hydrogen they should undergo structural rearrangement which may be achieved after reduction.

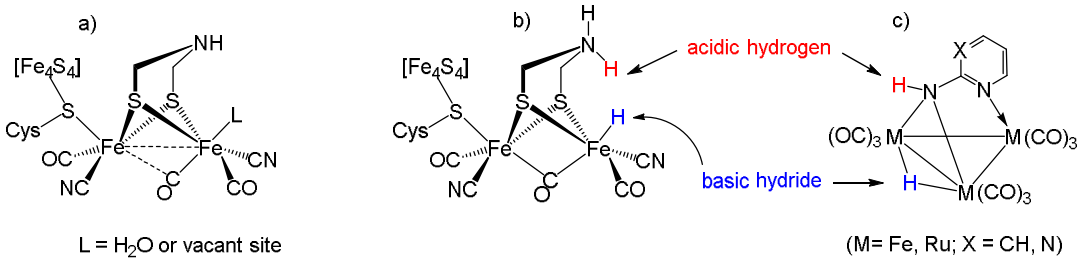

Chart 10.1. a) The active site of the [FeFe]-hydrogenase enzyme and b) proposed hydride-proton interaction at the active site of [FeFe]-hydrogenase enzyme during catalysis, c) $M_3(CO)_9(\mu_3\text{-ampy})(\mu\text{-H})$ as functional models active site.

Although several ruthenium and osmium clusters bearing 2-aminopyridinates have been reported, no attempt has been taken to synthesize their triiron analogues [11-24]. Thus as part of a preliminary study we have synthesized the triiron 2-aminopyridinate (pyNH) cluster $Fe_3(CO)_9(\mu_3\text{-pyNH})(\mu\text{-H})$ (**10.1**) and tested its proton reduction ability. The analogous 2-aminopyrimidinate (pymNH) cluster $Fe_3(CO)_9(\mu_3\text{-pymNH})(\mu\text{-H})$ (**10.2**) that contains an extra nitrogen atom within the heterocyclic ring is also tested. The bridging nitrogen in both clusters has complete octet, so unable to bind an incoming proton. In contrast, the free lone pair electrons on the ring nitrogen in the later can readily bind with a proton and may transfer it to the cluster core during catalysis akin to the bridgehead nitrogen in the active site.

It is well-known that heavier transition metal clusters show greater stability compared to their first row analogues due to relatively stronger metal-metal bonds [25] which can allow for the identification of reaction intermediates. In this way valuable information about the mechanism, as well as various kinetic and thermodynamic parameters, can be obtained. With this in mind we also examined the ruthenium analogues of the above mentioned iron clusters namely $Ru_3(CO)_9(\mu_3\text{-pyNH})(\mu\text{-H})$ (**10.3**) [13] and $Ru_3(CO)_9(\mu_3\text{-pymNH})(\mu\text{-H})$ (**10.4**) [12].

10.2. Results and discussion

10.2.1. Synthesis and structure. Clusters **10.1** and **10.2** were synthesized from the direct reaction between $Fe_3(CO)_{12}$ and the corresponding heterocyclic amine at 80°C (Scheme 10.1). Both clusters were obtained in low yield (4% for **10.1** and 8% for **10.1**) and attempts to improve this by changing the solvent and reaction conditions were unsuccessful. Treatment of $Fe_3(CO)_{12}$ with two molar equivalents of 2-aminopyridines in boiling benzene for 1 h afforded **10.1** and **10.2** in optimal yield. Both clusters are air-stable in the solid-state but decompose slowly in solution over time when exposed to air.

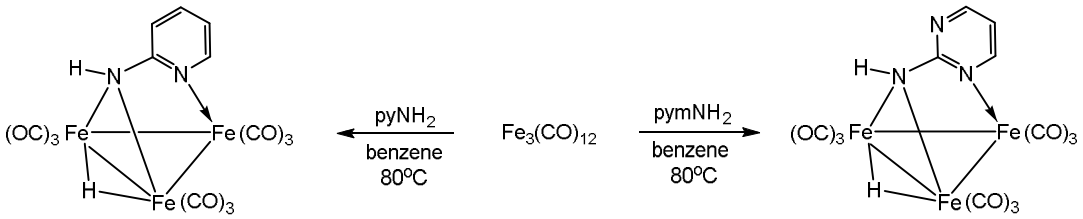

10.1 **10.2**

Scheme 10.1. Synthesis of $Fe_3(CO)_9(\mu_3\text{-pyNH})(\mu\text{-H})$ (**10.1**) and $Fe_3(CO)_9(\mu_3\text{-pymNH})(\mu\text{-H})$ (**10.2**).

Clusters **10.1** and **10.2** have been appropriately characterized by spectroscopic and analytical data together with single crystal X-ray diffraction studies for **10.2**. Both display a high field singlet (δ –12.66 and –12.65 ppm for **10.1** and **10.2** respectively) attributed to the bridging hydride in addition to resonances for the heterocyclic ring protons in the aromatic region. An ORTEP diagram of the molecular structure of **10.2** is depicted in Figure 10.1, with the caption containing selected bond length and angles. This shows that the molecule consists of a triiron core ligated by a face-capping 2-aminopyrimidinate (pymNH) ligand, the nine carbonyls being equally distributed over three iron atoms. A hydride was located from a difference map and spans across the same Fe─Fe edge that is symmetrically bridged by the exocyclic nitrogen of the capping ligand [Fe(2)─N(1) 1.971(2), Fe(3)─N(1) 1.978(1) Å]. This Fe─Fe edge [Fe(2)─Fe(3) 2.5223(7) Å] is significantly shorter (*ca.* 0.1 Å) than the others [Fe(1)─Fe(2) 2.6113(7), Fe(1)─Fe(3) 2.5999(8) Å] probably as a consequence of the amide bridge. The pymNH ligand is also bonded to the remote iron through one of the ring nitrogen atoms and lies almost perpendicular to the metallic plane. The hydride ligand resides on the opposite face of the metallic plane with respect to the 2-pymNH ligand and the non-bonding distance between the hydride and the amino-hydrogen is 2.809 Å.

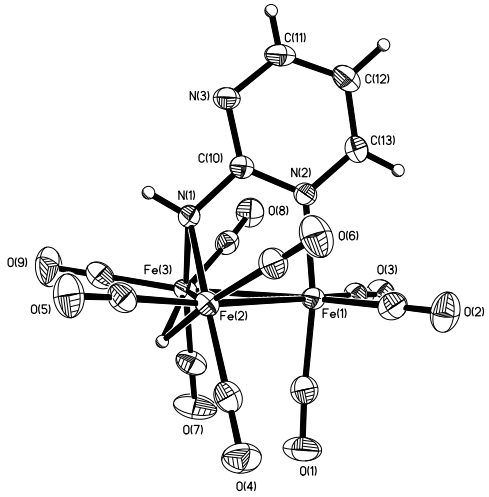

Figure 10.1. Molecular structure of $Fe_3(CO)_9(\mu_3\text{-pymNH})(\mu\text{-H})$ (**10.2**). Selected bond distances [Å] and angles [º]: Fe(1)─Fe(2) 2.6113(7), Fe(2)─Fe(3) 2.5223(7), Fe(1)─Fe(3) 2.5999(8), Fe(1)─N(2) 1.9974(2), Fe(2)─N(1) 1.971(2), Fe(3)─N(1) 1.978(1), Fe(2)─N(2)─Fe(3) 79.39(7), N(1)─Fe(2)─Fe(3) 50.44(6), N(1)─Fe(3)─Fe(2) 50.17(6), N(1)─Fe(2)─Fe(1) 76.67(6), N(2)─Fe(1)─Fe(2) 84.36(6), Fe(1)─Fe(2)─Fe(3) 60.82(6), Fe(3)─Fe(1)─Fe(2) 57.898(2), Fe(2)─Fe(3)─Fe(1) 61.280(2).

The triruthenium clusters **10.3** and **10.4** were prepared following a similar method i.e. by reacting $Ru_3(CO)_{12}$ with 2-aminopyridinates in boiling toluene (Scheme 10.2). Yields are much better (33% for **10.3** and 41% for **10.4**) possibly as a consequence of relatively strong ruthenium-ruthenium bonds. Clusters **10.3** and **10.4** were reported earlier by Cabeza and co-workers but were characterised by spectroscopic data only [16,17]. We were able to grow single crystals and carried out X-ray diffraction analysis, the results of which are shown in Figures 10.2 and 10.3.

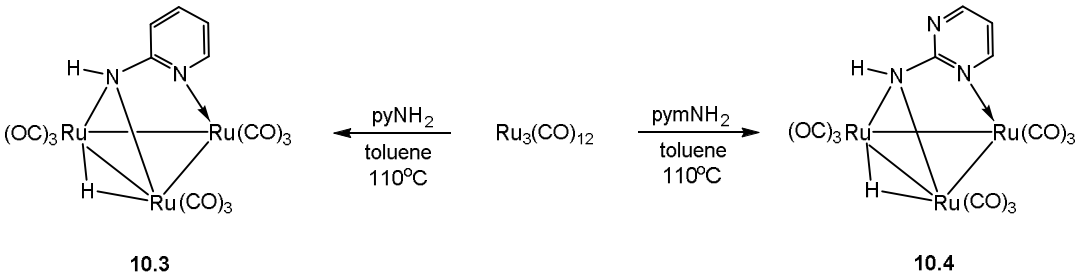

10.3 **10.4**

Scheme 10.2. Synthesis of $Ru_3(CO)_9(\mu_3\text{-pyNH})(\mu\text{-H})$ (**10.3**) and $Ru_3(CO)_9(\mu_3\text{-pymNH})(\mu\text{-H})$ (**10.4**).

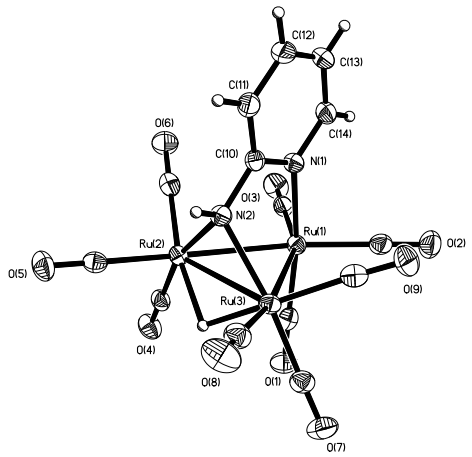

Figure 10.2. Molecular structure of $Ru_3(CO)_9(\mu_3\text{-pyNH})(\mu\text{-H})$ (**10.3**). Selected bond distances [Å] and angles [º]: Ru(1)─Ru(2) 2.7261(5), Ru(2)─Ru(3) 2.7556(5), Ru(1)─Ru(3) 2.7289(6), Ru(1)─N(1) 2.142(2), Ru(2)─N(2) 2.119(2), Ru(3)─N(2) 2.119(2), N(1)─Ru(1)─Ru(2) 83.31(6), N(1)─Ru(1)─Ru(3) 84.02(6), Ru(2)─N(2)─Ru(3) 81.10(7), N(2)─Ru(2)─Ru(3) 49.45(6), N(2)─Ru(3)─Ru(2) 49.45(6), Ru(1)─Ru(2)─Ru(3) 59.710(14), Ru(3)─Ru(1)─Ru(2) 60.683(12), Ru(2)─Ru(3)─Ru(1) 59.607(9), C(4)─Ru(2)─Ru(3) 116.33(8), C(5)─Ru(2)─Ru(3) 112.82(8), C(7)─Ru(3)─Ru(2) 117.71(8), C(8)─Ru(3)─Ru(2) 112.77(8).

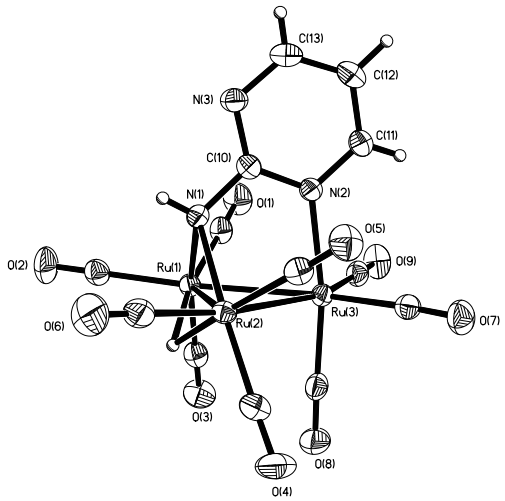

Figure 10.3. Molecular structure of $Ru_3(CO)_9(\mu_3\text{-pymNH})(\mu\text{-H})$ (**10.4**). Selected bond distances [Å] and angles [º]: Ru(1)─Ru(2) 2.7532(4), Ru(2)─Ru(3) 2.7248(5), Ru(1)─Ru(3) 2.7303(5), Ru(3)─N(2) 2.136(2), Ru(1)─N(1) 2.123(2), Ru(2)─N(1) 2.128(2), N(2)─Ru(3)─Ru(1) 83.29(6), N(2)─Ru(3)─Ru(2) 84.01(5), Ru(1)─N(1)─Ru(2) 80.73(8), N(1)─Ru(1)─Ru(2) 49.71(6), N(1)─Ru(2)─Ru(1) 49.57(6), Ru(1)─Ru(2)─Ru(3) 59.786(9), Ru(3)─Ru(1)─Ru(2) 59.590(14), Ru(2)─Ru(3)─Ru(1) 60.624(9), C(3)─Ru(1)─Ru(2) 116.64(8), C(2)─Ru(1)─Ru(2) 114.06(8), C(4)─Ru(2)─Ru(1) 117.00(8), C(6)─Ru(2)─Ru(1) 113.52(8).

The structures are very similar to that of **10.2** and also the related triruthenium complex $Ru_3(CO)_9(\mu_3\text{-pyNPh})(\mu\text{-H})$ [17]. In both **10.3** and **10.4** the hydride ligand was located from a difference map and spans across the longest Ru–Ru vector [Ru(2)─Ru(3) 2.7556(5) Å in **10.3** and Ru(1)─Ru(2) 2.7532(4) Å in **10.4**], which is also symmetrically bridged by the exocyclic nitrogen of the heterocyclic amine [Ru(2)─N(2) 2.119(2) and Ru(3)─N(2) 2.119(2) Å in **10.3**; Ru(1)─N(1) 2.123(2) and Ru(2)─N(1) 2.128(2) Å in **10.4**]. This is in contrast with **10.2** in which the Fe–Fe vector simultaneously bridged by 2-aminopyrimidinate and hydride is the shortest edge. In both clusters, the face-capping heterocyclic amine lies almost perpendicular to the metallic plane by coordinating to the third ruthenium using (one of) the ring nitrogen(s). Akin to **10.2**, the bridging hydride is located on the opposite face of the metallic plane with respect to the heterocyclic amine and the nonbonding distance between the hydride and amino nitrogen is 2.834 Å in **10.3** and 2.873 Å in **10.4**.

10.2.2. Electrochemistry. The electrochemical response of **10.1**-**10.4** was studied in MeCN by cyclic voltammetry. The CV of both the triiron clusters (**10.1**-**10.2**) exhibit single irreversible reduction and oxidation waves (Figure 10.4 and Table 10.1) at a scan rate of 0.1 V/s. The reversibility of these processes does not improve when the scan rate is varied. The radical ions of these clusters are unstable in MeCN, which probably undergo solvolysis after reduction/oxidation. The 2-aminopyrimidinate cluster **10.2**, which contains an extra electronegative nitrogen within the heterocyclic ring, reduces the positive potential by 140 mV as compared to that of **10.1** suggesting that the reduction potential of these clusters can be tuned by modifying the pyridinate ring. Consequently, cluster **10.2** undergoes oxidation at a potential 90 mV more positive as compared to **10.1** (Table 10.1).

Table 10.1. Redox potentials of **10.1**-**10.4**.

Compounds	E_p^{red1} / V	E_p^{red2} / V	E_p^{ox1} / V	E_p^{ox2} / V
$Fe_3(CO)_9(\mu_3\text{-pyNH})(\mu\text{-H})$ (**10.1**)	–1.61	–	0.26	–
$Fe_3(CO)_9(\mu_3\text{-pymNH})(\mu\text{-H})$ (**10.2**)	–1.47	–	0.35	–
$Ru_3(CO)_9(\mu_3\text{-pyNH})(\mu\text{-H})$ (**10.3**)	–2.01	–2.15	0.08	0.31
$Ru_3(CO)_9(\mu_3\text{-pymNH})(\mu\text{-H})$ (**10.4**)	–1.93	–2.09	0.24	0.45

The triruthenium clusters undergo two closely spaced irreversible reductions in the cathodic region (Figure 10.5) with the pyrimidinate cluster **10.4** reduces 80 mV more

positive potential compared to the pyridinate cluster **10.3** (Table 10.1). Both also exhibit two irreversible oxidation waves in the anodic region. No significant change was observed when the scan rate was varied.

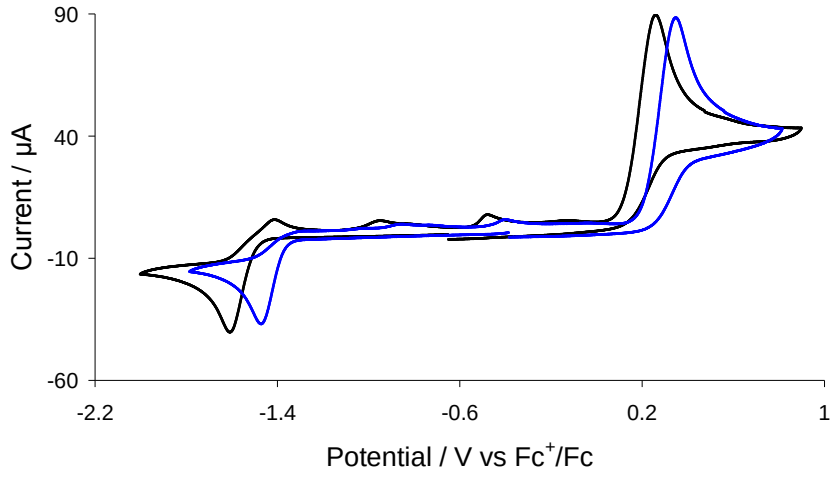

Figure 10.4. CVs of $Fe_3(CO)_9(\mu_3\text{-pyNH})(\mu\text{-H})$ (**10.1**) (black) and $Fe_3(CO)_9(\mu_3\text{-pymNH})(\mu\text{-H})$ (**10.2**) (blue) in MeCN (1 mM solution, supporting electrolyte $[NBu_4][PF_6]$, scan rate 0.1 Vs^{-1}, glassy carbon electrode, potential vs Fc^+/Fc).

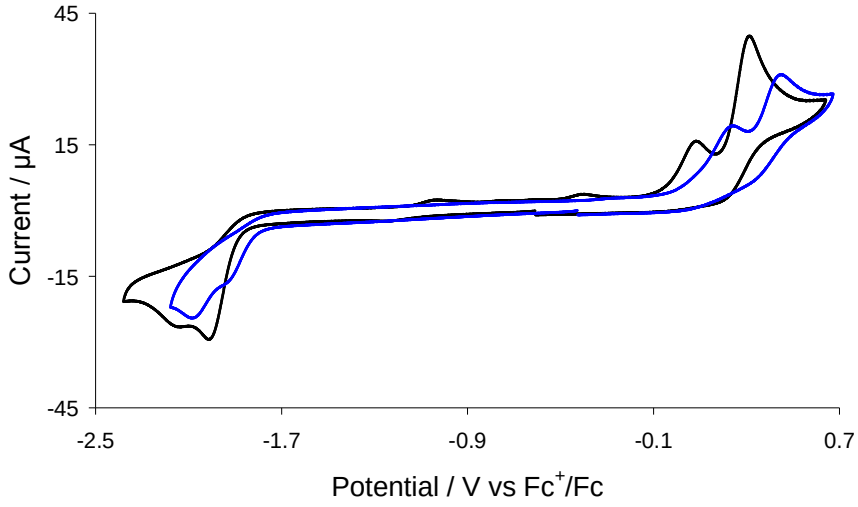

Figure 10.5. CVs of $Ru_3(CO)_9(\mu_3\text{-pyNH})(\mu\text{-H})$ (**10.3**) (black) and $Ru_3(CO)_9(\mu_3\text{-pymNH})(\mu\text{-H})$ (**10.4**) (blue) in MeCN (1 mM solution, supporting electrolyte $[NBu_4][PF_6]$, scan rate 0.1 Vs^{-1}, glassy carbon electrode, potential vs Fc^+/Fc).

10.2.3. Reactions with acid. The protonation behaviour of **10.1-10.4** was investigated by adding $TsOH{\cdot}H_2O$ ($pK_a \approx 8.5$ in MeCN) [26] or $HBF_4{\cdot}Et_2O$ ($pK_a \approx 0.1$ in MeCN) [26].

Cluster **10.1** is not protonated by $TsOH \cdot H_2O$ albeit it could accommodate protons across non-bridged Fe─Fe vectors, and it decomposes rapidly in the presence of $HBF_4 \cdot Et_2O$. Protonation of **10.2** is expected to occur either at the unbound nitrogen of the pyrimidine ring or across one of the non-bridged Fe─Fe vectors and these events can be easily differentiated by IR spectroscopy. Addition of one molar equivalent of $HBF_4 \cdot Et_2O$ to a CH_2Cl_2 solution of **10.2** leads to partial protonation of the cluster. Two new absorption bands appear at 2086 and 2054 cm^{-1} in addition to the absorption band displayed by the neutral cluster which decays over time with the original spectrum being recovered after 1 h indicating the reversibility of the process. The small blue shift of the highest energy absorption band (12 cm^{-1}) reveals that the proton is located at the pyrimidine ring. The reversibility of this process is also tested in MeCN (the solvent used for catalysis) by adding pyridine into a protonated solution of **10.2**. The original spectrum was recovered upon addition of equivalent amount of pyridine into a protonated solution of **10.2** indicating that protonation at the free ring nitrogen of pymNH ligand is fully reversible. When a slight excess of $HBF_4 \cdot Et_2O$ (3 equivalents) was added to this solution, complete protonation at pyrimidine ring nitrogen was observed and the carbonyl absorption bands of **10.2** were clearly replaced by a new set of absorptions at 2086, 2054, 2031, 2006 and 1995 cm^{-1} (Figure 10.6) which decay over time.

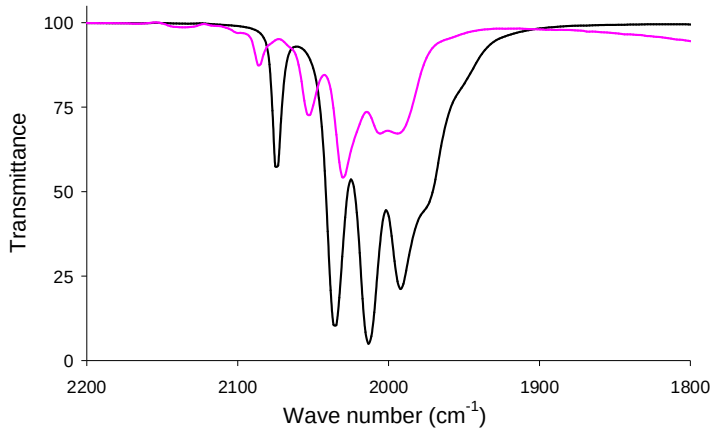

Figure 10.6. IR spectra of $Fe_3(CO)_9(\mu_3\text{-pymNH})(\mu\text{-H})$ (**10.2**) in CH_2Cl_2 - in the absence of acid (black) and in the presence of 3 equiv. $HBF_4 \cdot Et_2O$ (pink).

Protonation of **10.2** was also monitored by ^1H NMR spectroscopy in CD_3CN. Figure 10.7 shows the hydride region of the spectrum recorded before and after addition of 3 molar equivalents of $HBF_4 \cdot Et_2O$ as a function of time. After acid addition the spectrum displays

two new resonances in the hydride region at δ –9.62 and –9.66 ppm at the expense of the resonance attributed to the neutral complex at δ –12.66 ppm. We suggest that the appearance of two new hydride resonances is due to the presence of two different isomers of protonated **10.2** as shown in Scheme 10.3. Although in the solid-state the hydride is static and resides across the Fe─Fe edge bridged by the exocyclic nitrogen of heterocyclic amine, it rapidly moves across all three Fe─Fe edges in solution. Protonation at the free ring nitrogen apparently slows down this movement and two isomers are seen.

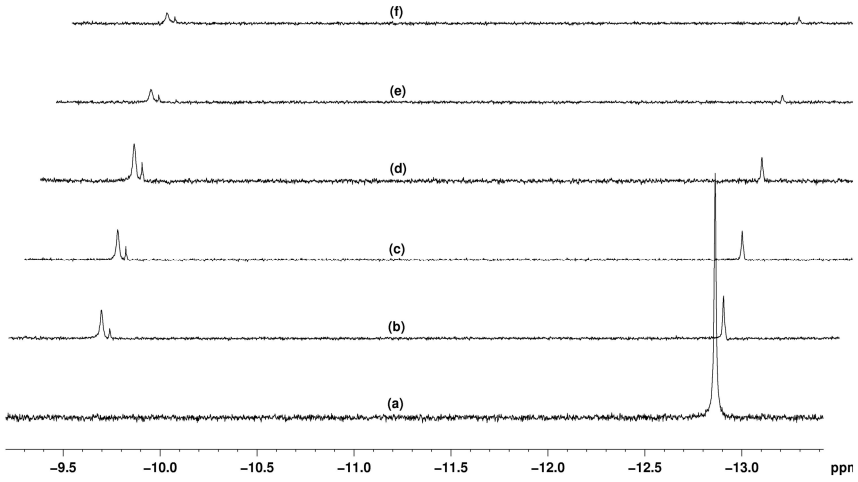

Figure 10.7. Hydride region of the ^{1}H NMR spectrum of **10.2** in CD_3CN – (a) in the absence of acid, (b) after addition of 3 molar equivalents of $HBF_4{\cdot}Et_2O$, (c) after 10 min of acid addition, (d) after 30 min of acid addition, (e) after 90 min of acid addition and (f) after 2 h of acid addition.

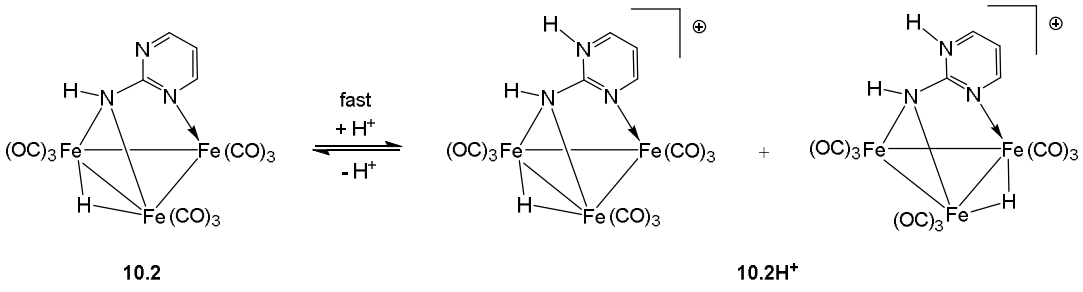

Scheme 10.3. Protonation of $Fe_3(CO)_9(\mu_3\text{-pymNH})(\mu\text{-H})$ (**10.2**).

Addition of $HBF_4{\cdot}Et_2O$ into a CH_2Cl_2 solution of **10.3** and **10.4** resulted in the formation of cloudy suspensions, so their protonation behaviour was investigated in MeCN using $TsOH{\cdot}H_2O$ as the proton source. Unlike **10.1** which is not protonated by $TsOH{\cdot}H_2O$, the

ruthenium analogue **10.3** reacts slowly with $TsOH \cdot H_2O$ in MeCN to form **10.3H**$^+$ owing to the greater basicity of the triruthenium over triiron core. Upon addition of 3 molar equivalent of $TsOH \cdot H_2O$ two relatively weak new absorptions were observed at 2121 and 2102 cm^{-1} with complete protonation occurring over 30 min. Protonated **10.3H**$^+$ displays absorptions at 2121m, 2102m, 2072vs, 2033vs, 2007vs, 1994 vs cm^{-1} (Figure 10.8) and the ~ 40 cm^{-1} blue shift of the highest energy absorption band suggests protonation across a Ru–Ru vector. The hydride resonance of **10.3** at δ –11.60 ppm was replaced by a new singlets at δ –12.39 ppm indicating that both hydrides in **10.3H**$^+$ move rapidly across the Ru–Ru vectors becoming equivalent on the NMR timescale (Scheme 10.4).

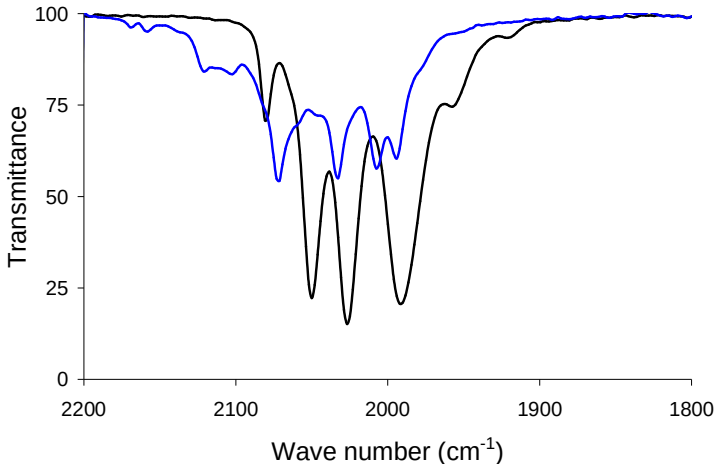

Figure 10.8. IR spectra of $Ru_3(CO)_9(\mu_3\text{-pyNH})(\mu\text{-H})$ (**10.3**) in MeCN - in the absence of acid (black) and in the presence of 3 equiv. $TsOH \cdot H_2O$.

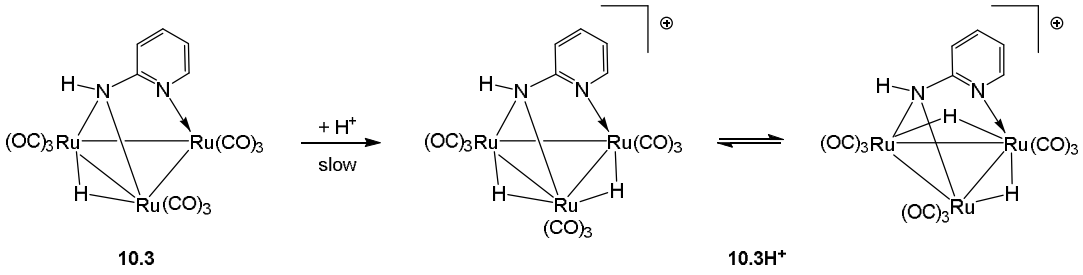

Scheme 10.4. Protonation of $Ru_3(CO)_9(\mu_3\text{-pyNH})(\mu\text{-H})$ (**10.3**).

Akin to **10.2**, cluster **10.4** protonates rapidly at the free ring nitrogen of the pymNH ligand in MeCN upon addition of 3 molar equivalent of $TsOH \cdot H_2O$. The highest energy

absorption band shows only *ca*. 11 cm^{-1} blue shift upon protonation (Figure 10.9) compared to *ca*. 40 cm^{-1} shift observed for **10.3**. The hydride resonances at δ –11.58 ppm was replaced by two new resonances at and δ –12.39 and –12.42 ppm suggesting that the movement of bridging hydride across the Ru–Ru vectors stopped upon protonation, a feature also observed for **10.2** (Scheme 10.5).

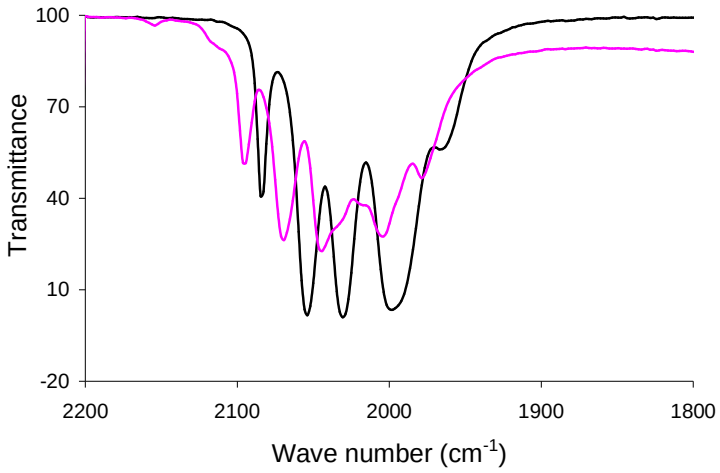

Figure 10.9. IR spectra of $Ru_3(CO)_9(\mu_3\text{-pymNH})(\mu\text{-H})$ (**10.4**) in MeCN - in the absence of acid (black) and in the presence of 3 equiv. $TsOH{\cdot}H_2O$.

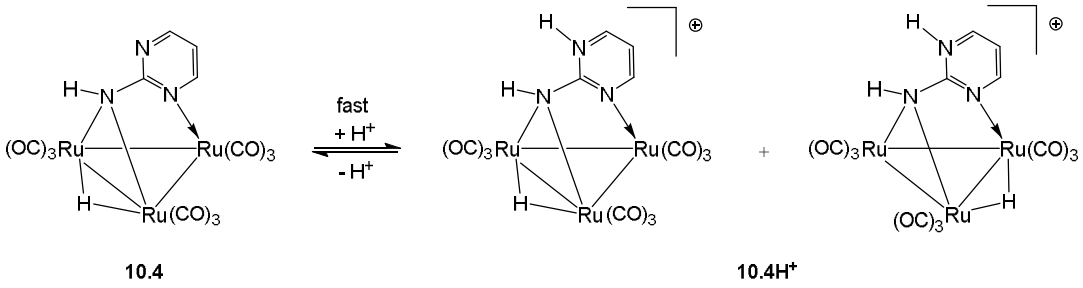

Scheme 10.5. Protonation of $Ru_3(CO)_9(\mu_3\text{-pymNH})(\mu\text{-H})$ (**10.4**).

While the triiron cluster **10.1** does not undergo protonation, the ruthenium analogue **10.3** protonates across a Ru–Ru edge the difference being related to the basicity of the cluster core. On the other hand, both **10.2** and **10.4** undergoes rapid protonation at the pyrimidine ring nitrogen, a process which we believe is thermodynamically favoured as the proton did not migrate to the metal core even after several hours of standing in solution.

10.2.4. Electrocatalysis. The proton reduction ability of **10.1**-**10.4** was tested using *p*-TsOH·H_2O as the proton source. CVs of **10.1** and **10.2** recorded upon addition of 1-5 molar equivalents are shown in Figure 10.10. Cluster **10.1** displays two new reduction peaks in presence of acid at E_p = –1.77 V and E_p = –1.94 V in addition to the peak observed for the neutral complex at E_p = –1.61 V (Figure 10.10a). The height of all these peaks increases with the concentration of acid, characteristic of proton reduction. The peak height of the second and third waves increases more rapidly than that of the first wave. On the other hand, the CV of **10.2** shows two new reduction peaks at E_p = –1.24 V and E_p = –1.69 V in presence of acid (Figure 10.10b). The peak current of the first wave does not increase substantially with concentration of acid to be recognised as a catalytic wave, while that of the second wave increases rapidly with acid concentration.

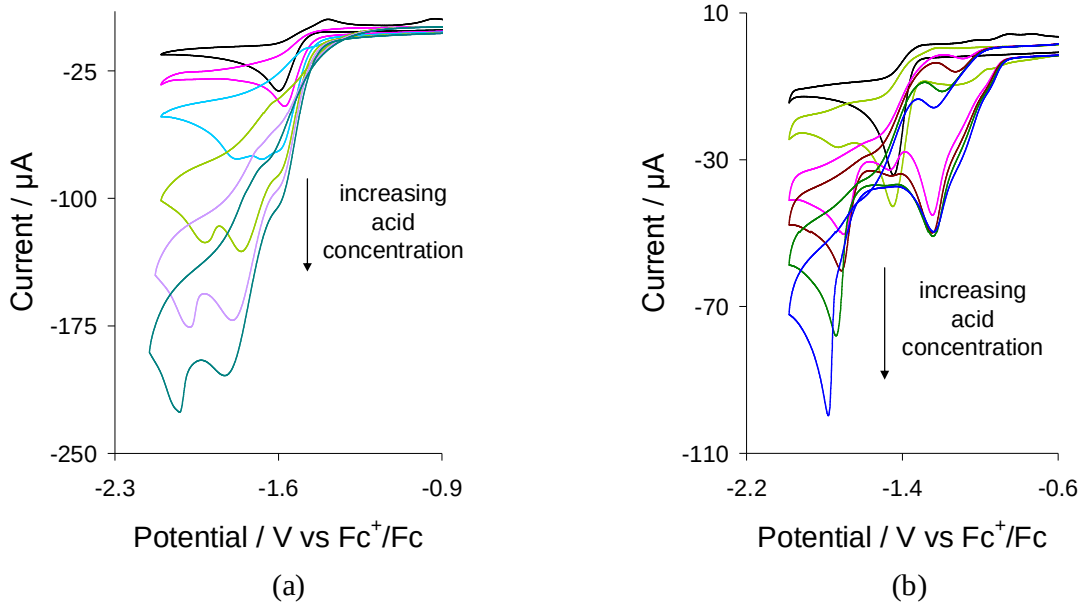

Figure 10.10. CVs of $Fe_3(CO)_9(\mu_3\text{-pyNH})(\mu\text{-H})$ (**10.1**) (a) and $Fe_3(CO)_9(\mu_3\text{-pymNH})(\mu\text{-H})$ (**10.2**) (b) in the absence of acid and in the presence of 1-5 equivalents of TsOH·H_2O (in MeCN, 1 mM solution, supporting electrolyte $[NBu_4][PF_6]$, scan rate 0.1 Vs^{-1}, glassy carbon electrode, potential vs Fc^+/Fc).

Electrocatalytic data shows that both **10.1** and **10.2** can catalyse proton reduction but they follow quite different mechanisms. Since **10.1** is not protonated by TsOH·H_2O, it needs to be reduced before protonation. Three reductive features (catalytic waves) have been seen in its CV at E_p = –1.61, –1.77 and –1.94 V in presence of acid (Figure 10.10a). We assume that radical anion **10.1**$^-$ undergoes rapid protonation to form the neutral dihydride **10.1H,** which releases hydrogen and account for the catalytic wave observed at

the first reduction potential of **10.1** (at E_p = –1.61 V) (Scheme 10.6). We speculate that the release of dihydrogen from **10.1H** is slow, hence it has time to undergo a further reduction (at E_p = –1.77 V) to form **10.1H**$^-$ which then reacts with proton to release hydrogen as shown in Scheme 10.6. The CV of **10.2** shows two new reduction peaks at E_p = –1.24 and –1.69 V and it catalyses proton reduction at later potential. Its reduction shifted by ~0.2 V in presence of acid due to protonation at pyrimidine ring nitrogen. The neutral hydride can not release hydrogen, so it undergoes a further reduction at E_p = –1.69 V to form **10.2H**$^-$ which reacts with a second proton before release of hydrogen (Scheme 10.7). Overall, cluster **10.1** follows an *ECEC* mechanism, whereas **10.2** follows a *CEEC* mechanism for electrocatalytic proton reduction.

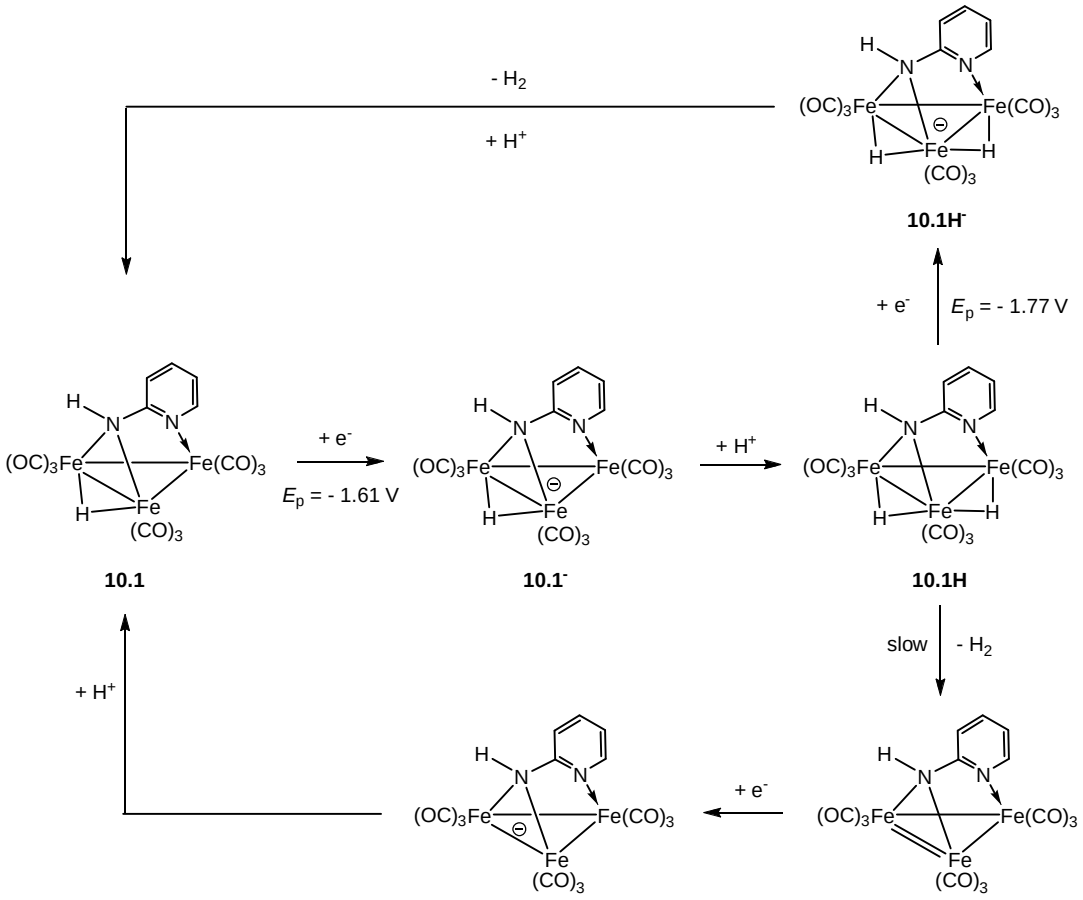

Scheme 10.6. Proposed mechanism for the electrocatalytic proton reduction by $Fe_3(CO)_9(\mu_3\text{-pyNH})(\mu\text{-H})$ (**10.1**).

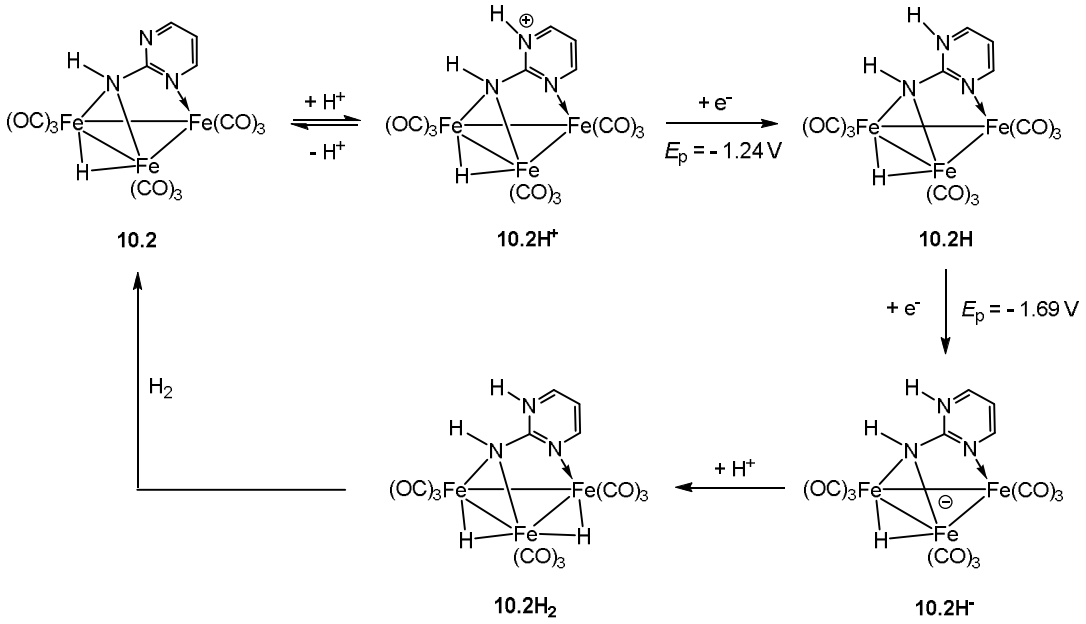

Scheme 10.7. Proposed mechanism for the electrocatalytic proton reduction by $Fe_3(CO)_9(\mu_3\text{-pymNH})(\mu\text{-H})$ (**10.2**).

In general, 49-electron carbonyl clusters are unstable and undergo ligand dissociation reactions [27], whereas the 50-electron clusters often undergo metal-metal bond scission [25] for stabilization. Here we make the assumption (possibly erroneously) that the clusters remain intact throughout the catalysis or that any metal-ligand or metal-metal bond scission is both fully reversible and rapid. Labelling of either the acidic amino hydrogen or the basic hydride with deuterium and then analysis of the products (H_2/HD/D_2) will be required in order to shed light on mechanistic pathway(s).

As is apparent, the introduction of proton relay (replacing a CH unit by nitrogen at the heterocyclic ring) changes the catalytic pathway of this system. However, this change neither increases the efficiency of the catalyst as shown by the plot of limiting currents *vs.* acid concentration (Figure 10.11) nor reduces the overpotential of catalysis. The catalytic current of **10.2** (at E_p = –1.69 V) is even less than that of the first catalytic wave of **10.1** (at E_p = –1.61 V) where it is least efficient. We obtained at least twice the current at the second and third catalytic waves of **10.1** as compared to that of the first wave. The current at first wave levels off as the concentration of acid is increased indicating that the production of hydrogen at this potential is independent of acid concentration in accord

with the proposed mechanism, whilst that of the second and third waves increases linearly with acid concentration.

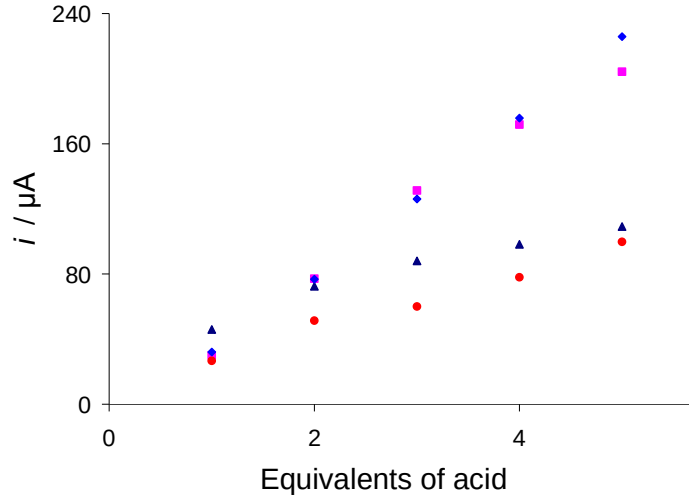

Figure 10.11. Plot of limiting currents *vs.* equivalents of acid added for **10.1** (black triangles for the first wave, pink squares for the second wave and blue diamonds for the third wave) and **10.2** (red circles).

Figure 10.12 shows CVs of **10.3** and **10.4** recorded in presence of 1-5 molar equivalents of $TsOH{\cdot}H_2O$. Cluster **10.3** displays a single catalytic wave at its reduction potential (E_p = –2.01 V) due to slow protonation across Ru–Ru vector by $TsOH{\cdot}H_2O$. Nevertheless, a minor reduction peak has also been observed at E_p = –1.33 V due to the reduction of $\mathbf{10.3H^+}$ formed in small amounts upon addition of acid. In the proposed mechanism for the electrocatalytic proton reduction by **10.3** (Scheme 10.8), catalysis is initiated by reduction of **10.3** at E_p = –2.01 V. No catalytic event has been seen beyond this potential indicating that release of hydrogen from the neutral dihydride **10.3H** is fast (Scheme 10.8). This is in contrast with that observed for the triiron cluster **10.1** whereby the release of hydrogen from **10.1H** is proposed to be relatively slow leading to the development of multiple catalytic waves *via* reduction of **10.1H**.

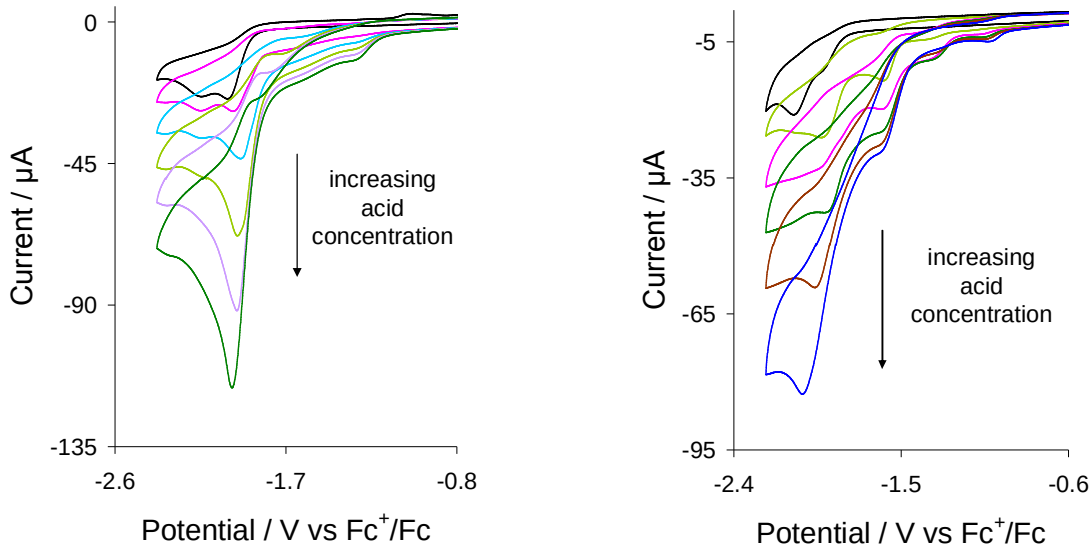

Figure 10.12. CVs $Ru_3(CO)_9(\mu_3\text{-pyNH})(\mu\text{-H})$ (**10.3**) (a) and $Ru_3(CO)_9(\mu_3\text{-pymNH})(\mu\text{-H})$ (**10.4**) (b) in the absence of acid and in the presence of 1-5 equivalents of $TsOH{\cdot}H_2O$ (in MeCN, 1 mM solution, supporting electrolyte $[NBu_4][PF_6]$, scan rate 0.1 Vs^{-1}, glassy carbon electrode, potential vs Fc^+/Fc).

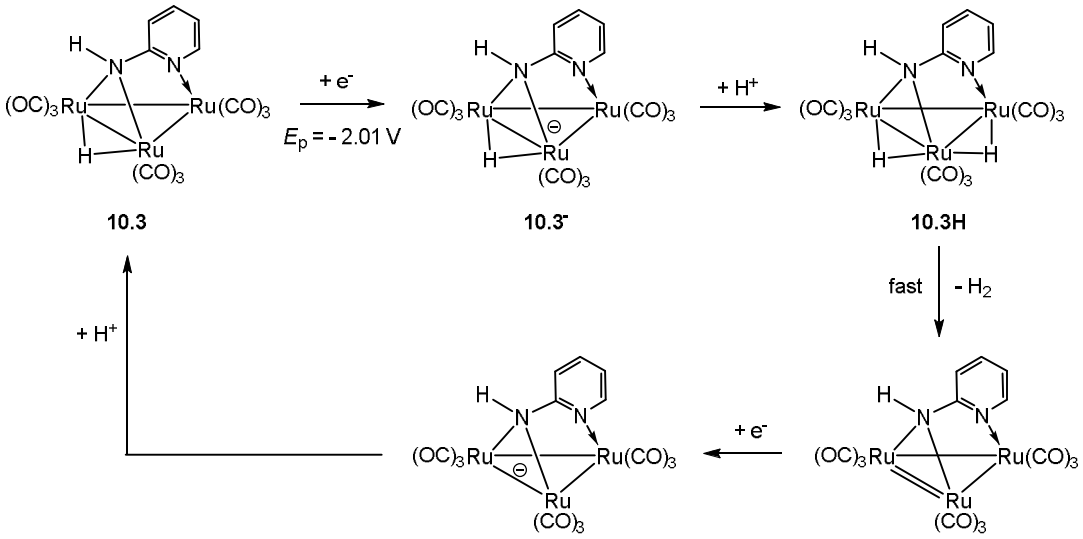

Scheme 10.8. Proposed mechanism for the electrocatalytic proton reduction by $Ru_3(CO)_9(\mu_3\text{-pyNH})(\mu\text{-H})$ (**10.3**).

The CV of **10.4** exhibits two new reduction peaks at E_p = –1.60 and –1.90 V upon addition of $TsOH{\cdot}H_2O$. Since it protonates rapidly at the free ring nitrogen of pymNH ligand, we attribute the first event to the reduction of **10.4H**$^+$, while the later to the reduction of neutral hydride **10.4H** (Scheme 10.9). The peak current of both waves

increases as the concentration of acid is increased, the second wave increasing more rapidly than the first wave. This is in contrast with the catalysis shown by **10.2** where we saw increase in peak current only at the second wave. Ruthenium is more electropositive than iron and we speculate that this feature makes the cluster core of **10.4H** basic enough for hydrogen liberation, unlike **10.2H** which could not liberate hydrogen. Release of hydrogen from **10.4H** is relatively slow thereby competing with the reduction at E_p = – 1.90 V to form **10.4H**$^-$ (Scheme 10.9). This reacts with a proton to form **10.4H**$_2$ which release hydrogen and regenerate the catalyst (Scheme 10.9).

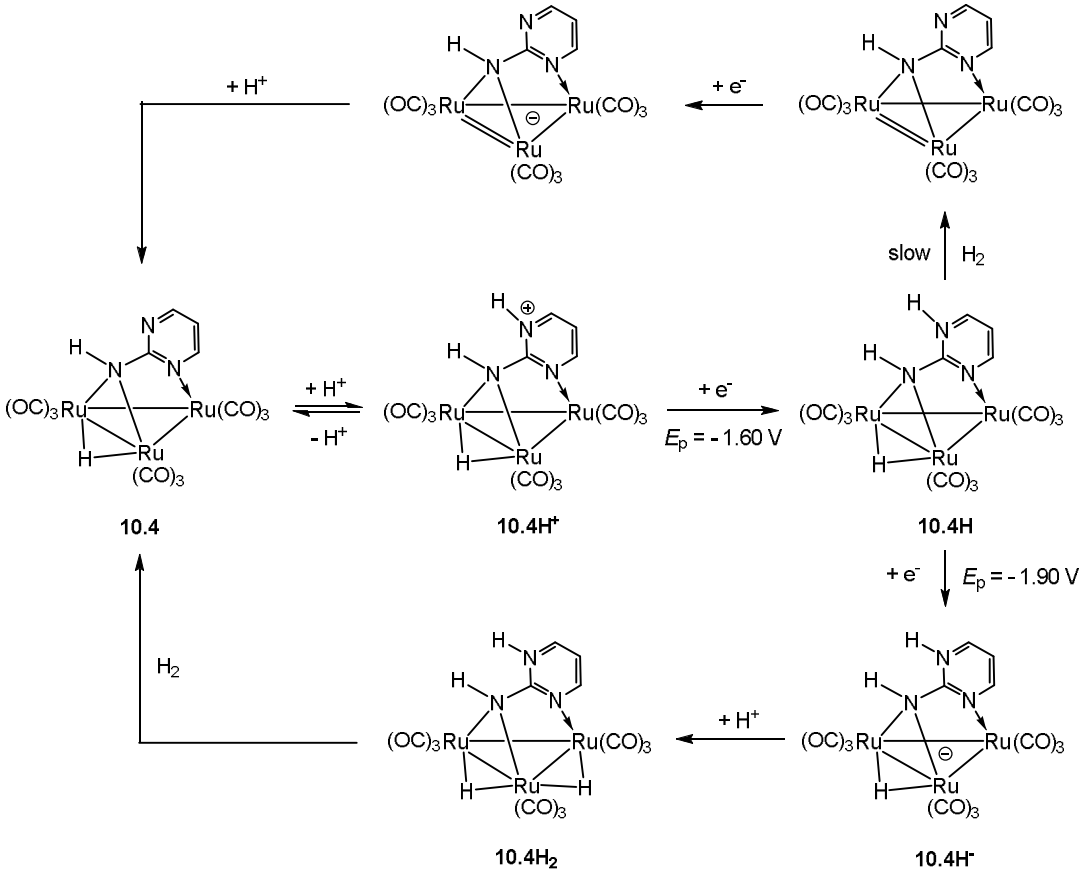

Scheme 10.9. Proposed mechanism for the electrocatalytic proton reduction by $Ru_3(CO)_9(\mu_3\text{-pymNH})(\mu\text{-H})$ (**10.4**).

Akin to the iron clusters, introduction of proton relay alters the catalytic pathway without any improvement of catalytic efficiency and overpotential. A plot of catalytic limiting current against concentration of acid reveals that **10.3** is a better catalysts than **10.4** as the former produces greater current than the later during catalysis (Figure 10.13). Although

10.4 shows catalytic activity at E_p = –1.60 V, a reduction of overpotential by *ca.* 0.4 V compared to the catalytic potential of **10.3** (–2.01 V), the amount of catalytic current is almost negligible at this potential.

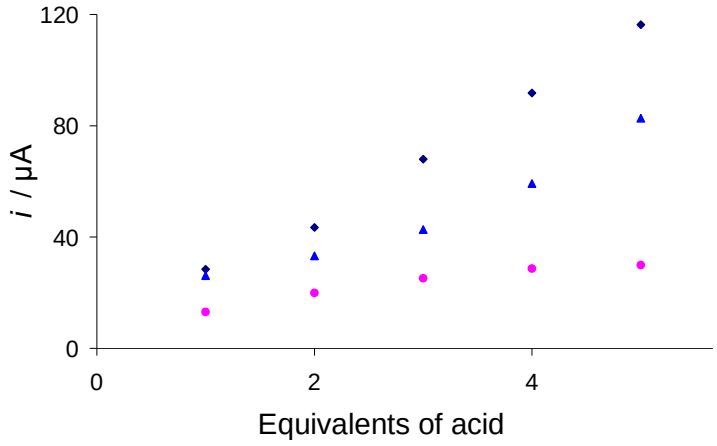

Figure 10.13. Plot of limiting currents *vs.* equivalents of acid added for **10.3** (black diamonds) and **10.4** (pink circles for the first wave and blue triangles for the second wave).

The catalytic limiting currents of **10.3** and **10.4** were also compared with those of their iron analogues **10.1** and **10.2**, respectively, which reveals that the triiron clusters are better catalysts than their triruthenium analogues (Figures 10.14 and 10.15).

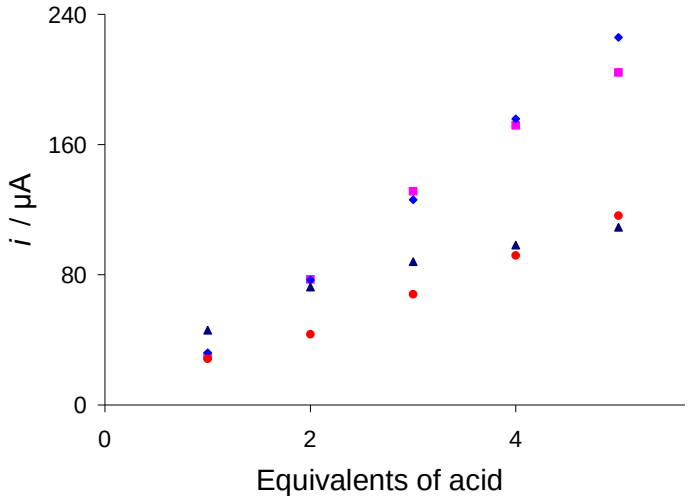

Figure 10.14. Plot of limiting currents *vs.* equivalents of acid added for **10.1** (black triangles for the first wave, pink squares for the second wave and blue diamonds for the third wave) and **10.3** (red circles).

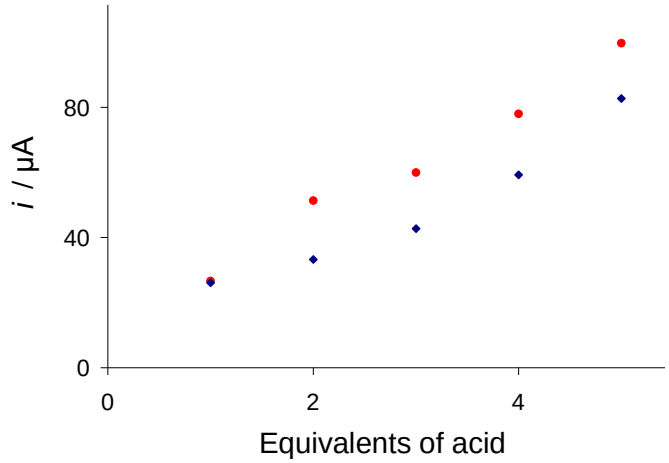

Figure 10.15. Plot of limiting currents *vs.* equivalents of acid added for **10.2** (red circles) and **10.4** (black diamonds).

10.3. Summary and conclusions

The triiron and triruthenium amino pyridinate clusters **10.1**-**10.4** have been prepared and tested as electrocatalysts for proton reduction. All theses clusters contain both acidic and hydridic hydrogens in close proximity as revealed by single crystal X-ray diffraction analysis. In MeCN, CV of each of the triiron clusters display single reduction and oxidation events, while that of the triruthenium clusters exhibit two sequential reductive and oxidative features. All redox events are irreversible in nature due to solvolysis of the resulted ions. The reduction potential of these clusters is sensitive to the nature of the heterocyclic amine which can be easily tuned by modifying the later.

The triiron 2-aminopyridinate cluster (**10.1**) is not protonated by $TsOH{\cdot}H_2O$ used as the proton source during catalysis, whilst the corresponding triruthenium cluster **10.3** slowly reacts with $TsOH{\cdot}H_2O$ to form $\mathbf{10.3H^+}$ in which the incoming proton bridges a Ru–Ru vector. On the other hand, both 2-aminopyrimidinate cluster (**10.2** and **10.4**) undergoes rapid protonation at the free ring nitrogen of the heterocyclic ring. All of them catalyze proton reduction in presence of $TsOH{\cdot}H_2O$ following different mechanisms. Electrocatalytic data suggests that the 2-aminopyridinate clusters (**10.1** and **10.3**) mainly follow an *ECEC* mechanism whereas *CEEC* mechanism dominates the proton reduction pathway of the 2-aminopyrimidinate clusters (**10.2** and **10.4**).

Analysis of catalytic limiting current shows that the 2-aminopyridinate clusters **10.1** and **10.3** are more efficient than the 2-aminopyrimidinate clusters **10.1** and **10.3**. The presence of a proton relay neither increases the efficiency nor reduces the overpotential of catalysis. DFT calculations are ongoing in order to validate the proposed mechanisms. Further studies which involve substitution of one or more carbonyls of **10.1** and **10.3** by basic phosphines to facilitate rapid protonation across metal-metal bond as well as use of more electron withdrawing 2-aminopyridines has been going on to reduce the overpotential of the catalytic process.

10.4. Experimental

10.4.1. General. Unless otherwise stated, all manipulations were carried out under a nitrogen atmosphere using standard Schlenk techniques. Reagent-grade solvents were dried using appropriate drying agents and distilled prior to use by standard methods. Infrared spectra were recorded using a Nicolet 6700 FT-IR spectrometer in a solution cell fitted with calcium fluoride plates, subtraction of the solvent absorptions being achieved by computation. NMR spectra were run on a Bruker AMX400 instrument. All chemical shifts are reported in δ units with reference to the residual protons of the deuterated solvents for proton and to external $P(OMe)_3$ for ^{31}P chemical shifts. Preparative thin layer chromatography was carried out on 0.25 mm plates prepared from silica gel GHLF (UV254, Analtech).

10.4.2. Synthesis of $Fe_3(CO)_9(\mu_3\text{-}pyNH)(\mu\text{-}H)$ (10.1). To a benzene (20 mL) solution of $Fe_3(CO)_{12}$ (500 mg, 0.993 mmol) and $pyNH_2$ (190 mg, 1.997 mmol) was heated to reflux for 1 h. The solvent was removed under vacuum and the residue separated by chromatography on TLC plates. Elution with hexane/CH_2Cl_2/MeCN (5:5:1, v/v) developed four bands on TLC plate. The first and fourth bands were unconsumed $Fe_3(CO)_{12}$ (trace) and $pyNH_2$ (trace) respectively. The third band afforded $Fe_3(CO)_9(\mu_3\text{-}pyNH)(\mu\text{-}H)$ (**10.1**) (21 mg, 4%) as red crystals after recrystallization from hexane/CH_2Cl_2 at 4°C. The contents of the second band were two small for characterisation. Data for **10.1**: IR (νCO, CH_2Cl_2): 2071m, 2032vs, 2010vs, 1981s, 1973sh cm^{-1}. ^1H NMR ($CDCl_3$): δ 8.26 (m, 1H), 7.39 (m, 1H), 6.82 (m, 1H), 6.61 (m, 1H), 3.55 (br, s, 1H), –12.66 (s, 1H). Elemental analysis calc. for $C_{14}H_6Fe_3N_2$ (found): C 32.73 (33.62), H 1.17 (1.26), N 5.45 (5.51).

10.4.3. Synthesis of $Fe_3(CO)_9(\mu_3$-pymNH)(μ-H) (10.2). A benzene (20 mL) solution of $Fe_3(CO)_{12}$ (500 mg, 0.993 mmol) and $pymNH_2$ (190 mg, 1.998 mmol) was heated to reflux for 1 h. The solvent was removed under reduced pressure and the residue chromatographed by TLC on silica gel. Elution with hexane/CH_2Cl_2 (1:1, v/v) developed two bands on the TLC plates. The first band afforded $Fe_3(CO)_9(\mu_3$-pymNH)(μ-H) (**10.2**) (40 mg, 8%) as red crystals after recrystallization from hexane/CH_2Cl_2 at 4°C. The second band was unconsumed $pymNH_2$ (trace). Data for **10.2**: IR ($\nu_{co,}$ CH_2Cl_2): 2074m, 2036vs, 2013vs, 1992s, 1975sh cm^{-1}. ^1H NMR ($CDCl_3$): δ 8.54 (dd, J 5.0, 2.2, 1H), 8.18 (dd, J 5.0, 2.2, 1H), 6.82 (t, J 5.0, 1H), 3.68 (br, s, 1H), –12.65 (s, 1H). Elemental analysis calc. for $C_{13}H_5Fe_3N_2$ (found): C 30.33 (30.82), H 0.98 (1.03), N 8.17 (8.24).
Crystallographic data for **10.2**: red block, dimensions 0.44 × 0.42 × 0.36 mm^3, monoclinic, space group $P2_1n$, a = 10.639(3), b = 11.114(3), c = 14.553(4) Å, α = 90, β = 102.534(4), γ = 90°, V = 1679.8(8) $Å^3$, Z = 4, F(000) 1016, d_{calc} = 2.035 g cm^{-3}, μ = 2.613 mm^{-1}. 13520 reflections were collected, 3922 unique [R(int) = 0.0400] of which 3019 were observed [$I > 2.0\sigma(I)$]. At convergence, R_1 = 0.0308, wR_2 = 0.0665 [$I > 2.0\sigma(I)$] and R_1 = 0.0418, wR_2 = 0.0678 (all data), for 273 parameters.

10.4.4. Synthesis of $Ru_3(CO)_9(\mu_3$-pyNH)(μ-H) (10.3). To a toluene (20 mL) solution of $Ru_3(CO)_{12}$ (100 mg, 0.156 mmol) and $pyNH_2$ (30 mg, 0.319 mmol) was heated to reflux for 90 min. The reaction mixture was then allowed to cool at room temperature and pass through a short column (1 cm) made of silica (0.5 cm) and celite (0.5 cm) with the latter on top. The volatiles from the filtrate were removed by rotary evaporation and the residue redissolved in minimum amount of CH_2Cl_2 (3 mL). A layer of hexane was poured over this solution which was then left standing at room temperature for crystallization. $Ru_3(CO)_9(\mu_3$-pyNH)(μ-H) (**10.3**) (34 mg, 33%) was obtained as orange crystals from this solution after several days. Data for **10.3**: IR (νCO, CH_2Cl_2): 2081m, 2050vs, 2027vs, 1995vs, 1964w cm^{-1}. ^1H NMR ($CDCl_3$): δ 8.15 (dd, J 8.0, 4.0, 1H), 7.44 (m, 1H), 6.77 (m, 1H), 6.57 (d, J 8.0, 1H), 4.46 (br, s, 1H), –11.39 (s, 1H). Elemental analysis calc. for $C_{14}H_6N_2O_9Ru_3$ (found): C 25.89 (26.61), H 0.93(1.01), N 4.31 (4.34).
Crystallographic data for **10.3**: orange block, dimensions 0.40 × 0.20 × 0.16 mm^3, monoclinic, space group $P2_1c$, a = 10.020(2), b = 15.737(4), c = 11.524(3) Å, α = 90, β = 97.259(4), γ = 90°, V = 1802.7(7) $Å^3$, Z = 4, F(000) 1232, d_{calc} = 2.393 g cm^{-3}, μ = 2.533 mm^{-1}. 14158 reflections were collected, 4113 unique [R(int) = 0.0307] of which 3401

were observed [$I > 2.0\sigma(I)$]. At convergence, $R_1 = 0.0214$, $wR_2 = 0.0424$ [$I > 2.0\sigma(I)$] and $R_1 = 0.0289$, $wR_2 = 0.0432$ (all data), for 277 parameters.

10.4.5. Synthesis of $Ru_3(CO)_9(\mu_3$-pymNH)(μ-H) (10.4). A toluene (20 mL) solution of $Ru_3(CO)_{12}$ (100 mg, 0.156 mmol) and $pymNH_2$ (30 mg, 0.315 mmol) was heated to reflux for 90 min. A similar work up described as above afforded $Ru_3(CO)_9(\mu_3$-pymNH)(μ-H) (**10.4**) (42 mg, 41%) as orange crystals. Data for **10.4**: IR (νCO, CH_2Cl_2): 2084m, 2055vs, 2031vs, 2000vs, 1965w cm^{-1}. ^1H NMR ($CDCl_3$): δ 8.42 (dd, J 8.0, 4.0, 1H), 8.20 (dd, J 8.0, 4.0, 1H), 6.76 (t, J 8.0, 1H), 4.55 (br, s, 1H), –11.38 (s, 1H). Elemental analysis calc. for $C_{13}H_5N_3O_9Ru_3$ (found): C 24.00 (24.47), H 0.77 (0.81), N 6.46 (6.53).

Crystallographic data for **10.4**: orange block, dimensions 0.46 × 0.44 × 0.40 mm^3, monoclinic, space group $P2_1/n$, a = 10.751(2), b = 11.279(2), c = 15.009(3) Å, α = 90, β = 102.088(3), γ = 90°, V = 1779.6(5) $Å^3$, Z = 4, F(000) 1232, d_{calc} = 2.428 g cm^{-3}, μ = 2.568 mm^{-1}. 13869 reflections were collected, 4082 unique [R(int) = 0.0343] of which 3614 were observed [$I > 2.0\sigma(I)$]. At convergence, $R_1 = 0.0221$, $wR_2 = 0.0518$ [$I > 2.0\sigma(I)$] and $R_1 = 0.0260$, $wR_2 = 0.0527$ (all data), for 274 parameters.

10.5. References

(1) S. Ghosh, G. Hogarth, K. B. Holt, S. E. Kabir, A. Rahaman and D. G. Unwin, *Chem. Commun.*, 2011, **47**, 11222-11224.

(2) A. Rahaman, S. Ghosh, D. G. Unwin, S. Basak-Modi, K. B. Holt, S. E. Kabir, E. Nordlander, M. G. Richmond and G. Hogarth, *Organometallics*, 2014, **33**, 1356-1366.

(3) Z. Li, X. Zeng, Z. Niu and X. Liu, *Electrochimica Acta*, 2009, **54**, 3638-3644.

(4) J. Yeo, M. H. Cheah, M. I. Bondin and S. P. Best, *Aust. J. Chem.*, 2012, **65**, 241-253.

(5) W. Gao, J. Sun, M. Li, T. Åkermark, K. Romare, L. Sun and B. Åkermark, *Eur. J. Inorg. Chem.*, 2011, 1100-1105.

(6) C. A. Mebi, K. E. Brigance and R. B. Bowman, *J. Braz. Chem. Soc.*, 2012, **23**, 186-189.

(7) M. H. Cheah, C. Tard, S. J. Borg, X. Liu, S. K. Ibrahim, C. J. Pickett and S. P. Best, *J. Am. Chem. Soc.*, 2007, **129**, 11085-11092.

(8) C. Tard, X. Liu, D. L. Hughes and C. J. Pickett, *Chem. Commun*., 2005, 133-135.

(9) H.J. Fan and M.B. Hall, *J. Am. Chem. Soc.*, 2001, **123**, 3828-3829.

(10) C. Greco, M. Bruschi, L. D. Gioia and U. Ryde, *Inorg. Chem.* **2007**, *46*, 5911.

(11) A. J. Cornish, K. Gärtner, H. Yang, J. W. Peters and E. L. Hegg, *J. Biol. Chem.*, 2011, **286**, 38341-38347.

(12) B. E. Schultz and S. I. Chan, *Annu. Rev. Biophys. Biomol. Struct.*, 2001, **30**, 23-65.

(13) S. Cukierman, *Biochim. Biophys. Acta*, 2006, **1757**, 876-885.

(14) S. J. Whitehead, M. Iwaki, N. P. Cotton, P. R. Rich and J. B. Jackson, *Biochim. Biophys. Acta*, 2009, **1787**, 1276-1288.

(15) J. A. Cabeza, *Eur. J. Inorg. Chem.*, 2002, 1559-1570.

(16) J. A. Cabeza, I. del Río, M. Moreno, S. García-Granda, M. Pérez-Priede and V. Riera, *Eur. J. Inorg. Chem.*, 2002, 3204-3209.

(17) P. L. Andreu, J. A. Cabeza and V. Riera, *J. Chem. Soc., Dalton Trans.*, 1990, 2201-2206.

(18) P. L. Andreu, J. A. Cabeza, V. Riera, C. Bois and Y. Jeannin, *J. Organomet. Chem.*, 1990, **384**, C25-C28.

(19) P. L. Andreu, J. A. Cabeza and V. Riera, *J. Chem. Soc., Dalton Trans.*, 1990, 3347-3353.

(20) P. L. Andreu, J. A. Cabeza, M. A. Pellinghelli and V. Riera, *Inorg. Chem.*, 1991, **30**, 4611-4616.

(21) P. L. Andreu, J. A. Cabeza, J. L. Cuyás and V. Riera, *J. Organomet. Chem.*, 1992, **427**, 363-368.

(22) J. A. Cabeza, I. del Río, P. García-Álvarez and D. Miguel, *Can. J. Chem.*, 2006, **84**, 105-110.

(23) J. A. Cabeza, I. del Río, S. García-Granda, L. Martínez-Méndez, M. Moreno and V. Riera, *Organometallics*, 2003, **22**, 1164-1166.

(24) J. A. Cabeza, I. del Río, S. García-Granda, M. Moreno, E. Pérez-Carreño and M. Suárez, *Organometallics*, 2004, **23**, 5849-5855.

(25) B. F. G. Johnson and A. Rodgers, in *The Chemistry of Metal Cluster Complexes*, Eds. D. F. Shriver, H. D. Kaesz and R. D. Adams, 1990, 303-325.

(26) K. Izutsu, in *Acid-Base Dissociation Constants in Dipolar Aprotic Solvents*, Blackwell Scientific Publications, Oxford, 1990.

(27) M. I. Bruce, B. K. Nicholson and M. L. Williams, *Inorg. Synth.*, 1990, **28**, 221-230.

Chapter 11

Conclusions

The work presented in this thesis detailed the synthesis, structure and electrocatalytic proton reduction by a variety of iron complexes. The inspiration of this work stems from nature as it has been doing reversible reduction of protons and electrons into H_2 efficiently for billions of years, using a group of metalloenzymes collectively known as hydrogenase. In this thesis, we reported some biomimetic models of the active site of one such enzyme namely the [FeFe]-hydrogenase together with a number of non-biomimetic catalysts developed alongside with biomimetic models.

In chapter 2, we reported the synthesis, structure, chelate-bridge isomerisation and electrocatalytic proton reduction by diiron biomimics containing 2,2'-bis(diphenyl-phosphino)propane. Although a large number of diiron-dithiolate complexes containing either a chelating or a bridging diphosphine have been made and tested for electrocatalytic proton reduction, the chelate-bridge isomerisation within these complexes is relatively neglected which prompted us to investigate such isomerisation using 2,2'-bis(diphenylphosphino)propane, a diphosphine well-known for its ability to coordinate metal centre(s) in both chelating and bridging fashions. Both isomers were prepared and structurally characterised with the bridged isomer being thermodynamically favoured as indicated by both experimental observations and theoretical investigations. A plausible mechanism was also proposed for conversion of the chelate isomer $Fe_2(CO)_4\{\kappa^2\text{-}Ph_2PC(Me_2)PPh_2\}(\mu\text{-pdt})$ (**2.1**) to the bridged isomer $Fe_2(CO)_4\{\mu\text{-}Ph_2PC(Me_2)PPh_2\}(\mu\text{-pdt})$ (**2.2**). The chelate isomer **2.1** was found to catalyse proton reduction in presence of a proton source and DFT methods were applied to validate the mechanism proposed for this catalytic process.

Biomimetic models containing redox-active ligand were reported in chapters 3-5. The incorporation of electrochemically non-innocent ligand within the biomimetic models was stimulated by the fact that the electronic communication between the diiron and tetrairon sites in the active site of [FeFe]-hydrogenase controls its activity and is also responsible for its high efficiency. In chapter 3, we reported the synthesis, structure and electrocatalytic properties of diiron biomimics $Fe_2(CO)_4(\kappa^2\text{-}2,2'\text{-bipy})(\mu\text{-edt})$ (**3.1-edt**) and $Fe_2(CO)_4(\kappa^2\text{-}1,10\text{-phen})(\mu\text{-edt})$ (**3.2-edt**) containing redox-active diamines 2,2′-

bipyridine and 1,10-phenanthroline respectively. Both of them showed complex redox-properties and were found to catalyse proton reduction. DFT calculations have been ongoing to get better understanding about the redox-behaviour of these complexes. This work also revealed that the electrocatalytic pathway of diiron biomimics containing these diamines can be influenced significantly by a small change in dithiolate backbone.

Biomimetic model complex $Fe_2(CO)_4(\kappa^2\text{-bpcd})(\mu\text{-edt})$ (**4.2**) that contains the non-innocent diphosphine 4,5-bis(diphenylphosphino)-4-cyclopenten-1,3-dione (bpcd) was reported in chapter 4. Both chemical oxidation and electrocatalytic studies indicated electronic communication between the diiron core and coordinated bpcd ligand within this complex. In both instances, it has been found that the coordinated bpcd ligand give electron(s) to the diiron core. DFT calculations have been ongoing to fully understand this intra-molecular electron transfer (ET) in **4.2**. The catalytic efficiency of **4.2** was found to be similar to that of 1,2-bis(diphenylphosphino)ethene (dppv) complex $Fe_2(CO)_4(\kappa^2\text{-dppv})(\mu\text{-edt})$ (**4.3**) which implies that the intra-molecular electron transfer in **4.2** during catalysis does not improve its catalytic efficiency.

Biomimetic model catalyst $Fe_2(CO)_4(\mu\text{-dppf})(\mu\text{-pdt})$ (**5.1**) which contains a bridging 1,1′-bis(diphenylphosphino)ferrocene (dppf) ligand was reported in chapter 5. Complex **5.1** is the first diiron biomimic that has been shown to catalyse both proton reduction and dihydrogen oxidation. Intra-molecular electron transfer from the diiron core to the ferrocene iron plays key role during H_2 oxidation by this complex as indicated by electrocatalytic data. Theoretical investigations are currently ongoing to shed light on this electron transfer process in **5.1**.

Since the substrate (H^+ or H_2) binding and the hydride-proton reaction occur exclusively at the iron distal to the Fe4S4 cluster within the active site of [FeFe]-hydrogenase, we have prepared several non-biomimetic model complexes which show close structural resemblance to the distal iron of the active site. The octahedral mononuclear complexes $Fe(CO)_2(\kappa^2\text{-dppv})(\kappa^1\text{-SR})_2$ (**6.1**, R = C_6F_5; **6.2**, R = Ph; **6.3**, R = $C_6H_4CH_3$-*p*) reported in chapter 6 were found to protonate at sulphur atom(s) and then lose a thiol to create a vacant coordination site on iron. The resultant penta-coordinated $Fe(CO)_2(\kappa^2\text{-dppv})(\kappa^1\text{-SR})$ is the actual catalytically active species as shown by spectroscopic and electrocatalytic data. In chapter 7, we reported electrocatalytic proton reduction by the

mononuclear square-pyramidal complex $Fe(CO)(\kappa^2\text{-dppn})(\kappa^2\text{-tdt})$ (**7.2**). This complex already has a free coordination site for proton binding and show complex redox-features due to the electronic influence of the coordinated 1,1′-bis(diphenylphosphino)-naphthalene (dppn). DFT calculations have been ongoing to get better understanding of its redox-responses and also to validate the proposed mechanism for electrocatalytic proton reduction.

Chapters 8-10 detailed electrocatalytic proton reduction by low-valent iron carbonyl clusters. The use of such clusters as proton reduction catalysts was inspired by the fact that the highly delocalised nature of the bonding within the cluster core often leads to low reduction potentials and stable reduced species. The tetrairon-oxo cluster $Fe_4(CO)_{10}(\kappa^2\text{-dppn})(\mu_4\text{-O})$ (**8.1**) reported in chapter 8 that contains an electronegative oxygen within the cluster core was found to be catalytically active in its doubly reduced (2^-) state whereas the radical anions of the thiolate-capped triiron clusters $Fe_3(CO)_9(\mu_3\text{-SR})(\mu\text{-H})$ (**9.1**, R = ^{i}Pr; **9.2**, R = ^{t}Bu) were found to reduce protons into H_2 under electrochemical conditions as reported in chapter 9. The thiolate-capped triiron clusters **9.1** and **9.2** were stable in presence of a wide variety of acids (pK_a ranging from 0.1 to 22.3) but the tetrairon-oxo cluster **8.1** degrades rapidly in presence of strong acids such as $HBF_4{\cdot}Et_2O$ ($pK_a \approx 0.1$ in MeCN).

The synthesis, structure and electrocatalytic proton reduction by triiron aminopyridinate clusters were reported in chapter 10. These clusters contain a bridging hydride and a residual amino-hydrogen in close proximity, as shown by single crystal X-ray diffraction analysis, much like the enzyme's active site during catalysis. Their reduction potentials can be tuned by simple modification of the heterocyclic ring as shown by cyclic voltammetry. These clusters were shown to catalyse proton-reduction under electrochemical conditions and the catalytic pathway followed by them depends on the presence or absence of artificial proton relay. Electrocatalytic proton reduction by analogous triruthenium aminopyridinate clusters were also detailed in this chapter.

Appendix I

Electrochemistry

The electrochemical behaviour of the reported complexes and their proton reduction ability have been studied by cyclic voltammetry, which is the most common electroanalytical technique used for the determination of redox reaction parameters. In this technique, the potential of an electrode is varied with time in a preset manner with the current passed through this electrode being measured simultaneously (Figure S1a). During the experiment the potential is swept from a value where the molecule under investigation is redox inactive (*i.e.* no electrochemical reaction takes place) to a value where oxidation or reduction occurs; this is followed by a backward sweep of the potential to the initial value. The resulting plot of the applied potential *vs.* the measured current is known as a cyclic voltammogram (Figure S1b) and generally contains peaks on both forward and return scans. The magnitude of the peak is called the peak current whilst its position along the potential axis is termed as peak potential. Using the values of peak current and peak potential obtained from a cyclic voltammogram for a particular electron transfer reaction, a number of thermodynamic and kinetic parameters associated with that redox reaction can be deduced.

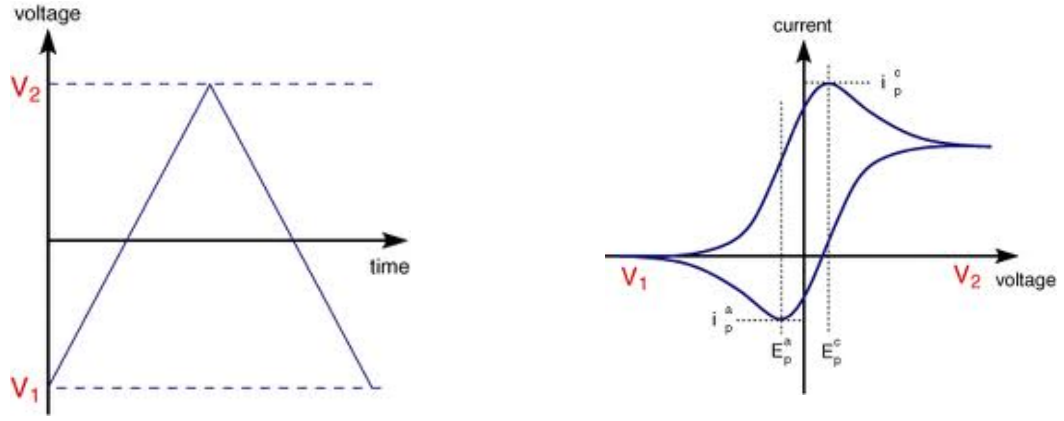

(a) (b)

Figure S1. The potential-time (a) and potential-current (b) relationship in cyclic voltammetry.

The shape of a peak on a cyclic voltammogram depends on both chemical and electrochemical reversibility of the redox process. For a chemically reversible system, the peak current for the forward and reverse scans are equal which simply indicates that the electrogenerated species is stable on the voltammogram timescale. The

electrochemical reversibility depends on the rate of the heterogeneous electron-transfer reaction within the timescale of the voltammogram. Electrochemical reversibility is observed when the rate of the heterogeneous electron-transfer is very large, and for an electrochemically reversible one-electron process, the peaks for the forward and reverse scans are always separated by ~ 59 mV (298 K); that is $\Delta E_p = |E_p^{ox} - E_p^{red}| = 59$ mV where E_p^{ox} and E_p^{red} are the anodic and cathodic peak potentials respectively. The voltammogram for an electrochemically and chemically irreversible process does not show a peak on the reverse scan which means that the electrogenerated species is consumed rapidly in a subsequent process such as a redox-initiated chemical reaction, deposition on the electrode surface or even complete decomposition. Many electrochemical reactions show intermediate redox kinetics which are termed as quasi-reversible.

The size of the peak current for a reversible reaction is given by the following equation:

$$i_p = (2.69 \times 10^5)\, n^{3/2} A D^{1/2} C v^{1/2}$$

where n is the number of electrons transferred, A is area of the electrode (cm^2), D is the diffusion constant (cm^2s^{-1}), C is the bulk concentration ($molcm^{-3}$) and v is the scan rate (Vs^{-1}). As for a reversible reaction the peak current (i_p) varies with the square root of the scan rate (v), by plotting these experimental values further information on the electrode kinetics can be obtained.

Typically a three electrode set up is used for cyclic voltammetry (Figure S3), The three electrodes are termed as the working electrode (WE), where the reaction of interest occurs, the reference electrode (RE), which provides a stable potential to measure against, and a counter or auxiliary electrode (CE) to complete the circuit. During the experiment the RE is placed as close to the WE as possible to minimize the voltage drop in solution and the current is only allowed to flow around the circuit between WE and CE to preserve the chemical composition of the RE throughout the measurement. Typically the mass transport of the substances during the experiment is allowed to occur only by diffusion which means that the redox reaction at the electrode only affects the molecules within the diffusion layer of the electrode. As a result only irreversible peaks are observed during electrochemical proton reduction, since the H_2 molecules formed during

catalysis leave the system. The height of the catalytic peak increases with the concentration of acid and the voltammograms obtained by varying the concentration of acids also provide qualitative information about catalytic efficiency. The simple ratio of the catalytic current and the current for the reduction of the catalyst in absence of acid gives a qualitative description of the catalytic efficiency [1]. According to this method the catalytic efficiency (*C.E.*) is given by the following equation:

$$C.E. = (i_{cat} / i_d) / (C_{HA} / C_{cat})$$

where i_{cat} = catalytic current, i_d = current for reduction of the catalyst in absence of acid, C_{HA} = concentration of acid, C_{cat} = concentration of catalyst. The catalytic current is proportional to concentration of acid since the catalytic current is controlled by the diffusion of acid (HA) to the electrode when maximum efficiency is obtained; i_d , on the other hand, is related to C_{cat}. The value of the catalytic efficiency (*C.E.*) calculated using this method varies between 0 and 1. The *C.E.* becomes zero when i_{cat} is zero i.e., when there is no catalytic current at all, while at maximum efficiency *C.E.* will equal unity. Accordingly, a strong catalyst should have *C.E.* > 0.75.

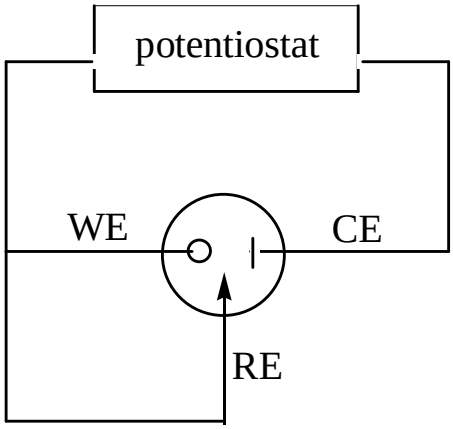

Figure S3. Schematic representation of the experimental setup for cyclic voltammetry.

The electrochemistry (cyclic voltammetry) of the reported complexes was carried out in deoxygenated acetonitrile (MeCN) solution with tetrabutylammonium hexafluorophosphate ($TBAPF_6$) as the supporting electrolyte. The working electrode was a 3 mm diameter glassy carbon electrode which was polished with 0.3 μm alumina slurry prior to each scan. The counter electrode was a Pt wire and the quasi-reference electrode

was a silver wire. All CVs were referenced to the Fc/Fc^+ redox couple. An Autolab potentiostat (EcoChemie, Netherlands) was used for all electrochemical measurements. Catalysis studies were carried out by adding equivalents of acid ($HBF_4 \cdot Et_2O$, $TsOH \cdot H_2O$, CF_3CO_2H) purchased from Sigma-Aldrich.

Reference

(1) G. A. N. Felton, C. A. Mebi, B. J. Petro, A. K. Vannucci, D. H. Evans, R. S. Glass and D. L. Lichtenberger, *J. Organomet. Chem.*, 2009, **694**, 2681-2699.

Appendix II

X-ray structure determination

Single crystals of **2.1-2.3, 3.1-edt, 3.2-edt, 5.1, 10.2-10.4** were mounted on glass fibres and all geometric and intensity data were taken from these samples using a Bruker SMART APEX CCD diffractometer using graphite-monochromated Mo-Kα radiation (λ = 0.71073 Å) at 150 ± 2 K. Data collection, indexing and initial cell refinements were all done using SMART [1] software. Data reduction were carried out with SAINT PLUS [2] and absorption corrections applied using the programme SADABS [3]. Structures were solved by direct methods or Patterson methods and developed using alternating cycles of least-squares refinement and difference-Fourier synthesis. All non-hydrogen atoms were refined anisotropically. Hydrogens were placed in calculated positions (riding model). Structure solution used SHELXTL PLUS V6.10 program package [4].

Single crystals of **7.2** was mounted on a SuperNova, Dual, Cu at zero, Atlas diffractometer. The crystal was kept at 134(1) K during data collection. Using Olex2 [5], the structure was solved with the ShelXS [4] structure solution program using Direct Methods and refined with the olex2.refine [6] refinement package using Gauss-Newton minimisation.

Single crystals of **9.1** was mounted on a SuperNova, Dual, Cu at zero, Atlas diffractometer. The crystal was kept at 150 K during data collection. Using Olex2 [5], the structure was solved with the Superflip [7-9] structure solution program using Charge Flipping and refined with the olex2.refine [6] refinement package using Gauss-Newton minimisation.

Single-crystal X-ray diffraction experiment for **4.2** and **6.1-6.3** were conducted on a Rigaku Saturn CCD diffractometer (λ = 0.6889 Å) on Station I19 at the Diamond Light Source [10].

References

(1) SMART Version 5.628; Bruker AXS, Inc., 5465 East Cheryl Parkway, Madison, WI 53711-5373, 2003.

(2) SAINT Version 6.36A; Bruker AXS, Inc., 5465 East Cheryl Parkway, Madison, WI 53711-5373, 2002.

(3) G. M. Sheldrick, SADABS Version 2.10; University of Göttingen, Göttingen, Germany, 2003.

(4) G. M. Sheldrick, A short history of SHELX. *Acta Crystallogr.*, 2008, **A64**, 112.

(5) O. V. Dolomanov, L. J. Bourhis, R. J. Gildea, J. A. K. Howard and H. Puschmann, *J. Appl. Cryst.*, 2009, **42**, 339-341.

(6) L. J. Bourhis, O. V. Dolomanov, R. J. Gildea, J. A. K. Howard and H. Puschmann, 2013, in preparation.

(7) L. Palatinus and Chapuis, *J. Appl. Cryst.*, 2007, **40**, 786-790.

(8) L. Palatinus and A. van der Lee, *J. Appl. Cryst.*, 2008, 41, 975-984.

(9) L. Palatinus, S. J. Prathapa and S. van Smaalen, *J. Appl. Cryst.*, 2012, 45, 575- 580.

(10) H. Nowell, S. A. Barnett, K. E. Christensen, S. J. Teat and D. R. Allan, *J. Synchrotron Rad.*, 2012, **19**, 435-441.

Appendix III

Computational methodology

All calculations were performed with the hybrid DFT functional B3LYP, as implemented by the Gaussian 09 program package [1]. This functional utilizes the Becke three-parameter exchange functional (B3) [2], combined with the correlation functional of Lee, Yang and Parr (LYP) [3]. The iron atoms were described by Stuttgart–Dresden effective core potentials (ecp) and a SDD basis set, while the 6-31G(d′) basis set, as implemented in the Gaussian09 program suite, was employed for the remaining atoms. Zero imaginary frequencies (positive eigenvalues) correspond to an intermediate or minimum, and an imaginary frequency (negative eigenvalue) designates a transition state. All transition states on the potential energy surface were evaluated by IRC calculations. The computed frequencies were used to make zero-point and thermal corrections to the electronic energies; the reported potential energies and enthalpies are quoted in kcal mol^{-1} relative to the specified standard. The natural charges and Wiberg bond indices reported here were computed using Weinhold's natural bond orbital (NBO) program, as executed by Gaussian 09 [4,5]. The geometry-optimized structures have been drawn with the JIMP2 molecular visualization and manipulation program [6,7].

References

(1) M. J. Frisch, G. W. Trucks, H. B. Schlegel, G. E. Scuseria, M. A. Robb, J. R. Cheeseman, G. Scalmani, V. Barone, B. Mennucci, G. A. Petersson, H. Nakatsuji, M. Caricato, X. Li, H. P. Hratchian, A. F. Izmaylov, J. Bloino, G. Zheng, J. L. Sonnenberg, M. Hada, M. Ehara, K. Toyota, R. Fukuda, J. Hasegawa, M. Ishida, T. Nakajima, Y. Honda, O. Kitao, H. Nakai, T. Vreven, J. A. Montgomery Jr., J. E. Peralta, F. Ogliaro, M. Bearpark, J. J. Heyd, E. Brothers, K. N. Kudin, V. N. Staroverov, R. Kobayashi, J. Normand, K. Raghavachari, A. Rendell, J. C. Burant, S. S. Iyengar, J. Tomasi, M. Cossi, N. Rega, J. M. Millam, M. Klene, J. E. Knox, J. B. Cross, V. Bakken, C. Adamo, J. Jaramillo, R. Gomperts, R. E. Stratmann, O. Yazyev, A. J. Austin, R. Cammi, C. Pomelli, J. W. Ochterski, R. L. Martin, K. Morokuma, V. G. Zakrzewski, G. A. Voth, P. Salvador, J. J. Dannenberg, S. Dapprich, A. D. Daniels, O. Farkas, J. B.

Foresman, J. V. Ortiz, J. Cioslowski and D. J. Fox, GAUSSIAN 09 (Revision A.02), Gaussian, Inc., Wallingford, CT, 2009.

(2) A. D. Becke, *J. Chem. Phys.*, 1993, **98**, 5648-5652.

(3) C. Lee, W. Yang and R. G. Parr, *Phys. Rev. B: Condens. Matter*, 1988, 37, 785-789.

(4) A. E. Reed, L. A. Curtiss and F. Weinhold, *Chem. Rev.*, 1988, **88**, 899-926.

(5) K. B. Wiberg, *Tetrahedron*, 1968, **24**, 1083-1096.

(6) JIMP2, version 0.091, a free program for the visualization and manipulation of molecules: M. B. Hall and R. F. Fenske, *Inorg. Chem.*, 1972, **11**, 768-775.

(7) J. Manson, C. E. Webster and M. B. Hall, Texas A&M University, College Station, TX, 2006, http://www.chem.tamu.edu/jimp2/index.html.